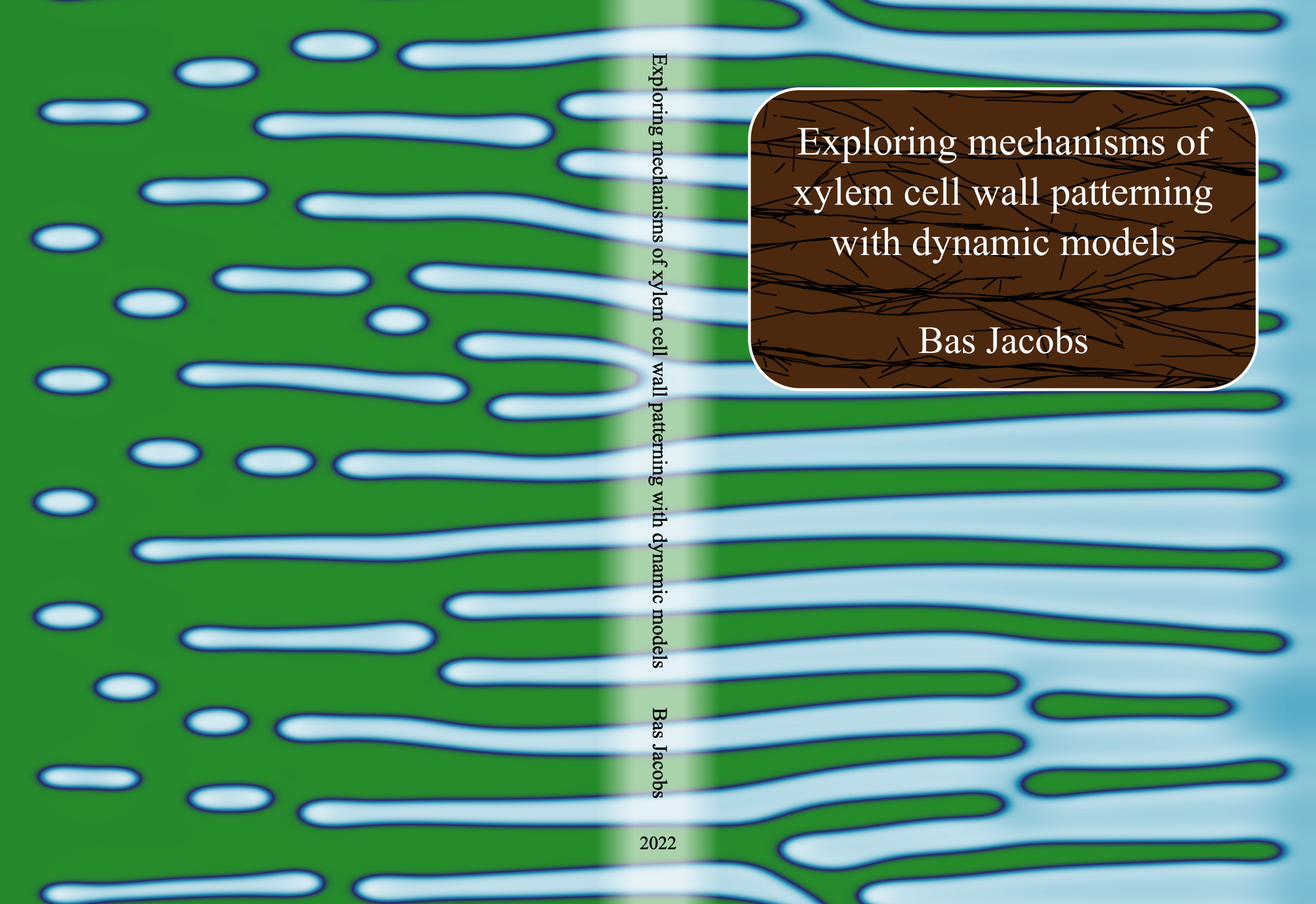

Exploring mechanisms of xylem cell wall patterning with dynamic models

Bas Jacobs

2022

Propositions

1. Protoxylem patterning requires a mutual interaction between microtubules and Rho of Plant (ROP) proteins.
   (this thesis)

2. Pattern coarsening is a mathematically convenient, but not a biologically plausible mechanism for formation of a pattern of a single cluster.
   (this thesis)

3. A full scientific explanation of a phenomenon does not only describe which interactions give rise to it, but also *how*.

4. The current fashion of creating digital twins promotes a fundamental misunderstanding of what a model is among the general public.

5. The higher the impact factor of a journal, the more critically readers should evaluate the validity of its content.

6. The benefits to scientific collaborations are usually insufficient justification for environmentally unfriendly long distance travel.

7. To demand ethical justification for every animal used in experiments, but not for all those used in food production, is an awkward double standard.

Propositions belonging to the thesis, entitled

Exploring mechanisms of xylem cell wall patterning with dynamic models

Bas Jacobs
Wageningen, 1 July 2022

Exploring mechanisms of xylem cell wall patterning with dynamic models

Bas Jacobs

Thesis committee

Promotor
Prof. Dr Jaap Molenaar
Professor of Applied Mathematics
Wageningen University & Research

Co-promotor
Dr Eva E. Deinum
Assistant professor, Mathematical and Statistical Methods - Biometris
Wageningen University & Research

Other members
Prof. Dr Dolf Weijers, Wageningen University & Research
Prof. Dr Bela M. Mulder, Utrecht University
Prof. Dr Kirsten H.J.W. ten Tusscher, Utrecht University
Dr Liedewij Laan, Delft University of Technology

This research was conducted under the auspices of the Graduate School of Experimental Plant Sciences.

Exploring mechanisms of xylem cell wall patterning with dynamic models

Bas Jacobs

Thesis
submitted in fulfilment of the requirements for the degree of doctor
at Wageningen University
by the authority of the Rector Magnificus
Prof. Dr A.P.J. Mol,
in the presence of the
Thesis Committee appointed by the Academic Board
to be defended in public
on Friday 1 July 2022
at 11 a.m. in the Omnia Auditorium.

Bas Jacobs
Exploring mechanisms of xylem cell wall patterning with dynamic models
246 pages

PhD thesis, Wageningen University, Wageningen, the Netherlands (2022)
With references, with summaries in English and Dutch

ISBN: 978-94-6447-219-6
DOI: 10.18174/569429

Contents

1

General introduction

1.1 Xylem cell wall patterning

Plants need water to grow, and even the tallest trees acquire their water via their roots, which poses a challenge in transporting this water from the roots all the way up to the leaves. To meet this challenge, plants possess a system of vessels known as the xylem. Water transport through these xylem vessels is thought to be driven by evaporation of water at the leaves, creating a negative pressure that pulls the water trapped in the vessels upwards (the 'cohesion-tension theory') [1]. The walls of the xylem vessels must be strong enough to withstand this negative pressure, otherwise they would collapse, blocking water transport [2].

Xylem vessels are formed by cells that deposit thick secondary cell wall reinforcements after which they undergo programmed cell death [3, 4]. The secondary cell wall depositions give the xylem vessels their strength [5] and show a variety of intricate and highly functional patterns, in particular in primary xylem, the xylem that develops first in the growing tips of roots and shoots. Primary xylem exists in two types: protoxylem and metaxylem [6]. Protoxylem develops first, when the surrounding tissue is still elongating and must be able to expand along with it. Therefore, protoxylem cell walls are reinforced in rings or spirals. Metaxylem develops when this expansion has stopped, and can therefore be more rigid and durable. Consequently, its secondary cell wall only contains some regularly spaced pits for radial transport [7–9] (Fig 1.1).

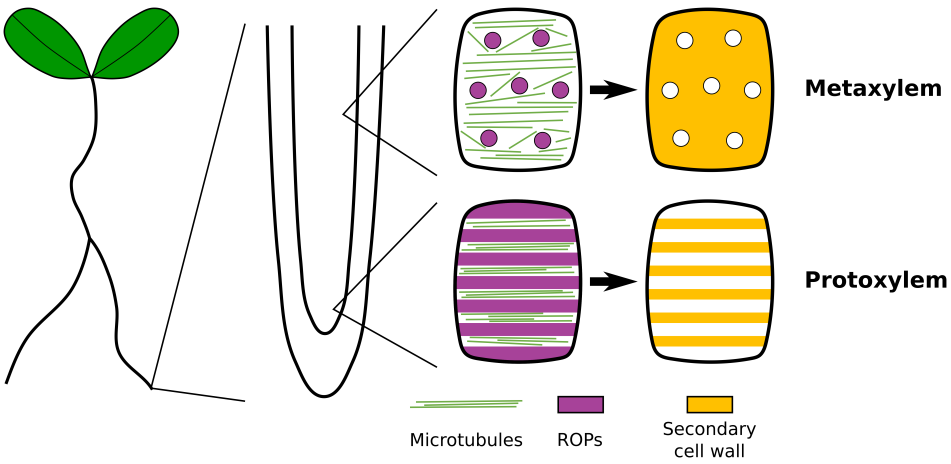

Fig. 1.1. Primary xylem patterning. Patterned secondary cell walls follow an underlying pattern of cortical microtubules, which is specified by the local activity of ROP proteins at places where microtubules are absent. Early developing protoxylem forms ringed or spiral cell wall reinforcements to allow further stretching, whereas later developing metaxylem forms a more rigid secondary cell wall with regular gaps for radial transport.

This thesis is about trying to understand these patterning processes. Models are useful tools to increase our understanding of patterning processes, both to test if a proposed set of biological interactions can in principle explain the observed patterns, and to explore and understand the underlying mechanisms through which these interactions form the pattern. Well-known examples of patterns that have been modelled include coloured patterns on fur [10, 11], skin [12–14], or shells [15, 16], and patterned growth of vegetation [17–21].

These patterns have mostly been modelled with so-called reaction-diffusion mechanisms that will be covered in more detail below. Patterning processes, however, are much more abundant and diverse than those examples. They also include, for example, the regular spacing of hairs [22], feathers [23], and trichomes (leaf hairs) [24], and the positioning of our digits [25], plant vascular bundles [26], lateral roots [27, 28] and root nodules [29]. Models have also been vital in understanding patterning processes within a cell. Examples include processes that determine cell shape [30, 31] and cell wall structure [32, 33], but also processes that establish cell polarity, e.g., for directed movement [34], tip growth [35–37], or cell division [38–42].

At the cellular level, two vital molecular players often play a role in patterning processes at the cell membrane: small GTPases and the cytoskeleton. In xylem patterning, ROP (Rho of Plants) proteins (the small GTPases of plants) and microtubules (part of the cytoskeleton) interact to generate the final cell wall pattern [43] (Fig 1.1). It is this interaction that makes developing xylem a particularly interesting model system for understanding spatial organisation at the cellular level. Furthermore, their molecular properties allow ROPs and other small GTPases to spontaneously form patterns through reaction-diffusion mechanisms [44, 45]. Therefore, I will first discuss the concept and applicability of these reaction-diffusion systems. Then, I will introduce small GTPases and microtubules and their models in more detail, before returning to our current understanding of their interaction in xylem patterning and the gaps in our knowledge that this thesis aims to fill.

1.2 Pattern formation mechanisms

1.2.1 Reaction-diffusion mechanisms

Reaction-diffusion mechanisms are a well-known way of spontaneous pattern formation. Reaction-diffusion systems can spontaneously give rise to a heterogeneous pattern from an initially homogeneous state with a small amount of random noise. They were first proposed as a patterning mechanism for morphogenesis by Alan Turing in 1952 [46], with major contributions towards biological applications by Gierer and Meinhardt [47]. Classically, these mechanisms are based on local self-enhancement and long-range inhibition of a diffusive activator, with many variants that are mathematically equivalent at a deep level [48, 49]. Interestingly, diffusion is actually essential to this type of patterning, even though it is usually associated with homogenisation.

The two best known examples are activator-inhibitor and activator-substrate-depletion models. In the former, a slowly diffusing activator induces the production of a fast diffusing inhibitor, such that self-amplification of the activator can occur locally, while the resulting production of inhibitor prevents the same in the surrounding area. In substrate-depletion models, a slowly diffusing activator consumes a fast diffusing substrate, such that local self-amplification drains the substrate from the surrounding area, preventing further activator accumulation in this drained area. Both these mechanisms satisfy the criteria of local self-enhancement and long range inhibition [47]. On two-dimensional spatial domains, both mechanisms are able to create a wide variety of patterns, including spots, stripes, and gaps, depending on the precise structure of the model, the parameter values, and the shape and size of the domain. [50–52].

1.2.2 Not every pattern is a Turing pattern

Since Turing-style reaction-diffusion systems offer a convenient description of spontaneous pattern formation, it is tempting to see Turing patterns everywhere. However, there are alternative ways of pattern formation, especially when some form of positional information is already available. A classical model for these situations is the so-called 'French flag model', in which a gradient of a so-called 'morphogen' provides positional information that can be used to divide a domain into distinct regions [53]. Such a gradient may be formed, for example, by local production and subsequent diffusion of a signal molecule. In multicellular systems, a secondary pattern can then be formed by expression of genes above or below certain morphogen concentration thresholds [54]. In *Drosophila*, a periodic pattern of 14 bands along the length of the embryo, with alternating expression of so-called pair-rule genes, is affected by multiple morphogen gradients, rather than a Turing mechanism [55, 56]. Alternatively, a periodic pattern may be generated by a moving wavefront that triggers a different response depending on the status of an oscillator. This 'clock and wavefront' mechanism is implicated in segmentation in a variety of other arthropods than *Drosophila* [57] as well as in vertebrate somitogenesis [58].

In general, we can expect these kind of mechanisms when pre-existing polarity information is required (e.g, the orientation of the body axis), whereas Turing patterns excel in forming periodic patterns in absence of such information, merely specifying distances between spots or stripes [59]. Sometimes, a Turing pattern must be combined with pre-existing polarity information to obtain a regular pattern in the right orientation. For example, in digit specification, a Turing mechanism specifies which cells become digits, while a morphogen gradient specifies digit identity [60]. Xylem patterning may also involve a combination of Turing patterning and pre-existing polarity information, as the large periodic patterns suggest a Turing mechanism, while the transversely banded protoxylem pattern requires information from the orientation of the cell to be incorporated. In addition, small GTPases like ROPs are ideal proteins for reaction-diffusion mechanisms.

1.3 Small GTPases

Small GTPases (henceforth referred to as GTPases) are a type of signalling proteins that function as molecular switches (Fig 1.2). They include Ras GTPases (absent in plants) involved in cell proliferation, Ran GTPases involved in nuclear transport, Rab GTPases involved in membrane trafficking, Arf GTPases involved in vesicle budding, and Rho GTPases (ROPs in plants) involved in cytoskeletal regulation [61]. They can exist in a GTP-bound active form and a GDP-bound inactive form. The active form can be inactivated by hydrolysing its own GTP molecule to GDP [62], whereas the inactive form can be activated by exchanging its GDP for a fresh molecule of GTP [63]. The activity of the GTPases is regulated by other proteins. GAPs (GTPase activating proteins) deactivate GTPases by promoting their GTP hydrolysing activity [64], while GEFs (Guanine nucleotide Exchange Factors) activate GTPases by promoting exchange of GDP for GTP [63]. In addition, active GTPases are largely membrane-bound, while inactive GTPases are actively removed from the membrane by GDIs (GDP dissociation inhibitors) [65].

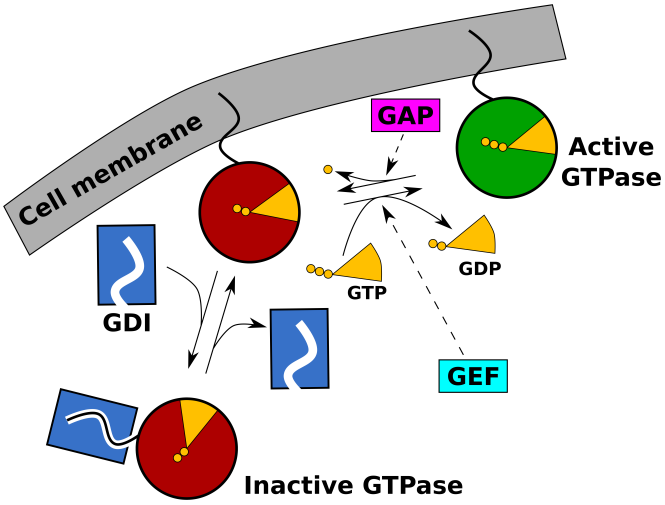

Fig. 1.2. Small GTPases as molecular switches. Active GTPases are bound to GTP and inactive GTPases to GDP. Active GTPases can be inactivated by hydrolysing their GTP. GAPs can accelerate this process. Inactive GTPases can be activated by exchanging their GDP for GTP under the influence of GEFs. Active GTPases are bound to the cell membrane with a hydrophobic tail. Inactive GTPases are selectively removed from the membrane by GDIs.

1.3.1 Small GTPases in reaction-diffusion systems

A major consequence of this GDI cycling is that active GTPases diffuse much slower than inactive GTPases [66, 67]. Consequently, small GTPases are ideal molecules for pattern formation through Turing mechanisms, in particular the substrate depletion variant. The only remaining requirement of a substrate depletion mechanism is a form of self-activation, i.e., the active form must promote activation of the inactive form. This self-activation has been demonstrated experimentally for several systems [68] and has been shown to be sufficient for spontaneous pattern formation *in vitro* [69]. For these reasons, it is not surprising that small GTPases are involved in many instances of cellular patterning, including numerous tip growing systems [35, 70–73], directed cell movement [74], cell division site selection [39, 75–77], pavement cell morphogenesis [78], and xylem cell wall patterning [43, 79].

1.3.2 Mass conservation

Two of the GTPase patterning processes most often explored with models are those underlying bud formation in yeast and directed movement of animal cells [44, 45, 80]. Both are examples of cell polarisation, where a single cluster of active GTPases forms to specify the site of the future bud [81] or the front of the moving cell [82]. These models classically assume that the total amount of GTPase is conserved, often referred to as ‘mass conservation’ [45]. Since the GTPase dynamics and interactions are based on activity, rather than on production and degradation, this is a reasonable assumption in studies with time scales on which GTPase turnover can be neglected.

In contrast to the classical Turing models, these mass conserved reaction-diffusion models have a tendency to ultimately yield only one single cluster of active GTPase. The reason for this property is that different clusters compete for available GTPase and the initially largest cluster usually wins [40, 83–86], in a process is similar to surface-tension-driven coarsening [87]. Therefore, mass conservation is a convenient ingredient for polarisation models that must ensure that a single spot is designated as the front of the cell or the site of bud formation [85]. However, this property of mass conserved models is undesirable in situations where multiple GTPase clusters are required, such as during the splitting of tip growing hyphae [88], the development of the lobes and indents of pavement cells [89–91], and the patterning of the xylem cell wall [7]. A central question, therefore, is how GTPase models can realistically be adjusted to allow the formation of these patterns with multiple GTPase clusters.

1.4 Microtubules

Another key player in pattern formation at the cell membrane is the cytoskeleton [92–94]. The cytoskeleton consists of different types of filaments of which actin filaments and microtubules are the most well-known [95]. For membrane patterning in animals, it is mostly the actin cytoskeleton that is involved, which interacts with GTPases to establish cell polarity and influences cell shape and motility [82, 96]. While actin is also involved in membrane patterning in plants [97], a more central role is played by the so-called cortical array of microtubules attached to the inside of the cell membrane [98]. The cortical microtubule array determines the structure and orientation of new cell wall material and is involved in a variety of patterning processes, including pavement cell morphogenesis and xylem cell wall patterning [92]. The main focus of this thesis is on xylem patterning in plants, so we will elaborate a bit more on microtubules in this section.

1.4.1 Microtubule properties

At the molecular level, microtubules are stiff tube-shaped polymers made up of typically 13 protofilaments that in turn consist of a chain of tubulin subunits. The tubulin subunits are dimers of α- and β-tubulin proteins, which in the microtubule are all oriented in the same direction, giving the microtubule two distinct ends: a minus end with exposed α-tubulin, and a plus end with exposed β-tubulin [99].

Microtubules are highly dynamic structures. Their plus ends switch between growing and shrinking states in a process called dynamic instability. Microtubule stability depends on the presence of a so-called GTP cap, which stabilises the microtubule, preventing shrinking [100]. The newly incorporated tubulin dimers at a growing plus end are bound to two molecules of GTP: one for the α- and one for the β-tubulin. The α-tubulin-bound GTP is stable, but the other one is hydrolysed to GDP at some point of time after incorporation. Therefore, the terms GTP-tubulin and GDP-tubulin will refer to subunits of which the β-tubulin is bound to GTP or GDP, respectively. The conversion of GTP-tubulin to GDP-tubulin after incorporation gives the growing microtubule a GTP cap, while the remaining microtubule lattice consists of GDP-tubulin. If the GTP cap shrinks, the microtubule is eventually destabilised, causing it to start shrinking by releasing its

GDP-tubulin (a so-called 'catastrophe'; Fig 1.3A) [101]. *In vivo*, microtubule plus ends sometimes switch back from shrinking to growing by recruiting a new GTP-cap (a so-called 'rescue') [99]. These rescues may occur, for example, at sites where a damaged microtubule lattice was repaired with GTP-tubulin or under influence of rescue-promoting proteins [102]. Microtubule plus ends may also exist in a paused state, neither growing nor shrinking. However, the existence of this state does not seem important for the overall behaviour of the array, as the three state model (growing, shrinking, pausing), can be mathematically mapped onto the two state model (growing and shrinking only) [103]. The minus-ends are less dynamic and tend to show net retraction, leading to microtubules that appear to move forward by gaining tubulin at one end and losing it at the other, a process known as 'hybrid treadmilling' [104].

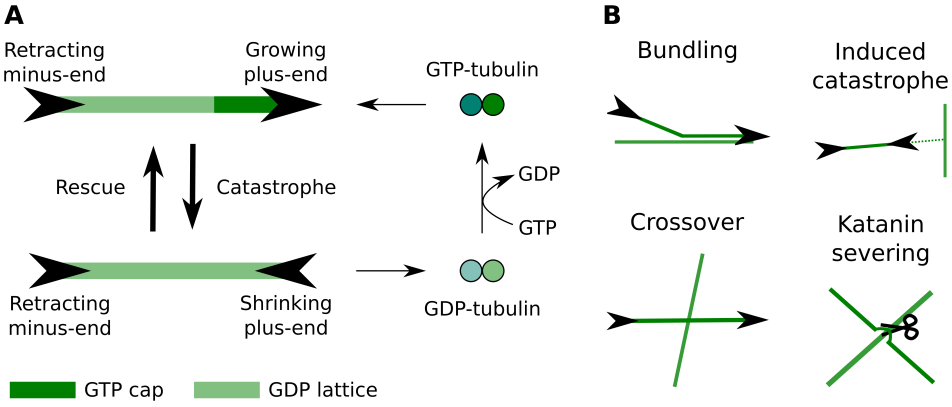

Fig. 1.3. Microtubule dynamics. (A) Microtubules switch between growing and shrinking states. Growing plus-ends consume GTP-tubulin. When the GTP cap is running out, it becomes increasingly likely that the microtubule undergoes a catastrophe and starts shrinking. Shrinking releases GDP-tubulin, which must be turned into GTP-tubulin before it can be used again. When a shrinking microtubule undergoes a rescue, it starts growing again. (B) Microtubule interactions. Collisions at small angles result in bundling, while collisions at larger angles give rise to crossovers or induced catastrophes. Katanin severs the overlying microtubule at crossover intersections.

In plants, new microtubules form at large protein complexes with rings made up of a γ-tubulin, the so-called 'γ-tubulin ring complexes' [105, 106]. These complexes bind microtubules and tend to nucleate faster when they are microtubule-bound [107, 108]. As a consequence, the majority of nucleations typically occur from existing microtubules, oriented either parallel or antiparallel to the parent microtubule or branching at an angle of around 35° [109].

Since plant cortical microtubules are attached to the inside of the cell membrane, they effectively exist in a two-dimensional space, making regular collisions of growing microtubules inevitable. The outcome of such collisions depends strongly on the collision angle. Small collision angles ($\lesssim$ 40 °) generally result in microtubule bundling, where the colliding microtubule continues growing along the microtubule it ran into [110] (Fig 1.3B). Larger collision angles, in contrast, generally either result in an induced catastrophe, where the colliding microtubule starts shrinking, or a crossover, where the colliding microtubule grows over the other one and continues growing in (approximately) its

original direction [110]. The resulting crossover intersections are a preferred target of the microtubule severing protein katanin (Fig 1.3B), which predominantly severs the overlying microtubule (i.e., the one that came last) [111, 112]. The severing creates a new minus end on the front part that starts retracting and a new plus end on the back part that, in general, starts shrinking as it doesn't start with a GTP-cap [112]. However, in some special cases, like during blue light induced array reorientation, many severed plus-ends undergo rescues under the influence of CLASP proteins and will start growing instead [113].

1.4.2 Microtubules and cell wall structure

An important function of the cortical array is to guide cell wall deposition [114–116]. The cortical microtubules determine the position where both cellulose synthase complexes [117, 118] and secretory vesicles with cell wall components [119] are delivered. They also guide the cellulose synthase complexes while these create cellulose microfibrils on the outside of the cell membrane, such that the orientation of these microfibrils follows the orientation of guiding microtubules [120–122]. The position and orientation of the cellulose fibres, in turn, affects the shape of the cell by restricting the directions in which the cell can expand [123]. In this way, microtubules affect the shape and mechanical properties of the plant cell. The microtubule array also responds to a wide variety of cues, including cell shape [124–127], mechanical forces [128, 129], environmental signals [31], and developmental cues [33, 130]. The array integrates these different kinds of information and adjusts the cell wall accordingly, which in turn affects the mechanical information the array receives, creating a feedback loop [131].

1.4.3 Microtubule self-organisation

Plant cells come in many shapes and sizes, requiring a wide variety of cell wall structures, and consequently, cortical array organisations, to adopt a wide range of forms, from the fairly standard elongated cell to the puzzle-piece-shaped pavement cell and the intricately patterned xylem cell wall [92]. This large variety is possible, not just because of the various external signals the array responds to, but also due to its remarkable ability to organise itself in many different ways [132]. Modelling studies have proven to be instrumental in understanding the mechanisms behind microtubule self-organisation, in particular regarding the ability to form aligned arrays with most microtubules oriented in the same direction [133]. These studies have shown that the core mechanism behind this alignment (often referred to as 'survival of the aligned') is that microtubules that don't follow the prevalent direction are more likely to suffer an induced catastrophe and subsequently disappear [134–137]. Typically, a crossover followed by katanin severing will have a similar effect [138], consistent with the finding that katanin promotes alignment in experiments [139]. Moreover, the system can be tuned such that katanin has an opposite effect [140], such as during blue light induced array reorientation, where a large fraction of severed plus-ends is rescued by CLASP [113]. In that case, katanin severing can become a way of amplifying discordant microtubules, kickstarting the reorientation of the microtubule array [31, 141–144]. Models have also provided insight into other aspects of microtubule self-organisation, including selection of the cell division plane [42], formation of the preprophase band [145], and feedback from cell shape [125, 127].

Models of microtubule self-organisation mostly describe the formation of homogeneous arrays. Interaction of microtubules with ROPs allows the formation of various more elaborate patterns. For example, the pavement cells of the leaf epidermis get their characteristic puzzle-piece shape from the local activity of three ROPs, with ROP2 and ROP4 acting redundantly in the lobes and ROP6 active in the indents, combined with microtubules guiding cellulose deposition in the indents and actin filaments involved in lobe extension [78, 146]. Developing primary xylem (protoxylem and metaxylem) is another example, since a combination of ROPs and microtubules is involved in the deposition of the intricately patterned secondary cell wall [43]. As xylem development involves cells of a constant and relatively simple cylindrical shape, it makes an ideal model system for studying membrane patterning by ROPs and microtubules, which is why it forms the main focus of this thesis.

1.5 ROPs and microtubules in xylem patterning

During primary xylem development, the microtubule array, which guides cell wall deposition, must organise itself into the patterns that are later on observed in the secondary cell wall depositions of both protoxylem [122] and metaxylem [147] patterns. In metaxylem, this microtubule organisation has been shown to depend on the local activity of a ROP protein (ROP11) at the future pit sites, where it recruits effector proteins (MIDD1, Kinesin13A) that destabilise microtubules [147–149]. Less is known about protoxylem development, but there are also indications of ROP involvement [150]. Moreover, it has been found that the same ROP effectors are expressed as in metaxylem [151, 152], and that microtubules are locally destabilised in future gap regions [33], further implicating ROPs in protoxylem development.

If the formation of the xylem microtubule pattern requires a ROP pattern, this raises the question how this ROP pattern is formed. We have already seen that small GTPases like ROPs are ideal candidates for spontaneous pattern formation through a reaction-diffusion mechanism. Such a mechanism has also been proposed for ROP11 in metaxylem, where a GEF and a GAP protein have been identified that both accumulate at sites of high ROP activity, suggesting potential positive and negative feedback loops [148]. A recent modelling study found parameter regimes in which interactions between these components could generate a spotted ROP pattern, as required for metaxylem [32].

From the above, it may seem that the patterning process of primary xylem is a linear process: a ROP pattern forms spontaneously and determines the microtubule pattern, which in turn determines the cell wall pattern. This view already raises the question how the microtubule array can adjust to the underlying ROP pattern. Microtubules, however, also influence the ROP patterning. In metaxylem, the ROP pattern can be flattened to an almost protoxylem-like appearance by adding the microtubule-stabilising drug taxol [148] or altering the expression of various MAPs (microtubule-associated proteins) [153–155]. These effects appear to be the result of microtubules acting as a kind of diffusion barrier for membrane-bound active ROP and associated effectors [148]. This barrier function requires IQD13, a protein that can bind to both microtubules and the plasma membrane [154, 156], and is counteracted by detachment of microtubules from the membrane by CORD (cortical microtubule disordering) proteins [155]. How this interplay between

ROPs and microtubules is capable of generating the variety of protoxylem and metaxylem patterns is still an open question and will be the main theme of this thesis.

1.6 Aim and thesis outline

In this thesis, I aim to answer several crucial questions about the mechanisms behind xylem patterning. In particular, I aim to gain insights into how the ROP patterns form, how microtubules influence ROP patterning, and how microtubules can follow an existing ROP pattern, uncovering various aspects of the mutual interaction between the two in the process. Since the mechanisms to be studied are underlying many other patterning processes in nature, the answers will be relevant to many other systems than xylem patterning alone.

First of all, a ROP pattern of multiple stripes (protoxylem) or spots (metaxylem) is required (Fig 1.1), which is not possible with the commonly used mass-conserved small GTPase models, as these consistently generate but a single cluster [40, 83–86]. **Chapter 2** will, therefore, focus on the question how stable patterns with multiple coexisting clusters of ROPs (or other small GTPases) can be formed. Clues from existing literature [86, 157] and comparisons with other models [16, 158] lead to the hypotheses that including either GTPase turnover or a form of negative feedback can stabilise cluster coexistence. In addition to a detailed exploration of these hypotheses, chapter 2 also includes an investigation of the mechanisms behind polarisation and coexistence.

The ringed or spiral protoxylem pattern requires a pattern of coexisting stripes, which, moreover, must have the correct orientation. How this orientation is achieved, is the central question of **chapter 3**. Classical reaction-diffusion systems tend to generate curved patterns because of unresolved topological defects [49, 50]. They only produce bands with a controlled orientation in presence of an oriented prepattern [13] or when the domain is narrow relative to the wavelength of the pattern [10, 49]. The latter is the case for some animal tails, but not for protoxylem. Therefore, there must be another mechanism that orients the stripes relative to the cell axis. Chapter 3 explores the hypothesis that this mechanism is based on a longitudinal diffusion restriction of active ROP imposed by an initially homogeneous microtubule array with a transverse orientation. This hypothesis is based on the diffusion barrier effect of microtubules [148, 154] and the observation that band formation starts from a transversely oriented microtubule array [159]. We further analyse the effect of diffusion restriction to gain a mechanistic understanding of the orienting power of the proposed mechanism.

The remaining chapters revolve around the patterning of microtubules. **Chapter 4** deals with the question how microtubules can be equally distributed over an array structure when most nucleations occur from existing microtubules [109]. All efforts to include this microtubule-bound nucleation in simulations have resulted in highly inhomogeneous microtubule-arrays [135, 136, 160, 161]. This effect is strong in protoxylem simulations, in which most microtubules turn out to end up in only one or two bands [33]. However, this inhomogeneity problem also applies to all situations where an even distribution of microtubules is required, including in metaxylem patterning and the formation of transverse arrays in elongating cells. The inhomogeneity problem is caused by the density-dependent implementation of microtubule-based nucleations, in which larger clusters of

microtubules attract more nucleations and grow even larger at the expense of smaller clusters (see, e.g., [160]). The result is a global competition for nucleations much like the GTPase competition observed in mass-conserved reaction-diffusion models. Chapter 4 compares two competing hypotheses for how cells avoid this inhomogeneity problem: (1) a local limitation of the amount of tubulin available for making microtubules and (2) a local limitation of the number of nucleation complexes available for nucleating new microtubules. These hypotheses are tested using a simplified microtubule model in which all microtubules have a perfectly transverse orientation, allowing for a computationally efficient implementation of these two very different mechanisms. Additionally, combining this modelling effort with experiments reveals new aspects of nucleation complex dynamics.

With these new insights on microtubule nucleation and array homogeneity, we move back to the full two-dimensional array context in **chapter 5**. We focus on the case of protoxylem patterning, for which detailed experimental data on microtubule dynamics is available [33]. Contrary to the simple model of chapter 4, co-alignment between microtubules and the ROP pattern is no longer automatic. It turns out that some co-alignment is, in fact, expected, since the ROP pattern can orient itself to the initial microtubule array (chapter 3). Microtubules also appear curved in microscopic pictures (e.g., [33, 90, 122, 144, 162]). Therefore, some microtubule modelling studies include microtubule flexibility by adding random fluctuations to the microtubule growth direction [126, 127]. This feature may allow for correction of small deviations in co-alignment. In chapter 5, we therefore add co-alignment, microtubule flexibility, and a simplified nucleation mode based on the findings from chapter 4 to existing two-dimensional microtubule simulations of protoxylem [33]. With these improvements, we are much better able to simulate protoxylem band formation with measured microtubule dynamics than in the original manuscript [33]. Moreover, the issues that remain point to additional requirements for band formation that fall outside the measured data.

Together, these chapters provide new insights into the way microtubules affect ROP patterning and ROPs affect microtubule patterning and emphasise the importance of the mutual interaction between the two in xylem patterning.

2

Small GTPase patterning: How to stabilise cluster coexistence

Bas Jacobs

Jaap Molenaar

Eva E. Deinum

Published in PLoS one [163]

Abstract

Many biological processes have to occur at specific locations on the cell membrane. These locations are often specified by the localised activity of small GTPase proteins. Some processes require the formation of a single cluster of active GTPase, also called unipolar polarisation (here "polarisation"), whereas others need multiple coexisting clusters. Moreover, sometimes the pattern of GTPase clusters is dynamically regulated after its formation. This raises the question how the same interacting protein components can produce such a rich variety of naturally occurring patterns. Most currently used models for GTPase-based patterning inherently yield polarisation. Such models may at best yield transient coexistence of at most a few clusters, and hence fail to explain several important biological phenomena. These existing models are all based on mass conservation of total GTPase and some form of direct or indirect positive feedback. Here, we show that either of two biologically plausible modifications can yield stable coexistence: including explicit GTPase turnover, i.e., breaking mass conservation, or negative feedback by activation of an inhibitor like a GAP. Since we start from two different polarising models our findings seem independent of the precise self-activation mechanism. By studying the net GTPase flows among clusters, we provide insight into how these mechanisms operate. Our coexistence models also allow for dynamical regulation of the final pattern, which we illustrate with examples of pollen tube growth and the branching of fungal hyphae. Together, these results provide a better understanding of how cells can tune a single system to generate a wide variety of biologically relevant patterns.

2.1 Introduction

Many cellular processes must occur at specific locations on the cell membrane. Examples range from the formation of a yeast bud [164], to the localised reinforcements of plant cell walls [165], to coordination of directed cell movement in animals [74]. The localisation of these processes is determined by the local activity of highly conserved small GTPase proteins (e.g., Rho, ROP, Rac, Ras, henceforth referred to as GTPases) [166]. In some cases, such as yeast budding, a single cluster of active GTPase forms, resulting in unipolar polarisation (henceforth referred to as polarisation). In others, e.g., patterned plant cell wall reinforcement, the GTPase pattern consists of many coexisting clusters (Fig 2.1A). This raises the question how the same biological system can generate different types of patterns. Mathematical models are an important tool in understanding the mechanisms of *de novo* pattern formation, but thus far, the commonly used models for GTPase-based patterning, which were initially developed for explaining polarisation, cannot produce stable coexistence [44, 45].

Small GTPases function as molecular switches with an active, GTP-bound form and an inactive, GDP-bound form (Fig 2.1B). They can be switched on by Guanine nucleotide Exchange Factors (GEFs), which facilitate exchange of GDP for GTP, and off by GTP hydrolysis, which can be accelerated by GTPase Activating Proteins (GAPs) [64, 167]. The active form is membrane-bound, whereas the inactive form is removed from the membrane by Guanine nucleotide Dissociation Inhibitors (GDIs) [65]. Since diffusion in the cytosol is much faster than at the membrane [66, 67], the inactive form effectively diffuses much faster than the active form. This difference in diffusion is one of the classical ingredients for pattern formation through a Turing-type reaction-diffusion mechanism [46, 47], making these GTPases particularly suitable for membrane patterning in biological systems.

Many theoretical studies have been performed on the role of GTPases in polarisation, for cells of organisms as diverse as animals, yeast, and the cellular slime mold *Dictyostelium discoideum* [44]. Most of these models involve some form of positive feedback, either through direct or indirect self-activation or through double negative feedback between two antagonistic GTPases. In addition, these models generally do not include protein turnover, so GTPase is only interconverted between active and inactive form, and not produced or degraded (generally referred to as *mass conservation*). These two properties seem to form a robust recipe for polarisation [40, 83, 84, 168, 169].

However, GTPases also play important roles in the formation of other patterns than simple polarisation. For example, cell wall patterning in at least one common type of plant vasculature, the metaxylem, relies on a pattern of multiple clusters of a GTPase [147–149]. The interdigitated pattern of plant leaf epidermal cells (pavement cells) is under the control of two antagonistic classes of GTPase [89–91]. Furthermore, several GTPases are implicated in the outgrowth of multiple dendrites from neuron cell bodies [166].

Particularly interesting in this context is the role of GTPases in tip growing systems, where the pattern of GTPase clusters may be dynamically regulated, adding an extra layer of complexity. In these systems, a cluster of active GTPase determines the tip region of a growing tube. Some of these systems, such as root hairs [70] and pollen tubes [71], have a single growing tip. In others, such as fungal hyphae, multiple tips can exist si-

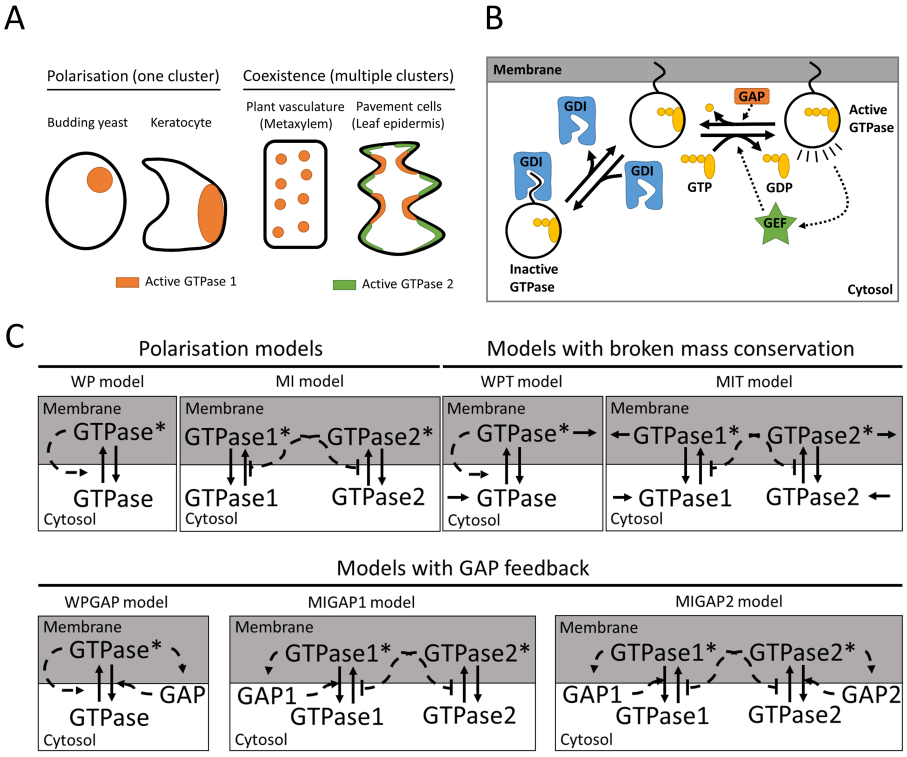

Fig. 2.1. Models for GTPase-based membrane patterning. A: Types of GTPase-based membrane patterns that occur in living cells. Some situations require the formation of a single cluster of GTPase (polarisation, left), whereas others require stable coexistence of multiple clusters (right). B: Active GTP-bound GTPases are inactivated by hydrolysis of GTP to GDP under the influence of GAP proteins. Inactive GTPases can be activated by GEF proteins that promote the exchange of GDP for GTP. GTPases can bind to the cell membrane with their hydrophobic tails, but the inactive form is selectively taken out by GDI proteins. C: Interaction motifs of the reaction diffusion models. Solid lines indicate conversions and dashed lines indicate interactions. Positive interactions are indicated by arrowheads and negative interactions by perpendicular lines. Stars indicate the active form of GTPase.

multaneously, each with their own cap of active GTPase. More importantly, new clusters can appear even after others have already been established, resulting in branching. This is important for the establishment of a mycelial network [73, 170]. Additionally, in both pollen tubes and hyphae, growth can proceed in pulses, with the GTPase cap diminishing or disappearing as growth slows or halts [171, 172].

This more complex growth requires the coexistence of multiple clusters as well as the *de novo* generation of new clusters besides existing ones. Studying these processes in one dimension (1D), as is often done for polarisation, saves computational time, but can produce misleading results. For example, many mass conserved reaction-diffusion models for polarisation show phase separating behaviour [84, 173, 174]. Phase separation is characterised by the minimisation of interface length and total curvature in two dimensions

(2D), causing clusters to compete until only one remains [175]. In 1D, however, only the (discrete) number of interfaces can be minimised. Consequently, the meta-stable state with multiple clusters that these polarisation models can produce in 1D [84, 173, 174], is likely to be much less stable in 2D.

All this implies that in 2D, multiple domains can only (apparently) stably coexist if supported by an irregular geometry such as the lobe-and-indent shape of leaf epidermal (pavement) cells [30]. A phase separating system, however, cannot explain the initial formation of such a geometry, nor the appearance of additional lobes as these cells grow [176]. These issues of dimensionality and *de novo* cluster formation also apply to a recent theoretical study that proposes that saturation of self-activation, resulting in flat concentration profiles, could slow down the competition between clusters to the extent that they can coexist on biologically relevant time scales [177]. Therefore, a mechanism that allows for truly stable coexistence would offer a more parsimonious explanation for phenomena that require multiple GTPase clusters in a single cell.

From literature we have found two potential ways of obtaining stable coexistence. Firstly, where GTPase-based polarisation models are typically mass conserved, turnover is present in highly similar classical activator substrate-depletion models, which are able to produce stable coexistence (e.g., [16]). Mass conservation has been suggested to play an important role in the winner-takes-all mechanism [83] and an adaptation of a polarisation model with production and degradation terms can generate multiple peaks in 1D [158]. These results indicate that sufficiently large GTPase turnover on relevant time scales might explain the stable coexistence of multiple GTPase clusters. Whether that is a reasonable assumption may depend on the system.

Secondly, a parameter regime that allows stable coexistence has been reported without further investigation in a modelling study on negative feedback in polarisation of budding yeast [157]. This suggests a negative feedback that limits the growth of larger clusters may also explain stable coexistence, but this mechanism remains to be fully characterised. Some experimental evidence for negative feedback through the recruitment of GAPs has been found in the case of metaxylem patterning [148].

Here, we aim for a unified understanding of all biologically relevant GTPase-based patterns. Our goal is threefold: (1) to find out which GTPase interaction motifs can make the difference between polarisation and stable coexistence in *de novo* GTPase-based patterning of 2D membranes, (2) to understand why these differences in GTPase interactions lead to different patterns, and (3) to explore the options these mechanisms offer for dynamic regulation of membrane patterning.

We consider the interaction motifs from two existing partial differential equation (PDE) models for polarisation and extensions thereof with GTPase turnover and with negative feedback (See Fig 2.1C and Table 2.1 for an overview). These polarisation models are the so-called "Wave Pinning" (WP) model [84] with a single GTPase directly stimulating its own activation, and the "Mutual Inhibition" (MI) model [168] with two GTPases inhibiting each other's activation. The use of these two different models allows us to draw conclusions that do not depend on the positive feedback mechanism. We break the mass conservation of these models by adding turnover (WPT and MIT, respectively). Negative feedback is included by having mass conserved GTPases activate their own GAP. We consider the WP model with a single GAP (WPGAP) and the MI model both with a GAP for one GTPase (MIGAP1) and GAPs for both GTPases (MIGAP2). To study the entire

process of *de novo* cluster formation, we perform simulations starting from a homogeneous state with noise on a 2D domain sufficiently large for the formation of complex patterns. We found that both polarisation models indeed robustly yield a single GTPase cluster, whereas either breaking mass conservation or adding GAP feedback appears to be sufficient for stable coexistence. We also provide insight into the way these mechanisms operate, by using ordinary differential equation (ODE) models derived from the PDEs to study fluxes between competing clusters. Finally, we revisit the tip growing systems to explore the options that the different mechanisms offer for dynamically regulating established patterns. In particular, our findings reveal conditions that allow for branching.

Table 2.1. Characteristics of the different models. WP = wave pinning, MI = mutual inhibition, WPT = WP with turnover, MIT = MI with turnover, WPGAP = WP with GAP feedback, MIGAP1 = MI with GAP feedback on one GTPase, MIGAP2 = MI with GAP feedback on both GTPases.

Model	Positive feedback	Mass conservation	Number of GTPases	Number of GAPs	Number of variables
WP	Direct	Yes	1	0	2
MI	Double negative	Yes	2	0	4
WPT	Direct	No	1	0	2
MIT	Double negative	No	2	0	4
WPGAP	Direct	Yes	1	1	4
MIGAP1	Double negative	Yes	2	1	6
MIGAP2	Double negative	Yes	2	2	8

2.2 Results

2.2.1 Simple mass conserved models can only result in polarisation

In this section we study the wave pinning (WP) and mutual inhibition (MI) models, which have in common that the total amount of GTPase is conserved. Both can be written in the following dimensionless form (see Appendices 2.8.1):

$$\begin{aligned} \frac{\partial u_i}{\partial t} &= f(u_i, v_i, u_j) + \nabla^2 u_i \\ \frac{\partial v_i}{\partial t} &= -f(u_i, v_i, u_j) + D_v \nabla^2 v_i \\ &\text{for } i, j \in \{1,2\}, i \neq j, \end{aligned} \tag{2.1}$$

where u_i and v_i are the concentrations of the i^{th} active and inactive GTPase respectively, D_v is the ratio between diffusion coefficients of inactive and active GTPase ($\gg 1$), and f represents the interconversion between active and inactive form. For the WP model $u_i = u_j = u$ and $v_i = v_j = v$, and function f consists of constant activation and inactivation terms and a saturating self-activation term. The dimensionless form of f is given by:

$$f(u,v) = bv + \gamma \frac{u^n}{1+u^n} v - u, \tag{2.2}$$

where b is a constant activation rate, γ the self-activation rate at saturation, and n the hill coefficient describing saturating self-activation. Due to mass conservation, the av-

erage total (dimensionless) GTPase concentration T is a constant determined by initial conditions.

For the MI model, function f has constant activation and inactivation terms and a saturating inhibition term. The dimensionless form is given by:

$$f(u_i, v_i, u_j) = b_i v_i + \gamma_i \frac{1}{1+u_j^n} v_i - u_i \quad \text{for } i, j \in \{1,2\}, i \neq j, \tag{2.3}$$

where b_i is the constant activation rate of GTPase i, γ_i the activation rate of GTPase i that can be inhibited by GTPase j, and n the hill coefficient describing inhibition. Again, the total amount of each GTPase is constant and we use the average total GTPase concentrations T_1 and T_2 as parameters.

We simulated these models on a 2D rectangular domain with periodic boundary conditions in the horizontal direction and zero-flux boundary conditions in the vertical direction. In this way, our domain is an open cylinder resembling the membrane of a large, elongated cell with both cytosolic and membrane-bound components diffusing along the cell periphery, albeit at different rates. For various cell types the actual 3D diffusion of the cytosolic components may affect shape and/or location of clusters or the precise parameter regime of their formation (e.g., [178]). It is unlikely, however, that the simplification to 2D affects appearance of phase separating behaviour. Domain sizes were large compared to those used by the original WP model study on polarisation [84], but the other parameters had similar values (Table 2.2). We enlarged the domain size to ensure domain size was not limiting the formation of multiple clusters. All simulations started in the homogeneous steady state (HSS) with a small amount of noise added (see Methods for details).

As previously predicted [83, 84], both polarisation models consistently generate a single cluster of active GTPase in a pattern that changes from a spot to a stripe to a gap as the amount of GTPase increases (Fig 2.2A–C). Transiently, the spot and gap patterns form from many small clusters of varying sizes, where the larger clusters grow at the expense of the smaller ones, a process similar to Ostwald ripening [179], although also a few fusions events occurred (Fig 2.3, S1 Video). Also the single stripe forms from a finer structure, an elaborate network of band-like structures. In all three cases investigated, patterning was initiated simultaneously throughout the domain (Fig S2.2, S2 Video), reminiscent of spinodal decomposition [180]. Typically, spinodal decomposition occurs if there is no barrier to nucleation, i.e., the system is released in a state where the mixed state is unstable and immediately starts demixing everywhere. For the spot and gap patterns, the typical near percolating network and continual pattern coarsening was only visible early on (mostly $t < 100$), followed by the amplification of the near-initial set of transient clusters.

Because of the varying sizes of these transient clusters (Fig 2.3), most disappear quickly and only the last few compete for a long time. This shows that the previously proposed mechanism of slow competition [177] cannot explain *de novo* formation of patterns of many coexisting clusters.

Linear stability analysis (LSA, see Methods) performed on the WP model, reveals that the domain size used allows multiple different wave numbers to become unstable

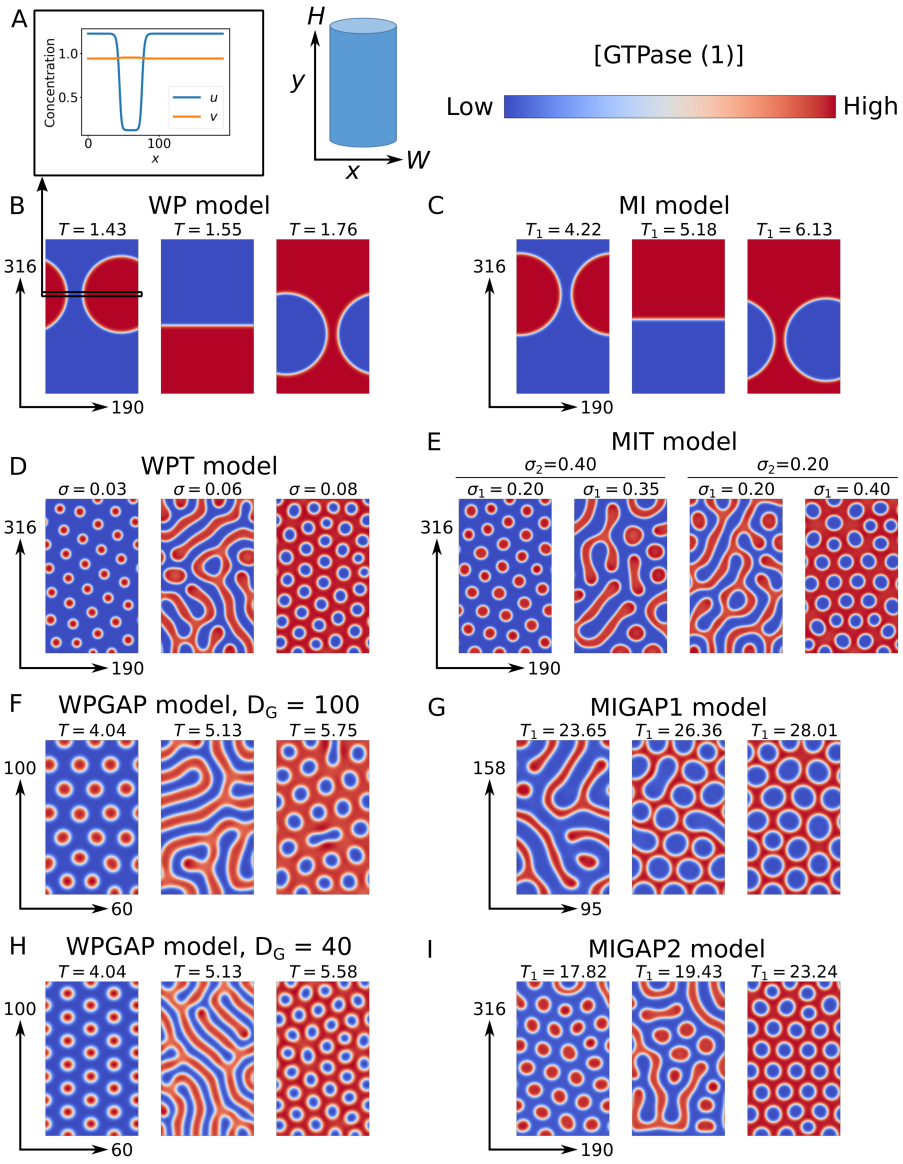

Fig. 2.2. B-I: Steady state active GTPase concentrations ([GTPase]) obtained by model simulations. T = total amount of GTPase, σ = GTPase production rate. All simulation domains have periodic boundary conditions in the x-direction and zero flux boundary conditions in the y-direction. Dimensionless domain heights (H) and widths (W) are indicated by arrows. For models with two GTPases, only the concentrations of the first GTPase are shown. In these cases, the second GTPase always clusters where the first does not. Similarly, concentration profiles of active (u) and inactive (v) GTPase are opposite, with difference in v being much smaller due to the much higher diffusion constant (A). Default parameters (Table 2.2) were used with indicated values of T and σ. For the WPGAP model, two different values were used for the active GAP diffusion coefficient (D_G). Concentration ranges and simulation end times for each simulation are shown in Fig S2.1.

Table 2.2. Descriptions and default values of parameters used for the dimensionless PDE models. In case of multiple GTPases or GAPs the same values for b, γ, c, d, ξ, and T_g were used for both variants. N.A. = not applicable.

Parameter	Description	Model WP	MI	WPT	MIT	WPGAP	MIGAP1	MIGAP2
b	Base activation rate	0.1	0.1	0.1	0.1	0.1	0.1	0.1
γ	Feedback activation rate	2	2	2	2	2	2	2
n	Hill exponent of feedback saturation	2	2	2	2	2	2	2
c	GAP activation rate	N.A.	N.A.	N.A.	N.A.	1	1	1
d	GAP inactivation rate	N.A.	N.A.	N.A.	N.A.	1	1	1
$T_{(1)}$	Average concentration of total GTPase (1)	Variable						
T_2	Average concentration of total GTPase 2	N.A.	5	N.A.	N.A.	N.A.	5	20
$\sigma_{(1)}$	Production rate of GTPase (1)	Variable						
σ_2	Production rate of GTPase 2	N.A.	N.A.	N.A.	0.2 or 0.4	N.A.	N.A.	N.A.
ξ	GTPase degradation rate	N.A.	N.A.	0.1	0.1	N.A.	N.A.	N.A.
T_g	Average concentration of total GAP	N.A.	N.A.	N.A.	N.A.	10	10	10
D_v	Ratio diffusion coefficients of inactive to active GTPase	100	100	100	100	100	100	100
D_G	Ratio diffusion coefficients of active GAP to active GTPase	100	100	100	100	100 or 40	100	100
D_g	Ratio diffusion coefficients of inactive GAP to active GTPase	100	100	100	100	100	100	100

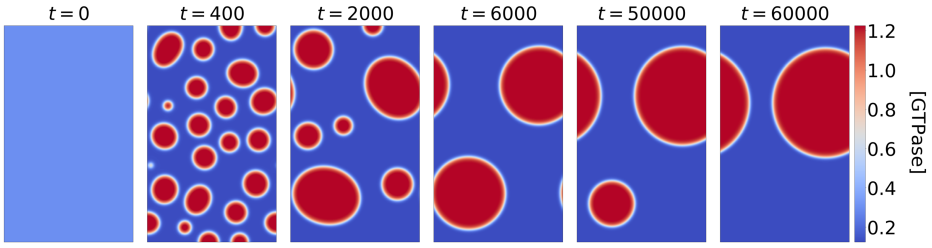

Fig. 2.3. Transient active GTPase concentrations ([GTPase]) from simulations of the WP model with $T = 1.43$. Simulation conditions were as in Fig 2.2.

(Fig S2.3). Therefore, the formation of a single cluster cannot be due to the growth of a single wavelength the size of the domain. Instead, it must result from dynamics that occur after the initial symmetry breaking, when linearisation is no longer appropriate. This also means, as previously noted [181], that LSA cannot be used to determine the length scale of the final pattern, because it is only valid around the homogeneous state.

To visualise regions of parameter space where the homogeneous state is unstable and patterns form spontaneously (so-called Turing regimes), we generated two parameter bifurcation plots. For models with two variables, we used both LSA and the computa-

tionally simpler asymptotic approximation called "local perturbation analysis" (LPA, see methods). In these cases, LSA and LPA yielded highly similar results for the Turing regimes (Fig 2.4). For these reasons, we only used LPA for the larger models. The resulting Turing regimes predict where spontaneous pattern formation occurs, but not which type of patterns are formed. The latter we investigated using numerical simulations. For the WP model, a pattern (a single cluster, stripe, or gap in this case) can only form if positive feedback is sufficiently strong (γ must be large enough) and GTPase concentrations are within a certain range close to where positive feedback is most sensitive. For the MI model, LPA predicts that a wide range of total GTPase amounts give rise to spontaneous pattern formation, as long as the amounts of both GTPases are similar (Fig 2.5A). LPA of both models also predicts a bistable regime surrounding the Turing regime where patterns do not form spontaneously, but may form and be maintained after a sufficiently large perturbation.

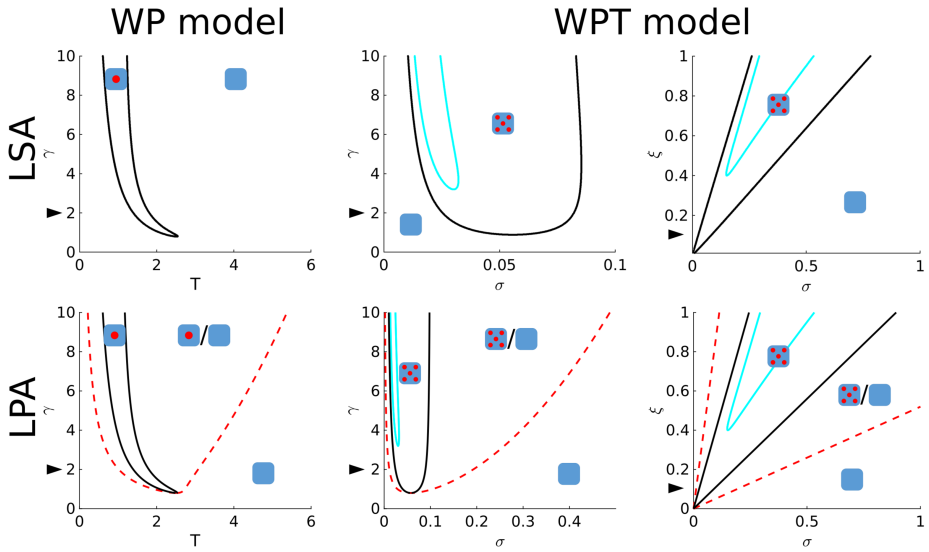

Fig. 2.4. Two parameter bifurcation plots for models with two variables (WP and WPT). Both LSA (top) and LPA (bottom) analyses were performed on the WP model for parameters T and γ (left) and on the WPT model for parameters σ and γ, and σ and ξ (right). Cartoons indicate kind of pattern formed in different regimes (empty square: no pattern, single spot: polarisation, five spots: coexistence). Solid black lines delimit Turing regimes in which the homogeneous steady state is unstable. Dashed red lines (LPA only) delimit predictions of regimes in which heterogeneous states exist that may be reached from the homogeneous state by an arbitrarily large local perturbation. Cyan lines indicate Hopf regimes. Arrowheads indicate default parameters.

2.2.2 Breaking mass conservation is sufficient to allow stable coexistence of multiple active GTPase clusters

To investigate the effect of breaking mass conservation, we extended the two polarisation models with production and degradation terms. Since translation is a cytosolic process, we assume that GTPases are produced in their inactive form. Following a previous study [158], we here consider degradation of the active form. Later, we will also consider

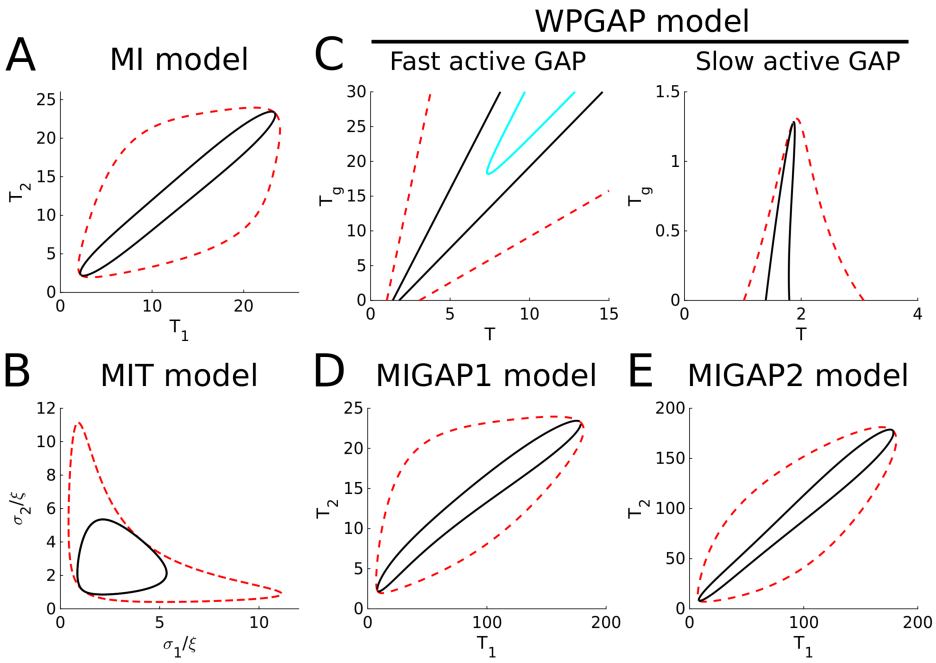

Fig. 2.5. Two parameter bifurcation plots for LPA analyses on models with more than two variables. Default parameters were used. The bifurcation plot for the two ratios σ/ξ in the MIT model (B) appears to be the same regardless of the value of $\xi_1 = \xi_2 = \xi$ (tested for $\xi \in \{0.05, 0.1, 0.2, 1\}$). For the WPGAP (C) model, the active GAP diffusion coefficient (D_G) was considered both in the limit $D_G \to \infty$ (Fast active GAP) and in the limit $D_G \to 0$ (slow active GAP). Lines delimiting different regimes are coloured as in Fig 2.4. For the MI models with GAP feedback (D and E) we only considered fast active GAP.

degradation of the inactive form. These assumptions result in the following dimensionless model equations:

$$\begin{aligned} \frac{\partial u_i}{\partial t} &= f(u_i, v_i, u_j) - \xi_i u_i + \nabla^2 u_i \\ \frac{\partial v_i}{\partial t} &= -f(u_i, v_i, u_j) + \sigma_i + D_v \nabla^2 v_i \\ &\text{for } i, j \in \{1,2\},\ i \neq j, \end{aligned} \tag{2.4}$$

with constant production σ_i of the inactive form, degradation of the active form with factor ξ_i, and f given by Eq. 2.2 or Eq. 2.3. The equations for the WPT model are equivalent to those used in a previous study [158].

Consistent with previous results in 1D [158], breaking mass conservation allows multiple clusters to survive (Fig 2.2D and E, S1 Video). As for classical Turing systems [49], higher GTPase production shifts the pattern from spots to stripes to gaps, suggesting that the most important difference between these models and polarisation models is indeed mass conservation. In the limit of no turnover, the WPT model converges to the WP model. Simulations show a gradual decrease in the number of stably coexisting clusters per unit area with decreasing turnover, until a single one remains and polarisation behaviour is recovered (Fig S2.4).

As for the WP model, LSA performed on the WPT model reveals many different unstable wave numbers (Fig S2.3), although simulations show a different class of patterns (coexistence instead of polarisation). Bifurcation analysis reveals that, for patterning to occur, the WPT model also requires a sufficiently large self-activation parameter γ. In addition, the GTPase production rate σ must be within certain boundaries determined by degradation rate ξ (Fig 2.4). As before, these results suggest that for patterns to form the positive feedback should be strong enough, while the active GTPase concentration (σ/ξ at the homogeneous steady state) should be in a range where it is sensitive to positive feedback (around 1 due to non-dimensionalisation). Bifurcation analysis also reveals a Hopf regime within the Turing regime for the WPT model. Simulations in the Hopf regime reveal no oscillations of the final pattern (S3 Video), likely because this regime only applies close to the homogeneous state. LPA shows that the Turing regime for the MIT model is considerably less elongated than that for the MI model (Fig 2.5B). In addition, the Turing regime appears to scale linearly with the degradation rate.

Both models considered here assume degradation of the active form only. Similar bifurcation and simulation analyses on a model with degradation of the inactive form only do not reveal regimes that admit stable patterns (see Appendices 2.8.5). This shows that turnover can only stabilise multiple coexisting clusters if the active form is (also) degraded. Such degradation could occur, for example, by recycling of membrane patches.

2.2.3 Adding GAP feedback to the mass conserved models is also sufficient to allow for coexistence

To investigate the effect of negative feedback, we modified both the WP and MI model by including GAP proteins in such a way that both the total amount of GTPase and the total amount of GAP are conserved. For the MI model, we considered both cases of a single GAP acting on one of the GTPases (MIGAP1) and one GAP for each GTPase (MIGAP2). This results in the following dimensionless equations for the GAP models:

$$\begin{aligned}
\frac{\partial u_i}{\partial t} &= f(u_i, v_i, u_j) - G_i u_i + \nabla^2 u_i \\
\frac{\partial v_i}{\partial t} &= -f(u_i, v_i, u_j) + G_i u_i + D_v \nabla^2 v_i \\
\frac{\partial G_i}{\partial t} &= c_i u_i g_i - d_i G_i + D_G \nabla^2 G_i \\
\frac{\partial g_i}{\partial t} &= -c_i u_i g_i + d_i G_i + D_g \nabla^2 g_i \\
&\text{for } i, j \in \{1,2\}, i \neq j,
\end{aligned} \tag{2.5}$$

where G_i and g_i are the dimensionless concentrations of active and inactive GAP respectively, D_G and D_g are the diffusion coefficients of active and inactive GAP relative to that of active GTPase respectively, c_i is the GTPase-dependent GAP activation rate, and d_i is a constant GAP inactivation rate. Function f is again defined by Eq. 2.2 or Eq. 2.3. For the MIGAP1 model, the second GAP (G_2 and g_2) is absent. Like the total amount of GTPase, the total amount of GAP is conserved, resulting in additional parameters for the average total GAP concentration $T_{g,i}$.

Consistent with previous indications [157], addition of GAP feedback results in similar patterns as found for breaking mass conservation: multiple clusters of active GTPase become stable and the pattern shifts from spots to stripes to gaps for increasing levels of total GTPase (Fig 2.2F–I, S1 Video). For the MI model, adding GAP feedback to only one of the two GTPases is sufficient to achieve this effect. The similar response of the two different polarisation models indicates that the difference between polarisation and coexistence does not depend on the self-activation mechanism.

Bifurcation analysis of the WPGAP model reveals that, as long as GAPs diffuse fast compared to active GTPase, the Turing regime widens and shifts to higher amounts of GTPase as the amount of GAP increases (Fig 2.5C). This is consistent with previous indications that negative feedback may act as a buffer against fluctuations in GTPase concentration [157]. However, when active GAP diffusion is equal to that of active GTPase, the picture changes completely and GAPs severely hamper pattern formation. Trial simulations in the narrow Turing regime all resulted in polarisation (Fig S2.5). Therefore, it seems that for GAP feedback to stabilise coexistence, the effective diffusion constant of active GAP must be larger than that of active GTPase. However, formation of coexisting GTPase clusters is still possible if active GAP diffuses more slowly than inactive GTPase (Fig 2.2H). A Hopf regime can also be found for the WPGAP model. As for the WPT model, simulations in the Hopf regime do not reveal any oscillations of the final pattern (S3 Video).

For the MIGAP2 model, there is a wide range of total GTPase amounts for which patterns form spontaneously, as long as the total amount of both GTPases is similar (Fig 2.5E). For the MIGAP1 model, a similar range is present, but there must be considerably more of the first GTPase than of the second, because the second is not hindered by GAP feedback (Fig 2.5D).

2.2.4 Multiple clusters drawing GTPase from a homogeneous pool compete until only the largest survives

To better understand why some models yield only polarisation, whereas others allow for multiple stable clusters, we considered a simplified model describing the competition between multiple clusters, as transiently generated by the polarisation models (Fig 2.3, S1 Video). This approximation treats each cluster as a compartment, with an additional non-cluster compartment representing a global pool of inactive GTPase. By using compartments, we implicitly assume that the clusters have sharp boundaries and constant active GTPase concentrations, making the total amount of GTPase in a cluster proportional to its area. Using these assumptions, we derived a system of ODEs from the PDE models (for derivation see Appendices 2.8.6), which is comparable to a more phenomenological two-cluster model presented by Howell et al. [85]. Clusters recruit active GTPase from the inactive pool at a rate proportional to their area or, equivalently, their total amount of GTPase (Fig 2.6A). They lose GTPase both at a constant rate, reflecting inactivation, and at a rate proportional to the circumference of the cluster, reflecting loss at the boundary (Fig 2.6A).

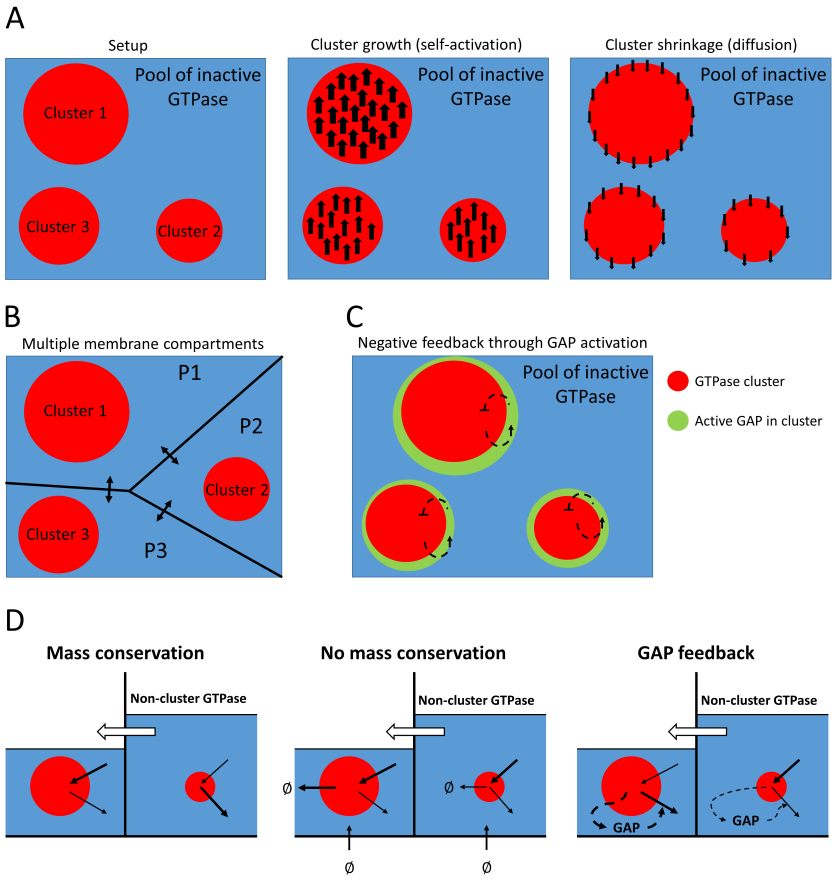

Fig. 2.6. Principles of the simplified ODE models. A: The basic mass conserved ODE model starts with an arbitrary number of differently sized clusters (left, three are shown). Clusters compete for the inactive GTPase from a shared homogeneous pool. Activation and inactivation of membrane GTPase occur proportional to cluster size (middle). Additional loss of active GTPase (by diffusion from cluster to pool) occurs proportional to cluster circumference (right). B: An adaptation of the basic ODE model where each cluster has its own local pool of inactive GTPase (P1-P3) with fluxes connecting these local compartments (arrows). C: An adaptation of the basic ODE model with GAP feedback, where each cluster recruits GAP from a shared homogeneous pool at a rate proportional to the cluster size and GAPs (green) inactivate the GTPase in the cluster. D: Larger clusters more effectively deplete their local pool (blue), resulting in a concentration gradient and corresponding flux of GTPase from compartments with small clusters to compartments with large clusters. With mass conservation, this process continues until the small cluster is depleted. GTPase turnover effectively redistributes GTPases by removing more from larger clusters and providing new GTPase homogeneously, allowing the smallest cluster to compete in spite of this flux. At the same time, the larger cluster suffers from a smaller GTPase pool to recruit from. When GAP feedback is added, larger clusters recruit more GAP enhancing their own depletion, allowing smaller clusters to compete.

The resulting basic ODE model is given by:

$$\begin{aligned}\frac{dh_{c,n}(t)}{dt} &= \alpha h_{c,n}(t)h_p(t) - \beta h_{c,n}(t)^{\eta} - \delta h_{c,n}(t)\\ \frac{dh_p(t)}{dt} &= -\alpha h_p(t)\sum_{j=1}^{N} h_{c,j}(t) + \beta\sum_{j=1}^{N} h_{c,j}(t)^{\eta} + \delta\sum_{j=1}^{N} h_{c,j}(t),\end{aligned} \tag{2.6}$$

where $h_{c,n}$ is the amount of (active) GTPase in cluster n (which is proportional to the area of cluster n), h_p is the amount of GTPase in the inactive pool, N is the total number of clusters, exponent η is $\frac{1}{2}$ for circular clusters (due to the relation between area and circumference), α is a positive constant determining self-activation, β is the rate at which clusters lose GTPase by diffusion across the circumference, and δ is a constant inactivation rate. This system is redundant, because the total amount of GTPase is conserved ($T = h_p + \sum_{j=1}^{N} h_{c,j}$).

We calculated the rate of change of the ratio between the sizes of two arbitrary clusters i and k:

$$\frac{d\left(\frac{h_{c,i}(t)}{h_{c,k}(t)}\right)}{dt} = \frac{\beta}{h_{c,k}(t)^{1-\eta}}\left(\left(\frac{h_{c,i}(t)}{h_{c,k}(t)}\right) - \left(\frac{h_{c,i}(t)}{h_{c,k}(t)}\right)^{\eta}\right). \tag{2.7}$$

Not only for 2D circular clusters ($\eta = \frac{1}{2}$), but for any $0 < \eta < 1$, the ratio $h_{c,i}/h_{c,k}$ always increases when $h_{c,i} > h_{c,k}$ and always decreases when $h_{c,i} < h_{c,k}$, so that differences in cluster size will always grow. This suggests that a single winner will emerge, and this winner will be the cluster that started out as the largest. Numerical simulations confirm this, even when the initial difference in cluster size is very small (Fig 2.7A). These results show that polarisation will occur when cluster growth increases with cluster size faster than shrinkage does and all clusters rely on the same homogeneous pool of inactive GTPase.

2.2.5 With GTPase turnover, smaller clusters can sustain themselves from their own local supply

The previous result does not depend on mass conservation, since, if present, the terms describing production and degradation cancel out in the derivation of Eq. 2.7. To understand the mechanism by which breaking mass conservation stabilises coexistence, we therefore have to take into account that the competing clusters actually are spatially separated, possibly resulting in local differences in inactive GTPase availability. We therefore extended the basic ODE model in Eq. 2.6 by giving every cluster its own local pool with an amount $h_{p,n}$ of inactive GTPase (Fig 2.6B, see Appendices 2.8.6 for details). Clusters can only draw GTPase from their own compartments. Inactive GTPase is passively exchanged between compartments at a constant rate resembling Fick's law for diffusion. This results

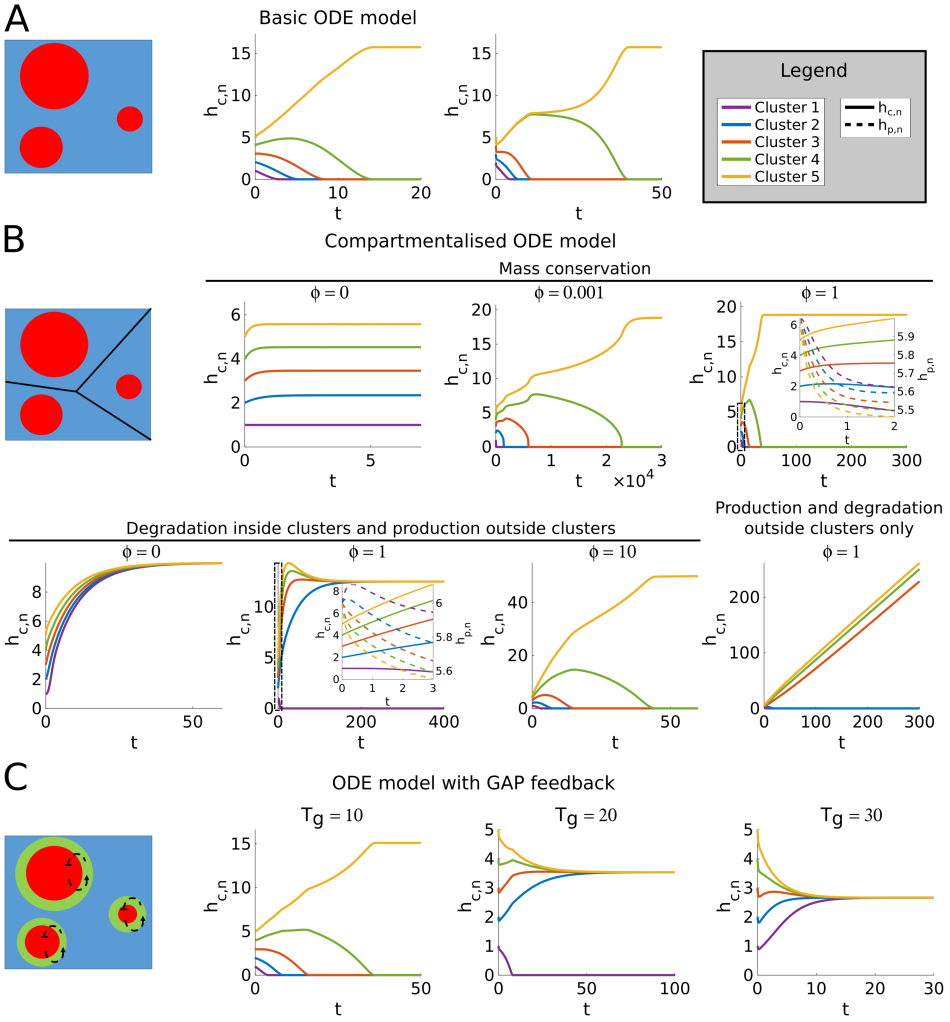

Fig. 2.7. Simulations of the ODE models. Cartoons correspond to model variants described in Fig 2.6. All simulations started with five clusters of different size ($h_{c,n}$, $n \in \{1,2,3,4,5\}$). Parameters α, β, and ε can be scaled out and were set to 1. Other parameter values were: $\delta = 5$, $\eta = 0.5$, and $\gamma = \zeta = 10$. A: Simulations of the basic mass conserved ODE model. The total amount of GTPase in the system (T) was set to 21. B: Simulations of the ODE model with membrane compartments. Clusters had starting levels of GTPase of 1, 2, 3, 4, and 5, while all membrane compartments had a starting level of 6. Exchange rates between compartments (ϕ) were varied for both mass conserved and non-mass conserved cases. For cases without mass conservation, GTPase production rates in the local pools were set to 1 and degradation rates in either clusters or local pool were set to 0.1. Insets show details of dynamics in boxed regions, including dynamics of GTPase in local pool compartments ($h_{p,n}$, dashed lines). C: For GAP simulations, total GAP (T_g) was varied, always starting with all GAP in the shared pool.

in:

$$\begin{aligned}\frac{dh_{c,n}(t)}{dt} &= \alpha h_{c,n}(t)h_{p,n}(t) - \beta h_{c,n}(t)^{\eta} - \delta h_{c,n}(t) - \xi h_{c,n}(t)\\ \frac{dh_{p,n}(t)}{dt} &= \sigma - \alpha h_{p,n}(t)h_{c,n}(t) + \beta h_{c,n}(t)^{\eta} + \delta h_{c,n}(t) - \xi_p h_{p,n}(t) + \phi \sum_{j=1}^{N}(h_{p,j} - h_{p,n}),\end{aligned} \tag{2.8}$$

where σ is a constant production rate, ξ and ξ_p are constant degradation rates of active and inactive GTPase respectively, and ϕ is the constant exchange rate between compartments due to diffusion of inactive GTPase.

The counterpart of Eq. 2.7 now reads as:

$$\frac{d}{dt}\left(\frac{h_{c,i}(t)}{h_{c,k}(t)}\right) = \frac{\beta}{h_{c,k}(t)^{1-\eta}}\left(\left(\frac{h_{c,i}(t)}{h_{c,k}(t)}\right) - \left(\frac{h_{c,i}(t)}{h_{c,k}(t)}\right)^{\eta}\right) + \alpha\frac{h_{c,i}(t)}{h_{c,k}(t)}(h_{p,i} - h_{p,k}). \tag{2.9}$$

The extra term depends on the difference between the amounts of GTPase in the two non-cluster compartments. Since larger clusters are expected to more effectively drain their local compartment, this term will act to decrease the ratio between sizes of clusters i and k if cluster i is larger and decrease this ratio if cluster k is larger. However, it is not a priori clear which of the two terms in Eq. 2.9 is dominant. This dominance may be affected by turnover.

Simulations suggest that without production and degradation ($\sigma = \xi = \xi_p = 0$, mass conservation) the compartmentalised model only allows coexistence in the trivial case where the exchange rate between compartments is zero (Fig 2.7B). When there is exchange between compartments, competition proceeds until only a single cluster remains, even though inactive GTPase levels outside large clusters are smaller than GTPase levels outside small clusters. These results indicate that in the mass conserved case larger clusters do indeed more effectively deplete their local GTPase pool. Although this hampers their further growth, it also results in a gradient and corresponding net flux of non-cluster GTPase from compartments with smaller clusters to those with larger clusters (Fig 2.6D). Since there is nothing to disrupt this flux or replenish the GTPase pools for smaller clusters, this process continues until only the largest cluster remains.

Simulations with turnover, but without degradation of non-cluster GTPase did yield coexistence (Fig 2.7B). Therefore, disruption of the flux form smaller to larger clusters by turnover does not seem to be required for coexistence. Instead, turnover seems to stabilise coexistence by removing GTPase mostly from larger clusters and redistributing it homogeneously, thereby compensating the diffusive flux to the domains of larger clusters (Fig 2.6D). At the same time, the growth of the larger clusters is hampered by their smaller pool of non-cluster GTPase, allowing the smaller clusters to catch up. The coexistence was lost at high rates of exchange between compartments, where the system converges to the basic model with a single homogeneous pool.

Simulations with degradation in non-cluster compartments instead of in clusters all resulted in unbounded growth of surviving clusters, again suggesting that removal must target active GTPase to allow stable patterns to form. Note that this unbounded growth is an artefact of the simplified model. In reality, described by the full spatial (PDE) model, cluster growth stops when all clusters have merged, forming a new homogeneous state (see Appendices 2.8.5 and S4 Video). When considering degradation of both active and

inactive form at the same time, stable coexistence can be found (Appendices 2.8.7 and S5 Video), indicating that degradation of the inactive form does not preclude coexistence.

2.2.6 GAP feedback stabilises coexistence by punishing larger clusters

To study the way in which GAPs stabilise coexistence of multiple GTPase clusters, we also considered an extension of the basic ODE model from Eq. 2.6 including the effect of GAPs (Fig 2.6C). In this extension, every cluster has its own amount of active GAP $G_{c,n}$ and all clusters share a common pool with an amount G_p of inactive GAP. Active GAPs inactivate GTPase at a rate proportional to GAP and GTPase concentrations. GAPs are activated by the active GTPase clusters, and inactivated at a constant rate and by diffusion across the boundaries of the cluster. Together, these assumptions lead to the following extended model:

$$\begin{aligned}
\frac{dh_{c,n}(t)}{dt} &= \alpha h_{c,n}(t)h_p(t) - \beta h_{c,n}(t)^\eta - \delta h_{c,n}(t) - \varepsilon G_{c,n}(t) \\
\frac{dh_p(t)}{dt} &= -\alpha h_p(t)\sum_{j=1}^{N} h_{c,j}(t) + \beta \sum_{j=1}^{N} h_{c,j}(t)^\eta + \delta \sum_{j=1}^{N} h_{c,j}(t) + \varepsilon \sum_{j=1}^{N} G_{c,j}(t) \\
\frac{dG_{c,n}(t)}{dt} &= \gamma h_{c,n}(t)G_p(t) - \delta_g G_{c,n}(t) - \zeta h_{c,n}(t)^{\eta-1} G_{c,n} \\
\frac{dG_p(t)}{dt} &= -\gamma G_p(t)\sum_{j=1}^{N} h_{c,j}(t) + \delta_g \sum_{j=1}^{N} G_{c,j}(t) + \zeta \sum_{j=1}^{N} h_{c,j}(t)^{\eta-1} G_{c,j}(t),
\end{aligned} \tag{2.10}$$

where $G_{c,n}$ is the total amount of active GAP in cluster n, γ is the GTPase-dependent GAP activation rate, δ_g is a constant GAP inactivation rate, ζ is the rate at which the cluster loses GAP by diffusion across the circumference, and ε the rate of GAP-dependent GTPase inactivation. The form of the GAP-related terms in these equations is a direct consequence of using amounts instead of concentrations (see Appendices 2.8.6). The total amount of GAP $T_g = G_p + \sum_{j=1}^{N} G_{c,j}$ is conserved.

In the same way as before, we obtained for each pair (i,k) of clusters:

$$\frac{d}{dt}\left(\frac{h_{c,i}(t)}{h_{c,k}(t)}\right) = \frac{\beta}{h_{c,k}(t)^{1-\eta}}\left(\left(\frac{h_{c,i}(t)}{h_{c,k}(t)}\right) - \left(\frac{h_{c,i}(t)}{h_{c,k}(t)}\right)^\eta\right) - \varepsilon\frac{G_{c,i}(t)h_{c,k}(t) - G_{c,k}(t)h_{c,i}(t)}{h_{c,k}(t)^2}. \tag{2.11}$$

Due to the extra GAP-dependent term, differences in cluster size no longer always increase. As the cluster size increases, the amount of GAP in the cluster will also increase, changing the rate at which the ratio between the two cluster sizes changes in favour of the smaller cluster. However, the net effect of the GAP-dependent term depends on the product of the amount of GAP in one cluster and the size of the other, so the sign of this term is not a priori clear. If we assume that GAP dynamics is fast compared to changes in cluster size, we can take a quasi steady state approximation, which allows the amounts of GAP to be written as a function of cluster size (see Appendices 2.8.8). This way Eq. 2.11

can be written as:

$$\frac{d}{dt}\left(\frac{h_{c,i}(t)}{h_{c,k}(t)}\right) = \frac{\beta}{h_{c,k}(t)^{1-\eta}}\left(\left(\frac{h_{c,i}(t)}{h_{c,k}(t)}\right) - \left(\frac{h_{c,i}(t)}{h_{c,k}(t)}\right)^{\eta}\right) - \varepsilon T_g \frac{h_{c,i}(t)}{h_{c,k}(t)} \cdot \frac{\frac{1}{h_{c,i}(t)^{\eta-1}+\delta_g/\zeta} - \frac{1}{h_{c,k}(t)^{\eta-1}+\delta_g/\zeta}}{\zeta/\gamma + \sum_{j=1}^{N} \frac{h_{c,j}(t)}{h_{c,j}(t)^{\eta-1}+\delta_g/\zeta}}. \tag{2.12}$$

Here, the first term always acts to increase differences in cluster size, whereas the second term always acts to decrease differences for the entire range of $0 < \eta < 1$. Which effect dominates depends on the parameters. The equation suggests that a larger total amount of GAP will shift the balance in favour of coexistence. Numerical simulations confirmed this (Fig 2.7C). This result indicates that GAP feedback stabilises the coexistence of multiple clusters by punishing larger clusters, which tend to activate more GAPs (Fig 2.6D).

Since the GAP dependent term in Eq. 2.12 is proportional to the total amount of GAP, one might expect that the number of stably coexisting clusters can be increased by simply increasing the amount of GAP. Numerical simulations of the ODE model seem to confirm this (Fig 2.7C). However, the ODE model assumes the existence of clusters which in the full PDE model is not guaranteed. This provides the additional constraint that the parameters must remain in the Turing regime, which strongly limits the extent to which the total amount of GAP can be increased (Fig 2.5C).

2.2.7 Dynamic regulation of established patterns: a case study of tip growing systems

Above, we established two mechanisms that can lead to stable coexistence of multiple GTPase clusters. As a case study, we now explore tip growing systems, where dynamical regulation of the GTPase pattern is often important. In pollen tube tip growth, the supply of GAP increases as the cap of active GTPase at the tip grows, so that the size of the GTPase cluster oscillates and the tip grows in pulses [171, 182]. In the fungus *Ashbya gossypii*, the tip growth complex (polarisome) sometimes disappears, corresponding with a stop in tip growth, after which it spontaneously re-establishes and growth continues, suggesting a negative feedback [172]. In addition, two types of branching occur in *A. gossypii*: lateral branching, where a new tip appears somewhere along the length of an existing hypha, and apical branching, where a growing tip splits in two [88]. We use proof of principle simulations of single GTPase clusters both to explore the options our mechanisms give for such dynamic regulation of the GTPase pattern and to offer possible explanations of these phenomena (see Methods for implementation details).

These simulations show that the cases of pulsing and disappearing GTPase caps can be reproduced by an increase in either the total amount of GAP (Fig 2.8A-E, S6 Video), or the GTPase degradation rate (Fig S2.6A-E, S6 Video). If these parameters return to their base levels after the cluster has shrunk or disappeared, it will immediately grow back or reappear, allowing the cycle to start again. The required change in parameters under the current settings is at most 50%, which could reasonably be achieved by changes in GAP production or release, or the recycling of membrane proteins. Alternatively, oscillations

might also arise from the internal dynamics of the GTPase system. For example, Meinhardt showed that oscillations of disappearing and reappearing clusters can be found for a system with both a fast global inhibitor and a slow local inhibitor [183]. This suggests that GAP could take the role of slow local inhibitor in our model. Slowing down the time scale of GAP accumulation (through reducing activation and inactivation rates ($c = 0.01$ and $d = 0.01$)) to much larger time scale differences than in Meinhardt [183], however, did not produce any oscillations in our model. Whether further adaptations of the WP-GAP model and its parameters would enable such autonomous oscillations, remains an interesting direction for future investigation.

Note that as long as we start off with an existing cluster, the total amount of GAP or the GTPase degradation rate may even end up somewhat outside the Turing regime without the cluster disappearing. However, the cluster disappears long before leaving the regime where LPA predicts a heterogeneous state to exist (Fig 2.8B and Fig S2.6B). This indicates that although Turing regimes are accurately predicted by LPA, regimes with a stable heterogeneous state are not.

It has been suggested that lateral branching in fungi may be the result of apical dominance factors in the tip that suppress branching in the vicinity [184, 185]. However, our finding that turnover or negative feedback is needed to prevent polarisation (Fig 2.2) suggests that apical dominance may well be the default state and not require any dominance factor. Inhibitors (e.g. GAPs) may well be involved, but rather than merely creating an inhibition zone where no new clusters can be formed, their main role could be to keep the existing cluster from expanding indefinitely, thereby actually enabling the formation of new clusters. Alternatively, at large distances from the tip, it may no longer be reasonable to assume mass conservation across the entire hypha, and GTPase turnover will break competition, allowing a new tip to form.

Apical branching requires the splitting of an existing cluster rather than the appearance of a new one. Previously, an accumulation of inhibitor in the cluster has been suggested as potential mechanism [86]. Our results on the ODE model with GAP feedback suggest this might be possible, if we could significantly increase the amount of GAP without leaving the Turing regime. We can achieve this by simultaneously raising the total amount of GTPase (Fig 2.8G). At higher levels of both total GTPase and GAP compared to the single cluster set-up used before, we indeed find that two stable clusters form (Fig 2.8F-H, S6 Video). Upon increasing the total amounts of GTPase and GAP to this level starting from a single cluster steady state, the single cluster splits in two (Fig 2.8I, S6 Video). This suggests that apical branching may occur by accumulation of GTPase and GAP from fusing vesicles during tip growth.

These results and considerations demonstrate that a mechanism that allows for stable coexistence can offer elegant explanations for a range of phenomena in tip growing systems that could not well be explained with a polarisation mechanism. The specifics of individual systems remain a topic for future investigation.

2.3 Discussion

In this study, we uncovered and investigated several mechanisms through which highly similar GTPase-based systems can generate different types of patterns. Polarisation is the

invariable result of a mass conserved GTPase under positive feedback activation, because the stronger activation in larger GTPase clusters leads to a gradient and corresponding net

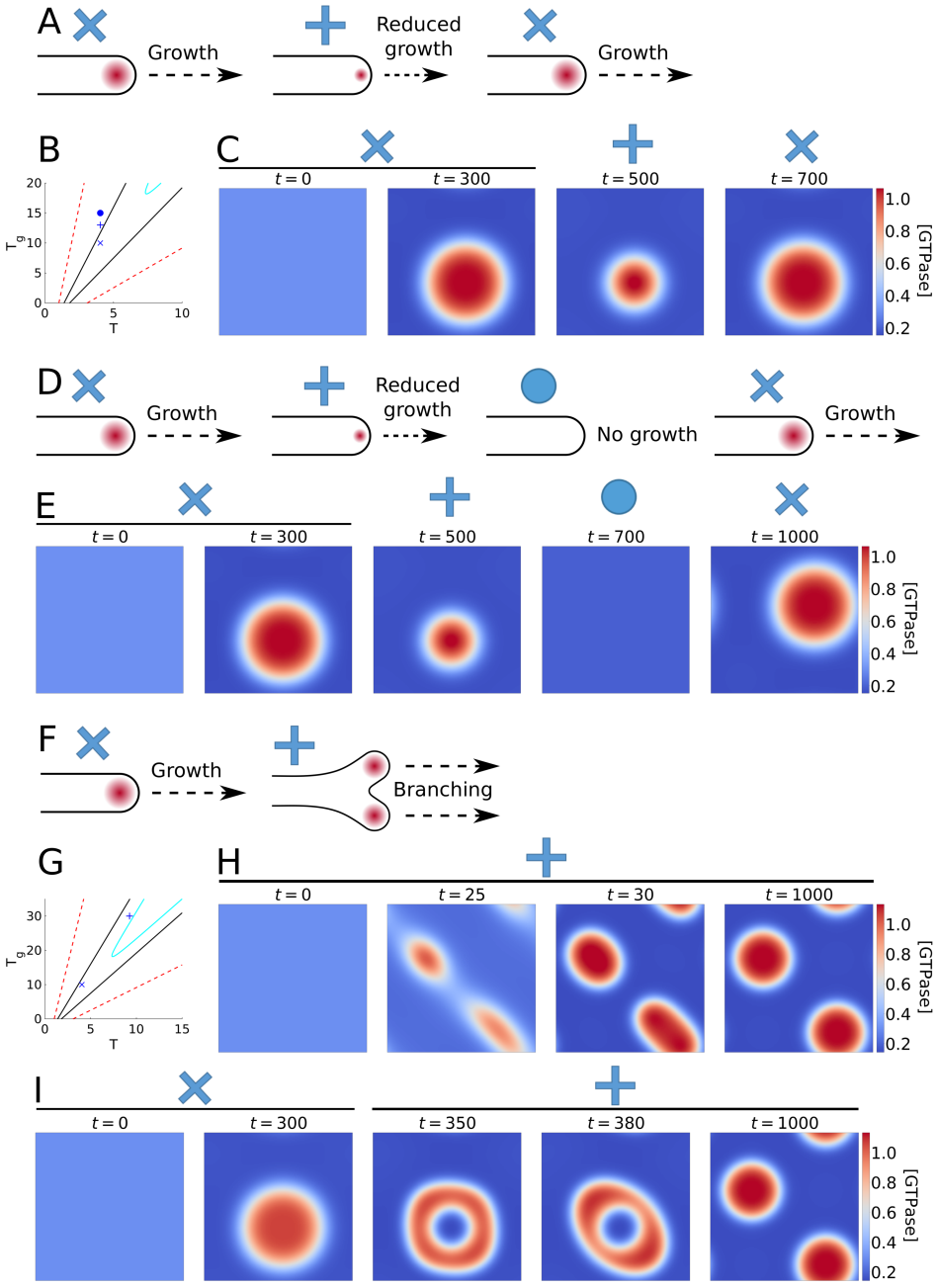

Fig. 2.8. Caption on next page.

Fig. 2.8. Tip growth simulations with the WPGAP model. B and G: Bifurcation plots with symbols showing parameter settings used in the simulations, corresponding to symbols above simulations and cartoons. For meaning of lines see Fig 2.5. A: In pollen tubes, growth occurs in pulses as negative feedback during growth results in an oscillatory GTPase cluster at the growing tip. C: Simulation of a single active GTPase cluster with increase in T_g upon reaching steady state followed by a return to starting levels. D: In growing hyphae of *A. gossypii*, the tip growth complex sometimes disappears corresponding to a halt in growth, suggesting involvement of negative feedback. E: Simulation with two subsequent increases in T_g, followed by a return to the starting level. F: In apical branching of growing hyphae, the tip growth complex and the growing tip itself split in two. H: Simulation at elevated GTPase (T) and GAP (T_g) levels (+) resulting in two clusters. I: Simulation starting in the one cluster regime (x) followed by a increase in T and T_g causing the single cluster to split. Time points (t) of snapshots are indicated inside each plot. All simulations domains have periodic boundary conditions in both directions. Colour bars indicate active GTPase concentrations ([GTPase]).

flux of inactive GTPase from smaller clusters to larger ones (Fig 2.9A). Stable coexistence of multiple GTPase clusters can be achieved either by breaking mass conservation, or adding negative feedback through the activation of an inhibitor. In the first case, a constant supply of fresh GTPase across the membrane allows smaller clusters to grow in spite of the net flux to larger clusters (Fig 2.9B). In the latter case, larger clusters activate more inhibitor, limiting their growth (Fig 2.9C). In contrast to a previously proposed mechanism based on saturation of self-activation, these mechanisms lead to actually stable coexistence and can also explain the emergence of additional clusters as occurs, e.g., during branching in tip growth. Our use of two different minimal models suggests that these conclusions do not depend on the precise positive feedback mechanism.

2.3.1 Mass conserved polarisation models cannot explain all relevant membrane patterns

Most existing models for polarisation involve mass conservation and some form of positive feedback [44]. Our results show that these two properties indeed consistently result in polarisation for both direct positive feedback and double negative feedback. Analysis of a simplified ODE approximation of a system of competing clusters suggests that this happens because larger clusters more effectively deplete their local reserve of inactive GTPase (Fig 2.9A). In the ODE model, the local pool of inactive GTPase is considered homogeneous. In reality, the level of inactive GTPase in the cluster will be lower than the level surrounding the cluster and inactive GTPase will flow towards both clusters from their direct surroundings. However, even in the worst case scenario the larger circumference of the larger cluster will cause more inactive GTPase to diffuse to the larger cluster. On a 1D domain, this effect would not be apparent. This insight may explain the longer competition times in 1D as compared to 2D.

A recent theoretical study proposed that severely slowed competition as a result of saturation could explain the difference between polarisation and coexistence [177]. On top of its inability to explain the appearance of new clusters after an initial pattern has been established, our findings show that this mechanism works less well when the formation of many clusters at the same time is considered. Therefore, the mechanisms for stable coexistence we propose here provide a better explanation for patterns as found in metaxylem [148], pavement cells [176], neurons [166], and fungal hyphae [170].

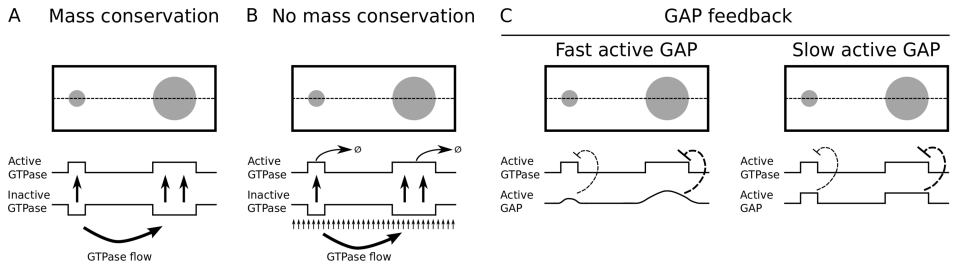

Fig. 2.9. Proposed mechanisms for polarisation and coexistence. A: In polarisation models, larger clusters of active GTPase more effectively deplete the local supply of inactive GTPase than smaller ones. This results in a gradient of inactive GTPase that favours diffusion towards the larger cluster allowing the larger cluster to grow at the expense of the smaller one. B: When mass conservation is broken, production provides a fresh supply of GTPase to sustain smaller clusters in spite of this flux while degradation prevents larger clusters from growing uncontrollably, enabling coexistence. C: When active GTPase promotes GAP activation, larger clusters activate GAPs more effectively, promoting their own inactivation and allowing smaller clusters to survive. However, if GAPs were to diffuse as slowly as active GTPase, they would not be able to escape the cluster and quench the ability of the system to give rise to patterns in the first place.

2.3.2 Two types of model extensions can stabilise coexisting clusters

Sufficiently strong GTPase turnover can stabilise coexistence

The main difference between existing polarisation models that generate a single cluster and classical activator substrate depletion models that generate multiple clusters [47] is the assumption of mass conservation. We showed in 2D that by simply adding production and degradation terms to the two polarisation models, stable steady states with multiple clusters can be obtained as has been shown before for the 1D case [158]. Our ODE approximation suggests that this coexistence results from a redistribution of GTPase, with degradation mostly affecting larger clusters while production is homogeneous (Fig 2.9B). Moreover, we found that stable coexistence requires degradation of the *active* form. If only the inactive form is degraded, active GTPase in clusters can escape degradation and clusters keep growing until they fill the entire domain.

Broken mass conservation can only explain patterns of coexisting clusters if there is sufficient GTPase turnover for a given domain size. When the turnover rate or domain size becomes too small, models with turnover will converge to mass conserved models and polarisation will occur. This explains, for example, how a study on root hair initiation could obtain a single GTPase cluster with a model containing production and degradation terms [35]. To obtain stable coexistence, half-lives should most likely be shorter than the 10 to 30 hours reported for GTPases from a macrophage cell line [186]. However, different GTPases may have different turnover rates, and even half-lives of the same GTPase may be altered significantly by regulation [187], so this does not seem unreasonable.

Stable coexistence through GTPase turnover seems especially plausible on large domains, such as plant cells. In contrast, mass conservation is more plausible on smaller domains, such as neuron cell bodies [188], so that other mechanisms may be required to explain coexistence there. Since larger domains can hold more stable clusters, broken mass conservation may also be able to explain the formation of new clusters in between existing ones on a growing domain. This may explain the appearance of new protrusions

during lateral branching of hyphae [88] and in growing pavement cells [176]. However, this behaviour does not provide the cell with much dynamic control, as it links cluster number to the domain size for any given turnover rate.

GAP feedback is a flexible alternative for stabilising coexistence

Even in cases of (near) mass conservation, coexistence is still possible through further additions to the interaction motif. Our results show that addition of negative feedback through activation of a sufficiently fast diffusing inhibitor (GAP) can stabilise coexistence in the two polarisation motifs studied. This is consistent with previous suggestions [157]. The ODE model indicates that GAP feedback fulfils this role by punishing larger clusters, which activate more GAP (Fig 2.9C). This mechanism only works when GAPs diffuse faster than active GTPase, possibly because too slowly diffusing GAPs will too strongly accumulate locally in clusters and extinguish them. This difference in diffusion rates could be achieved if active GAPs are not membrane-bound, or at least do not interact as strongly with the membrane or membrane-bound proteins as active GTPase.

GAP feedback and broken mass conservation are not mutually exclusive and which interaction motif is used in practice will have to be judged on a case by case basis. Experimental evidence suggests GAP feedback is involved in the spotted pattern found in metaxylem [148]. Our modelling results predict that if this feedback is indeed responsible for the coexistence of multiple GTPase clusters, experiments reducing GAP expression would result in fewer clusters.

Unlike broken mass conservation, GAPs provide extra options for regulation, making them more flexible. As shown by our tip splitting simulations, simultaneously providing extra GTPase and GAP can result in the splitting of a GTPase cluster. Previously, dilution due to repeated fusion of vesicles during tip growth has been suggested as a source of negative feedback to achieve tip splitting [86], but it would be hard to combine this with an increase in GTPase levels. Regulating GAP feedback, however, gives the cell the ability to control the number of clusters, even independent of the domain size.

Another example can be found in fission yeast (*Schizosaccharomyces pombe*), where a bipolar pattern of two active GTPase clusters promotes growth of the rod shaped cells in both directions. Upon cell division, both daughter cells start with a unipolar pattern and grow in a single direction until a certain size is reached at which a second GTPase cluster forms and bipolar growth is resumed ("new end take off"; NETO) [189]. The appearance of an additional cluster on a larger domain could be explained by both types of coexistence models. However, to also explain the reported oscillations between both tips requires a time delayed negative feedback [190, 191], which could not be achieved through linear GTPase degradation, whereas an extra molecular player (such as GAP) offers more flexibility to introduce a delay.

2.3.3 Dynamic regulation of GTPase patterns in tip growing systems

Our findings suggest that multiple as yet poorly understood phenomena in mycelial tip growth could be explained by assuming some form of (GAP-like) negative feedback as is also implicated in pollen tube growth [171, 192]. Such negative feedback could, for instance, explain the occasional disappearance and reappearance of the tip growth com-

plex observed in *A. gossypii* [172]. In our simulations, the GTPase cluster reappeared at a random position, whereas in reality it would have to reappear at the same position as the original cluster (i.e. the tip of the growing cell). In reality, the dome shape of the tip growing cell could provide the required positional guidance, as cell shape is known to affect the localisation of clusters [178] as well as their dynamics [34]. Cytoskeletal and vesicular processes may also play a role in maintaining the cluster of active GTPase at the actual tip and preventing it from drifting to or reappearing in some other location. Moreover, interactions between these processes and GTPase patterning could explain the oscillations we simply imposed here with abrupt parameter changes.

A combination of regulated negative feedback and an increase in total GTPase may explain apical branching observed in this species [88]. Root hairs in plants do not normally branch, but overexpression mutants of ROP2, the GTPase controlling tip growth in root hairs, have root hairs with strong apical branching [193]. This supports the hypothesis that an increase in total GTPase, combined with some form of negative feedback, can result in apical branching through splitting of the GTPase cluster at the tip. A modelling study of GTPase controlled keratocyte movement showed that a cell that extends in the direction of a GTPase cluster could have its growth front split in two after encountering a suitably sized obstacle [34]. This split may then be (apparently) stabilised by the induced shape changes, which seems to depend on the relative speed of shape changes and cluster competition. For cell-autonomous splitting, however, a GTPase model that allows for *de novo* cluster formation would be required.

Since our models show that a single cluster is obtained unless sufficient turnover or GAP feedback is involved, polarisation may well be the default state. In this case, hypothesized apical dominance factors [185] that suppress branching would not be required. Rather, there would be more need for a branching signal that either stimulates negative feedback or GTPase turnover. Indeed, for arbuscular mycorrhizal fungi, a branching signal seems to be present in the form of strigolactones, although the precise molecular mechanism is still poorly understood [194]. Therefore, studies on hyphal branching focusing on identifying and characterising such branching factors may prove more fruitful than studies looking for apical dominance factors.

2.4 Materials and methods

2.4.1 Initial conditions

We initiated PDE simulations at the homogeneous steady state (see Appendices 2.8.2) with an amount of noise added to each integration pixel for the active form and the same amount subtracted from the corresponding inactive form. This made it as if a random small amount was interconverted between active and inactive form, without changing the total mass at each pixel. Per pixel, the noise was drawn from a normal distribution with a mean of 0 and a standard deviation of 10^{-6}.

2.4.2 Numerical methods

We performed numerical simulations using the python package Dedalus [195], which implements a spectral solver method, with the recommended dealias factor of 1.5 and the

Runge-Kutta time-stepper. Fourier and Chebyshev basis functions were used for the x- and y-direction respectively, except for single cluster simulations, where Fourier basis functions were used in both directions. To determine appropriate temporal and spatial step sizes, we first performed several trial simulations for each model with reproducible perturbations as previously described [196], so that accuracy could be assessed using mesh refinement and time step reduction. We performed the final simulations with noise added directly to each integration pixel to ensure all possible wave lengths are represented. Integration steps used for final simulations are given in Table S2.1. We continued all simulations until a steady state was reached (no more noticeable changes in the concentrations). In some simulations, a stable pattern ended up drifting at a constant speed in the periodic direction. This can happen because with periodic boundary conditions any shift of a solution is also a solution. Therefore, such drifting patterns were regarded as steady states.

We performed simulations of the ODE models in matlab using the function ode45 with default parameters.

2.4.3 Bifurcation and stability analysis

For the models with only two variables (WP and WPT), we performed both a classical linear stability analysis (LSA) and the asymptotic local perturbation analysis (LPA). With more variables, LSA becomes exceedingly complicated (although not technically impossible [197, 198]). Therefore, we only used LPA for the remaining models. LSA can be used to determine under what conditions arbitrarily small spatial perturbations in a homogeneous state can grow. This way, parameter regimes where spontaneous patterning occurs can be identified. The wave numbers of the perturbations that become unstable have often been used to predict the length scales of the pattern, but these are only valid close to the homogeneous state and therefore not in general a good reflection of the length scales of the final pattern [181]. We performed LSA as previously described [199] as described in Appendices 2.8.3.

LPA is a recently developed asymptotic analysis for reaction-diffusion models [200, 201]. It works by considering the behaviour of a local pulse in the activator concentration, in the limiting case where the diffusion coefficients of slowly diffusing components approach zero and those of rapidly diffusing components approach infinity. This reduces the system of PDEs to a system of ODEs that can be analysed with existing bifurcation software. It is, therefore, not as exact as LSA, but it can be more easily scaled up to models with more than two components and it can also be used to chart the areas of parameter space where the homogeneous state is stable, but coexists with a stable heterogeneous state. In these regions, patterning will not occur spontaneously, but it may occur in response to a sufficiently large perturbation and an existing pattern will not disappear. In our case, we used strong differences (100 fold) in diffusion rates and, therefore, regimes predicted by LSA and LPA matched quite closely. We performed LPA on all our models as described by others [200] (see Appendices 2.8.4 for details) and analysed the resulting ODEs using the matcont package for matlab [202].

2.4.4 Single cluster simulations

To study phenomena observed during tip growth, we performed simulations with the same parameters as before, but on a smaller domain, such that only a single cluster formed. For these simulations we used a square domain with periodic boundary conditions on all sides to keep the small domain from being dominated by boundary effects. This domain represents the tip of the growing tube. The dimensionless domain size was 19.0x19.0 for the WPGAP models, and 31.6x31.6 for the WPT model. To ensure that any unstable states reached would be disrupted, we added noise not only at the beginning, but also every 10 time units. This noise was also drawn from a normal distribution with a mean of 0 and a standard deviation of 10^{-6}. Changes in parameters were applied by starting a new simulation with the altered parameter using the final state of the first part as an initial condition. The resulting abrupt changes function as a crude approximation of the likely more gradual changes in response to factors outside the scope of our models.

Acknowledgements

We thank Marcel Janson for useful comments on the tip growth case study.

2.5 Supplementary figures

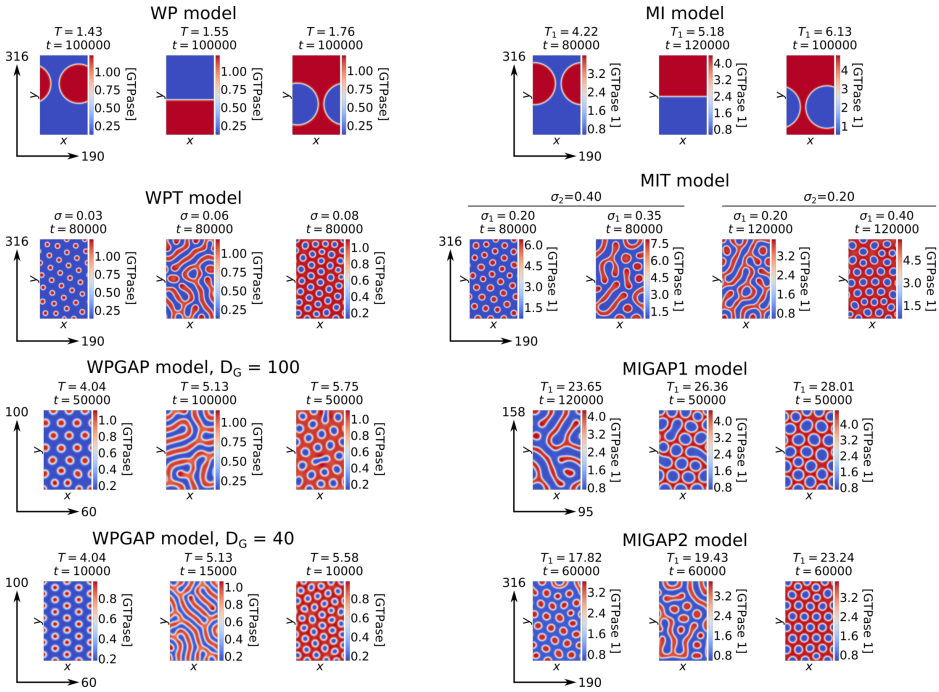

Fig. S2.1. Model simulations with concentrations and time points. Simulations are as in Fig 2.2, but concentration ranges and time points at which simulations were stopped are indicated.

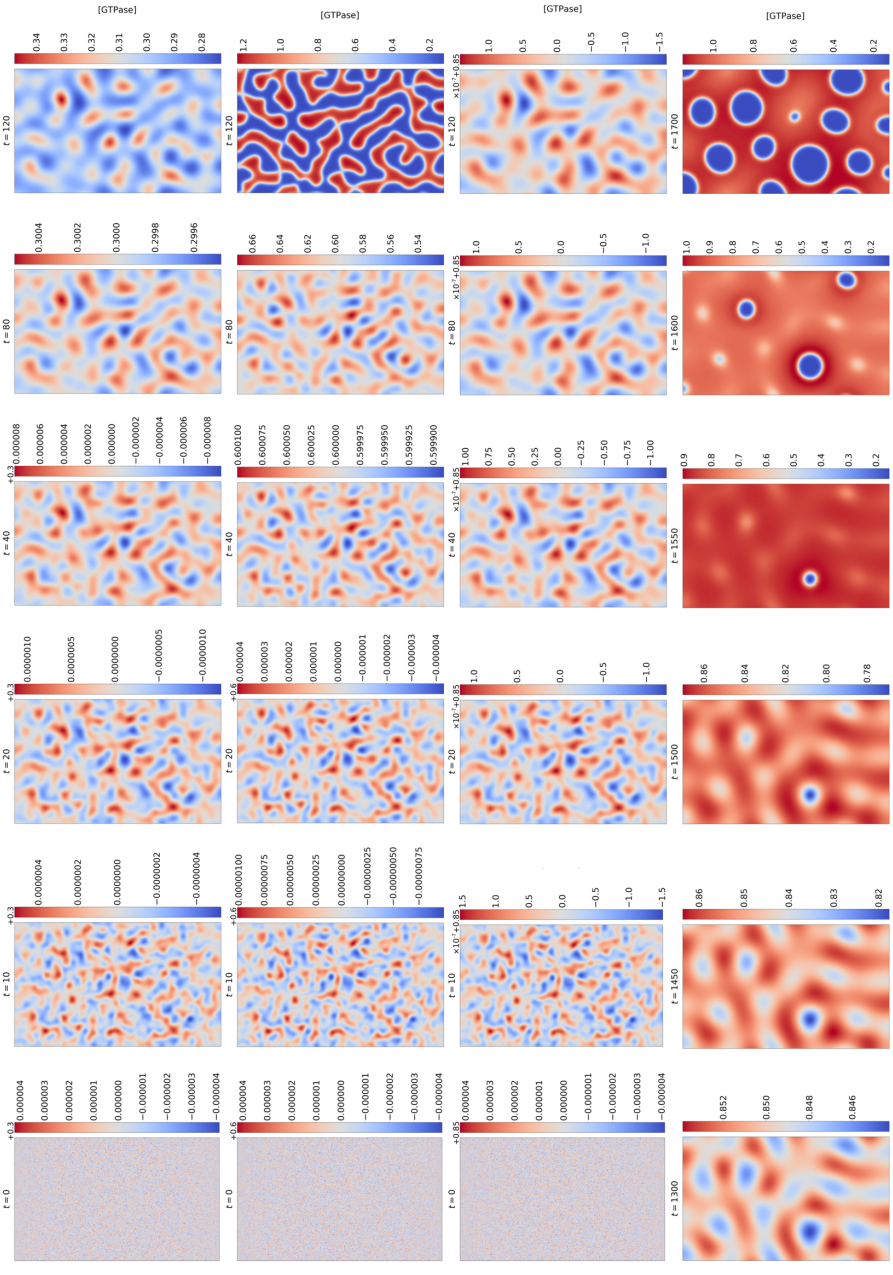

Fig. S2.2. Caption on next page.

Fig. S2.2. Early transient behaviour of the WP model for three values of parameter T. Active GTPase concentration profiles at various time points for WP model simulations from Fig 2.2. Figures show that in all three cases, pattern formation starts with gradual coarsening throughout the simulation domain (reminiscent of spinodal decomposition). All sharply delineated gaps at $t = 1700$ arise as continuous amplifications of an earlier pattern, even though, inside a limited time window, gaps seem to appear one after another (superficially resembling nucleation and growth).

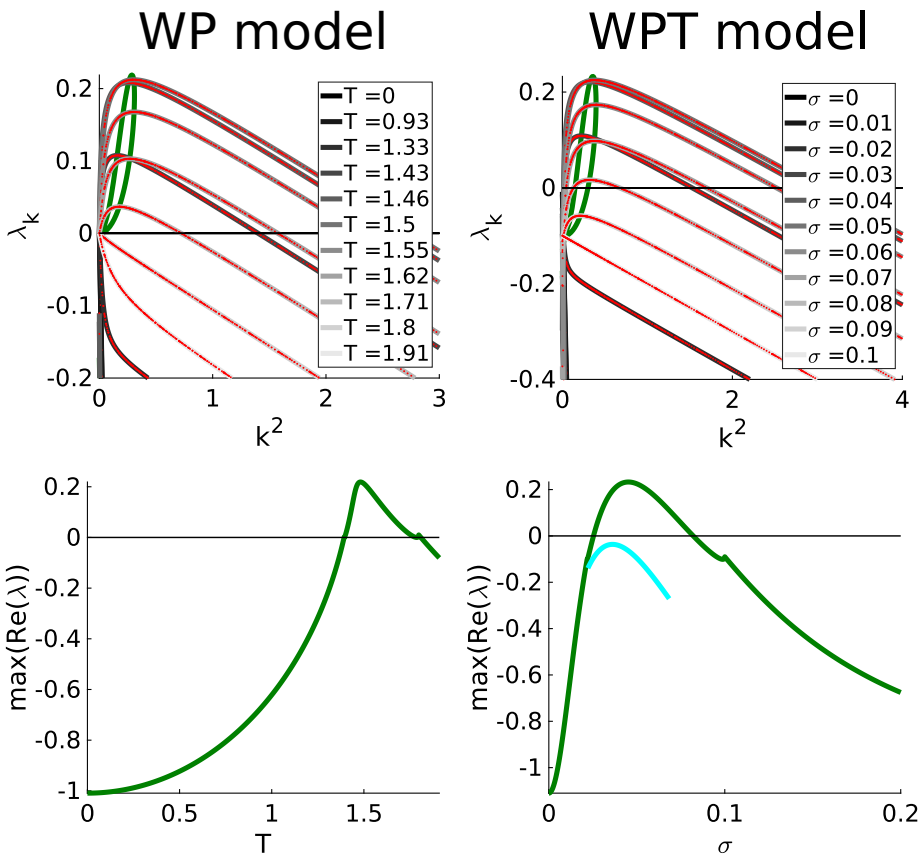

Fig. S2.3. Linear stability analysis for models with two variables. When the real part of at least one eigenvalue (λ) corresponding to a certain admissible wave number (k) is greater than zero the homogeneous state is unstable and a pattern forms. Top figures show λ as a function of k^2 for various parameter values. Admissible wave numbers for the geometry of the simulations are indicated on these lines with red dots. Green lines show the maximum real part of λ as a function of total GTPase (T, WP model) or GTPase production rate (σ, WPT model), plotted both against these parameters (bottom) and against the squared wave numbers (top). Cyan lines indicate real parts of complex eigenvalues where present.

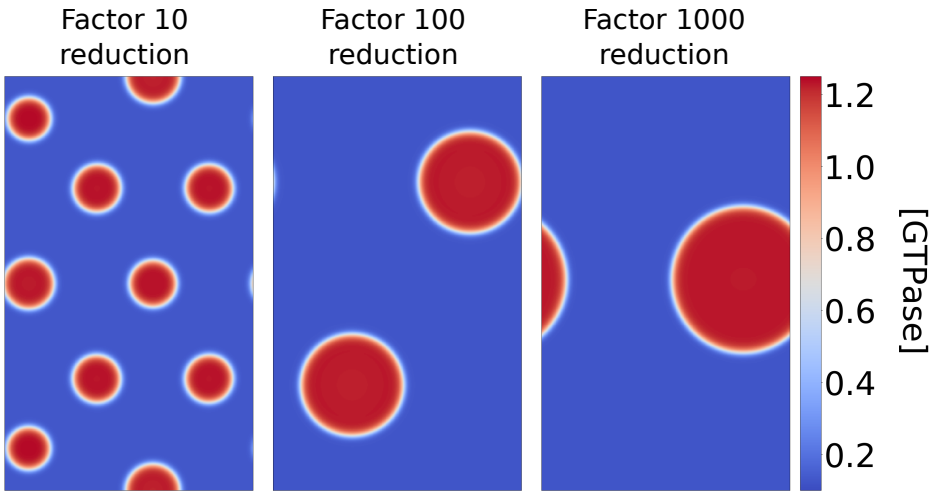

Fig. S2.4. Reduced turnover decreases the number of coexisting clusters generated by the WPT model. Steady state ($t = 200000$) active GTPase profiles generated by the WPT model with production (σ) and degradation (ξ) rates reduced by a factor 10, 100, and 1000 compared to default parameters.

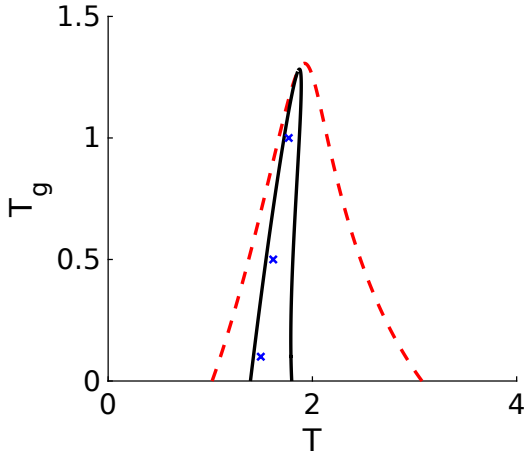

Fig. S2.5. Two parameter bifurcation plot for the WPGAP model with low active GAP diffusion from Fig 2.5C. Crosses indicate parameter settings where trial simulations were performed. All simulations resulted in polarisation.

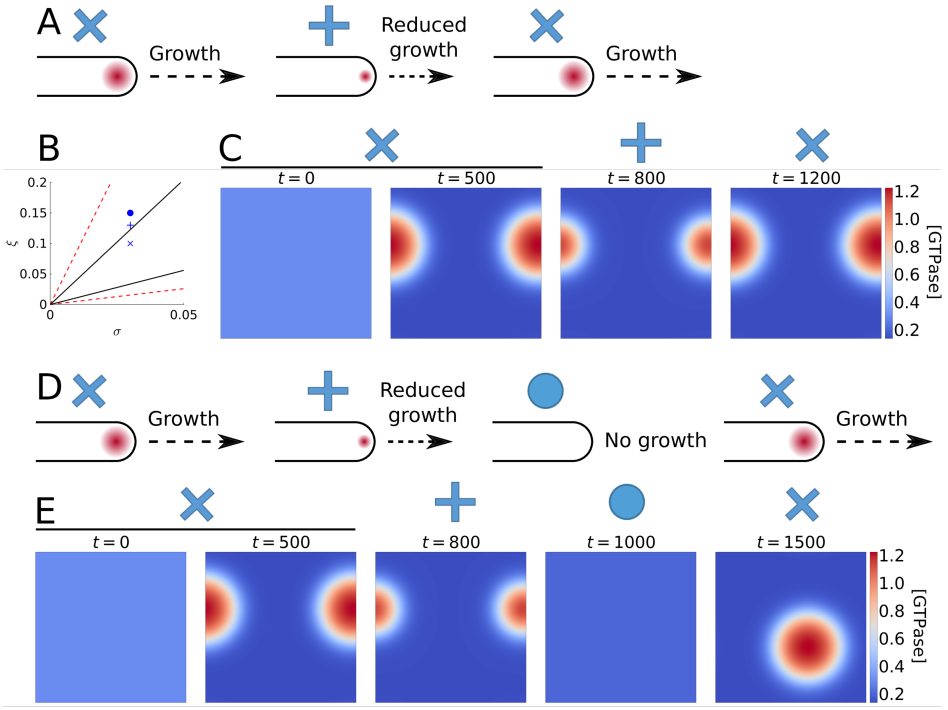

Fig. S2.6. Tip growth simulations with the WPT model. B: Bifurcation plot with symbols showing parameter settings used in the simulations, corresponding to symbols over simulations and cartoons. For meaning of lines see Fig 2.5. A: In pollen tubes, growth occurs in pulses as negative feedback during growth results in an oscillatory GTPase cluster at the growing tip. C: Simulation of a single active GTPase cluster with increase in ξ upon reaching steady state followed by a return to starting levels. D: In growing hyphae of *A. gossypii*, the tip growth complex sometimes disappears corresponding to a halt in growth, suggesting involvement of negative feedback. E: Simulation with two subsequent increases in ξ, followed by a return to the starting level. Symbols over simulations correspond to those in the bifurcation plot. Time points (t) of snapshots are indicated inside each plot. All simulations domains have periodic boundary conditions in both directions. Colour bars indicate active GTPase concentrations ([GTPase]).

2.6 Supplementary table

Table S2.1. Spatial and temporal integration step sizes used for numerical integration.

Model	dx = dy	dt
WP	0.2	0.5
MI	0.25	0.2
WPT	0.2	0.5
MIT	0.2	0.2
WPGAP, $D_G = 100$	0.25	0.2
WPGAP, $D_G = 40$	0.2	0.1
MIGAP1	0.25	0.2
MIGAP2	0.25	0.1
Tip growth simulations	0.05	0.05

2.7 Supplementary movies

Supplementary movies are available for download with the publication of this chapter [163] on the website of PLoS one. Captions are provided below.

S1 Video. Model simulations. Time lapse movies of model simulations from Fig 2.2, showing concentrations of active GTPase. For models with two GTPases only concentrations of the first are shown. The concentration profile of the second GTPase is always complementary to that of the first.

S2 Video. Early transient behaviour of WP model simulations. Time lapse movies of WP model simulations from Fig 2.2, showing concentrations of active GTPase with a higher temporal resolution for the initial patterning stages.

S3 Video. Model simulations in Hopf regimes. Time lapse movies of model simulations in Hopf regimes for the WPT and WPGAP models. Concentrations of active GTPase are shown. The WPT simulation was performed with parameters $\sigma = 0.4$ and $\xi = 1$, domain height $H = 316$, and domain width $W = 190$. The WPGAP simulation was performed with parameters $T = 34.83$ and $T_g = 100$, domain height $H = 50$ and domain width $W = 30$. All other parameters were at default values.

S4 Video. Simulation WPT model with degradation of inactive GTPase. Time lapse movie of model simulation described in Appendices 2.8.5, showing concentrations of active GTPase.

S5 Video. Simulation WPT model with degradation of both active and inactive GTPase. Time lapse movie of model simulation described in Appendices 2.8.7, showing concentrations of active GTPase.

S6 Video. Simulations of tip growth scenarios. Time lapse movies of model simulations from Fig 2.8 and Fig S2.6, showing concentrations of active GTPase.

2.8 Appendices

2.8.1 Non-dimensionalisation

Non-dimensionalisation of the WP model

The full dimension-carrying WP model is given by:

$$\begin{aligned}\frac{\partial u}{\partial t} &= bv + \gamma \frac{u^n}{K^n + u^n} v - \delta u + D_u \nabla^2 u \\ \frac{\partial v}{\partial t} &= -bv - \gamma \frac{u^n}{K^n + u^n} v + \delta u + D_v \nabla^2 v,\end{aligned} \tag{A2.1}$$

where u and v are the concentrations of active and inactive GTPase, respectively, t is the time, b is a constant activation rate, δ is a constant inactivation rate, γ determines the strength of the feedback activation, K is the concentration of active GTPase at which the feedback activation is half its maximum, exponent n is a hill coefficient, and D_u and D_v are the diffusion coefficients of active and inactive GTPase, respectively. Due to mass conservation, the average total GTPase concentration T is constant:

$$T = \frac{1}{A} \iint_A (u+v) dx dy = \frac{\text{Total GTPase}}{A}, \tag{A2.2}$$

where A is the domain area and x and y are the spatial coordinates. Non-dimensionalisation was performed as previously described [168]. GTPase concentrations were scaled with K, time with δ, and space with D_u and δ. The resulting dimensionless variables are:

$$\tilde{u} = \frac{u}{K}, \quad \tilde{v} = \frac{v}{K}, \quad \tilde{t} = \delta t, \quad \tilde{x} = \frac{x\sqrt{\delta}}{\sqrt{D_u}}, \quad \tilde{y} = \frac{y\sqrt{\delta}}{\sqrt{D_u}}, \tag{A2.3}$$

and the dimensionless parameters:

$$\tilde{T} = \frac{T}{K}, \quad \tilde{b} = \frac{b}{\delta}, \quad \tilde{\gamma} = \frac{\gamma}{\delta}, \quad \tilde{D}_v = \frac{D_v}{D_u}, \quad \tilde{A} = A\frac{\delta}{D_u}. \tag{A2.4}$$

This makes the dimensionless total amount of GTPase:

$$\text{Total } \tilde{\text{G}}\text{TPase} = \frac{\text{Total GTPase} \cdot \delta}{D_u K}. \tag{A2.5}$$

Dropping the tildes, we obtain the dimensionless WP model:

$$\begin{aligned}\frac{\partial u}{\partial t} &= bv + \gamma \frac{u^n}{1 + u^n} v - u + \nabla^2 u \\ \frac{\partial v}{\partial t} &= -bv - \gamma \frac{u^n}{1 + u^n} v + u + D_v \nabla^2 v,\end{aligned} \tag{A2.6}$$

with dimensionless average total GTPase concentration:

$$T = \frac{1}{A} \iint_A (u+v) dx dy = \frac{\text{Total GTPase}}{A}. \tag{A2.7}$$

Non-dimensionalisation of the MI model

The full dimension-carrying MI model is given by:

$$\begin{aligned}
\frac{\partial u_1}{\partial t} &= b_1 v_1 + \gamma_1 \frac{K_2^n}{K_2^n + u_2^n} v_1 - \delta u_1 + D_u \nabla^2 u_1 \\
\frac{\partial v_1}{\partial t} &= -b_1 v_1 - \gamma_1 \frac{K_2^n}{K_2^n + u_2^n} v_1 + \delta u_1 + D_v \nabla^2 v_1 \\
\frac{\partial u_2}{\partial t} &= b_2 v_2 + \gamma_2 \frac{K_1^n}{K_1^n + u_1^n} v_2 - \delta u_2 + D_u \nabla^2 u_2 \\
\frac{\partial v_2}{\partial t} &= -b_2 v_2 - \gamma_2 \frac{K_1^n}{K_1^n + u_1^n} v_2 + \delta u_2 + D_v \nabla^2 v_2,
\end{aligned} \tag{A2.8}$$

where u_i and v_i are the concentrations of active and inactive GTPase i respectively, γ_i is the activation rate of GTPase i that can be inhibited by the other GTPase, K_i is the active GTPase i concentration at which the γ of the other GTPase is halved. Other parameters are as in the WP model. For convenience, inactivation rate constant δ is assumed equal for both GTPases. The average concentrations T_1 and T_2 of GTPase_1 and GTPase_2 are as in Eq. A2.2. The dimensionless variables are:

$$\tilde{u}_1 = \frac{u_1}{K_1}, \quad \tilde{u}_2 = \frac{u_2}{K_2}, \quad \tilde{v}_1 = \frac{v_1}{K_1}, \quad \tilde{v}_2 = \frac{v_2}{K_2}, \quad \tilde{t} = \delta t, \quad \tilde{x} = \frac{x\sqrt{\delta}}{\sqrt{D_u}}, \quad \tilde{y} = \frac{y\sqrt{\delta}}{\sqrt{D_u}}, \tag{A2.9}$$

and the scaled parameters:

$$\begin{aligned}
&\tilde{T}_1 = \frac{T_1}{K_1}, \quad \tilde{T}_2 = \frac{T_2}{K_2}, \quad \tilde{b}_1 = \frac{b_1}{\delta}, \quad \tilde{b}_2 = \frac{b_2}{\delta}, \quad \tilde{\gamma}_1 = \frac{\gamma_1}{\delta}, \quad \tilde{\gamma}_2 = \frac{\gamma_2}{\delta}, \\
&\tilde{D}_v = \frac{D_v}{D_u}, \quad \tilde{A} = A\frac{\delta}{D_u}.
\end{aligned} \tag{A2.10}$$

This results in a dimensionless total amount of GTPase as in Eq. A2.5. Dropping the tildes, we obtain the dimensionless MI model:

$$\begin{aligned}
\frac{\partial u_1}{\partial t} &= b_1 v_1 + \gamma_1 \frac{1}{1 + u_2^n} v_1 - u_1 + \nabla^2 u_1 \\
\frac{\partial v_1}{\partial t} &= -b_1 v_1 - \gamma_1 \frac{1}{1 + u_2^n} v_1 + u_1 + D_v \nabla^2 v_1 \\
\frac{\partial u_2}{\partial t} &= b_2 v_2 + \gamma_2 \frac{1}{1 + u_1^n} v_2 - u_2 + \nabla^2 u_2 \\
\frac{\partial v_2}{\partial t} &= -b_2 v_2 - \gamma_2 \frac{1}{1 + u_1^n} v_2 + u_2 + D_v \nabla^2 v_2.
\end{aligned} \tag{A2.11}$$

Non-dimensionalisation of the WPT model

The full dimension-carrying WPT model is given by:

$$\begin{aligned}
\frac{\partial u}{\partial t} &= bv + \gamma \frac{u^n}{K^n + u^n} v - \delta u - \xi u + D_u \nabla^2 u \\
\frac{\partial v}{\partial t} &= -bv - \gamma \frac{u^n}{K^n + u^n} v + \delta u + \sigma + D_v \nabla^2 v,
\end{aligned} \tag{A2.12}$$

where ξ is the degradation rate of active GTPase and σ is a constant production term for inactive GTPase. Other symbols are as in previous models. The dimensionless variables are:

$$\tilde{u} = \frac{u}{K}, \quad \tilde{v} = \frac{v}{K}, \quad \tilde{t} = \delta t, \quad \tilde{x} = \frac{x\sqrt{\delta}}{\sqrt{D_u}}, \quad \tilde{y} = \frac{y\sqrt{\delta}}{\sqrt{D_u}}, \tag{A2.13}$$

and the scaled parameters:

$$\tilde{b} = \frac{b}{\delta}, \quad \tilde{\gamma} = \frac{\gamma}{\delta}, \quad \tilde{\xi} = \frac{\xi}{\delta}, \quad \tilde{\sigma} = \frac{\sigma}{\delta K}, \quad \tilde{D}_v = \frac{D_v}{D_u}. \tag{A2.14}$$

Dropping the tildes, we obtain the dimensionless WPT model:

$$\begin{aligned} \frac{\partial u}{\partial t} &= bv + \gamma \frac{u^n}{1+u^n} v - u - \xi u + \nabla^2 u \\ \frac{\partial v}{\partial t} &= -bv - \gamma \frac{u^n}{1+u^n} v + u + \sigma + D_v \nabla^2 v. \end{aligned} \tag{A2.15}$$

Non-dimensionalisation of the MIT model

The full dimension-carrying system is given by:

$$\begin{aligned} \frac{\partial u_1}{\partial t} &= b_1 v_1 + \gamma_1 \frac{K_2^n}{K_2^n + u_2^n} v_1 - \delta u_1 - \xi_1 u_1 + D_u \nabla^2 u_1 \\ \frac{\partial v_1}{\partial t} &= -b_1 v_1 - \gamma_1 \frac{K_2^n}{K_2^n + u_2^n} v_1 + \delta u_1 + \sigma_1 + D_v \nabla^2 v_1 \\ \frac{\partial u_2}{\partial t} &= b_2 v_2 + \gamma_2 \frac{K_1^n}{K_1^n + u_1^n} v_2 - \delta u_2 - \xi_2 u_2 + D_u \nabla^2 u_2 \\ \frac{\partial v_2}{\partial t} &= -b_2 v_2 - \gamma_2 \frac{K_1^n}{K_1^n + u_1^n} v_2 + \delta u_2 + \sigma_2 + D_v \nabla^2 v_2, \end{aligned} \tag{A2.16}$$

with variables and parameters as in the previous models. The dimensionless variables are:

$$\tilde{u}_1 = \frac{u_1}{K_1}, \quad \tilde{u}_2 = \frac{u_2}{K_2}, \quad \tilde{v}_1 = \frac{v_1}{K_1}, \quad \tilde{v}_2 = \frac{v_2}{K_2}, \quad \tilde{t} = \delta t, \quad \tilde{x} = \frac{x\sqrt{\delta}}{\sqrt{D_u}}, \quad \tilde{y} = \frac{y\sqrt{\delta}}{\sqrt{D_u}}, \tag{A2.17}$$

and the scaled parameters:

$$\begin{aligned} &\tilde{b}_1 = \frac{b_1}{\delta}, \quad \tilde{b}_2 = \frac{b_2}{\delta}, \quad \tilde{\gamma}_1 = \frac{\gamma_1}{\delta}, \quad \tilde{\gamma}_2 = \frac{\gamma_2}{\delta}, \quad \tilde{\xi}_1 = \frac{\xi_1}{\delta}, \quad \tilde{\xi}_2 = \frac{\xi_2}{\delta}, \\ &\tilde{\sigma}_1 = \frac{\sigma_1}{\delta K_1}, \quad \tilde{\sigma}_2 = \frac{\sigma_2}{\delta K_2}, \quad \tilde{D}_v = \frac{D_v}{D_u}. \end{aligned} \tag{A2.18}$$

Dropping the tildes, we obtain the dimensionless MIT model:

$$\begin{aligned}
\frac{\partial u_1}{\partial t} &= b_1 v_1 + \gamma_1 \frac{1}{1+u_2^n} v_1 - u_1 - \xi_1 u_1 + \nabla^2 u_1 \\
\frac{\partial v_1}{\partial t} &= -b_1 v_1 - \gamma_1 \frac{1}{1+u_2^n} v_1 + u_1 + \sigma_1 + D_v \nabla^2 v_1 \\
\frac{\partial u_2}{\partial t} &= b_2 v_2 + \gamma_2 \frac{1}{1+u_1^n} v_2 - u_2 - \xi_2 u_2 + \nabla^2 u_2 \\
\frac{\partial v_2}{\partial t} &= -b_2 v_2 - \gamma_2 \frac{1}{1+u_1^n} v_2 + u_2 + \sigma_2 + D_v \nabla^2 v_2.
\end{aligned} \tag{A2.19}$$

Non-dimensionalisation of the WPGAP model

The full dimension-carrying WPGAP model is given by:

$$\begin{aligned}
\frac{\partial u}{\partial t} &= bv + \gamma \frac{u^n}{K^n + u^n} v - \delta u - eGu + D_u \nabla^2 u \\
\frac{\partial v}{\partial t} &= -bv - \gamma \frac{u^n}{K^n + u^n} v + \delta u + eGu + D_v \nabla^2 v \\
\frac{\partial G}{\partial t} &= cug - dG + D_G \nabla^2 G \\
\frac{\partial g}{\partial t} &= -cug + dG + D_g \nabla^2 g,
\end{aligned} \tag{A2.20}$$

where G and g are the concentrations of active and inactive GAP respectively, D_G and D_g are the diffusion coefficients of active and inactive GAP respectively, c is a GTPase dependent GAP activation rate constant, d is the GAP inactivation rate constant, and e is a GAP dependent GTPase inactivation constant. This model has conservation parameter T as in Eq. A2.2 and an average total GAP concentration:

$$T_g = \frac{1}{A} \iint_A (G+g) dxdy = \frac{\text{Total GAP}}{A}. \tag{A2.21}$$

The dimensionless variables are:

$$\tilde{u} = \frac{u}{K}, \quad \tilde{v} = \frac{v}{K}, \quad \tilde{G} = \frac{e}{\delta} G, \quad \tilde{g} = \frac{e}{\delta} g, \quad \tilde{t} = \delta t, \quad \tilde{x} = \frac{x\sqrt{\delta}}{\sqrt{D_u}}, \quad \tilde{y} = \frac{y\sqrt{\delta}}{\sqrt{D_u}}, \tag{A2.22}$$

and the scaled parameters:

$$\begin{aligned}
&\tilde{T} = \frac{T}{K}, \quad \tilde{T}_g = \frac{eT_g}{\delta}, \quad \tilde{b} = \frac{b}{\delta}, \quad \tilde{\gamma} = \frac{\gamma}{\delta}, \quad \tilde{c} = \frac{cK}{\delta}, \quad \tilde{d} = \frac{d}{\delta}, \\
&\tilde{D}_v = \frac{D_v}{D_u}, \quad \tilde{D}_G = \frac{D_G}{D_u}, \quad \tilde{D}_g = \frac{D_g}{D_u}, \quad \tilde{A} = A\frac{\delta}{D_u}.
\end{aligned} \tag{A2.23}$$

This makes the dimensionless total amount of GTPase:

$$\tilde{\text{Total GAP}} = \frac{\text{Total GAP} \cdot e}{D_u}. \tag{A2.24}$$

Dropping the tildes, we obtain the dimensionless WPGAP model:

$$\begin{aligned}
\frac{\partial u}{\partial t} &= bv + \gamma \frac{u^n}{1+u^n} v - u - Gu + D_u \nabla^2 u \\
\frac{\partial v}{\partial t} &= -bv - \gamma \frac{u^n}{1+u^n} v + u + Gu + D_v \nabla^2 v \\
\frac{\partial G}{\partial t} &= cug - dG + D_G \nabla^2 G \\
\frac{\partial g}{\partial t} &= -cug + dG + D_g \nabla^2 g,
\end{aligned} \tag{A2.25}$$

with a dimensionless total average GAP concentration:

$$T_g = \frac{1}{A} \iint_A (G+g) dxdy = \frac{\text{Total GAP}}{A}. \tag{A2.26}$$

Non-dimensionalisation of the MIGAP1 model

The full dimension-carrying system is given by:

$$\begin{aligned}
\frac{\partial u_1}{\partial t} &= b_1 v_1 + \gamma_1 \frac{K_2^n}{K_2^n + u_2^n} v_1 - \delta u_1 - e_1 G_1 u_1 + D_u \nabla^2 u_1 \\
\frac{\partial v_1}{\partial t} &= -b_1 v_1 - \gamma_1 \frac{K_2^n}{K_2^n + u_2^n} v_1 + \delta u_1 + e_1 G_1 u_1 + D_v \nabla^2 v_1 \\
\frac{\partial u_2}{\partial t} &= b_2 v_2 + \gamma_2 \frac{K_1^n}{K_1^n + u_1^n} v_2 - \delta u_2 + D_u \nabla^2 u_2 \\
\frac{\partial v_2}{\partial t} &= -b_2 v_2 - \gamma_2 \frac{K_1^n}{K_1^n + u_1^n} v_2 + \delta u_2 + D_v \nabla^2 v_2 \\
\frac{\partial G_1}{\partial t} &= c_1 u_1 g_1 - d_1 G_1 + D_G \nabla^2 G_1 \\
\frac{\partial g_1}{\partial t} &= -c_1 u_1 g_1 + d_1 G_1 + D_g \nabla^2 g_1,
\end{aligned} \tag{A2.27}$$

with variables and parameters as in previous models. This system has two average total GTPase concentrations as in Eq. A2.2 and one average total GAP concentration as in Eq. A2.21. The dimensionless variables are:

$$\begin{aligned}
&\tilde{u}_1 = \frac{u_1}{K_1}, \quad \tilde{u}_2 = \frac{u_2}{K_2}, \quad \tilde{v}_1 = \frac{v_1}{K_1}, \quad \tilde{v}_2 = \frac{v_2}{K_2}, \quad \tilde{G}_1 = \frac{e_1}{\delta} G_1, \quad \tilde{g}_1 = \frac{e_1}{\delta} g_1, \\
&\tilde{t} = \delta t, \quad \tilde{x} = \frac{x\sqrt{\delta}}{\sqrt{D_u}}, \quad \tilde{y} = \frac{y\sqrt{\delta}}{\sqrt{D_u}},
\end{aligned} \tag{A2.28}$$

and the scaled parameters:

$$\begin{aligned}
&\tilde{T}_1 = \frac{T_1}{K_1}, \quad \tilde{T}_2 = \frac{T_2}{K_2}, \quad \tilde{T}_{g,1} = \frac{e_1 T_{g,1}}{\delta}, \quad \tilde{b}_1 = \frac{b_1}{\delta}, \quad \tilde{b}_2 = \frac{b_2}{\delta}, \quad \tilde{\gamma}_1 = \frac{\gamma_1}{\delta}, \quad \tilde{\gamma}_2 = \frac{\gamma_2}{\delta}, \\
&\tilde{c}_1 = \frac{c_1 K_1}{\delta}, \quad \tilde{d}_1 = \frac{d_1}{\delta}, \quad \tilde{D}_v = \frac{D_v}{D_u}, \quad \tilde{D}_G = \frac{D_G}{D_u}, \quad \tilde{D}_g = \frac{D_g}{D_u}, \quad \tilde{A} = A\frac{\delta}{D_u}.
\end{aligned} \tag{A2.29}$$

Dropping the tildes, we obtain the dimensionless MIGAP1 model:

$$\begin{aligned}
\frac{\partial u_1}{\partial t} &= b_1 v_1 + \gamma_1 \frac{1}{1+u_2^n} v_1 - u_1 - G_1 u_1 + \nabla^2 u_1 \\
\frac{\partial v_1}{\partial t} &= -b_1 v_1 - \gamma_1 \frac{1}{1+u_2^n} v_1 + u_1 + G_1 u_1 + D_v \nabla^2 v_1 \\
\frac{\partial u_2}{\partial t} &= b_2 v_2 + \gamma_2 \frac{1}{1+u_1^n} v_2 - u_2 + \nabla^2 u_2 \\
\frac{\partial v_2}{\partial t} &= -b_2 v_2 - \gamma_2 \frac{1}{1+u_1^n} v_2 + u_2 + D_v \nabla^2 v_2 \\
\frac{\partial G_1}{\partial t} &= c_1 u_1 g_1 - d_1 G_1 + D_G \nabla^2 G_1 \\
\frac{\partial g_1}{\partial t} &= -c_1 u_1 g_1 + d_1 G_1 + D_g \nabla^2 g_1.
\end{aligned} \tag{A2.30}$$

Non-dimensionalisation of the MIGAP2 model

The full dimension-carrying MIGAP2 system is given by:

$$\begin{aligned}
\frac{\partial u_1}{\partial t} &= b_1 v_1 + \gamma_1 \frac{K_2^n}{K_2^n + u_2^n} v_1 - \delta u_1 - e_1 G_1 u_1 + D_u \nabla^2 u_1 \\
\frac{\partial v_1}{\partial t} &= -b_1 v_1 - \gamma_1 \frac{K_2^n}{K_2^n + u_2^n} v_1 + \delta u_1 + e_1 G_1 u_1 + D_v \nabla^2 v_1 \\
\frac{\partial u_2}{\partial t} &= b_2 v_2 + \gamma_2 \frac{K_1^n}{K_1^n + u_1^n} v_2 - \delta u_2 - e_2 G_2 u_2 + D_u \nabla^2 u_2 \\
\frac{\partial v_2}{\partial t} &= -b_2 v_2 - \gamma_2 \frac{K_1^n}{K_1^n + u_1^n} v_2 + \delta u_2 + e_2 G_2 u_2 + D_v \nabla^2 v_2 \\
\frac{\partial G_1}{\partial t} &= c_1 u_1 g_1 - d_1 G_1 + D_G \nabla^2 G_1 \\
\frac{\partial g_1}{\partial t} &= -c_1 u_1 g_1 + d_1 G_1 + D_g \nabla^2 g_1 \\
\frac{\partial G_2}{\partial t} &= c_2 u_2 g_2 - d_2 G_2 + D_G \nabla^2 G_2 \\
\frac{\partial g_2}{\partial t} &= -c_2 u_2 g_2 + d_2 G_2 + D_g \nabla^2 g_2,
\end{aligned} \tag{A2.31}$$

with variables and parameters as in previous models. This model has two average total GTPase concentrations as in Eq. A2.2 and two average total GAP concentrations as in Eq. A2.21. The dimensionless variables are:

$$\begin{aligned}
&\tilde{u}_1 = \frac{u_1}{K_1}, \quad \tilde{u}_2 = \frac{u_2}{K_2}, \quad \tilde{v}_1 = \frac{v_1}{K_1}, \quad \tilde{v}_2 = \frac{v_2}{K_2}, \quad \tilde{G}_1 = \frac{e_1}{\delta} G_1, \quad \tilde{g}_1 = \frac{e_1}{\delta} g_1, \\
&\tilde{G}_2 = \frac{e_2}{\delta} G_2, \quad \tilde{g}_2 = \frac{e_2}{\delta} g_2, \quad \tilde{t} = \delta t, \quad \tilde{x} = \frac{x\sqrt{\delta}}{\sqrt{D_u}}, \quad \tilde{y} = \frac{y\sqrt{\delta}}{\sqrt{D_u}},
\end{aligned} \tag{A2.32}$$

and the scaled parameters:

$$\begin{aligned}
&\tilde{T}_1 = \frac{T_1}{K_1}, \quad \tilde{T}_2 = \frac{T_2}{K_2}, \quad \tilde{T}_{g,1} = \frac{e_1 T_{g,1}}{\delta}, \quad \tilde{T}_{g,2} = \frac{e_2 T_{g,2}}{\delta}, \quad \tilde{b}_1 = \frac{b_1}{\delta}, \quad \tilde{b}_2 = \frac{b_2}{\delta}, \\
&\tilde{\gamma}_1 = \frac{\gamma_1}{\delta}, \quad \tilde{\gamma}_2 = \frac{\gamma_2}{\delta}, \quad \tilde{c}_1 = \frac{c_1 K_1}{\delta}, \quad \tilde{d}_1 = \frac{d_1}{\delta}, \quad \tilde{c}_2 = \frac{c_2 K_2}{\delta}, \quad \tilde{d}_2 = \frac{d_2}{\delta}, \\
&\tilde{D}_v = \frac{D_v}{D_u}, \quad \tilde{D}_G = \frac{D_G}{D_u}, \quad \tilde{D}_g = \frac{D_g}{D_u}, \quad \tilde{A} = A\frac{\delta}{D_u}.
\end{aligned} \tag{A2.33}$$

Dropping the tildes, we obtain the dimensionless MIGAP2 model:

$$\begin{aligned}
\frac{\partial u_1}{\partial t} &= b_1 v_1 + \gamma_1 \frac{1}{1+u_2^n} v_1 - u_1 - G_1 u_1 + \nabla^2 u_1 \\
\frac{\partial v_1}{\partial t} &= -b_1 v_1 - \gamma_1 \frac{1}{1+u_2^n} v_1 + u_1 + G_1 u_1 + D_v \nabla^2 v_1 \\
\frac{\partial u_2}{\partial t} &= b_2 v_2 + \gamma_2 \frac{1}{1+u_1^n} v_2 - u_2 - G_2 u_2 + \nabla^2 u_2 \\
\frac{\partial v_2}{\partial t} &= -b_2 v_2 - \gamma_2 \frac{1}{1+u_1^n} v_2 + u_2 + G_2 u_2 + D_v \nabla^2 v_2 \\
\frac{\partial G_1}{\partial t} &= c_1 u_1 g_1 - d_1 G_1 + D_G \nabla^2 G_1 \\
\frac{\partial g_1}{\partial t} &= -c_1 u_1 g_1 + d_1 G_1 + D_g \nabla^2 g_1 \\
\frac{\partial G_2}{\partial t} &= c_2 u_2 g_2 - d_2 G_2 + D_G \nabla^2 G_2 \\
\frac{\partial g_2}{\partial t} &= -c_2 u_2 g_2 + d_2 G_2 + D_g \nabla^2 g_2.
\end{aligned} \tag{A2.34}$$

2.8.2 Homogeneous steady states

The WP model has the following homogeneous steady state (HSS):

$$\begin{aligned}
u_{HSS} &= u_0 \\
v_{HSS} &= \frac{u_0(1+u_0^n)}{(b+\gamma)u_0^n + b},
\end{aligned} \tag{A2.35}$$

where u_0 is the concentration of u at the homogeneous steady state for a specific average GTPase concentration $T = u_{HSS} + v_{HSS}$.

The MI model has the following homogeneous steady state:

$$\begin{aligned}
u_{1,HSS} &= u_{1,0} \\
v_{1,HSS} &= u_{1,0}\frac{1+\left(T_2\dfrac{b_2u_{1,0}^n+b_2+\gamma_2}{1+b_2u_{1,0}^n+u_{1,0}^n+b_2+\gamma_2}\right)^n}{b_1+\gamma_1+b_1\left(T_2\dfrac{b_2u_{1,0}^n+b_2+\gamma_2}{1+b_2u_{1,0}^n+u_{1,0}^n+b_2+\gamma_2}\right)^n} \\
u_{2,HSS} &= T_2\frac{b_2u_{1,0}^n+b_2+\gamma_2}{b_2u_{1,0}^n+u_{1,0}^n+b_2+\gamma_2+1} \\
v_{2,HSS} &= T_2-u_{2,HSS},
\end{aligned} \tag{A2.36}$$

where $u_{1,0}$ is the concentration of u at the homogeneous steady state for a specific average GTPase 1 concentration $T_1 = u_{1,HSS}+v_{1,HSS}$. For the second GTPase, the average concentration $T_2 = u_{2,HSS}+v_{2,HSS}$ was used as an extra parameter.

For the WPT model, the homogeneous steady state is:

$$\begin{aligned}
u_{HSS} &= \frac{\sigma}{\xi} \\
v_{HSS} &= \frac{\sigma\left(\left(\dfrac{\sigma}{\xi}\right)^n+1\right)(\xi+1)}{\xi\left((b+\gamma)\left(\dfrac{\sigma}{\xi}\right)^n+b\right)}.
\end{aligned} \tag{A2.37}$$

The MIT model has the following homogeneous steady state:

$$\begin{aligned}
u_{1,HSS} &= \frac{\sigma_1}{\xi_1} \\
v_{1,HSS} &= \frac{\sigma_1\left(\left(\dfrac{\sigma_2}{\xi_2}\right)^n+1\right)(\xi_1+1)}{\xi_1\left(b_1\left(\dfrac{\sigma_2}{\xi_2}\right)^n+b_1+\gamma_1\right)} \\
u_{2,HSS} &= \frac{\sigma_2}{\xi_2} \\
v_{2,HSS} &= \frac{\sigma_2\left(\left(\dfrac{\sigma_1}{\xi_1}\right)^n+1\right)(\xi_2+1)}{\xi_2\left(b_2\left(\dfrac{\sigma_1}{\xi_1}\right)^n+b_2+\gamma_2\right)}.
\end{aligned} \tag{A2.38}$$

The homogeneous steady state of the WPGAP model is:

$$\begin{aligned} u_{HSS} &= u_0 \\ v_{HSS} &= u_0 \frac{c(T_g+1)u_0^{n+1} + d \cdot u_0^n + c \cdot u_0(T_g+1) + d}{\left((b+\gamma)u_0^n + b\right)(c \cdot u_0 + d)} \\ G_{HSS} &= \frac{c \cdot u_0 \cdot T_g}{c \cdot u_0 + d} \\ g_{HSS} &= T_g - G_{HSS}, \end{aligned} \tag{A2.39}$$

where $T_g = G_{HSS} + g_{HSS}$ is the average concentration of GAP.

The homogeneous steady state of the MIGAP1 model is:

$$\begin{aligned} u_{1,HSS} &= u_{1,0} \\ v_{1,HSS} &= u_{1,0} \frac{\left(1 + \left(T_2 \frac{b_2 u_{1,0}^n + b_2 + \gamma_2}{1 + b_2 u_{1,0}^n + u_{1,0}^n + b_2 + \gamma_2}\right)^n\right)(c(T_g+1)u_{1,0} + d)}{\left(b_1 + \gamma_1 + b_1 \left(T_2 \frac{b_2 u_{1,0}^n + b2 + \gamma_2}{1 + b_2 u_{1,0}^n + u_{1,0}^n + b_2 + \gamma_2}\right)^n\right)(c \cdot u_{1,0} + d)} \\ u_{2,HSS} &= T_2 \frac{b_2 u_{1,0}^n + b_2 + \gamma_2}{b_2 u_{1,0}^n + u_{1,0}^n + b_2 + \gamma_2 + 1} \\ v_{2,HSS} &= T_2 - u_{2,HSS} \\ G_{1,HSS} &= \frac{c \cdot u_{1,0} \cdot T_g}{c \cdot u_{1,0} + d} \\ g_{1,HSS} &= T_g - G_{1,HSS}, \end{aligned} \tag{A2.40}$$

The MIGAP2 model has the following homogeneous steady state:

$$\begin{aligned} u_{1,HSS} &= u_{1,0} \\ v_{1,HSS} &= u_{1,0} \frac{(1 + u_{2,HSS}^n)(c_1(T_{g,1}+1)u_{1,0} + d_1)}{(b_1 u_{2,HSS}^n + b_1 + \gamma_1)(c_1 u_{1,0} + d_1)} \\ u_{2,HSS} &= \frac{-B \pm \sqrt{B^2 - 4AC}}{2A} \\ A &= (c_2 T_{g,2} + b_2 c_2 + c_2)u_{1,0}^n + c_2 T_{g,2} + b_2 c_2 + c_2 \gamma_2 + c_2 \\ B &= (b_2 d_2 + d_2 - c_2 b_2 T_2)u_{1,0}^n + b_2 d_2 + d_2 \gamma_2 + d_2 - c_2 b_2 T_2 - c_2 \gamma_2 T_2 \\ C &= -d_2 T_2 (u_{1,0}^n b_2 + b_2 + \gamma_2) \\ v_{2,HSS} &= T_2 - u_{2,HSS} \\ G_{1,HSS} &= \frac{c_1 \cdot u_{1,0} \cdot T_{g,1}}{c_1 \cdot u_{1,0} + d_1} \\ g_{1,HSS} &= T_{g,1} - G_{1,HSS} \\ G_{2,HSS} &= \frac{c_2 \cdot u_{2,0} \cdot T_{g,2}}{c_2 \cdot u_{2,0} + d_2} \\ g_{2,HSS} &= T_{g,2} - G_{2,HSS}. \end{aligned} \tag{A2.41}$$

There are two possibilities for $u_{2,HSS}$, resulting as solutions from a quadratic equation. However, since the term $-4AC$ is always positive, there is always exactly one positive option, which we used for the simulation.

2.8.3 Linear stability analysis for two-component reaction-diffusion systems in two dimensions

Linearisation and growth modes

Linear stability analysis (LSA) can be used to determine under what conditions arbitrarily small spatial perturbations in a homogeneous state can grow, leading to a heterogeneous state. LSA was performed as previously described [199] for reaction-diffusion systems of the following (dimensionless) structure:

$$\begin{aligned} \frac{\partial u}{\partial t} &= \nabla^2 u + f(u,v) \\ \frac{\partial v}{\partial t} &= D_v \nabla^2 v + g(u,v), \end{aligned} \tag{A2.42}$$

where u is the concentration of the slow-diffusing activator, v is the concentration of the fast-diffusing substrate, D_v the diffusion coefficient of v relative to that of u, ∇^2 the two-dimensional Laplace operator, and f and g are (non-linear) functions describing the interaction between u and v. Linearisation of this system about the homogeneous steady state gives (in matrix-vector form):

$$\begin{aligned} \frac{\partial w}{\partial t} &= D\nabla^2 w + Jw \\ w = \begin{bmatrix} \Delta u \\ \Delta v \end{bmatrix} \quad D = \begin{bmatrix} 1 & 0 \\ 0 & D_v \end{bmatrix} \quad J &= \begin{bmatrix} f_u & f_v \\ g_u & g_v \end{bmatrix} \\ \Delta u = u - u_{HSS} \quad \Delta v &= v - v_{HSS}, \end{aligned} \tag{A2.43}$$

where u_{HSS} and v_{HSS} are the concentrations of u and v at the homogeneous steady state respectively, and J is the Jacobian matrix with partial derivatives of f and g with respect to u and v evaluated at the homogeneous steady state. This linear system has solutions of the form:

$$w(x,y,t) = \sum_k c_k e^{\lambda_k t} W_k(x,y). \tag{A2.44}$$

Here, c_k is a constant (determined by initial conditions) belonging to wave number k, λ_k is a the growth mode belonging to wave number k and $W_k(x,y)$ is the time-independent solution of the following eigenvalue problem:

$$\nabla^2 W(x,y) = -k^2 W(x,y). \tag{A2.45}$$

On finite domains only discrete wave numbers are admissible. Which wave numbers are allowed is determined by the size of the domain and the boundary conditions.

The growth modes λ_k as a function of the wave number can be determined by substituting Eq. A2.44 and Eq. A2.45 into Eq. A2.43:

$$\begin{aligned} \lambda w &= -k^2 Dw + Jw \\ (J - k^2 D)w &= \lambda w. \end{aligned} \tag{A2.46}$$

These growth modes are then given by the roots of the following equation:

$$\det\left(J - k^2 D - \lambda_k I\right) = 0. \tag{A2.47}$$

This leads to the following solutions for λ_k:

$$\begin{aligned}\lambda_k = &-\frac{1}{2}k^2(1+D_v) + \frac{1}{2}(f_u+g_v) \pm \\ &\frac{1}{2}\sqrt{(1-D_v)^2k^4 - 2(f_u-g_v)(1-D_v)k^2 + f_u^2 - 2f_ug_v + 4f_vg_u + g_v^2}.\end{aligned} \tag{A2.48}$$

If the real part of any λ_k belonging to an admissible wave number is greater than zero, the homogeneous steady state is unstable, small perturbations will drive spontaneous pattern formation.

Wave numbers

Admissible wave numbers can be determined by solving Eq. A2.45. To this end we split $W_k(x,y)$ into an x-dependent and a y-dependent part:

$$W_k(x,y) = \bar{v}X(x)Y(y), \tag{A2.49}$$

where $X(x)$ is a scalar function of x, $Y(y)$ is a scalar function of y, and $\bar{v}$ is a constant vector containing the coefficients for components u and v. Substituting this into Eq. A2.45 results in:

$$\bar{v}X''(x)Y(y) + \bar{v}X(x)Y''(y) = -k^2\bar{v}X(x)Y(y). \tag{A2.50}$$

Division by $X(x)Y(y)$ gives:

$$\left(\frac{X''(x)}{X(x)} + \frac{Y''(y)}{Y(y)}\right)\bar{v} = -k^2\bar{v}. \tag{A2.51}$$

This equation can be separated into an x-dependent and a y-dependent part that both need to be constant:

$$\begin{aligned}\frac{X''(x)}{X(x)} &= a \\ \frac{Y''(y)}{Y(y)} &= b \\ a+b &= -k^2,\end{aligned} \tag{A2.52}$$

where a and b are constants to be solved from their respective one-dimensional boundary value problems. The results depend on the boundary conditions and the domain size. We will consider a rectangular domain with periodic boundary conditions in the x-direction and homogeneous Neumann boundary conditions in the y-direction. This results in a geometry resembling an open cylinder.

Periodic boundary conditions

The periodic boundary conditions in the x-direction result in the following boundary value problem:

$$\begin{aligned} X''(x) &= aX(x) \\ X(0) &= X(L) \\ X'(0) &= X'(L), \end{aligned} \tag{A2.53}$$

where L is the length of the domain in the x-direction (or the circumference of the open cylinder). This problem only has trivial solutions for $a > 0$. For $a = 0$, there is a single solution where $X(x)$ is constant. For $a < 0$, with $a = -\mu^2$, solutions follow:

$$\begin{aligned} X(x) &= A\cos(\mu x) + B\sin(\mu x) \\ X'(x) &= -A\mu\sin(\mu x) + B\mu\cos(\mu x), \end{aligned} \tag{A2.54}$$

where A and B are constants. Substituting these equations into the boundary conditions results in:

$$\begin{aligned} A\sin(\mu L) + B(1-\cos(\mu L)) &= 0 \\ A(1-\cos(\mu L)) - B\sin(\mu L) &= 0, \end{aligned} \tag{A2.55}$$

which can be rewritten in matrix-vector form:

$$\begin{bmatrix} \sin(\mu L) & 1-\cos(\mu L) \\ 1-\cos(\mu L) & -\sin(\mu L) \end{bmatrix} \begin{bmatrix} A \\ B \end{bmatrix} = \begin{bmatrix} 0 \\ 0 \end{bmatrix}. \tag{A2.56}$$

For non-trivial solutions, the determinant of the matrix should be zero, so:

$$\begin{aligned} &-\sin^2(\mu L) - (1-\cos(\mu L))^2 = 0 \\ &\sin^2(\mu L) + 1 - 2\cos(\mu L) + \cos^2(\mu L) = 0 \\ &2 - 2\cos(\mu L) = 0 \\ &\cos(\mu L) = 1 \\ &\mu_n = \frac{2n\pi}{L}, \quad n \in \mathbb{N}. \end{aligned} \tag{A2.57}$$

Therefore, admissible values of a with periodic boundary conditions in the x-direction are:

$$a_n = -\mu_n^2 = -\frac{4n^2\pi^2}{L^2}, \quad n \in \mathbb{N}. \tag{A2.58}$$

Zero flux boundary conditions

The zero flux boundary conditions in the y-direction determine the following boundary value problem:

$$\begin{aligned} Y''(y) &= bY(y) \\ Y'(0) &= 0 \\ Y'(H) &= 0, \end{aligned} \tag{A2.59}$$

where H is the length of the domain in the y-direction (the height of the open cylinder). For $b > 0$ only trivial solutions exist. For $b = 0$, there is again a single solution where $Y(y)$ is constant. For $b < 0$, with $b = -\nu^2$, solutions follow:

$$\begin{aligned} Y(y) &= A\cos(\nu y) + B\sin(\nu y) \\ Y'(y) &= -A\nu\sin(\nu y) + B\nu\cos(\nu y), \end{aligned} \tag{A2.60}$$

where A and B are constants. Substitution into the boundary conditions yields:

$$\begin{aligned} Y'(0) = \quad & \nu B = 0 \\ & B = 0 \\ Y'(H) = \quad & -\nu A\sin(\nu H) = 0 \\ & \sin(\nu H) = 0 \\ & \nu_m = \frac{m\pi}{H}, \quad m \in \mathbb{N}. \end{aligned} \tag{A2.61}$$

Therefore, with zero flux boundary conditions in the y-direction, the following values of b are admissible:

$$b_m = -\nu_m^2 = -\frac{m^2\pi^2}{H^2}, \quad m \in \mathbb{N}. \tag{A2.62}$$

Admissible wave numbers

Combining a and b, the admissible wave numbers for periodic boundary conditions in the x-direction and zero flux boundary conditions in the y-direction are given by:

$$k_{n,m}^2 = -(a_n + b_m) = \pi^2\left(\frac{4n^2}{L^2} + \frac{m^2}{H^2}\right). \tag{A2.63}$$

One parameter bifurcation analysis

Provided at least one admissible wave number exists, the homogeneous steady state becomes unstable when $\max(\mathrm{Re}(\lambda_k)) > 0$, with λ_k as given by Eq. A2.48. To determine how $\max(\mathrm{Re}(\lambda_k))$ depends on the parameters, the values of k^2 for which $\mathrm{Re}(\lambda_k)$ is maximal can be determined as previously described [203]. There are two branches of λ_k:

$$\begin{aligned} \lambda_{k+} &= E + \frac{1}{2}\sqrt{F} \\ \lambda_{k-} &= E - \frac{1}{2}\sqrt{F} \\ E &= -\frac{1}{2}k^2(1+D_v) + \frac{1}{2}(f_u + g_v) \\ F &= (1-D_v)^2k^4 - 2(f_u - g_v)(1-D_v)k^2 + f_u^2 - 2f_u g_v + 4f_v g_u + g_v^2. \end{aligned} \tag{A2.64}$$

Since $\mathrm{Re}(\lambda_{k+}) \geq \mathrm{Re}(\lambda_{k-})$, only λ_{k+} needs to be considered. To find the maximum we take the derivative of this branch of $\lambda_k$to k^2 and set it equal to zero:

$$\begin{aligned}\frac{d\lambda_{k+}}{dk^2} = &-\frac{1}{2}(1+D_v)+ \\ &\frac{1}{2}\frac{(1-D_v)^2k^2-(f_u-g_v)(1-D_v)}{\sqrt{(1-D_v)^2k^4-2(f_u-g_v)(1-D_v)k^2+f_u^2-2f_ug_v+4f_vg_u+g_v^2}} \\ &=0.\end{aligned} \tag{A2.65}$$

Solving this equation results in the following relation for k^2:

$$k^2 = \frac{-(f_u-g_v)D_v \pm (1+D_v)\sqrt{-D_vf_vg_u}}{D_v(D_v-1)}. \tag{A2.66}$$

Since $D_v > 1$ and $f_u - g_v > 0$ for substrate depletion models, and only positive values of k^2 are relevant (wave numbers should be real), this relation can be reduced to:

$$k^2 = \frac{-(f_u-g_v)D_v + (1+D_v)\sqrt{-D_vf_vg_u}}{D_v(D_v-1)}. \tag{A2.67}$$

Using Eq. A2.67 and Eq. A2.48, the maximum value of λ_k can be determined as a function of model parameters if the Jacobian matrix of the system at the homogeneous steady state is known. Homogeneous steady states are given in section 2.8.2. For the WP model the Jacobian matrix at the homogeneous steady state is given by:

$$J = \begin{bmatrix} \dfrac{((n-2)\gamma-3b)u_0^{2n}+(-b-\gamma)u_0^{3n}+((n-1)\gamma-3b)u_0^n-b}{((b+\gamma)u_0^n+b)(1+u_0^n)^2} & b+\dfrac{\gamma u_0^n}{1+u_0^n} \\ \dfrac{((-n+2)\gamma+3b)u_0^{2n}+(b+\gamma)u_0^{3n}+((-n+1)\gamma+3b)u_0^n+b}{((b+\gamma)u_0^n+b)(1+u_0^n)^2} & -b-\dfrac{\gamma u_0^n}{1+u_0^n} \end{bmatrix}. \tag{A2.68}$$

The WPT model has the following Jacobian matrix at this steady state:

$$J = \begin{bmatrix} \dfrac{-\left(((2-n)\gamma+3b)\left(\frac{\sigma}{\xi}\right)^{2n}+(b+\gamma)\left(\frac{\sigma}{\xi}\right)^{3n}+((1-n)\gamma+3b)\left(\frac{\sigma}{\xi}\right)^n+b\right)(\xi+1)}{\left(\left(\frac{\sigma}{\xi}\right)^n+1\right)^2\left((b+\gamma)\left(\frac{\sigma}{\xi}\right)^n+b\right)} & b+\dfrac{\gamma\left(\frac{\sigma}{\xi}\right)^n}{\left(\frac{\sigma}{\xi}\right)^n+1} \\ \dfrac{((2-(\xi+1)n)\gamma+3b)\left(\frac{\sigma}{\xi}\right)^{2n}+(b+\gamma)\left(\frac{\sigma}{\xi}\right)^{3n}+((1-(\xi+1)n)\gamma+3b)\left(\frac{\sigma}{\xi}\right)^n+b}{\left(\left(\frac{\sigma}{\xi}\right)^n+1\right)^2\left((b+\gamma)\left(\frac{\sigma}{\xi}\right)^n+b\right)} & -b-\dfrac{\gamma\left(\frac{\sigma}{\xi}\right)^n}{\left(\frac{\sigma}{\xi}\right)^n+1} \end{bmatrix}. \tag{A2.69}$$

Hopf bifurcations

Hopf bifurcations occur when complex eigenvalues with real parts greater than zero appear. In this case the real part of the eigenvalues is given by:

$$\mathrm{Re}(\lambda_k) = -\frac{1}{2}k^2(1+D_v)+\frac{1}{2}(f_u+g_v). \tag{A2.70}$$

The value of this real part will keep increasing as k^2 decreases. Since negative values for k^2 don't make sense, the real part will be maximal for $k^2 = 0$ as long as the complex branch exists for this value. Therefore, the maximum real part of λ_k is given by:

$$\max(\mathrm{Re}(\lambda_k)) = \frac{1}{2}(f_u + g_v). \tag{A2.71}$$

This expression can be used to make one parameter Hopf bifurcation plots, with $\max(\mathrm{Re}(\lambda_k))$ plotted against a parameter.

Two parameter bifurcation analysis

Two parameter bifurcation analysis was performed by repeating a one parameter bifurcation many times for different values of the second parameter and numerically determining at which value(s) of the first parameter $\max(\mathrm{Re}(\lambda_k)) = 0$. To have sufficient sampling points for both parameters, this process was repeated with the two parameters inverted. This process is the same for both Turing and Hopf regimes.

2.8.4 Local perturbation analysis

LPA is a relatively new technique for investigating the stability of the homogeneous steady state with respect to an arbitrarily large local perturbation. We will briefly explain it here. A more detailed overview [204], a practical guide [201], and a rigorous mathematical analysis [200] are available elsewhere. LPA relies on an asymptotic approximation where all rapidly diffusing components are assumed to be infinitely fast ($D \to \infty$) and all slowly diffusing components are assumed to be immobile ($D \to 0$). This way, the evolution of a local pulse in a slowly diffusing activator so narrow that it does not affect global concentrations can be modelled separately from the global level of that activator and any fast components. This reduces the system of PDEs to a system of ODEs, with equations for the local concentration of slow components, the global concentration of slow components and the global concentration of fast components. This system of ODEs can then be analysed using existing bifurcation software to determine the stability of homogeneous (local concentration same as global) and heterogeneous (different local and global concentrations) steady states. Therefore, this method provides similar information to classical LSA (stability of homogeneous states), in addition to information on where a stable homogeneous state could be disrupted by a sufficiently large perturbation.

LPA of the WP model

The LPA system has ODEs for the local (u_L) and global concentration (u_G) of active GTPase and the global concentration of inactive GTPase (v_G). Since the local perturbation is assumed narrow enough that it does not affect background levels, the global average GTPase concentration $T = u_G + v_G$ is conserved. Using this conservation, we eliminated v_G, leaving the following system:

$$\begin{aligned} \frac{du_L}{dt} &= b(T - u_G) + \gamma \frac{u_L^n}{1 + u_L^n}(T - u_G) - u_L \\ \frac{du_G}{dt} &= b(T - u_G) + \gamma \frac{u_G^n}{1 + u_G^n}(T - u_G) - u_G. \end{aligned} \tag{A2.72}$$

Using continuation software from matlab package matcont, we performed a bifurcation analysis on this system with T as bifurcation parameter (Figure A2.1). The results revealed three parameter regimes (disregarding Hopf regimes): (1) a regime outside the outermost fold bifurcations of the heterogeneous branch where only a homogeneous state exists, (2) a regime where stable homogeneous and heterogeneous states coexist and a sufficiently large perturbation could switch the system from the homogeneous to the heterogeneous state, and (3) a regime within the two transcritical bifurcations where the homogeneous state is linearly unstable (a Turing regime). To generate the two-parameter bifurcation plots, we performed further continuations of the transcritical bifurcations (black crosses) and outermost fold bifurcations (black dots).

Figure A2.1 also shows a pair of Hopf bifurcations. Stability does not change in these points and they do not seem to have any effect on the outcome of the simulations of the full PDE system, so we did not consider them any further. For some of the other models (WPT and WPGAP), Hopf bifurcations were found that changed the stability of the heterogeneous curve from stable to unstable in the region with an unstable homogeneous state. These Hopf bifurcations correspond to those found with LSA and we performed continuations on them to determine the Hopf regimes in the two parameter bifurcation plots.

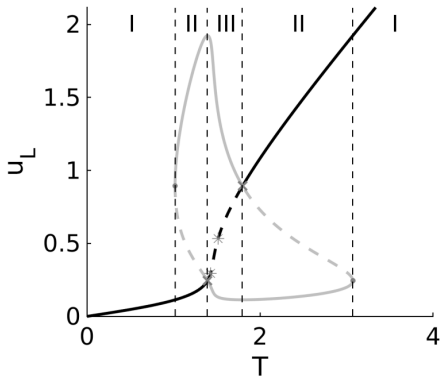

Fig. A2.1. Single parameter bifurcation analysis of the WP LPA system with T as bifurcation parameter and other parameters at default values. The black curve represents the homogeneous (global) steady state and the grey curve the heterogeneous (local) steady state. In regime I, only a homogeneous state exists. In regime II, both a stable homogeneous and heterogeneous steady state exist, so that a sufficiently large perturbation can change the system from a homogeneous to a heterogeneous state. In regime III (Turing regime), the homogeneous state is unstable, so that any small perturbation will result in pattern formation. Solid lines: stable states. Dashed lines: unstable states. Dots: fold bifurcations delimiting the borders of the regime with heterogeneous states. Crosses: transcritical bifurcations delimiting the unstable part of the homogeneous branch (Turing regime). Stars: Hopf bifurcations.

LPA of the MI model

The LPA method was performed on the MI model as previously described [168]. The full LPA ODE system has local and global concentrations for active GTPase 1 and 2 ($u_{1,L}$, $u_{1,G}$, $u_{2,L}$, and $u_{2,G}$) and global concentrations for inactive GTPase 1 and 2 ($v_{1,G}$, and $v_{2,G}$).

The global average concentration of GTPase 1 ($T_1 = u_{1,G} + v_{1,G}$) and 2 ($T_2 = u_{2,G} + v_{2,G}$) are conserved, allowing us to eliminate $v_{1,G}$, and $v_{2,G}$. This leads to the following system of ODEs:

$$\begin{aligned}
\frac{du_{1,L}}{dt} &= b_1(T_1 - u_{1,G}) + \gamma_1 \frac{1}{1+u_{2,L}^n}(T_1 - u_{1,G}) - u_{1,L} \\
\frac{du_{1,G}}{dt} &= b_1(T_1 - u_{1,G}) + \gamma_1 \frac{1}{1+u_{2,G}^n}(T_1 - u_{1,G}) - u_{1,G} \\
\frac{du_{2,L}}{dt} &= b_2(T_2 - u_{2,G}) + \gamma_2 \frac{1}{1+u_{1,L}^n}(T_2 - u_{2,G}) - u_{2,L} \\
\frac{du_{2,G}}{dt} &= b_2(T_2 - u_{2,G}) + \gamma_2 \frac{1}{1+u_{1,G}^n}(T_2 - u_{2,G}) - u_{2,G}.
\end{aligned} \tag{A2.73}$$

A one parameter bifurcation analysis with T_1 as bifurcation parameter and $T_2 = 5$, has a similar result as for the WP model with the same three regimes as for the WP model (Figure A2.2). We made two parameter bifurcation plots as before by continuation of the bifurcation points delimiting these regimes.

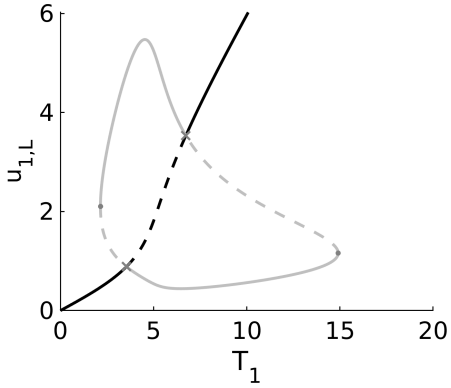

Fig. A2.2. Single parameter bifurcation analysis of the MI LPA system with T_1 as bifurcation parameter, $T_2 = 5$, and other parameters at default values. The black curve represents the homogeneous (global) steady state and the grey curve the heterogeneous (local) steady state. Solid lines: stable states. Dashed lines: unstable states. Dots: fold bifurcations delimiting the borders of the regime with heterogeneous states. Crosses: transcritical bifurcations delimiting the unstable part of the homogeneous branch (Turing regime).

LPA of the WPT model

The full LPA ODE system of the WPT model has equations for local and global concentrations of active GTPase ($u_{1,L}$ and $u_{1,G}$ respectively) and for the global concentration of

inactive GTPase ($v_{1,G}$):

$$\begin{aligned}
\frac{du_L}{dt} &= bv_G + \gamma \frac{u_L^n}{1+u_L^n} v_G - u_L - \xi u_L \\
\frac{du_G}{dt} &= bv_G + \gamma \frac{u_G^n}{1+u_G^n} v_G - u_G - \xi u_G \\
\frac{dv_G}{dt} &= -bv_G - \gamma \frac{u_G^n}{1+u_G^n} v_G + u_G + \sigma.
\end{aligned} \tag{A2.74}$$

Since this model is not mass conserved, none of these equations can be eliminated. A one parameter bifurcation analysis with σ as bifurcation parameter again reveals the same three regimes as for the WP model (Figure A2.3). We made two parameter bifurcation plots in the same way as before.

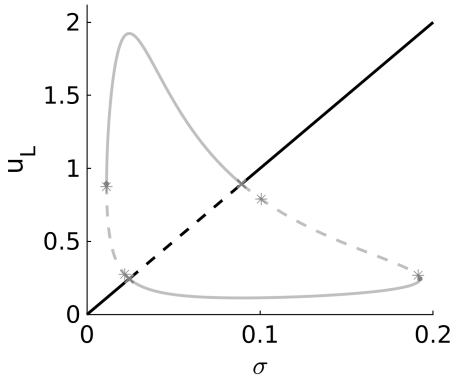

Fig. A2.3. Single parameter bifurcation analysis of the WPT LPA system with σ as bifurcation parameter and other parameters at default values. The black curve represents the homogeneous (global) steady state and the grey curve the heterogeneous (local) steady state. Solid lines: stable states. Dashed lines: unstable states. Dots: fold bifurcations delimiting the borders of the regime with heterogeneous states. Crosses: transcritical bifurcations delimiting the unstable part of the homogeneous branch (Turing regime). Stars: Hopf bifurcations.

LPA of the MIT model

The full LPA ODE system of the MIT has equations for local and global concentrations of active GTPase 1 and 2 ($u_{1,L}$, $u_{1,G}$, $u_{2,L}$, and $u_{2,G}$) and global concentrations of inactive

GTPase 1 and 2 ($v_{1,G}$, and $v_{2,G}$):

$$\begin{aligned}
\frac{du_{1,L}}{dt} &= b_1 v_{1,G} + \gamma_1 \frac{1}{1+u_{2,L}^n} v_{1,G} - u_{1,L} - \xi_1 u_{1,L} \\
\frac{du_{1,G}}{dt} &= b_1 v_{1,G} + \gamma_1 \frac{1}{1+u_{2,G}^n} v_{1,G} - u_{1,G} - \xi_1 u_{1,G} \\
\frac{dv_{1,G}}{dt} &= -b_1 v_{1,G} - \gamma_1 \frac{1}{1+u_{2,G}^n} v_{1,G} + u_{1,G} + \sigma_1 \\
\frac{du_{2,L}}{dt} &= b_2 v_{2,G} + \gamma_2 \frac{1}{1+u_{1,L}^n} v_{2,G} - u_{2,L} - \xi_2 u_{2,L} \\
\frac{du_{2,G}}{dt} &= b_2 v_{2,G} + \gamma_2 \frac{1}{1+u_{1,G}^n} v_{2,G} - u_{2,G} - \xi_2 u_{2,G} \\
\frac{dv_{2,G}}{dt} &= -b_2 v_{2,G} - \gamma_2 \frac{1}{1+u_{1,G}^n} v_{2,G} + u_{2,G} + \sigma_2.
\end{aligned} \tag{A2.75}$$

Since this model is not mass conserved, none of these equations can be eliminated. A one parameter bifurcation analysis with σ_1 as bifurcation parameter and $\sigma_2 = 0.2$ again reveals the same three regimes as for the WP model (Figure A2.4). We made two parameter bifurcation plots in the same way as before.

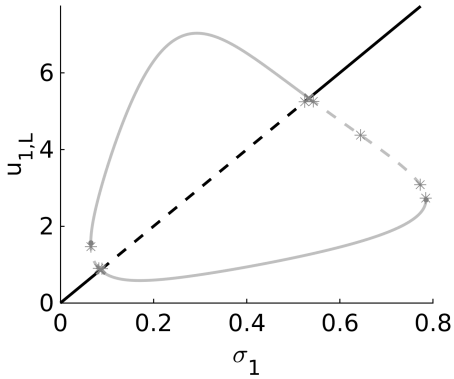

Fig. A2.4. Single parameter bifurcation analysis of the MIT LPA system with σ_1 as bifurcation parameter, $\sigma_2 = 0.2$, and other parameters at default values. The black curve represents the homogeneous (global) steady state and the grey curve the heterogeneous (local) steady state. Solid lines: stable states. Dashed lines: unstable states. Dots: fold bifurcations delimiting the borders of the regime with heterogeneous states. Crosses: transcritical bifurcations delimiting the unstable part of the homogeneous branch (Turing regime). Stars: Hopf bifurcations.

LPA of the WPGAP model

We performed LPA both with fast diffusing and slowly diffusing active GAP. For fast diffusing active GAP, the LPA system has ODEs for the local and global concentration of active GTPase (u_L and u_G respectively) and the global concentration of inactive GTPase,

active GAP, and inactive GAP (v_G, G_G, and g_G respectively). The global average GTPase concentration $T = u_G + v_G$ and GAP concentration $T_g = G_G + g_G$ are conserved. Using these conservations, we eliminated v_G and g_G, leaving the following system:

$$\begin{aligned}
\frac{du_L}{dt} &= b(T-u_G) + \gamma \frac{u_L^n}{1+u_L^n}(T-u_G) - u_L - G_G \cdot u_L \\
\frac{du_G}{dt} &= b(T-u_G) + \gamma \frac{u_G^n}{1+u_G^n}(T-u_G) - u_G - G_G \cdot u_G \\
\frac{dG_G}{dt} &= cu_G(T_g - G_G) - dG_G.
\end{aligned} \tag{A2.76}$$

For slowly diffusing active GAP, an additional local concentration of active GAP (G_L) has to be added to the LPA system:

$$\begin{aligned}
\frac{du_L}{dt} &= b(T-u_G) + \gamma \frac{u_L^n}{1+u_L^n}(T-u_G) - u_L - G_L \cdot u_L \\
\frac{du_G}{dt} &= b(T-u_G) + \gamma \frac{u_G^n}{1+u_G^n}(T-u_G) - u_G - G_G \cdot u_G \\
\frac{dG_L}{dt} &= cu_L(T_g - G_G) - dG_L \\
\frac{dG_G}{dt} &= cu_G(T_g - G_G) - dG_G.
\end{aligned} \tag{A2.77}$$

A one parameter bifurcation analysis with T as bifurcation parameter again reveals the same three regimes for the system with fast active GAP as for the WP model (Figure A2.5). For the system with slow active GAP there is no heterogeneous state at default T_g. For lower values of T_g, the three regimes can still be found for this system (Figure A2.5). We made two parameter bifurcation plots in the same way as before.

LPA of the MIGAP1 model

Based on our results for the WPGAP model, we performed LPA on the MI models with GAPs only for fast diffusing GAPs. The full LPA ODE system has local and global concentrations for active GTPase 1 and 2 ($u_{1,L}$, $u_{1,G}$, $u_{2,L}$, and $u_{2,G}$) and global concentrations for inactive GTPase 1 and 2 ($v_{1,G}$, and $v_{2,G}$) and active and inactive GAP ($G_{1,G}$ and $g_{1,G}$). The global average concentration of GTPase 1 ($T_1 = u_{1,G} + v_{1,G}$) and 2 ($T_2 = u_{2,G} + v_{2,G}$) and GAP ($T_{g,1} = G_{1,G} + g_{1,G}$) are conserved, allowing us to eliminate $v_{1,G}$, $v_{2,G}$, and $g_{1,G}$.

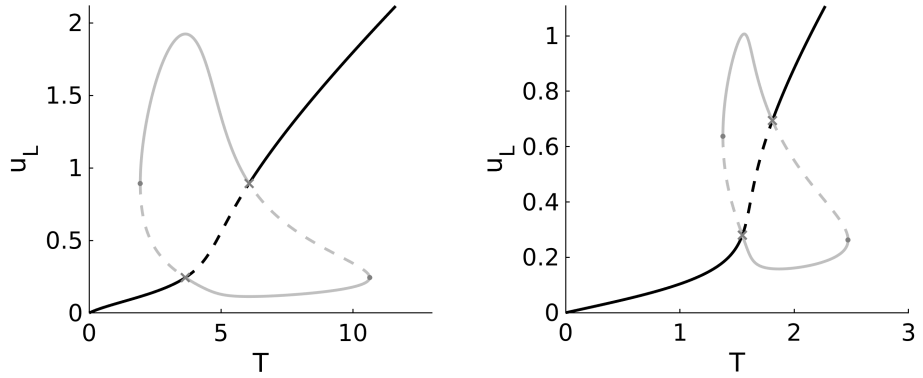

Fig. A2.5. Single parameter bifurcation analysis of the WPGAP LPA system with T as bifurcation parameter and other parameters at default values. Left: LPA system for fast active GAP. Right: LPA system for slow active GAP (with $T_g = 0.5$). The black curve represents the homogeneous (global) steady state and the grey curve the heterogeneous (local) steady state. Solid lines: stable states. Dashed lines: unstable states. Dots: fold bifurcations delimiting the borders of the regime with heterogeneous states. Crosses: transcritical bifurcations delimiting the unstable part of the homogeneous branch (Turing regime).

This leads to the following system of ODEs:

$$\begin{aligned}
\frac{du_{1,L}}{dt} &= b_1(T_1 - u_{1,G}) + \gamma_1 \frac{1}{1+u_{2,L}^n}(T_1 - u_{1,G}) - u_{1,L} - G_{1,G} \cdot u_{1,L} \\
\frac{du_{1,G}}{dt} &= b_1(T_1 - u_{1,G}) + \gamma_1 \frac{1}{1+u_{2,G}^n}(T_1 - u_{1,G}) - u_{1,G} - G_{1,G} \cdot u_{1,G} \\
\frac{du_{2,L}}{dt} &= b_2(T_2 - u_{2,G}) + \gamma_2 \frac{1}{1+u_{1,L}^n}(T_2 - u_{2,G}) - u_{2,L} \\
\frac{du_{2,G}}{dt} &= b_2(T_2 - u_{2,G}) + \gamma_2 \frac{1}{1+u_{1,G}^n}(T_2 - u_{2,G}) - u_{2,G} \\
\frac{dG_{1,G}}{dt} &= c_1 u_{1,G}(T_{g,1} - g_{1,G}) - d_1 G_{1,G}.
\end{aligned} \tag{A2.78}$$

A one parameter bifurcation analysis with T_1 as bifurcation parameter and $T_2 = 5$ again reveals the same three regimes as for the WP model (Figure A2.6). We made two parameter bifurcation plots in the same way as before.

LPA of the MIGAP2 model

The full LPA ODE system has local and global concentrations for active GTPase 1 and 2 ($u_{1,L}$, $u_{1,G}$, $u_{2,L}$, and $u_{2,G}$) and global concentrations for inactive GTPase 1 and 2 ($v_{1,G}$, and $v_{2,G}$) and acitve and inactive GAP 1 and 2 ($G_{1,G}$, $g_{1,G}$, $G_{2,G}$, and $g_{2,G}$). The global average concentration of GTPase 1 ($T_1 = u_{1,G} + v_{1,G}$) and 2 ($T_2 = u_{2,G} + v_{2,G}$) and GAP 1 ($T_{g,1} = G_{1,G} + g_{1,G}$) and 2 ($T_{g,2} = G_{2,G} + g_{2,G}$) are conserved, allowing us to eliminate

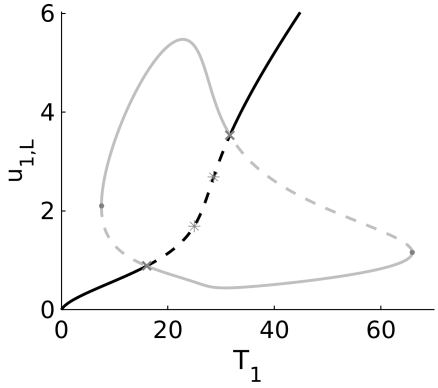

Fig. A2.6. Single parameter bifurcation analysis of the MIGAP1 LPA system with T_1 as bifurcation parameter, $T_2 = 5$, and other parameters at default values. The black curve represents the homogeneous (global) steady state and the grey curve the heterogeneous (local) steady state. Solid lines: stable states. Dashed lines: unstable states. Dots: fold bifurcations delimiting the borders of the regime with heterogeneous states. Crosses: transcritical bifurcations delimiting the unstable part of the homogeneous branch (Turing regime). Stars: Hopf bifurcations.

$v_{1,G}$, $v_{2,G}$, $g_{1,G}$, and $g_{2,G}$. This leads to the following system of ODEs:

$$\begin{aligned}
\frac{du_{1,L}}{dt} &= b_1(T_1 - u_{1,G}) + \gamma_1 \frac{1}{1+u_{2,L}^n}(T_1 - u_{1,G}) - u_{1,L} - G_{1,G} \cdot u_{1,L} \\
\frac{du_{1,G}}{dt} &= b_1(T_1 - u_{1,G}) + \gamma_1 \frac{1}{1+u_{2,G}^n}(T_1 - u_{1,G}) - u_{1,G} - G_{1,G} \cdot u_{1,G} \\
\frac{du_{2,L}}{dt} &= b_2(T_2 - u_{2,G}) + \gamma_2 \frac{1}{1+u_{1,L}^n}(T_2 - u_{2,G}) - u_{2,L} - G_{2,G} \cdot u_{2,L} \\
\frac{du_{2,G}}{dt} &= b_2(T_2 - u_{2,G}) + \gamma_2 \frac{1}{1+u_{1,G}^n}(T_2 - u_{2,G}) - u_{2,G} - G_{2,G} \cdot u_{2,G} \\
\frac{dG_{1,G}}{dt} &= c_1 u_{1,G}(T_{g,1} - G_{1,G}) - d_1 G_{1,G} \\
\frac{dG_{2,G}}{dt} &= c_2 u_{2,G}(T_{g,2} - G_{2,G}) - d_2 G_{2,G}.
\end{aligned} \tag{A2.79}$$

A one parameter bifurcation analysis with T_1 as bifurcation parameter and $T_2 = 20$ again reveals the same three regimes as for the WP model (Figure A2.7). We made two parameter bifurcation plots in the same way as before.

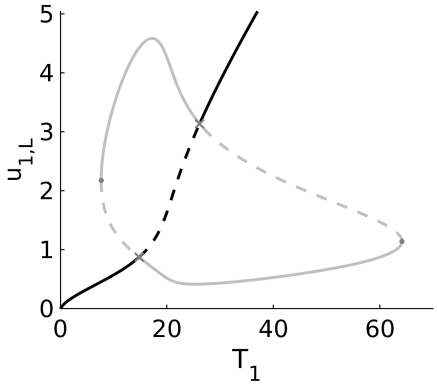

Fig. A2.7. Single parameter bifurcation analysis of the MIGAP2 LPA system with T_1 as bifurcation parameter, $T_2 = 20$, and other parameters at default values. The black curve represents the homogeneous (global) steady state and the grey curve the heterogeneous (local) steady state. Solid lines: stable states. Dashed lines: unstable states. Dots: fold bifurcations delimiting the borders of the regime with heterogeneous states. Crosses: transcritical bifurcations delimiting the unstable part of the homogeneous branch (Turing regime).

2.8.5 WPT model with degradation of inactive GTPase

If the degradation term from the WPT model is changed from degradation of active GTPase to degradation of inactive GTPase, the full dimension-carrying system is given by:

$$\begin{aligned}\frac{\partial \tilde{u}}{\partial \tilde{t}} &= \tilde{b}\tilde{v} + \tilde{\gamma}\frac{\tilde{u}^n}{K^n + \tilde{u}^n}\tilde{v} - \delta\tilde{u} + D_u\nabla^2\tilde{u} \\ \frac{\partial \tilde{v}}{\partial \tilde{t}} &= -\tilde{b}\tilde{v} - \tilde{\gamma}\frac{\tilde{u}^n}{K^n + \tilde{u}^n}\tilde{v} + \delta\tilde{u} + \tilde{\sigma} - \tilde{\xi}\tilde{v} + \tilde{D}_v\nabla^2\tilde{v}.\end{aligned} \tag{A2.80}$$

After non-dimensionalisation, the following system is obtained:

$$\begin{aligned}\frac{\partial u}{\partial t} &= bv + \gamma\frac{u^n}{1+u^n}v - u + \nabla^2 u \\ \frac{\partial v}{\partial t} &= -bv - \gamma\frac{u^n}{1+u^n}v + u + \sigma - \xi v + D_v\nabla^2 v,\end{aligned} \tag{A2.81}$$

with dimensionless variables:

$$u = \frac{\tilde{u}}{K}, \quad v = \frac{\tilde{v}}{K}, \quad t = \delta\tilde{t}, \quad x = \frac{\tilde{x}\sqrt{\delta}}{\sqrt{D_u}}, \quad y = \frac{\tilde{y}\sqrt{\delta}}{\sqrt{D_u}}, \tag{A2.82}$$

and scaled parameters:

$$b = \frac{\tilde{b}}{\delta}, \quad \gamma = \frac{\tilde{\gamma}}{\delta}, \quad \xi = \frac{\tilde{\xi}}{\delta}, \quad \sigma = \frac{\tilde{\sigma}}{\delta K}, \quad D_v = \frac{\tilde{D}_v}{D_u}. \tag{A2.83}$$

The corresponding LPA system is:

$$\begin{aligned}
\frac{du_L}{dt} &= bv_G + \gamma \frac{u_L^n}{1+u_L^n} v_G - u_L \\
\frac{du_G}{dt} &= bv_G + \gamma \frac{u_G^n}{1+u_G^n} v_G - u_G \\
\frac{dv_G}{dt} &= -bv_G - \gamma \frac{u_G^n}{1+u_G^n} v_G + u_G + \sigma - \xi v_G.
\end{aligned} \tag{A2.84}$$

A one parameter bifurcation analysis with σ as bifurcation parameter reveals a bistable regime with an unstable homogeneous state surrounded by two stable homogeneous steady states (Fig A2.8). The heterogeneous steady states follow the homogeneous ones so closely that the order of the curves could not be resolved numerically. Therefore, we further studied the behaviour of this system with a numerical simulation starting somewhere in the middle of the unstable part of the homogeneous branch. In this simulation, many clusters of active GTPase initially appear and start growing. However, they keep growing until they fill the domain and a new homogeneous state is reached (Fig A2.9), indicating that the unusual heterogeneous branch in the LPA plot does not represent a reachable heterogeneous state.

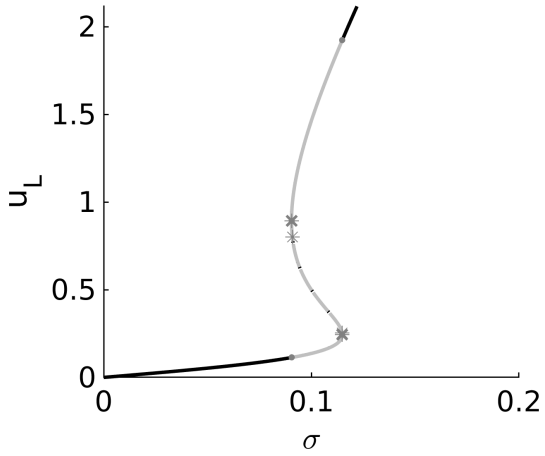

Fig. A2.8. Single parameter bifurcation analysis of the WPT LPA system with degradation of inactive GTPase with σ as bifurcation parameter and other parameters at default values. The black curve represents the homogeneous (global) steady state and the grey curve the heterogeneous (local) steady state. Inset shows details around $u_L = 0.5$. Solid lines: stable states. Dashed lines: unstable states. Dots: fold bifurcations delimiting the borders of the regime with heterogeneous states. Crosses: transcritical bifurcations delimiting the unstable part of the homogeneous branch (Turing regime). Stars: Hopf bifurcations.

Attempts with different parameters in the LPA system did not yield any bifurcation plots with clearly reachable heterogeneous states, indicating that it is at the vary least easier to obtain spontaneous pattern formation when degradation of the active form occurs. This suggests some removal of active GTPase (e.g. by membrane recycling) is important for pattern formation mechanisms with broken mass conservation.

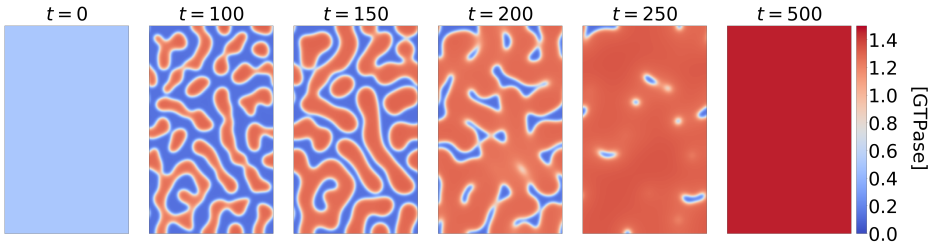

Fig. A2.9. Transient active GTPase concentrations ([GTPase]) from simulations of the WPT model with degradation of the inactive form of GTPase. Simulation conditions were as described in the main text for the WPT model, with $\sigma = 0.1$.

2.8.6 Derivation of ODE models

Basic ODE model

The homogeneous WP system is bistable, with points within the cluster being in the high steady state and points outside the cluster in the low steady sate [84]. Similarly, for the MI model, the area outside a cluster of GTPase 1 is dominated by GTPase 2 which promotes inactivation of GTPase 1. This property results in a relatively flat concentration profile inside clusters. We approximate this by a single, constant (high) concentration inside clusters and a single, constant (low) concentration outside clusters (Fig A2.10).

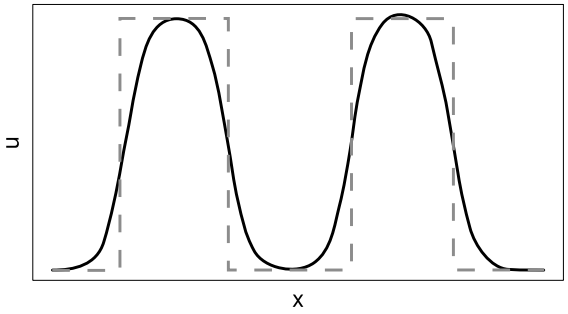

Fig. A2.10. Cartoon of cluster representation used in the ODE model. The solid black line represents a profile of the active GTPase concentration (u) as obtained with the PDE model along a 1D cross-section in direction x. The dashed grey line indicates a discrete cluster approximation based on this profile.

Under this approximation, cluster area is proportional to the amount of (active) GTPase $h_{c,n}$ in cluster n and cluster circumference is proportional to $h_{c,n}^{\eta}$ with $0 < \eta < 1$, depending on cluster shape (and system dimensionality). For circular clusters, $\eta = \frac{1}{2}$ because the area is directly proportional to the square root of the circumference. In addition, we assume diffusion of the inactive form is sufficiently fast that all clusters effectively draw from a single pool of inactive GTPase. Due to the constant area of the membrane, the constant inactive GTPase concentration v is directly proportional to the total amount of inactive GTPase h_p. Since the concentration of active GTPase in the clusters is assumed

constant ($u = u_c$), the interaction function f of the WP model can be simplified:

$$f(u,v) = bv + \gamma \frac{u^n}{1+u^n} v - u = \left(b + \gamma \frac{u_c^n}{1+u_c^n} \right) v - u_c = c_1 h_p - c_2, \tag{A2.85}$$

where c_1 and c_2 are constants. Similarly, interaction function f of the MI model can be simplified to obtain the same expression if we assume levels of active GTPase outside clusters to also be approximately constant:

$$f(u_i, v_i, u_j) = b_i v_i + \gamma_i \frac{1}{1+u_j^n} v_i - u_i = \left(b_i + \gamma_i \frac{1}{1+u_{j,c}^n} \right) v_i - u_{i,c} = c_1 h_{p,i} - c_2. \tag{A2.86}$$

Since these functions describe the change of concentrations and we are interested in cluster size, we have to integrate this expression across the area $A_{c,n}$ of the cluster, which is proportional to $h_{c,n}$. Because inactive GTPase concentration v is homogeneous, this integral is easily solved:

$$\iint_{A_{c,n}} (c_1 h_p - c_2) dA_{c,n} = (c_1 h_p - c_2) \iint_{A_{c,n}} dA_{c,n} = c_1 A_{c,n} h_p - c_2 A_{c,n} = \alpha h_{c,n} h_p - \delta h_{c,n}, \tag{A2.87}$$

where α and δ are constants. These terms describe changes in cluster sizes due to the interaction functions.

In addition to these terms, we consider loss of active GTPase through diffusion across the boundary of the cluster, where we assume it is immediately converted into the inactive form because of the low steady state of the active form outside the cluster. This results in an extra inactivation term proportional to the circumference of the cluster $h_{c,n}^{\eta}$. Combining this term (using proportionality constant β) with the terms derived from the interaction function results in the basic ODE model:

$$\begin{aligned} \frac{dh_{c,n}(t)}{dt} &= \alpha h_{c,n}(t) h_p(t) - \beta h_{c,n}(t)^{\eta} - \delta h_{c,n}(t) \\ \frac{dh_p(t)}{dt} &= -\alpha h_p(t) \sum_{j=1}^{N} h_{c,j}(t) + \beta \sum_{j=1}^{N} h_{c,j}(t)^{\eta} + \delta \sum_{j=1}^{N} h_{c,j}(t). \end{aligned} \tag{A2.88}$$

Compartmentalised ODE model

We account for the fact that a cluster can only incorporate inactive GTPase from its vicinity by giving each cluster its own local compartment containing an amount of inactive GTPase $h_{p,n}$. We can greatly simplify computations by assuming that all compartments have equal size and are connected to all other compartments with equally large interfaces. This is a reasonable approximation for the question we are most interested in: do small differences in cluster size increase (polarisation) or decrease (stable coexistence)? Under this approximation, diffusive fluxes of inactive GTPase become constant rates of exchange between compartments.

Upon adding a production term to the inactive form and degradation terms to both the

active and inactive forms, the system of PDEs reads:

$$\begin{aligned}\frac{\partial u}{\partial t} &= f(u,v) - \xi u \\ \frac{\partial v}{\partial t} &= -f(u,v) + \sigma - \xi_p v.\end{aligned} \tag{A2.89}$$

To obtain the terms of the ODE approximation, the extra terms can be treated as done before for function f. Since compartments have a constant size, concentration v in each compartment is proportional to $h_{p,n}$. In clusters, concentration u is still constant. Dropping function f for the moment, we get:

$$\begin{aligned}\frac{\partial u}{\partial t} &= -\xi u_c = -c_3 \\ \frac{\partial v}{\partial t} &= \sigma - c_4 h_{p,n},\end{aligned} \tag{A2.90}$$

where c_3 and c_4 are constants. To obtain expressions for $h_{c,n}$ and $h_{p,n}$, we integrate across the cluster area $A_{c,n}$ (for degradation of active form), or the compartment area $A_{p,n}$ (for production and degradation of inactive form):

$$\begin{aligned}\frac{dh_{c,n}}{dt} &= \iint_{A_{c,n}} -c_3 dA_{c,n} = -c_3 A_{c,n} = -\tilde{\xi} h_{c,n} \\ \frac{dh_{p,n}}{dt} &= \iint_{A_{p,n}} (\sigma - c_4 h_{p,n}) dA_{p,n} = \sigma A_{p,n} - c_4 A_{p,n} h_{p,n} = \tilde{\sigma} - \tilde{\xi}_p h_{p,n},\end{aligned} \tag{A2.91}$$

where $\tilde{\xi}$, $\tilde{\sigma}$, and $\tilde{\xi}_p$ are constants. Adding these terms and a constant exchange rate ϕ to the expression we already found in the previous section (and dropping the tildes) we obtain the compartmentalised ODE system:

$$\begin{aligned}\frac{dh_{c,n}(t)}{dt} &= \alpha h_{c,n}(t) h_{p,n}(t) - \beta h_{c,n}(t)^\eta - \delta h_{c,n}(t) - \xi h_{c,n}(t) \\ \frac{dh_{p,n}(t)}{dt} &= \sigma - \alpha h_{p,n}(t) h_{c,n}(t) + \beta h_{c,n}(t)^\eta + \delta h_{c,n}(t) - \xi_p h_{p,n}(t) + \phi \sum_{j=1}^{N} (h_{p,j} - h_{p,n}).\end{aligned} \tag{A2.92}$$

ODE model with GAP feedback

If we write $G_{c,n}$ for the total amount of active GAP in cluster n, then the concentration of active GAP in that cluster is proportional to $G_{c,n}/h_{c,n}$. Since $h_{c,n}$ is proportional to both the area of and the total amount of GTPase in cluster n, the GTPase concentration in that cluster is proportional to $h_{c,n}/h_{c,n}$ (constant). Since we modelled GAP-based GTPase inactivation proportional to the product of GAP and GTPase concentrations, the rate at which GAPs reduce the total amount of GTPase in cluster n is proportional to $G_{c,n}/h_{c,n} \cdot h_{c,n}/h_{c,n} \cdot h_{c,n} = G_{c,n}$. Loss of GAPs from the cluster by diffusion is proportional to the GAP concentration and the circumference of the cluster and therefore to $G_{c,n}/h_{c,n} \cdot h_{c,n}^\eta = h_{c,n}^{\eta-1} G_{c,n}$. GAPs lost by diffusion are assumed to be inactivated outside

the cluster. In addition, GAPs are inactivated inside the cluster at a constant rate, so proportional to the GAP concentration $G_{c,n}/h_{c,n}$. This makes the change in the amount of active GAP due to constant inactivation proportional to $G_{c,n}/h_{c,n} \cdot h_{c,n} = G_{c,n}$. GTPase-dependent GAP activation was modelled proportional to the active GTPase and inactive GAP concentrations in the PDE model. Therefore, the rate at which GTPase inactivates GAP in a cluster is proportional to the (constant) GTPase concentration and the non-cluster inactive GAP concentration G_p (in a constant area). This results in a total GAP activation proportional to $h_{c,n}/h_{c,n} \cdot G_p \cdot h_{c,n} = h_{c,n} G_p$. Combining these relations with the relevant rate constants results in the system of the ODE model with GAP feedback:

$$\begin{aligned}
\frac{dh_{c,n}(t)}{dt} &= \alpha h_{c,n}(t) h_p(t) - \beta h_{c,n}(t)^\eta - \delta h_{c,n}(t) - \varepsilon G_{c,n}(t) \\
\frac{dh_p(t)}{dt} &= -\alpha h_p(t) \sum_{j=1}^{N} h_{c,j}(t) + \beta \sum_{j=1}^{N} h_{c,j}(t)^\eta + \delta \sum_{j=1}^{N} h_{c,j}(t) + \varepsilon \sum_{j=1}^{N} G_{c,j}(t) \\
\frac{dG_{c,n}(t)}{dt} &= \gamma h_{c,n}(t) G_p(t) - \delta_g G_{c,n}(t) - \zeta h_{c,n}(t)^{\eta-1} G_{c,n} \\
\frac{dG_p(t)}{dt} &= -\gamma G_p(t) \sum_{j=1}^{N} h_{c,j}(t) + \delta_g \sum_{j=1}^{N} G_{c,j}(t) + \zeta \sum_{j=1}^{N} h_{c,j}(t)^{\eta-1} G_{c,j}(t).
\end{aligned} \tag{A2.93}$$

2.8.7 WPT model with degradation of both active and inactive GTPase

Since degradation of inactive GTPase only does not seem to yield any stable patterns, we ask if some degree of degradation of inactive GTPase can be tolerated as long as there is also degradation of active GTPase. Simulations with the compartmentalised ODE model with degradation of both active and inactive forms suggests that patterns of stably coexisting GTPase clusters are indeed possible (Fig A2.11A). To confirm this, we consider the WPT model is with degradation of both active and inactive GTPase. The full dimension-carrying system is given by:

$$\begin{aligned}
\frac{\partial \tilde{u}}{\partial \tilde{t}} &= \tilde{b}\tilde{v} + \tilde{\gamma}\frac{\tilde{u}^n}{K^n + \tilde{u}^n}\tilde{v} - \delta\tilde{u} - \tilde{\xi}\tilde{u} + D_u \nabla^2 \tilde{u} \\
\frac{\partial \tilde{v}}{\partial \tilde{t}} &= -\tilde{b}\tilde{v} - \tilde{\gamma}\frac{\tilde{u}^n}{K^n + \tilde{u}^n}\tilde{v} + \delta\tilde{u} + \tilde{\sigma} - \tilde{\xi}_p\tilde{v} + \tilde{D}_v \nabla^2 \tilde{v}.
\end{aligned} \tag{A2.94}$$

After non-dimensionalisation, the following system is obtained:

$$\begin{aligned}
\frac{\partial u}{\partial t} &= bv + \gamma\frac{u^n}{1+u^n}v - u - \xi u + \nabla^2 u \\
\frac{\partial v}{\partial t} &= -bv - \gamma\frac{u^n}{1+u^n}v + u + \sigma - \xi_p v + D_v \nabla^2 v,
\end{aligned} \tag{A2.95}$$

with dimensionless variables:

$$u = \frac{\tilde{u}}{K}, \quad v = \frac{\tilde{v}}{K}, \quad t = \delta\tilde{t}, \quad x = \frac{\tilde{x}\sqrt{\delta}}{\sqrt{D_u}}, \quad y = \frac{\tilde{y}\sqrt{\delta}}{\sqrt{D_u}}, \tag{A2.96}$$

and scaled parameters:

$$b=\frac{\tilde{b}}{\delta},\quad \gamma=\frac{\tilde{\gamma}}{\delta},\quad \xi=\frac{\tilde{\xi}}{\delta},\quad \xi_p=\frac{\tilde{\xi}_p}{\delta},\quad \sigma=\frac{\tilde{\sigma}}{\delta K},\quad D_v=\frac{\tilde{D}_v}{D_u}. \tag{A2.97}$$

The corresponding LPA system is:

$$\begin{aligned}\frac{du_L}{dt}&=bv_G+\gamma\frac{u_L^n}{1+u_L^n}v_G-u_L-\xi u_L\\ \frac{du_G}{dt}&=bv_G+\gamma\frac{u_G^n}{1+u_G^n}v_G-u_G-\xi u_G\\ \frac{dv_G}{dt}&=-bv_G-\gamma\frac{u_G^n}{1+u_G^n}v_G+u_G+\sigma-\xi_p v_G.\end{aligned} \tag{A2.98}$$

A one parameter bifurcation analysis with σ as bifurcation parameter reveals three parameter regimes: a homogeneous regime, a Turing regime, and a regime where patterning may be induced by a sufficiently strong perturbation (Fig A2.11B). A simulation in the Turing regime reveals that this model can indeed yield a pattern of multiple stably coexisting clusters (Fig A2.11C).

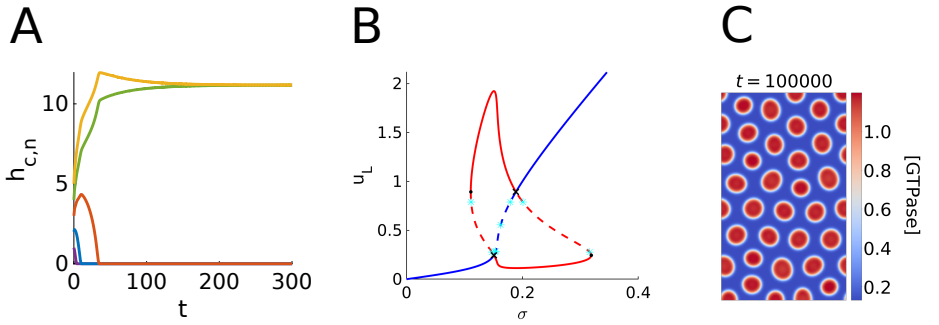

Fig. A2.11. Coexistence can be found even with degradation of both active and inactive forms. A: Simulation of compartmentalised ODE model with production and degradation. Parameters were as in main text, with $\phi=1$ and $\xi=\xi_p=0.1$. B: Single parameter bifurcation analysis of the WPT model with an additional degradation of inactive form at the same rate as the active form. The blue curve represents the homogeneous (global) steady state and the red curve the heterogeneous (local) steady state. Solid lines: stable states. Dashed lines: unstable states. Dots: fold bifurcations delimiting the borders of the regime with heterogeneous states. Crosses: transcritical bifurcations delimiting the unstable part of the homogeneous branch (Turing regime). Stars: Hopf bifurcations. C: Profile of steady active GTPase concentrations ([GTPase]) from simulations of the WPT model with degradation of both the active and inactive form of GTPase. Simulation conditions were as described in the main text for the WPT model, with $\sigma=0.155$ and a degradation rate of 0.1 for both active and inactive forms.

2.8.8 Quasi steady state approximation for GAPs in ODE model

Due to mass conservation, the equation for the amount of (inactive) GAP G_p outside the cluster is redundant. Using the conservation relation $T_g=G_p+\sum_{j=1}^{N}G_{c,j}$, this equation can be removed from the ODE system, leaving for GAP dynamics only the equations for

$G_{c,n}$:

$$\frac{dG_{c,n}(t)}{dt} = \gamma h_{c,n}(t)\left(T_g - \sum_{j=1}^{N} G_{c,j}(t)\right) - \zeta G_{c,n}(t) h_{c,n}(t)^{\eta-1} - \delta_g G_{c,n}(t). \tag{A2.99}$$

In the case where GAP dynamics is fast compared to GTPase dynamics, we can take a quasi steady state approximation for the amounts of GAP. This results in:

$$G_{c,n} = \frac{\gamma h_{c,n}(t)}{\zeta h_{c,n}(t)^{\eta-1} + \delta_g}\left(T_g - \sum_{j=1}^{N} G_{c,j}\right). \tag{A2.100}$$

To obtain an expression for $\sum_{j=1}^{N} G_{c,j}$, we sum $G_{c,n}$ over all clusters:

$$\begin{aligned}\sum_{j=1}^{N} G_{c,j} &= \sum_{n=1}^{N} G_{c,n} = \sum_{n=1}^{N} \frac{\gamma h_{c,n}(t)}{\zeta h_{c,n}(t)^{\eta-1} + \delta_g}\left(T_g - \sum_{j=1}^{N} G_{c,j}\right) \\ &= \left(T_g - \sum_{j=1}^{N} G_{c,j}\right) \sum_{n=1}^{N} \frac{\gamma h_{c,n}(t)}{\zeta h_{c,n}(t)^{\eta-1} + \delta_g}.\end{aligned} \tag{A2.101}$$

Solving for $\sum_{j=1}^{N} G_{c,j}$ and (trivially) changing summation indices gives:

$$\sum_{j=1}^{N} G_{c,j} = T_g \frac{\sum_{j=1}^{N} \dfrac{h_{c,j}(t)}{h_{c,j}(t)^{\eta-1} + \delta_g/\zeta}}{\zeta/\gamma + \sum_{j=1}^{N} \dfrac{h_{c,j}(t)}{h_{c,j}(t)^{\eta-1} + \delta_g/\zeta}} \tag{A2.102}$$

Substituting this expression into Eq. A2.100 gives:

$$\begin{aligned} G_{c,n} &= \frac{\gamma h_{c,n}(t)}{\zeta h_{c,n}(t)^{\eta-1} + \delta_g}\left(T_g - T_g \frac{\sum_{j=1}^{N} \dfrac{h_{c,j}(t)}{h_{c,j}(t)^{\eta-1} + \delta_g/\zeta}}{\zeta/\gamma + \sum_{j=1}^{N} \dfrac{h_{c,j}(t)}{h_{c,j}(t)^{\eta-1} + \delta_g/\zeta}}\right) \\ &= T_g \frac{\gamma h_{c,n}(t)}{\zeta h_{c,n}(t)^{\eta-1} + \delta_g} \cdot \frac{\zeta/\gamma}{\zeta/\gamma + \sum_{j=1}^{N} \dfrac{h_{c,j}(t)}{h_{c,j}(t)^{\eta-1} + \delta_g/\zeta}} \\ &= T_g \frac{\dfrac{h_{c,n}(t)}{h_{c,n}(t)^{\eta-1} + \delta_g/\zeta}}{\zeta/\gamma + \sum_{j=1}^{N} \dfrac{h_{c,j}(t)}{h_{c,j}(t)^{\eta-1} + \delta_g/\zeta}}. \end{aligned} \tag{A2.103}$$

We now have an expression for $G_{c,n}$ that only depends on $h_{c,n}$ and other $h_{c,i}$. With this we can close the equations for $h_{c,n}$ in terms of h_c.

3

Robust banded protoxylem pattern formation through microtubule-based directional ROP diffusion restriction

Bas Jacobs

Jaap Molenaar

Eva E. Deinum

Published in the Journal of Theoretical Biology [205]

Abstract

In plant vascular tissue development, different cell wall patterns are formed, offering different mechanical properties optimised for different growth stages. Critical in these patterning processes are Rho of Plants (ROP) proteins, a class of evolutionarily conserved small GTPase proteins responsible for local membrane domain formation in many organisms. While the spotted metaxylem pattern can easily be understood as a result of a Turing-style reaction-diffusion mechanism, it remains an open question how the consistent orientation of evenly spaced bands and spirals as found in protoxylem is achieved. We hypothesise that this orientation results from an interaction between ROPs and an array of transversely oriented cortical microtubules that acts as a directional diffusion barrier. Here, we explore this hypothesis using partial differential equation models with anisotropic ROP diffusion and show that a horizontal microtubule array acting as a vertical diffusion barrier to active ROP can yield a horizontally banded ROP pattern. We then study the underlying mechanism in more detail, finding that it can only orient curved pattern features but not straight lines. This implies that, once formed, banded and spiral patterns cannot be reoriented by this mechanism. Finally, we observe that ROPs and microtubules together only form ultimately static patterns if the interaction is implemented with sufficient biological realism.

3.1 Introduction

Plants are able to transport water and nutrients from the ground all the way up to the leaves, potentially more than a hundred meters high, thanks to a highly specialised system of vessels known as the xylem [1]. These xylem vessels are formed by cells that deposit a thick secondary cell wall followed by programmed cell death, leaving a hollow tube [3]. The cell wall reinforcements function to withstand the pressures generated during water transport and may be deposited in intricate patterns depending on the type of xylem. In protoxylem, the secondary wall forms bands or spirals, allowing the vessels to stretch with the surrounding tissue, while metaxylem, formed when longitudinal tissue growth has ceased, tends to be more rigid, with only some well-separated pits for radial transport [7–9] (Fig. 3.1A).

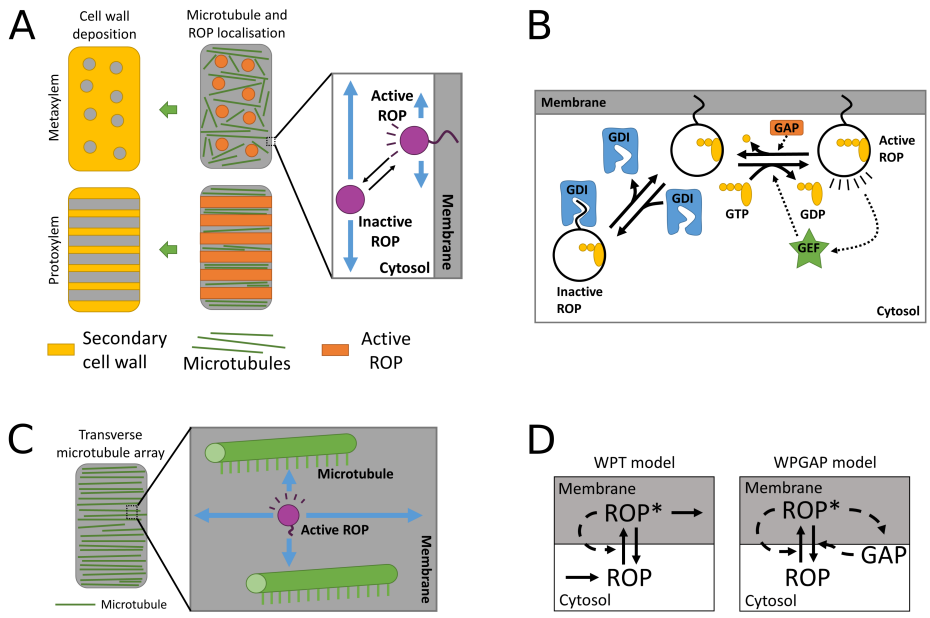

Fig. 3.1. The role of ROP in xylem patterning. (A) General hypothesis of cell wall patterning in metaxylem and protoxylem. Local ROP activity destabilises the microtubules that function as a template for secondary cell wall deposition. (B) Mechanism of ROP activation and inactivation. GEFs promote ROP activation by exchanging GDP for GTP, GAPs promote inactivation by GTP hydrolysis and GDIs selectively remove inactive ROP from the membrane. (C) Cortical microtubules can self-organise into a transverse array and may act as a molecular fence, directionally restricting the diffusion of membrane-bound active ROP. (D) Interactions of active (ROP*) and inactive ROP (ROP) for two simple reaction-diffusion models for ROP-based pattern formation. Blue arrows indicate diffusion, solid black arrows indicate conversions, and dashed arrows indicate positive interactions. Panels (B) and (D) are adapted from chapter 2.

The deposition of this secondary cell wall is determined by the position of cortical microtubules on the inside of the membrane that direct cell wall depositing cellulose synthase complexes [117, 118, 120, 122] and secretory vesicles [119]. The microtubule pattern, in turn, depends on the localised activity of ROP (Rho of Plants) proteins that re-

cruit effectors capable of influencing microtubule dynamics, which is best demonstrated for metaxylem development. Through these effectors, ROP activity reduces the local microtubule density, creating the mirotubule pattern [147–149] (Fig. 3.1A). Since ROP involvement has also been indicated in protoxylem differentiation [150] and the same effectors (MIDD1, Kinesin13A) are expressed during protoxylem development [151, 152], patterning of protoxylem is expected to have a similar mechanism to that of metaxylem.

ROPs are a type of small GTPase, an evolutionarily conserved class of proteins often involved in membrane domain formation. Small GTPases are signalling proteins that function like a molecular switch. They have an active GTP-bound form and an inactive GDP-bound form (Fig. 3.1B). Guanine nucleotide Exchange Factors (GEFs) promote activation by exchanging GDP for GTP, while GTPase Activating Proteins (GAPs) promote inactivation by stimulating the intrinsic GTPase activity of the ROP [64, 167]. The active form is tethered to the cell membrane, while the inactive form is selectively taken out of the membrane by Guanine nucleotide Dissociation Inhibitors (GDIs) [65]. Because diffusion at the membrane is much slower than in the cytosol [66, 67], the active form diffuses only slowly compared to the inactive form. If this difference in diffusion rates is complemented by a positive feedback mechanism, all ingredients for Turing-style pattern formation are present [46, 47]. Such positive feedback loops have been demonstrated for a variety of small GTPase systems [68]. Therefore, ROPs and other small GTPases are extremely suitable for *de novo* membrane patterning. Consequently, reaction-diffusion models involving small GTPases have been proposed for a wide variety of membrane patterning processes [32, 35, 44, 178].

Generating a spotted metaxylem-like pattern using a ROP-like reaction-diffusion system is straightforward [32, 49, 163]. These same systems can also generate stripes, but these tend to be curved, without any specific orientation (e.g., patterns in first column of Fig 3.2), making the horizontally banded protoxylem pattern harder to obtain with a reaction-diffusion mechanism. A banded pattern can be obtained on a sufficiently narrow periodic domain, when the circumference of the domain (i.e., the width of the periodic axis) is smaller than the wave length of the pattern as suggested for, e.g., animal tails [10]. However, in microscopic pictures of protoxylem patterns, even the widest band and gap lengths combined are rarely larger than the visible width of the cell, let alone the entire circumference [122, 149]. Therefore, some other mechanism must impose the orientation of the protoxylem ROP pattern.

The protoxylem pattern has to be properly oriented relative to the cell's growth axis, suggesting that information from the orientation of the cell is transmitted to the ROP pattern. An obvious candidate for the agent of this transmission is the microtubule array itself, since it is well-known for its ability to self-organise into a wide variety of structures, including aligned cortical arrays with a transverse orientation [98, 124, 134]. This idea is consistent with the observation that, during protoxylem development, microtubules reorient to a transverse array before apparent band formation [159]. In addition, IQD13, a protein interacting with both microtubules and the plasma membrane, can cause microtubules to act as a "molecular fence" that physically restricts the movement of active ROP and increased expression of this protein results in more flattened spots in metaxylem [154]. Increasing microtubule stability with taxol treatment or overexpression of MAP70 (a Microtubule-Associated Protein) has a similar effect [148, 153]. These observations suggest that, during protoxylem patterning, a transverse microtubule array will pose a bar-

rier to any ROPs moving perpendicular to the array orientation, resulting in anisotropic ROP diffusion (Fig. 3.1C).

Anisotropic diffusion in reaction-diffusion systems has long been known to influence the shapes of patterns in experimental chemical systems [206] and in models used for texture synthesis [207]. A study on pattern formation in fish skin also reported pattern orientations shaped by anisotropic diffusion [208]. There, however, anisotropic diffusion was considered to be diffusion dependent on the angle of the concentration gradient, rather than a directional reduction in the diffusion coefficient. Nevertheless, since the concentration gradient determines the main direction of diffusion, their approach indirectly also results in a diffusive flow that is stronger in a certain direction. More recently, anisotropic diffusion has been proposed as a general mechanism for orienting stripes formed by Turing-like mechanisms, with horizontal diffusion restriction of a fast-diffusing component (comparable to the inactive form of ROP) resulting in horizontally oriented stripes [209]. Interestingly, in the case of protoxylem patterning we need the opposite: vertical restriction of the active form resulting in horizontally oriented stripes.

Here, we use partial differential equation (PDE) models of ROP-based reaction-diffusion systems with anisotropic diffusion to study active ROP diffusion restriction as a mechanism of ROP pattern orientation in protoxylem development. We also employ a functional decomposition of the diffusion tensor to gain additional mechanistic insight into the orienting power of this mechanism.

3.2 Methods

3.2.1 Modelling approach

We start with two simple reaction-diffusion models for small GTPase-based membrane patterning that can generate coexisting spots, stripes, and gaps (chapter 2). Both models are adaptations of the wave pinning model from Mori et al. [84], with the addition of either protein turnover (WPT model; see Fig. 3.1D) or negative feedback through GAP activation (WPGAP model) to prevent accumulation of all active ROP into a single cluster (see chapter 2 for a mechanistic explanation). The models assume that active ROP is exclusively membrane bound and inactive ROP is exclusively cytosolic. Consequently, we assume only the diffusion of active ROP will be affected by the microtubule diffusion barriers. Therefore, we will focus our investigation on the diffusion tensor D_u of active ROP (of concentration u), assuming the diffusion of inactive ROP (of concentration v), active GAP (G), and inactive GAP (g) to be constant and isotropic.

The dimensionless WPT model is given by:

$$\begin{aligned}\frac{\partial u}{\partial t} &= bv + \gamma\frac{u^n}{1+u^n}v - u - \xi u + \nabla\cdot D_u\nabla u \\ \frac{\partial v}{\partial t} &= -bv - \gamma\frac{u^n}{1+u^n}v + u + \sigma + D_v\nabla^2 v,\end{aligned} \tag{3.1}$$

where b is the constant activation rate, γ the maximum self-activation rate, n the hill function exponent of self-activation, ξ the active ROP degradation rate, σ the inactive ROP production rate, D_v the inactive ROP diffusion coefficient, and D_u the dimensionless diffusion tensor for u. To arrive at the dimensionless forms, all diffusion coefficients

and tensors were normalised with the (dimension carrying) diffusion coefficient of unrestricted active ROP ($D_{u,max}$).

The dimensionless WPGAP model is given by:

$$\begin{aligned}
\frac{\partial u}{\partial t} &= bv + \gamma \frac{u^n}{1+u^n} v - u - Gu + \nabla \cdot D_u \nabla u \\
\frac{\partial v}{\partial t} &= -bv - \gamma \frac{u^n}{1+u^n} v + u + Gu + D_v \nabla^2 v \\
\frac{\partial G}{\partial t} &= cug - dG + D_G \nabla^2 G \\
\frac{\partial g}{\partial t} &= -cug + dG + D_g \nabla^2 g,
\end{aligned} \tag{3.2}$$

where active ROP promotes GAP activation at rate c, GAPs are inactivated at constant rate d, and D_G and D_g are the diffusion coefficients of active and inactive GAP, respectively. In the WPGAP model, the total amounts of ROP and GAP are conserved, so that the average total ROP concentration T and average total GAP concentration T_g are constants determined by initial conditions.

We used identical values for the parameters for the reaction parts and the unrestricted diffusion coefficients as in chapter 2. We have previously performed extensive bifurcation analyses of these models (chapter 2) to locate parameter regimes where spontaneous patterning can occur from a homogeneous state (so-called Turing regimes). This analysis directed us to relevant parameter sets that remained useful in the case of anisotropic diffusion.

3.2.2 Numerical simulations

We used an Alternating Direction Implicit (ADI) algorithm [210] to solve the reaction-diffusion equations on a two dimensional domain (see Appendix 3.7.1 for details on discretisation schemes). We chose a rectangular domain (190x316 or 60x100 dimensionless length units) with periodic boundary conditions in the horizontal direction and zero-flux boundary conditions in the vertical direction, representing the membrane of an elongated cylindrical cell, resembling those found in plant vascular tissue. Smaller square domains (95x95 or 63x63) with fully periodic boundary conditions were used for investigating the orientation mechanism. Unless stated otherwise, simulations were initiated at the homogeneous steady state (see chapter 2) with a small amount of noise added to each integration pixel. To ensure numerical accuracy, small scale tests were performed using reproducible perturbations as described by Cleary [196] to determine the optimal time step and pixel size.

3.2.3 Pattern angle analysis

To characterise the orientation of the simulated patterns, we determined the angle of the patterns ϑ with respect to the horizontal axis at each point on the domain. Since the direction of the pattern essentially runs perpendicular to the concentration gradient, we determined ϑ by taking the angle of the direction perpendicular to the gradient, such that $\vartheta \in \left[-\frac{1}{2}\pi, \frac{1}{2}\pi\right)$. This way, $\vartheta = 0$ corresponds to a transverse pattern, while $\vartheta = -\frac{1}{2}\pi$

and $\vartheta = \frac{1}{2}\pi$ correspond to a longitudinal pattern. An average pattern angle $\bar{\vartheta}$ over N angles was calculated as follows:

$$\bar{\vartheta} = \frac{1}{2}\arg\left(\frac{1}{N}\sum_{n=1}^{N} e^{i2\vartheta_n}\right), \tag{3.3}$$

where arg is the argument or phase of a complex number and ϑ_n is the local angle at each integration pixel.

3.3 Results

3.3.1 Homogeneous reduction of active ROP diffusion in vertical direction

In the early stages of protoxylem patterning, before ROP activity starts to affect microtubule density, the density of the microtubule array will be more or less homogeneous. Assuming a transverse array orientation, this homogeneous vertical diffusion barrier can be represented by a spatially homogeneous reduction of active ROP diffusion in the vertical direction, yielding the following dimensionless diffusion tensor:

$$D_u = \begin{bmatrix} 1 & 0 \\ 0 & \psi \end{bmatrix}, \tag{3.4}$$

where $\psi \in (0,1]$ is the ratio between diffusion coefficients for restricted and unrestricted diffusion. For isotropic diffusion $\psi = 1$. Because all off-diagonal elements of D_u are zero, the diffusion term simplifies to:

$$\nabla \cdot D_u \nabla u = \frac{\partial^2 u}{\partial x^2} + \psi \frac{\partial^2 u}{\partial y^2}. \tag{3.5}$$

Simulation results for various values of ψ are shown in Fig. 3.2. Increasing the ROP production rate (for the WPT model) or the total amount of ROP (for the WPGAP model) changes the native pattern (i.e., the pattern formed with isotropic diffusion) from spots to stripes to gaps (chapter 2), a sequence of patterns often observed in similar models [49]. Vertical diffusion restriction of active ROP flattens spots and gaps and imposes a horizontal orientation on stripes. The stronger the restriction (the smaller ψ), the more the pattern is flattened. Ultimately, this turns the stripes into horizontal bands or, occasionally, spirals and forces spots and gaps to merge, resulting in banded patterns. These results show that vertical diffusion restriction of active ROP can impose a pattern of horizontal bands. Furthermore, to obtain such bands, the native pattern type does not need to be striped.

We note that the observed changes of pattern type require that the diffusion restriction only, or at least predominantly, applies to active ROP. This can be understood from a simple scaling argument: an equal diffusion reduction for both active and inactive forms is equivalent to independently scaling the x- and y-axis, which will only affect the aspect ratio of the pattern (see Appendix 3.7.2 for details). Similar reasoning (Appendix 3.7.3)

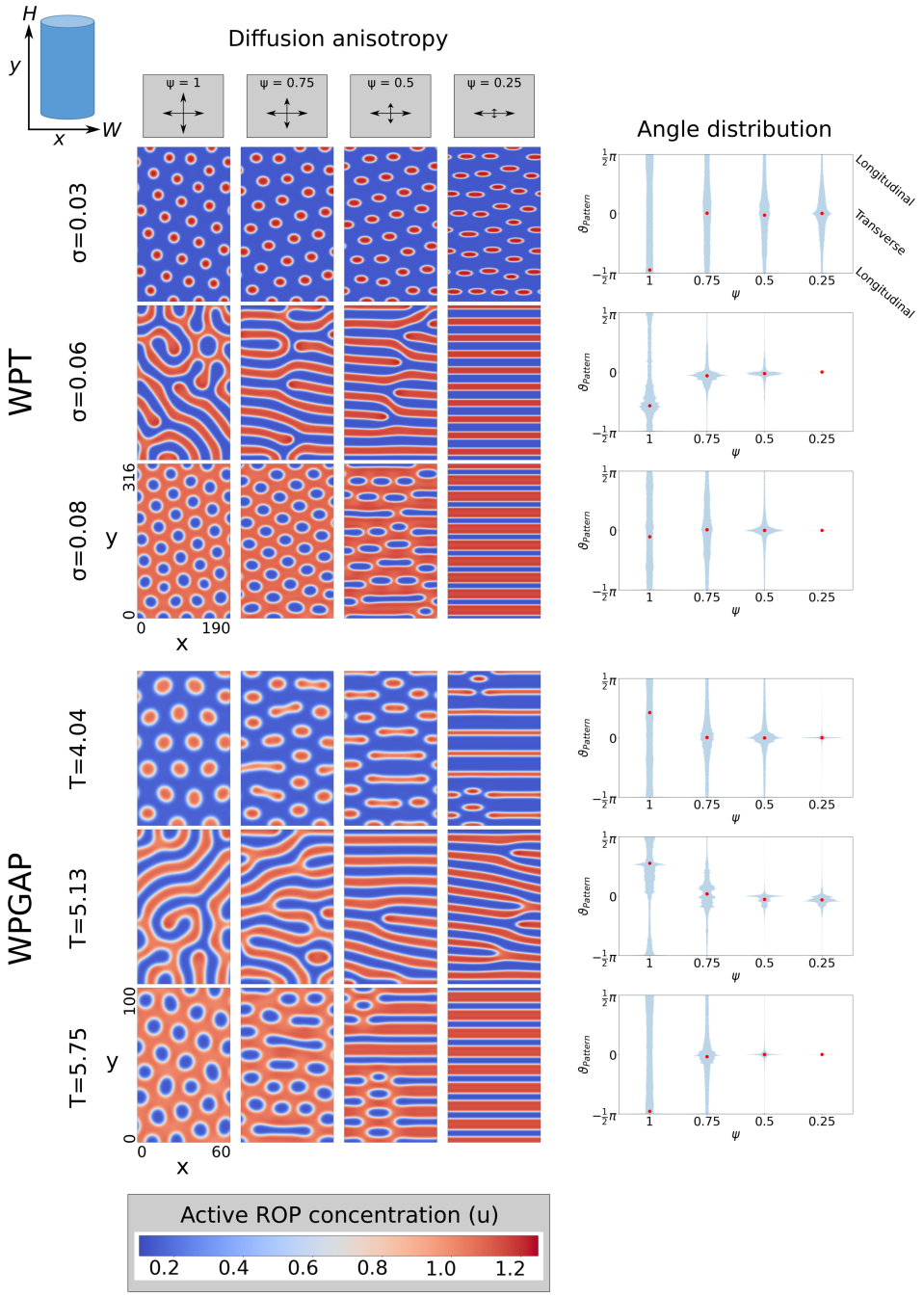

Fig. 3.2. Caption on next page.

Fig. 3.2. Vertical diffusion restriction of active ROP imposes a horizontal orientation on the pattern. Left: Steady state active ROP concentrations in regimes for spots, stripes, and gaps of the WPT model (top, $\sigma = 0.03, 0.06$, and 0.08 respectively) and the WPGAP model (bottom, $T = 4.04, 5.13$, and 5.75 respectively) for different levels of vertical diffusion restriction (ψ). WPT snapshots taken at $t = 200000$ and WPGAP snapshots at $t = 40000$. Right: Distributions of the pattern angles $\vartheta_{Pattern}$ (defined as orientation perpendicular to the local gradient) in the snapshots shown. Red circles indicate the average orientation. Time-lapse videos of the corresponding simulations are available online.

suggests that a horizontal pattern can also be obtained by horizontal diffusion restriction of the fast-diffusing component only, which has previously been demonstrated in a study comparing several other reaction-diffusion systems [209]. However, in the case of protoxylem patterning, the latter scenario is not supported by the available biological evidence and, therefore, not further investigated here.

Since both WPT and WPGAP models behave very similarly, we will continue our analyses with the WPT model only.

3.3.2 Oblique diffusion restriction promotes spiral formation

In reality, the initial microtubule array, and therefore the direction in which active ROP diffusion is restricted, does not have to be completely transverse, but may be somewhat oblique. We define $\phi \in [0, \pi)$ as the angle of minimal diffusion restriction with the horizontal axis. This rotates the diffusion tensor resulting in the following diffusion term for active ROP (see Appendix 3.7.4 for derivation):

$$\begin{aligned} \nabla \cdot D_u \nabla u &= D_u^{xx} \frac{\partial^2 u}{\partial x^2} + D_u^{yy} \frac{\partial^2 u}{\partial y^2} + 2 D_u^{xy} \frac{\partial^2 u}{\partial x \partial y} \\ D_u^{xx} &= \cos^2(\phi) + \psi \sin^2(\phi) \\ D_u^{yy} &= \sin^2(\phi) + \psi \cos^2(\phi) \\ D_u^{xy} &= \sin(\phi)\cos(\phi) - \psi \sin(\phi)\cos(\phi), \end{aligned} \tag{3.6}$$

where ψ is again the ratio between the diffusion coefficients of active ROP in the restricted and unrestricted direction.

Such oblique diffusion restriction promotes formation of spirals (Fig. 3.3, Fig. S3.1, where sloping lines are connected by the periodic boundary conditions in the horizontal direction). With increasing ϕ, double, triple, etc. spirals may form. The resulting angle of the spiral pattern ϑ depends on several factors. While the pattern angle depends strongly on the angle ϕ of diffusion restriction, particularly in early stages, it is also influenced by the boundary conditions. The periodic boundaries dictate a discrete set of preferred angles that allow connecting spirals without changing the distance between bands (Appendix 3.7.5). In addition, the zero flux boundaries at the top and bottom of the domain demand that the local gradient there is perpendicular to the boundary. Consequently, spiral angles become slightly steeper than expected based on diffusion angle ϕ and the periodic boundaries alone.

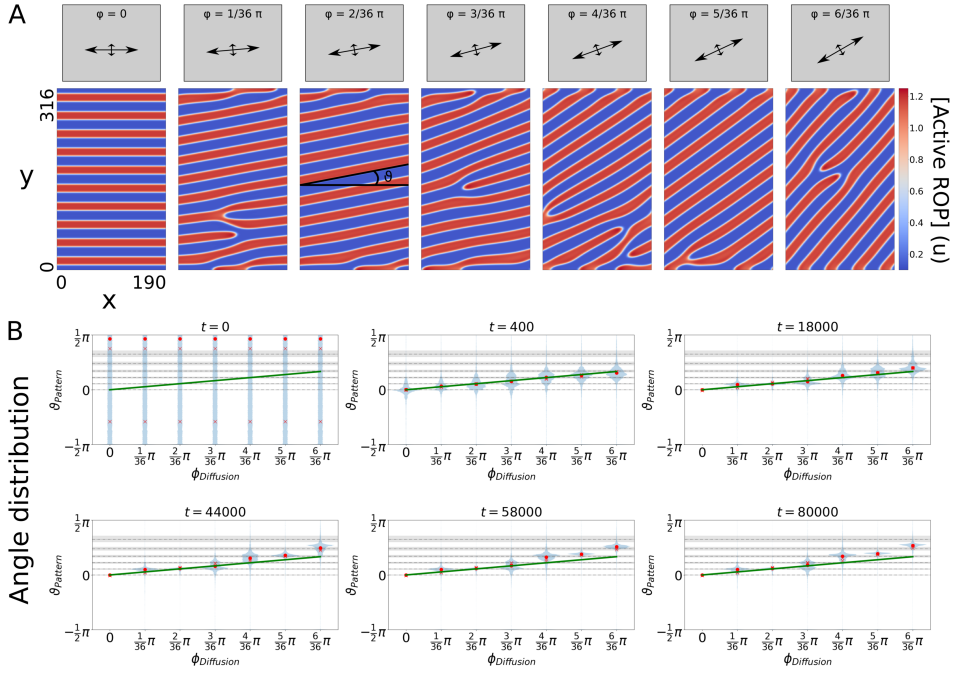

Fig. 3.3. Oblique diffusion restriction of active ROP results in spirals with angles ϑ depending on the diffusion angle ϕ. (A) Active ROP concentrations at $t = 80000$ (close to steady state) in the stripe regime of the unrestricted WPT model ($\sigma = 0.06$) for $\psi = 0.25$. (B) Distributions of the pattern angles (defined as orientation perpendicular to the gradient) are shown for various time points. Circles indicate the average orientation, crosses indicate average orientations for replicate runs with different initial conditions (for most time points crosses are invisible due to overlap with circles), solid green lines indicate the angle of maximum diffusion ϕ, dashed lines indicate estimated angles for spiral patterns with band-band distances as in the banded patterns of Fig. 3.2, and shaded regions indicate uncertainty on those estimates due to boundary effects. Time-lapse videos of the corresponding simulations are available online.

3.3.3 Orientation mechanism and reorientability

We have seen that the restriction of active ROP diffusion in one direction promotes the formation of bands oriented perpendicular to that direction. Here, we propose a mechanism for this orientation process and investigate the implications of this mechanism on the reorientability of the pattern. Expansion of existing clusters of high ROP activity can occur when diffusion of active ROP results in ROP activation in neighbouring regions through positive feedback. Conversely, clusters of low ROP activity may expand if diffusion of active ROP from neighbouring regions lowers their activity levels such that they escape positive feedback. This suggests that the speed of expansion is related to the active ROP diffusion coefficient, so that faster diffusion in a certain direction results in faster expansion in that direction. One may hypothesise that this could lead to a change in the orientation of the pattern. From a geometrical consideration (sketched in Fig. 3.4A), however, it is to be expected that faster expansion in one direction can only change the orientation of curves, but not of straight lines.

A decomposition of the diffusion tensor in components along and orthogonal to the

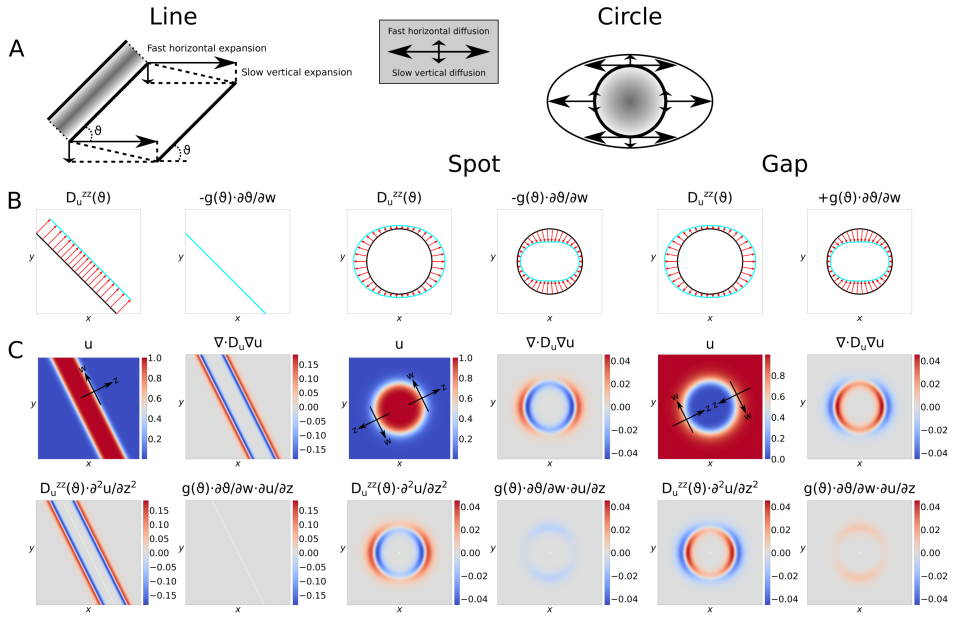

Fig. 3.4. Comparison of vertical diffusion restriction effects on pattern expansion for a straight band (left) and a circular spot or gap (right). (A) Cartoon showing intuitive effect of fast horizontal expansion and slow vertical expansion. (B) Magnitude of geometry-dependent diffusion term components. Black lines indicate the local pattern geometry. Positive magnitudes are indicated by outward pointing arrows. Blue lines trace the ends of all red lines that can be drawn on the black curves. The length of the red lines reflects the magnitude of the indicated component. Since $\partial u/\partial z$ is always negative and $g(\vartheta)$ is always positive, $\partial\vartheta/\partial w$ determines the sign of the second term from Eq. 3.7. To emphasise the equal magnitude but opposite effect $g(\vartheta)\cdot\partial\vartheta/\partial w$ has for spots and gaps, opposite signs of this term have been plotted for these two cases. (C) Magnitudes of diffusion components for stereotypical concentration profiles. Shown are: the concentration profile (u) with examples of axes z and w, the diffusion term corresponding to that profile ($\nabla\cdot D_u\nabla u$), and the two separate terms of the decomposed diffusion term ($D_u^{zz}(\vartheta)\cdot\partial^2u/\partial z^2$ and $g(\vartheta)\cdot\partial\vartheta/\partial w\cdot\partial u/\partial z$).

pattern gradient shows that indeed only spots and richly curved patterns can be reoriented by this mechanism, but not straight lines or bands. For this decomposition, we define directions z and w, such that z is oriented along the concentration gradient in descending direction and w is perpendicular to z (Fig. 3.4C). Then we can rewrite the diffusion term from Eq. 3.5 in terms of z, w, and the local pattern angle ϑ, defined as the angle between the positive x-axis and the w-direction (see Appendix 3.7.6):

$$\begin{aligned}\nabla\cdot D_u\nabla u &= D_u^{zz}(\vartheta)\frac{\partial^2 u}{\partial z^2}+g(\vartheta)\frac{\partial\vartheta}{\partial w}\frac{\partial u}{\partial z}\\ D_u^{zz}(\vartheta) &= \sin^2(\vartheta)+\psi\cos^2(\vartheta)\\ g(\vartheta) &= \cos^2(\vartheta)+\psi\sin^2(\vartheta).\end{aligned}\tag{3.7}$$

In this case, $\vartheta\in[-\pi,\pi)$. The first term resembles a standard diffusion term in the z-direction. Its diffusion coefficient D_u^{zz} depends on ϑ and is therefore constant along straight lines, but larger in the unrestricted than in the restricted direction for circular patterns (Fig. 3.4B). The second term depends on the pattern curvature $\partial\vartheta/\partial w$, which

is positive for convex clusters, such as spots, and negative for concave clusters, such as gaps and zero for straight lines (Fig. 3.4B). Because function $g(\vartheta)$ is always positive, and $\partial u/\partial z$ is always negative, the second term always represents a removal of active ROP for spots and an addition for gaps. Since $g(\vartheta)$ is largest in the restricted direction, the second term tends to promote the flattening of circular patterns.

As an illustration, we calculated the magnitude of the complete diffusion terms for some stereotypical patterns generated by the hill function:

$$u = \frac{1}{1+(r/5)^{10}}, \tag{3.8}$$

where we used $r = 2x+y$ for a line and $r = \sqrt{x^2+y^2}$ for a circle. To turn the circle from a spot into a gap we used $u_{gap} = 1-u_{spot}$. The results show that expansion of straight line patterns is dependent solely on diffusion down the gradient, which is the same everywhere along the line (Fig. 3.4C). Only curved patterns can expand in other ways, allowing their net orientation to change.

These results imply that completely non-curved patterns cannot be reoriented even if the orientation of the diffusion restriction changes, while patterns that contain curves remain open to reorientation. Simulations in which the direction of diffusion restriction is altered after straight bands have been formed confirm this (Fig. 3.5). Even when the native pattern consists of gaps rather than stripes, a banded pattern was maintained upon returning to isotropic diffusion (Fig. S3.2).

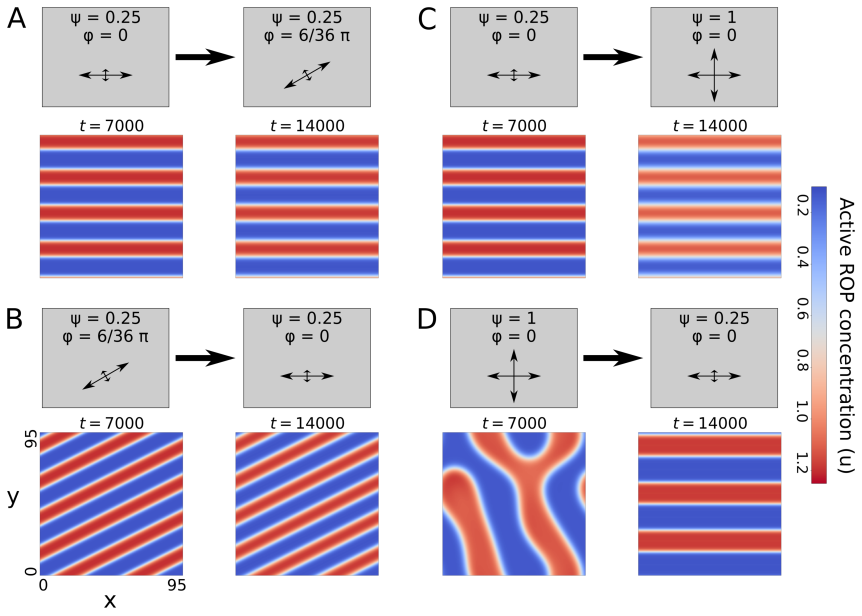

Fig. 3.5. Effect of altering diffusion restriction for established patterns of the WPT model in the stripe regime ($\sigma = 0.06$). (A) Oblique diffusion restriction on horizontal bands. (B) Horizontal diffusion restriction on oblique bands. (C) Isotropic diffusion with horizontal bands. (D) Horizontal diffusion restriction on a pattern resulting from isotropic diffusion. Time-lapse videos of the corresponding simulations are available online.

We next investigated which kind of perturbations at the pattern level could reorient a banded pattern to better match the orientation imposed by diffusion restriction. Fully formed horizontal bands were locally stable to small amounts of spatial noise after rotating the diffusion restriction angle (Fig. 3.6A). Furthermore, they were also stable to moderate local vertical shifts (Fig. 3.6B-C), but larger shifts could trigger reorientation in the direction imposed by diffusion restriction (Fig. 3.6D). This reorientation is not simply an artefact of the severe deformation, since the pattern returned to the horizontal band state after applying the same deformation under vertical diffusion restriction (Fig. 3.6E).

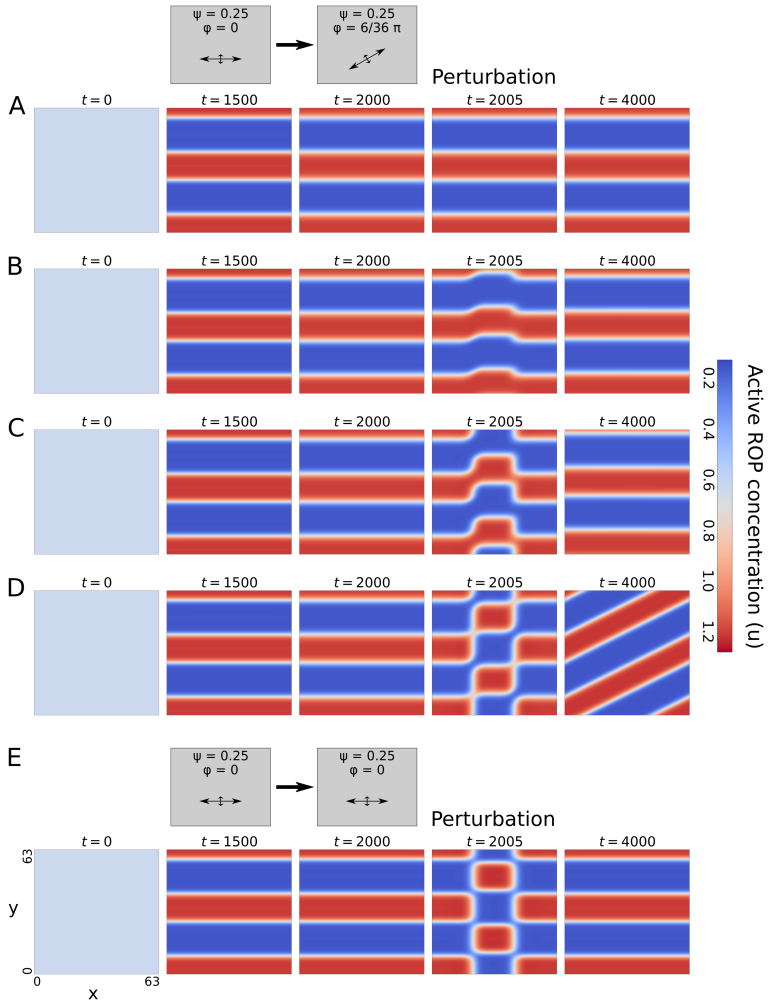

Fig. 3.6. Effect of random noise and local vertical shifts on the reorientation of a horizontal band pattern with oblique diffusion restriction. A. Small random noise added every 10 time units starting from $t = 2000$. B. Small vertical shift of the central part of the pattern after $t = 2000$. C. Like B, but with a larger shift. D. Like C, but with a larger shift. E. Like D, but with vertical diffusion restriction throughout the simulation. Time-lapse videos of the corresponding simulations are available online.

These findings all suggest that diffusion restriction can impose an orientation only on patterns with curves. Since patterns start out fairly rugged from a noisy initial condition, the early stages of pattern formation are expected to be particularly susceptible to reorientation. Indeed, the preferred orientation can already be seen very early during *de novo* pattern formation (Fig. S3.3). However, fully formed patterns with sufficient curvature can also still be reoriented (Fig. 3.5D).

3.3.4 ROP-dependent ROP diffusion

Initially, the microtubule array may form an approximately homogeneous barrier to the vertical diffusion of active ROP. Ultimately, however, ROP activity is presumed to result in gaps in the microtubule array (see Fig. 3.1A), which, in turn, determines the final cell wall pattern (through recruitment of downstream targets). This also means that the diffusion restriction will decrease in these gaps. To study this effect, we made the ratio ψ between unrestricted and restricted active ROP diffusion coefficients a function of active ROP concentration u, such that:

$$\nabla \cdot D_u \nabla u = \frac{\partial^2 u}{\partial x^2} + \frac{\partial}{\partial y}\psi(u)\frac{\partial u}{\partial y}. \tag{3.9}$$

To start, we assumed a linear relation between ψ and the dimensionless microtubule density ρ (Fig. 3.7A):

$$\psi(u) = \psi(\rho(u)) = 1 - (1 - \psi_{min})\rho(u) \quad \rho(u) \in [0,1], \tag{3.10}$$

where ψ_{min} is the ratio between the maximally restricted and unrestricted active ROP diffusion components and the maximum of ρ is reached in absence of ROP activity. We take active ROP to reduce microtubule density instantaneously via a hill function:

$$\rho(u) = \frac{K_\rho^{n_\rho}}{K_\rho^{n_\rho} + u^{n_\rho}}, \tag{3.11}$$

where K_ρ is the active ROP concentration at which microtubule density is halved and n_ρ is the hill exponent (see Appendix 3.7.7 for parameter choices). Combining Eq. 3.10 and 3.11 yields a hill function for the relation between active ROP diffusion and active ROP concentration:

$$\psi(u) = 1 - (1 - \psi_{min})\frac{K_\rho^{n_\rho}}{K_\rho^{n_\rho} + u^{n_\rho}}. \tag{3.12}$$

Our simulations using these relations for an instantaneous effect of ROP on its own diffusion generally resulted in poorer horizontal band formation (Fig. 3.7B, Fig. S3.4B). Some simulations got closer to horizontal bands than others, but we could no longer find a broad parameter regime that consistently yielded proper band formation, suggesting that the robustness of the orientation mechanism was greatly reduced.

3.3.5 Delayed microtubule density reduction

We saw earlier that developing patterns are particularly susceptible to reorientation, while fully formed banded patterns can be quite resistant to it. These results suggest that a more

or less homogeneous diffusion restriction may only be necessary during the development of the ROP pattern, allowing patterning of the microtubule array afterwards, without in-

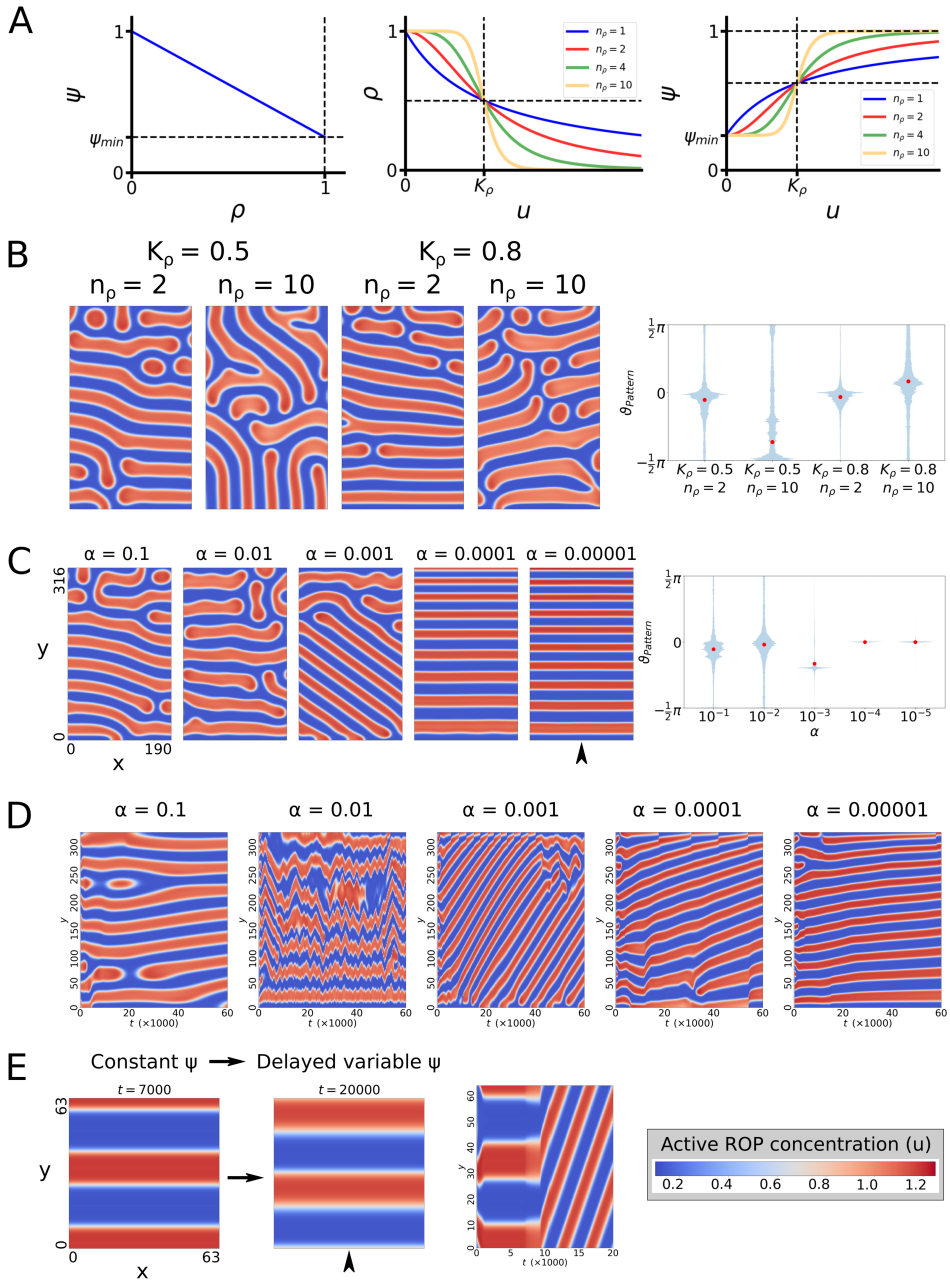

Fig. 3.7. Caption on next page.

Fig. 3.7. Effect of ROP-dependent microtubule density reductions on the formation of banded patterns in the stripe regime ($\sigma = 0.06$). (A) Relations between vertical diffusion component, (steady state) microtubule density, and active ROP concentration. (B) An instantaneous effect of ROP activity on microtubule density greatly hampers the robustness of the orientation mechanism. Snapshots at $t = 60000$. (C) Greater delays in the negative effect of active ROP on its own vertical diffusion restriction (smaller α) result in straighter band formation. Snapshots at $t = 60000$. (D) Time evolution of concentrations from simulations shown in (C) at the horizontal position indicated by the arrowhead. Travelling waves (recognisable by diagonal lines) occur for larger delays (smaller α), with wave speeds reducing as the delay becomes larger. (E) Travelling waves occur even when a static banded pattern is created first with a constant ψ and delayed density reduction (delayed variable ψ) is initiated afterwards (at $t = 7000$, using $\alpha = 0.001$). Time evolution graph shows concentrations at the horizontal position of the arrowhead. Time-lapse videos of the corresponding simulations are available online.

fluencing the ROP pattern. Therefore, we investigated the effect of a delayed response of the microtubule density to ROP activity. Taking a first order approximation for the rate of change towards steady state density ρ^*, we get:

$$\begin{aligned} \frac{d\rho}{dt} &= \alpha(\rho^* - \rho) \\ \rho^* &= \frac{K_\rho^{n_\rho}}{K_\rho^{n_\rho} + u^{n_\rho}}, \end{aligned} \tag{3.13}$$

where α is a rate constant. This means that the diffusion ratio ψ will approach its steady state ψ^* according to:

$$\begin{aligned} \frac{d\psi}{dt} &= \alpha(\psi^* - \psi) \\ \psi^* &= 1 - (1 - \psi_{min})\frac{K_\rho^{n_\rho}}{K_\rho^{n_\rho} + u^{n_\rho}}. \end{aligned} \tag{3.14}$$

Simulations with a homogeneous starting density of $\rho = 1$ (the maximum, so $\psi = \psi_{min}$) and small delays ($\alpha = 0.1$) yielded patterns comparable to those of the no delay scenario (Fig. 3.7C, Fig. S3.4C). Larger delays did result in straighter bands, but these bands were constantly moving, either up and down, or in one direction like a travelling wave (Fig. 3.7D, Fig. S3.4D). These waves occurred even when starting from a fully formed static banded pattern (Fig. 3.7E, Fig. S3.4E). Such non-static patterns are unrealistic as a basis of cell wall pattern formation.

3.3.6 Positive feedback in microtubule density can prevent travelling waves, stabilising a banded pattern

Thus far, we assumed microtubule density to be merely a reflection of ROP activity, possibly with a delay. However, microtubules have their own complex dynamics that may well have a stabilising influence on the patterning process. Therefore, we will consider a potential positive feedback loop acting on the microtubule density. Microtubule growth occurs only at the tips of existing microtubules. In addition, nucleation of new microtubules occurs predominantly from existing microtubules, with predominantly congruent orientation [107, 109, 160]. Therefore, we can expect stronger increases in microtubule density

at places with higher existing density. The resulting positive feedback loop between microtubule density and microtubule nucleation might serve to stabilise local regions of high microtubule density, thereby preventing travelling wave patterns.

To test this idea, we model this positive feedback with a hill function and let ROP activity promote microtubule degradation, so that dimensionless microtubule density ρ obeys the equation:

$$\frac{\partial \rho}{\partial t} = \alpha \left(\gamma_\rho \frac{\rho^{n_\rho}}{1+\rho^{n_\rho}} + \sigma_\rho - \xi_\rho \rho - \zeta u \rho + D_\rho \nabla^2 \rho \right), \tag{3.15}$$

where γ_ρ is the maximum microtubule-dependent growth rate, n_ρ is the hill exponent, σ_ρ is a constant background increase in microtubule density by nucleation and growth, ξ_ρ is a constant linear degradation rate, and ζ is a ROP-dependent degradation rate. Here, ρ is scaled with the density at which positive feedback is half its maximum. In addition, we include a diffusion term with coefficient D_ρ to maintain a connection between neighbouring integration pixels and prevent artefacts. We take $D_\rho \ll 1$ to keep microtubule "diffusion" well below unrestricted active ROP diffusion. Although microtubules don't really diffuse in their entirety, they tend to spread through growth and nucleation. These processes also favour the existing orientation [109], which could further promote stable bands. Here, we assume isotropic diffusion as a worst case scenario. Finally, we use α as a tuning parameter for the time scale of the microtubule dynamics relative to the ROP dynamics.

The steady state of the homogeneous system is determined by:

$$\begin{aligned} h(\rho) &= q(\rho,u), \quad \text{with} \\ h(\rho) &= \gamma_\rho \frac{\rho^{n_\rho}}{1+\rho^{n_\rho}} + \sigma_\rho \\ q(\rho,u) &= \xi_\rho \rho + \zeta u \rho, \end{aligned} \tag{3.16}$$

which allows for bistability as long as $n_\rho > 1$ (Fig. 3.8A). In that case, the steady state microtubule density may switch from low to high or the other way around as ROP activity changes.

We use a hill function for ψ to ensure that vertical diffusion is close to its maximum ($\psi = 1$) for low densities, and close to its minimum ($\psi = \psi_{min}$) for high densities (Fig. 3.8A):

$$\psi = (1-\psi_{min}) \frac{K_D^{n_D}}{\rho^{n_D} + K_D^{n_D}} + \psi_{min}, \tag{3.17}$$

where K_D is the density at which vertical diffusion is halfway between its minimum and its maximum and n_D is a hill exponent.

Even when starting from a banded pattern, the positive feedback model without bistability ($n_\rho = 1$) at moderate delay ($\alpha = 0.001$) yielded travelling waves (Fig. 3.8B), just like we observed for a direct ROP-dependency with a simple delay. However, when we included bistability ($n_\rho = 2$), the banded pattern remained static.

However, when simulating *de novo* patterning of a large domain we still observed non-static patterns at $\alpha = 0.001$, even with bistability (Fig. 3.8C–D). For large delays ($\alpha = 0.00001$), a banded ROP pattern had sufficient time to develop before significant changes

in microtubule density occurred and the banded pattern remained stable. Interestingly, a stable banded pattern seems to form more readily in the gap regime ($\sigma = 0.08$) than in the stripe regime ($\sigma = 0.06$). We also found some static banded patterns, particularly

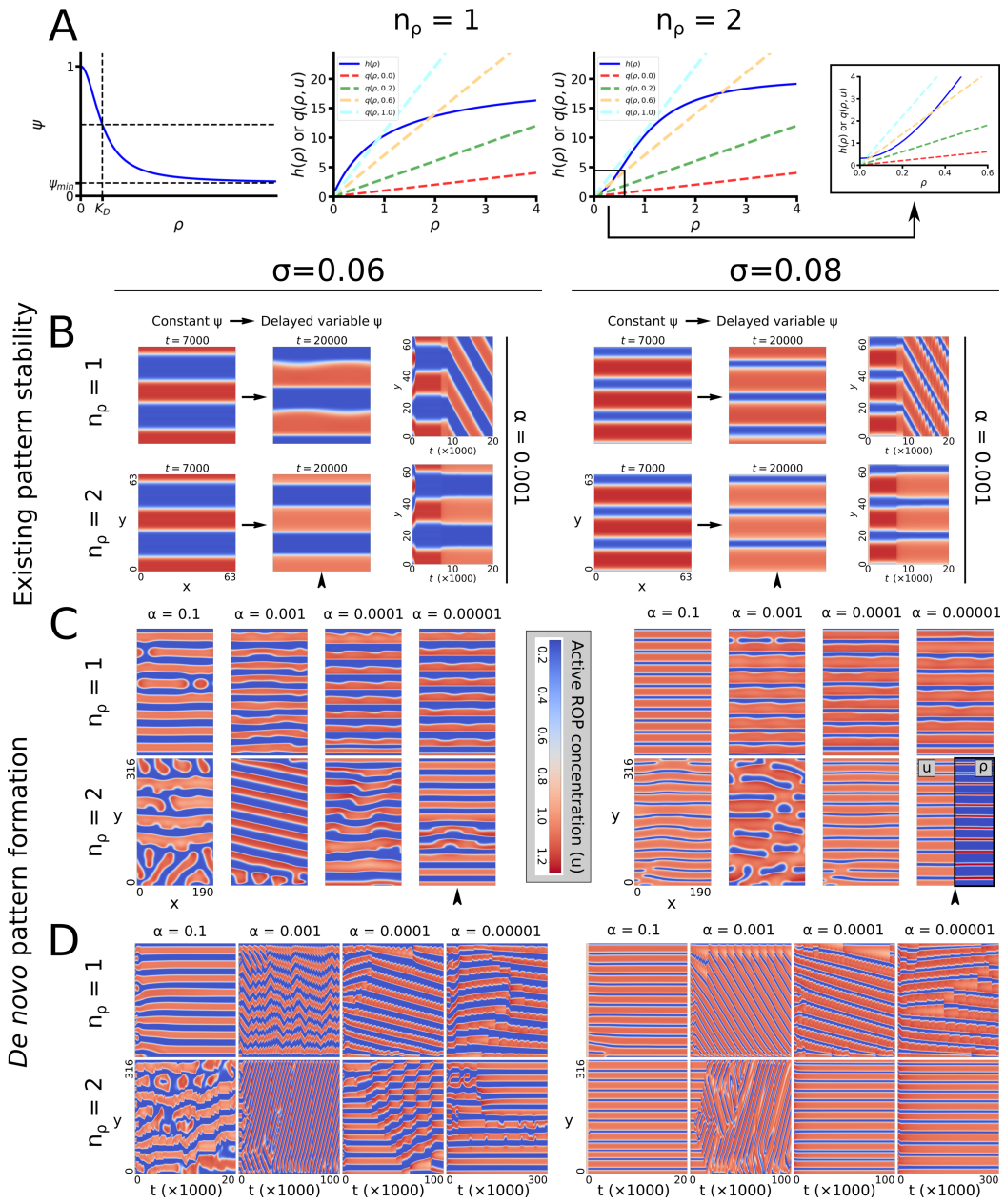

Fig. 3.8. Caption on next page.

Fig. 3.8. Positive feedback in microtubule density can prevent bands from moving vertically. All simulations were performed in both the stripe ($\sigma = 0.06$) and the gap ($\sigma = 0.08$) regime of the WPT model. (A) Left: Relation between microtubule density (ρ) and vertical diffusion of active ROP. Right: Values of hill function and linear components of the microtubule density equation for various values of u. Intersections indicate steady states. Bistability can occur only for $n_\rho > 1$. (B) Stability of a banded pattern established with a constant microtubule density until $t = 7000$ for unistable ($n_\rho = 1$) and bistable ($n_\rho = 2$) microtubule dynamics. In all cases, $\alpha = 0.001$ and fully periodic boundary conditions were used. Graphs to the right show time evolution of concentrations at the horizontal position of the arrowhead. (C) Full *de novo* patterning with positive feedback of microtubule density starting from the homogeneous state for ROP concentrations and $\rho_0 = 2$. Snapshots were taken at the final time points indicated in (D). Inset in bottom right snapshot shows microtubule densities (ρ) for comparison. (D) Time evolution of simulations from (C) at the horizontal position indicated by the arrowhead. Time-lapse videos of the corresponding simulations are available online. Corresponding microtubule densities (ρ) for the entire figure are shown in Fig. S3.5.

in the gap regime, for small delays ($\alpha = 0.1$) that were apparently insufficient to trigger travelling waves.

For the static patterns, microtubule density is essentially a readout of ROP activity (Fig. 3.8C, inset). For the moving patterns, especially in the bistable case, the delay causes the microtubule density to lag behind the ROP pattern and never fully reach its high steady state (Fig. S3.5), as the pattern has already moved on before it got the chance. This may also explain the stuttering of the moving patterns in the bistable case for ROPs and microtubules.

These results show that the precise implementation of microtubule dynamics and the interactions between ROPs and microtubules matters and inclusion of more realistic biological details seems to result in more stable banded patterns.

3.4 Discussion

3.4.1 Directional diffusion restriction can orient ROP patterns into bands and spirals

We have shown that restricting active ROP diffusion in a specific direction is sufficient to change the output from a ROP-based Turing-style pattern formation mechanism from patterns without specific orientation into banded or spiral patterns with controlled orientation. Given sufficiently large diffusion restriction, bands and spirals can be generated, regardless of whether the native pattern would consist of spots, stripes, or gaps. The parameters that normally distinguish between these regimes then control only the thickness of the bands. This means that the relatively thick active ROP bands that would be needed to generate the relatively thin microtubule bands observed in protoxylem patterning [122] may actually originate from a Turing mechanism that would generate gaps without diffusion restriction. Additionally, the finding that diffusion restriction can essentially turn spot, stripe, and gap regimes into one large band regime may imply an increased robustness of the protoxylem pattern to changes in ROP activity. By comparison, the spotted metaxylem pattern would more easily be disrupted.

At intermediate levels of diffusion restriction, spots, stripes, and gaps can still be distinguished, but they are flattened horizontally. This finding is in line with the experimental observation that higher expression of a protein responsible for a stronger microtubule

barrier effect results in more flattened pits in metaxylem [154]. Therefore, protoxylem patterning may be very similar to metaxylem patterning, with a stronger diffusion barrier effect to obtain a banded pattern and a higher ROP expression to obtain thicker ROP bands. In addition, our finding that the angle of diffusion restriction largely determines the angle of *de novo* banded pattern formation, predicts that the initial orientation of the microtubule array before apparent band formation determines the final orientation of the banded array.

While the precise molecular players and interactions involved in protoxylem patterning remain largely unknown, ROP involvement has been implicated [150]. In addition, we show that different ROP-based Turing mechanisms have a very similar response to a directional reduction in activator diffusion. Therefore, the proposed orientation mechanism seems sufficiently general to apply to different reaction-diffusion systems able to generate coexisting spots, stripes, and gaps, of which many variants exist [32, 49, 163]. However, it is important that diffusion restriction applies predominantly to the active form, because diffusion restriction of all components in the same way will not yield banded patterns with controlled orientation (Appendix 3.7.2). The inactive form must therefore be able to bypass the microtubule barriers. This requirement is naturally fulfilled by the predominantly cytosolic localisation of the inactive form.

3.4.2 Fully formed banded patterns are relatively robust structures compared to more curved patterns

While anisotropic diffusion has long been known to affect the shape of patterns generated by reaction-diffusion systems [206, 207], we not only demonstrated its potential for generating bands and spirals, but also investigated the underlying orientation mechanism. Our decomposition analysis of the diffusion term suggests that if ROP cluster expansion is related to diffusion of the active form, any curved structures tend to expand more in the direction in which diffusion is unrestricted. However, straight patterns cannot be reoriented in this way, making fully formed bands and spirals insensitive to any subsequent changes in the direction of diffusion restriction, even in the presence of moderate spatial perturbations.

This robustness of straight patterns has several benefits for the biological system. Firstly, in order to create the actual cell wall pattern, the underlying ROP and microtubule patterns will need to remain approximately stationary for the duration of secondary cell wall synthesis, which may take many hours [122], so the ROP pattern should be robust to any perturbations that may occur in this time frame. Secondly, due to the difficulty of reorienting a pattern of oblique bands, it seems important that the reorientation of the microtubule array to a transverse state occurs before the start of ROP patterning. Experimental observations suggest that this reorientation at least occurs before visible band formation in the microtubule array [159]. In addition, aberrant protoxylem patterns have been observed in the Katanin mutant, where proper microtubule alignment prior to band formation is hindered [211]. Finally, once a transverse microtubule array has contributed to the generation of a banded ROP pattern, the robustness of the banded pattern allows microtubules to disappear in areas of high ROP activity without disrupting the ROP pattern.

3.4.3 Static band formation depends on the precise implementation of microtubule dynamics.

Our findings show that an instantaneous or very fast response of microtubule density to ROP activity can be disruptive to proper band formation. A sufficiently slow microtubule response, however, gives a robust banded pattern time to form before the diffusion restriction is undone. However, this dynamic also results in a kind of delayed negative feedback, which is known for its potential to generate oscillations [191] and travelling waves [183, 212] in models. With more realistic microtubule dynamics, we were able to stabilise the banded pattern again. The required difference in time scales of ROP protein and microtubule density dynamics (approximately a factor α) does, however, seem quite large, particularly where the native pattern would consist of stripes. Partly, a large difference may actually be realistic, since changes in microtubule density during protoxylem patterning can take hours [122], whereas GTPase inactivation and removal from the membrane occurs in the order of seconds [213, 214]. Also, since the microtubule bands formed in protoxylem patterning are relatively thin [122], the underlying ROP pattern must have relatively thick bands, like those from the gap regime, in which generation of static bands occurred already with smaller delays.

Other biological factors not included here may also help stabilise a banded pattern, potentially reducing the required difference in time scales. Firstly, ROP pattern formation may already start before the ROP effectors that interact with microtubules become active, allowing the ROP pattern time to establish without ROP activity having any impact on microtubule density. Transcriptomic data seem to suggest that, in metaxylem, expression of effectors like MIDD1 and Kinesin-13A peaks later than that of ROP11, although the temporal resolution is not very good [215]. Secondly, microtubules are not simply slowly diffusing molecules, but discrete linear structures with complex dynamics and membrane attachment preventing translational movement. Their rigid and linear nature may well contribute to the formation of robust linear bands. Furthermore, microtubule-dependent microtubule nucleation tends to favour the direction of the parent microtubule [109], so that any partial microtubule bands will tend to expand in the direction they already have. Finally, microtubule dynamics are governed largely by processes occurring at their growing or shrinking tips [99]. This suggests ROP activity cannot destabilise existing microtubules except at their ends. Such details of microtubule dynamics have no straightforward implementation in the present modelling paradigm, but detailed stochastic simulation models of the cortical microtubule array with explicit dynamic instability exist [103, 126, 133, 135, 136]. Building upon those, a hybrid model combining PDE integration for ROP dynamics with stochastic microtubule dynamics offers an exciting direction for future research on protoxylem patterning.

Acknowledgements

We thank Tijs Ketelaar for insightful discussions on the topic.

3.5 Supplementary figures

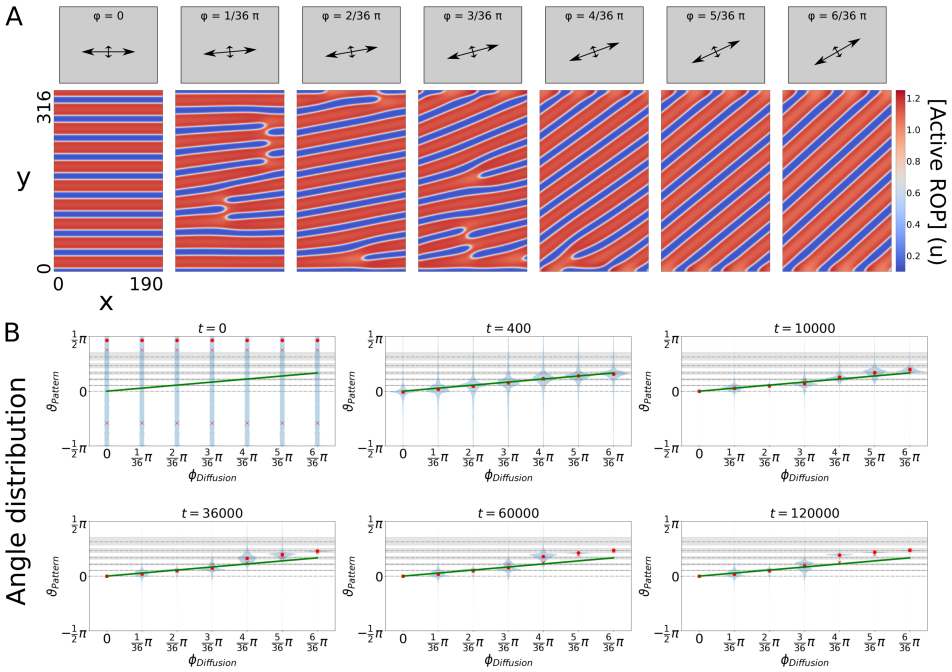

Fig. S3.1. Oblique diffusion restriction of active ROP results in spirals with angles ϑ depending on the diffusion angle ϕ. (A) Active ROP concentrations at $t = 120000$ (close to steady state) in the gap regime of the unrestricted WPT model ($\sigma = 0.08$) for $\psi = 0.25$. (B) Distributions of the pattern angles (defined as orientation perpendicular to the gradient) are shown for various time points. Circles indicate the average orientation, crosses indicate average orientations for replicate runs with different initial conditions (for most time points crosses are invisible due to overlap with circles), solid green lines indicate the angle of maximum diffusion ϕ, dashed lines indicate estimated angles for spiral patterns with band-band distances as in the banded patterns of Fig. 2, and shaded regions indicate uncertainty on those estimates due to boundary effects. Time-lapse videos of the corresponding simulations are available online.

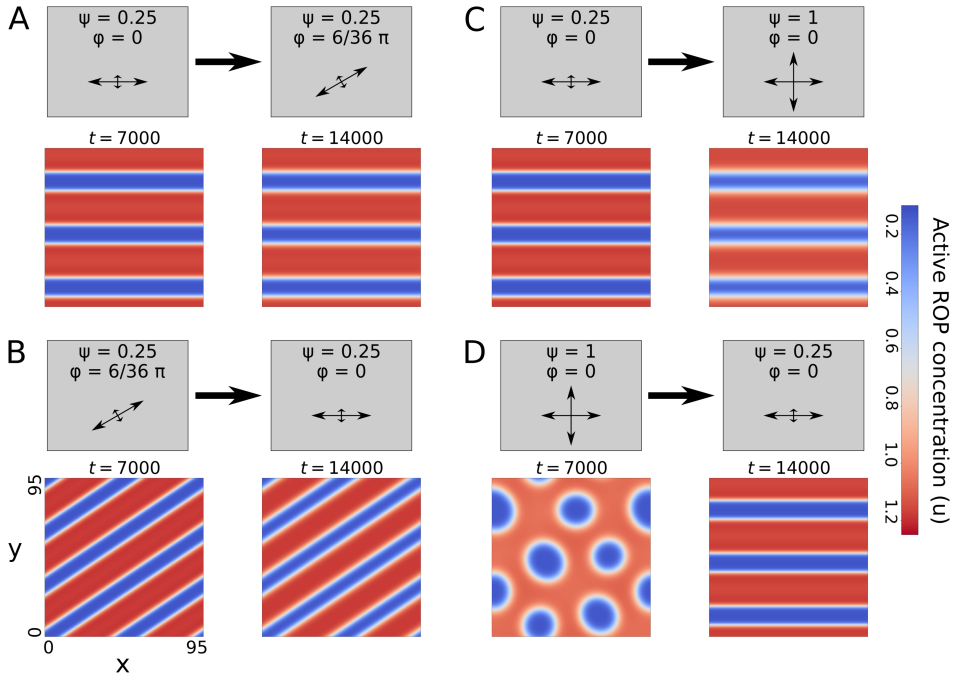

Fig. S3.2. Effect of altering diffusion restriction for established patterns of the WPT model in the gap regime ($\sigma = 0.08$). (A) Oblique diffusion restriction on horizontal bands. (B) Horizontal diffusion restriction on oblique bands. (C) Isotropic diffusion with horizontal bands. (D) Horizontal diffusion restriction on a pattern resulting from isotropic diffusion. Time-lapse videos of the corresponding simulations are available online.

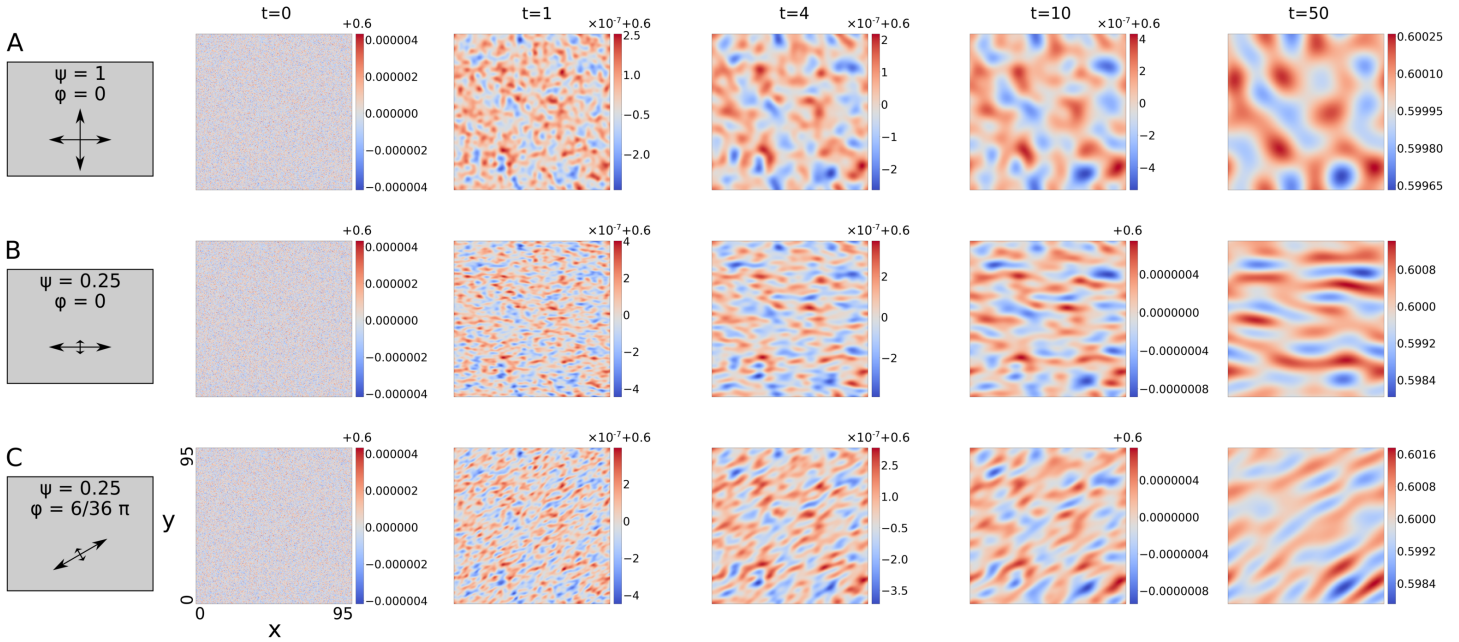

Fig. S3.3. Early stages of pattern formation with the WPT model ($\sigma = 0.06$). A. Isotropic diffusion. B. Horizontal diffusion restriction. C. Oblique diffusion restriction. Time-lapse videos of the corresponding simulations are available online.

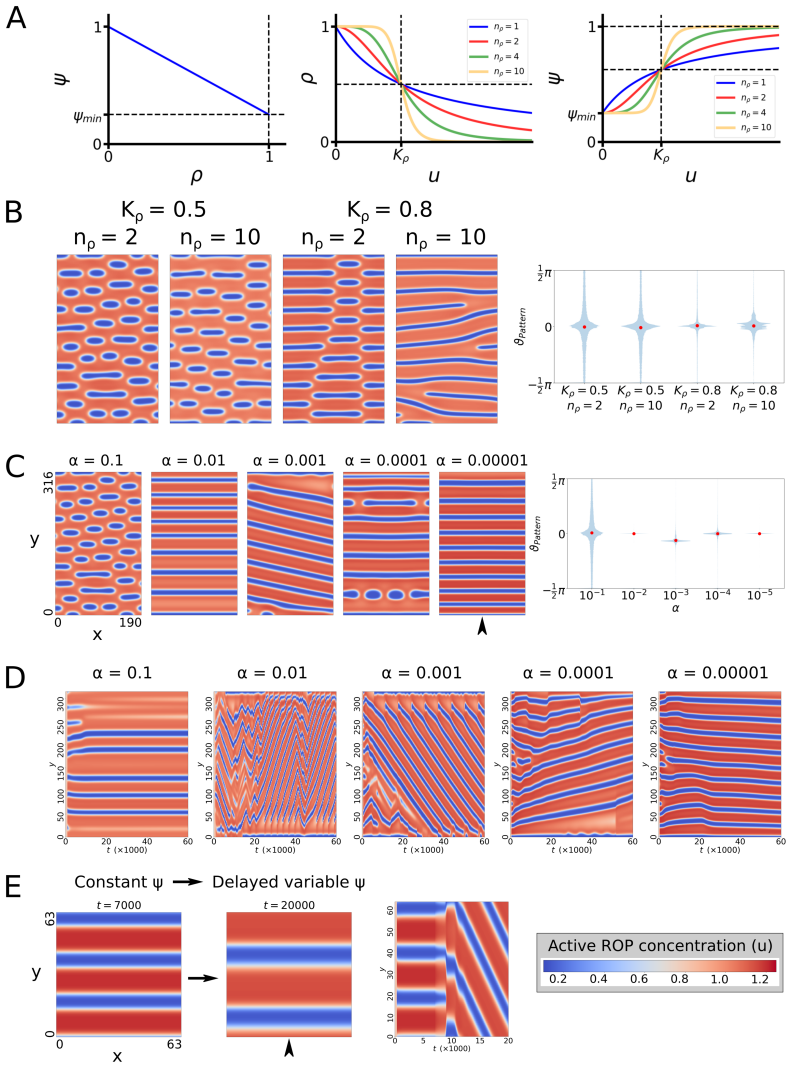

Fig. S3.4. Effect of ROP-dependent microtubule density reductions on the formation of banded patterns in the gap regime ($\sigma = 0.08$)**.** (A) Relations between vertical diffusion component, (steady state) microtubule density, and active ROP concentration. (B) An instantaneous effect of ROP activity on microtubule density greatly hampers the robustness of the orientation mechanism. Snapshots at $t = 30000$. (C) Greater delays in the negative effect of active ROP on its own vertical diffusion restriction (smaller α) result in straighter band formation. Snapshots at $t = 60000$. (D) Time evolution of concentrations from simulations shown in (C) at the horizontal position indicated by the arrowhead. Travelling waves (recognisable by diagonal lines) occur for larger delays (smaller α), with wave speeds reducing as the delay becomes larger. (E) Travelling waves occur even when a static banded pattern is created first with a constant ψ and delayed density reduction (delayed variable ψ) is initiated afterwards (at $t = 7000$, using $\alpha = 0.001$). Time evolution graph shows concentrations at the horizontal position of the arrowhead. Time-lapse videos of the corresponding simulations are available online.

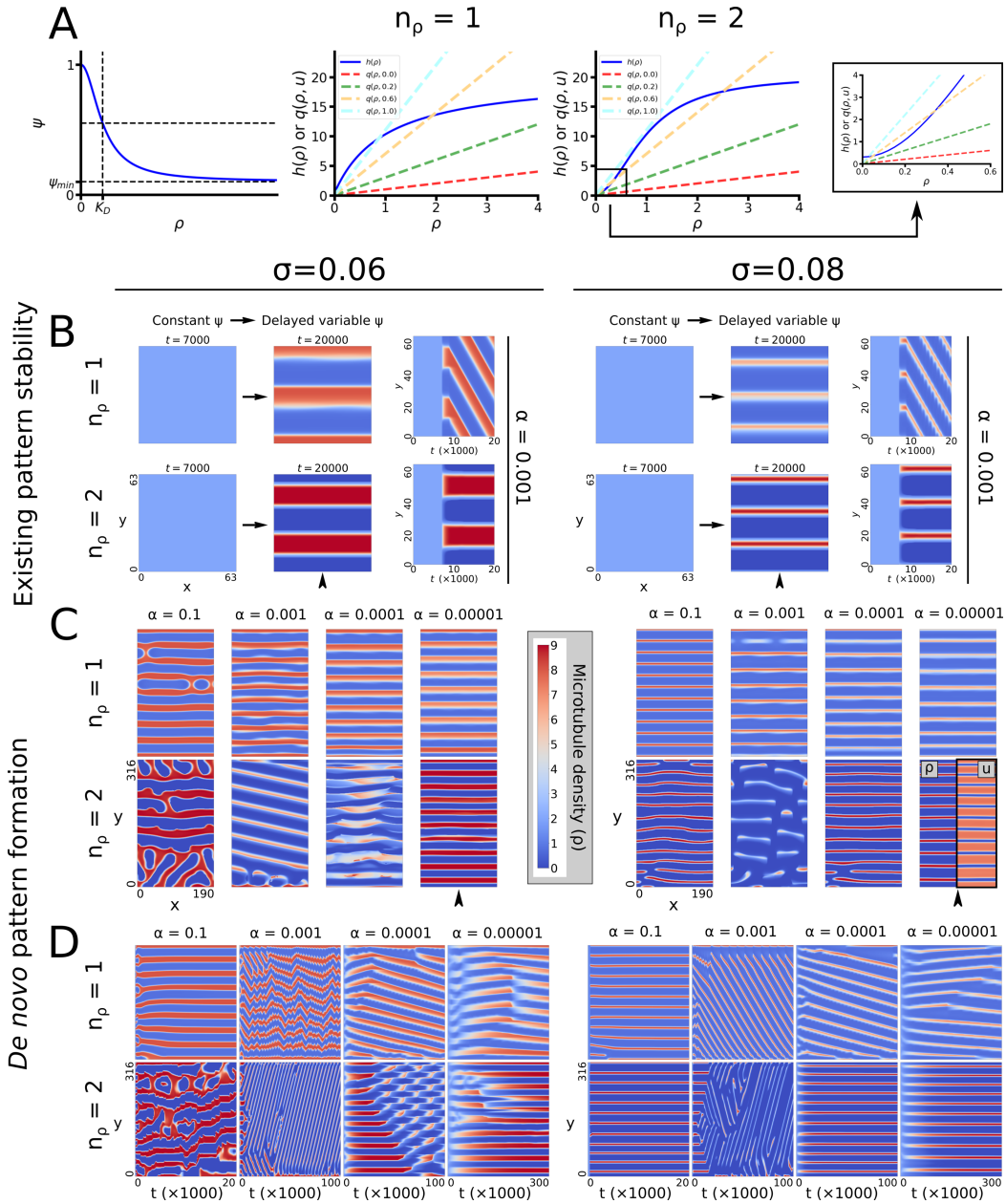

Fig. S3.5. Caption on next page.

Fig. S3.5. Positive feedback in microtubule density can prevent bands from moving vertically. All simulations were performed in both the stripe ($\sigma = 0.06$) and the gap ($\sigma = 0.08$) regime of the WPT model. (A) Left: Relation between microtubule density (ρ) and vertical diffusion of active ROP. Right: Values of hill function and linear components of the microtubule density equation for various values of u. Intersections indicate steady states. Bistability can occur only for $n_\rho > 1$. (B) Stability of a banded pattern established with a constant microtubule density until $t = 7000$ for unistable ($n_\rho = 1$) and bistable ($n_\rho = 2$) microtubule dynamics. In all cases, $\alpha = 0.001$ and fully periodic boundary conditions were used. Graphs to the right show time evolution of microtubule densities at the horizontal position of the arrowhead. (C) Full *de novo* patterning with positive feedback of microtubule density starting from the homogeneous state for ROP concentrations and $\rho_0 = 2$. Snapshots were taken at the final time points indicated in (D). Inset in bottom right snapshot shows active ROP concentrations (u) for comparison. (D) Time evolution of simulations from (C) at the horizontal position indicated by the arrowhead. Corresponding active ROP concentrations for the entire figure are shown in Fig. 8 in the main text.

3.6 Supplementary movies

Time-lapse videos of the simulations are available for download with the publication of this chapter [205] on the website of the Journal of Theoretical Biology.

3.7 Appendices

3.7.1 Discretisation of the diffusion equation for numerical integration

In general, a diffusion term has the following form:

$$\nabla \cdot D\nabla u = \frac{\partial}{\partial x} D^{xx} \frac{\partial u}{\partial x} + \frac{\partial}{\partial y} D^{yy} \frac{\partial u}{\partial y} + \frac{\partial u}{\partial x} D^{xy} \frac{\partial u}{\partial y} + \frac{\partial u}{\partial y} D^{yx} \frac{\partial u}{\partial x}, \tag{A3.1}$$

where u is the concentration of the diffusing component, D is the diffusion tensor, and $D^{xy} = D^{yx}$. When the diffusion coefficient is homogeneous (i.e. independent of space), this simplifies to:

$$\nabla \cdot D\nabla u = D^{xx} \frac{\partial^2 u}{\partial x^2} + D^{yy} \frac{\partial^2 u}{\partial y^2} + 2D^{xy} \frac{\partial^2 u}{\partial x \partial y}. \tag{A3.2}$$

In this case, the diffusion coefficients do not need to be discretised and discretising the concentrations is straightforward, with u_{xx} at position (x_i, y_j) given by:

$$u_{xx}^{i,j} = \frac{u^{i-1,j} + u^{i+1,j} - 2u^{i,j}}{(\Delta x)^2}, \tag{A3.3}$$

where Δx is the spatial step size in the x-direction. The discretisation of u_{yy} is done in the same way. For cases with oblique diffusion restriction, u_{xy} can be discretised as follows:

$$u_{xy}^{i,j} = \frac{u^{i-1,j-1} + u^{i+1,j+1} - u^{i+1,j-1} - u^{i-1,j+1}}{\Delta x \Delta y}. \tag{A3.4}$$

For periodic boundary conditions, the last grid point in the periodic direction is simply treated as if it were attached to the first grid point in that direction. For zero-flux boundary

conditions, an extra virtual grid point is added at the ends with the same concentration as the grid point before, such that:

$$\frac{\partial u^{N,j}}{\partial x} \approx \frac{u^{N+1,j} - u^{N,j}}{\Delta x} = 0, \tag{A3.5}$$

or the equivalent in the y-direction, where N is the number of the last grid point. As long as at least one of the directions has periodic boundary conditions, this scheme will guarantee mass conservation.

For inhomogeneous diffusion, the diffusion coefficients from Eq. A3.1 also need to be discretised, because they depend on x and y. For the diffusion term in the x-direction, this was done as follows:

$$\begin{aligned}
[Du_x]_x^{i,j} &= \frac{[Du_x]^{i+\frac{1}{2},j} - [Du_x]^{i-\frac{1}{2},j}}{\Delta x} \\
&= \frac{D^{i+\frac{1}{2},j}\ \frac{u^{i+1,j}-u^{i,j}}{\Delta x} - D^{i-\frac{1}{2},j}\ \frac{u^{i,j}-u^{i-1,j}}{\Delta x}}{\Delta x} \\
&= \frac{D^{i+\frac{1}{2},j}\left(u^{i+1,j} - u^{i,j}\right) - D^{i-\frac{1}{2},j}\left(u^{i,j} - u^{i-1,j}\right)}{(\Delta x)^2},
\end{aligned} \tag{A3.6}$$

where D represents D^{xx}. The diffusion term in the y-direction can be discretised in the same way. This scheme requires the concentrations to be known at the grid points and the diffusion coefficients between grid points (Fig. A3.1). To determine the diffusion coefficients between grid points, the average of the two nearest neighbouring grid points was used. For periodic boundary conditions, an extra diffusion node can be added, connecting the last and the first grid points. Zero-flux boundary conditions can be imposed in the same way as before, or by setting the diffusion coefficient between the last grid point and the virtual grid point equal to zero.

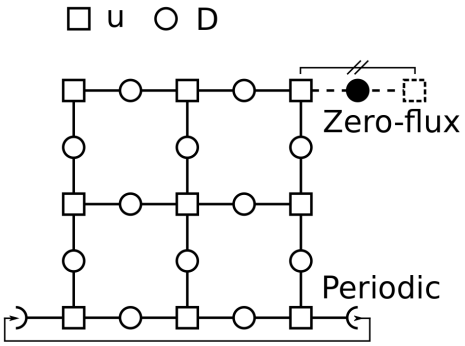

Fig. A3.1. Discretisation scheme and boundary conditions for models with inhomogeneous diffusion coefficients. Squares indicate grid points at which concentrations (u) are known. Open circles indicate points at which diffusion coefficients are imputed. Closed circles indicate diffusion coefficients set to zero for zero-flux boundary conditions.

If oblique diffusion restriction were to be used as well, the xy-terms would also need

to be discretised. This can be done as follows:

$$
\begin{aligned}
[Du_y]_x^{i,j} &= \frac{[Du_y]^{i+\frac{1}{2},j} - [Du_y]^{i-\frac{1}{2},j}}{\Delta x} \\
&= \frac{D^{i+\frac{1}{2},j}\ \frac{u^{i+\frac{1}{2},j+\frac{1}{2}} - u^{i+\frac{1}{2},j-\frac{1}{2}}}{\Delta y} - D^{i-\frac{1}{2},j}\ \frac{u^{i-\frac{1}{2},j+\frac{1}{2}} - u^{i-\frac{1}{2},j-\frac{1}{2}}}{\Delta y}}{\Delta x} \\
&= \frac{D^{i+\frac{1}{2},j}\left(u^{i+\frac{1}{2},j+\frac{1}{2}} - u^{i+\frac{1}{2},j-\frac{1}{2}}\right) - D^{i-\frac{1}{2},j}\left(u^{i-\frac{1}{2},j+\frac{1}{2}} - u^{i-\frac{1}{2},j-\frac{1}{2}}\right)}{\Delta x \Delta y},
\end{aligned}
\tag{A3.7}
$$

where D represents D^{xy}. The other xy-term can be discretised in the same way. This scheme also requires concentrations at half steps in both directions (Fig. A3.2). These can be calculated by taking the average of the four nearest neighbours. For periodic boundary conditions these averages also have to be determined between the last and first grid points. For zero-flux boundary conditions, additional virtual concentration points are required that have the same value as their neighbours. Again, these schemes will guarantee mass conservation as long as at least one of the directions has periodic boundary conditions.

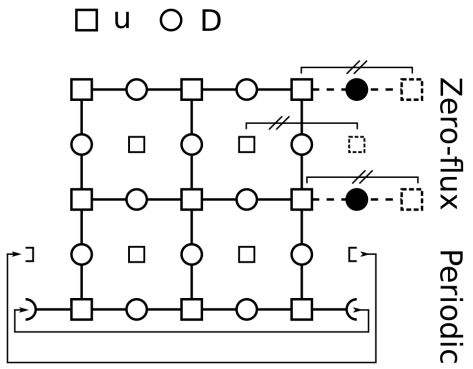

Fig. A3.2. Discretisation scheme and boundary conditions for the xy-terms of models with inhomogeneous diffusion coefficients and oblique diffusion restriction. Large squares indicate grid points at which concentrations (u) are known. Smaller squares indicate grid points at which the concentrations need to be imputed. Open circles indicate points at which diffusion coefficients are imputed. Closed circles indicate diffusion coefficients set to zero for zero-flux boundary conditions.

3.7.2 Effect of vertical diffusion reduction for all variables

In this study, we have focused on vertical diffusion restriction of active ROP only, which is the scenario that seems most congruent with the biological evidence. Here, we will elaborate a simple scaling argument for why vertical diffusion restriction of all components, in fact, cannot similarly function as a mechanism for obtaining horizontally banded patterns.

For every variable w in both the WPT and WPGAP model, we have:

$$
\frac{\partial w}{\partial t} = f_{R,w} + D_{w,max}\frac{\partial^2 w}{\partial x^2} + D_{w,min}\frac{\partial^2 w}{\partial y^2}, \tag{A3.8}
$$

where $f_{R,w}$ is the reaction function of w and other variables. If the vertical diffusion coefficient is reduced by a factor q, so that:

$$D_{w,min} = \frac{D_{w,max}}{q}, \tag{A3.9}$$

then we get:

$$\begin{aligned}\frac{\partial w}{\partial t} &= f_{R,w} + D_{w,max}\frac{\partial^2 w}{\partial x^2} + \frac{D_{w,max}}{q}\frac{\partial^2 w}{\partial y^2} \\ &= f_{R,w} + D_{w,max}\frac{\partial^2 w}{\partial x^2} + D_{w,max}\frac{\partial^2 w}{\partial \left(y\sqrt{q}\right)^2} \\ &= f_{R,w} + D_{w,max}\left(\frac{\partial^2 w}{\partial x^2} + \frac{\partial^2 w}{\partial \tilde{y}^2}\right) = f_{R,w} + D_{w,max}\nabla^2 w,\end{aligned} \tag{A3.10}$$

where $\tilde{y} = y\sqrt{q}$. This shows that reducing the vertical diffusion coefficients of all variables by a factor q yields the same results as compressing vertical space by a factor $\sqrt{q}$.

3.7.3 Effect of alternative anisotropic diffusion scenarios

This is a purely mathematical consideration of a alternative scenarios for obtaining banded patterns using anisotropic diffusion. There are no biological indications supporting these scenarios in the case of xylogenesis.

In our main scenario of vertical restriction of active ROP diffusion, only the equation for u can be scaled as in Appendix 3.7.2:

$$\frac{\partial u}{\partial t} = f_{R,u} + D_{u,max}\left(\frac{\partial^2 u}{\partial x^2} + \frac{\partial^2 u}{\partial \tilde{y}^2}\right). \tag{A3.11}$$

If we enforce the same scaling to $\tilde{y}$ on all other equations, we get for every component w except u:

$$\begin{aligned}\frac{\partial w}{\partial t} &= f_{R,w} + D_{w,max}\left(\frac{\partial^2 w}{\partial x^2} + \frac{\partial^2 w}{\partial y^2}\right) \\ &= f_{R,w} + D_{w,max}\left(\frac{\partial^2 w}{\partial x^2} + \frac{\partial^2 w}{\partial \left(\tilde{y}/\sqrt{q}\right)^2}\right) \\ &= f_{R,w} + D_{w,max}\left(\frac{\partial^2 w}{\partial x^2} + q\frac{\partial^2 w}{\partial \tilde{y}^2}\right) \\ &= f_{R,w} + D_{w,max}\frac{\partial^2 w}{\partial x^2} + D_{w,\tilde{y}}\frac{\partial^2 w}{\partial \tilde{y}^2},\end{aligned} \tag{A3.12}$$

where $D_{w,\tilde{y}} = q \cdot D_{w,max}$. This means that reducing vertical active ROP diffusion by a factor q is equivalent to compressing vertical space by a factor $\sqrt{q}$, while raising the vertical diffusion of all other components by a factor q. This would suggest that a horizontal orientation can also be imposed on the final pattern by increasing the vertical diffusion of all components other than active ROP.

Selectively increasing the vertical diffusion of components may be difficult to achieve biologically. However, selectively reducing their horizontal diffusion seems intuitively equivalent and more realistically achievable in biology. We can demonstrate this as follows. Dividing Eq. A3.12 by q yields:

$$\frac{\partial w}{\partial \tilde{t}} = \frac{f_{R,w}}{q} + \frac{D_{w,max}}{q}\frac{\partial^2 w}{\partial x^2} + D_{w,max}\frac{\partial^2 w}{\partial \tilde{y}^2}, \tag{A3.13}$$

where $\tilde{t} = qt$. Transforming time in the same way for the equation of u, we obtain:

$$\frac{\partial u}{\partial \tilde{t}} = \frac{f_{R,u}}{q} + \frac{D_{u,max}}{q}\left(\frac{\partial^2 u}{\partial x^2} + \frac{\partial^2 u}{\partial \tilde{y}^2}\right). \tag{A3.14}$$

This means that vertical active ROP diffusion restriction is equivalent to horizontal diffusion restriction of all other components plus a scaling of y and t, a change in the parameters of the reaction function, and a reduction of the (isotropic) active ROP diffusion coefficient. Assuming the transformed parameters are chosen such that we remain in the Turing regime, we can therefore expect to obtain the same qualitative patterns, i.e., bands and spirals, for this alternative scenario.

Simulations show that horizontally restricting inactive ROP diffusion for the WPT model indeed leads to a horizontal orientation (Fig. A3.3), consistent with results from others [209]. While there are no biological indications for such a mechanism of imposing a horizontal orientation is involved in xylogenesis, it could be involved in other processes requiring banded patterns.

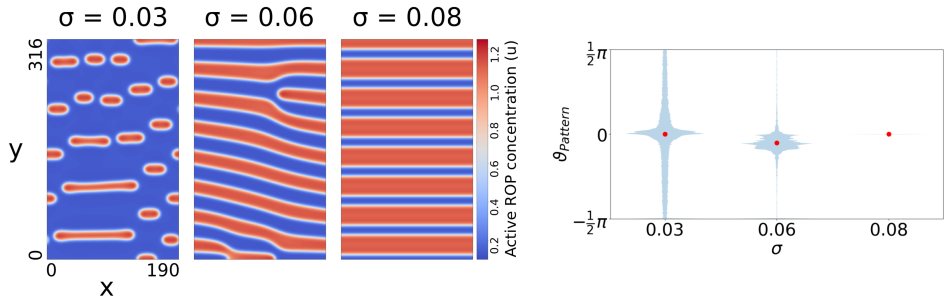

Fig. A3.3. Horizontal diffusion restriction of inactive ROP can also impose a horizontal orientation on the pattern. Horizontal diffusion of inactive ROP was reduced by a factor 4. Snapshots were taken at $t = 120000$. Other parameters were as in Fig. 3.2.

3.7.4 Diffusion tensor rotation

For anisotropic diffusion in two dimensions, the diffusion term has the following form:

$$\nabla \cdot D_u \nabla u = \begin{bmatrix} \frac{\partial}{\partial x} \\ \frac{\partial}{\partial y} \end{bmatrix} \cdot \begin{bmatrix} D_u^{xx} & D_u^{xy} \\ D_u^{yx} & D_u^{yy} \end{bmatrix} \begin{bmatrix} \frac{\partial u}{\partial x} \\ \frac{\partial u}{\partial y} \end{bmatrix}, \tag{A3.15}$$

where D_u^{xx}, D_u^{xy}, D_u^{yx}, and D_u^{yy} are the components of diffusion tensor D_u, with $D_u^{xy} = D_u^{yx}$. If diffusion is homogeneous, this simplifies to:

$$\nabla \cdot D_u \nabla u = D_u^{xx} \frac{\partial^2 u}{\partial x^2} + D_u^{yy} \frac{\partial^2 u}{\partial y^2} + 2D_u^{xy} \frac{\partial^2 u}{\partial x \partial y}. \tag{A3.16}$$

The components of the diffusion tensor can be derived from the diffusion rates in the unrestricted and restricted directions (1 and ψ, respectively) and the angle ϕ of the unrestricted direction with respect to the horizontal direction. For unrestricted diffusion along the x-axis and restricted diffusion along the y-axis, we have:

$$D'_u = \begin{bmatrix} 1 & 0 \\ 0 & \psi \end{bmatrix}. \tag{A3.17}$$

To obtain the diffusion tensor for the case where the unrestricted direction is rotated at an angle ϕ with respect to the x-axis, we need to rotate D'_u using rotation tensor $R(\phi)$:

$$R(\phi) = \begin{bmatrix} \cos(\phi) & -\sin(\phi) \\ \sin(\phi) & \cos(\phi) \end{bmatrix}. \tag{A3.18}$$

This way, we can obtain the diffusion tensor D_u:

$$\begin{aligned} D_u = R(\phi) D'_u R^T(\phi) &= \begin{bmatrix} D_u^{xx} & D_u^{xy} \\ D_u^{yx} & D_u^{yy} \end{bmatrix} \\ D_u^{xx} &= \cos^2(\phi) + \psi \sin^2(\phi) \\ D_u^{xy} = D_u^{yx} &= \sin(\phi)\cos(\phi) - \psi \sin(\phi)\cos(\phi) \\ D_u^{yy} &= \sin^2(\phi) + \psi \cos^2(\phi). \end{aligned} \tag{A3.19}$$

3.7.5 Preferred spiral angles

With a strictly vertical reduction in the diffusion of active ROP, a fully horizontal banded pattern may form (Fig. 3.2). The distance between these bands is determined by the dynamics of the system and the zero flux boundaries at the top and bottom, which demand that the pattern starts and ends with either a peak or a valley. This would mean that the preferred number of bands based on the dynamics alone (n_{bands}) should fall within a quarter of a band from the observed number of bands. However, the final steady state is also constrained by the initial emergence of the pattern, which depends on the random noise of the initial condition. Therefore, the final pattern may also contain a suboptimal number of bands, which increases the uncertainty on estimates of n_{bands}. The only real ways around this flaw would be to solve the system on an infinitely large domain, which is not feasible, or to average over many simulations with different random seeds for the initial conditions, which is computationally expensive. Therefore, we make a basic estimate of n_{bands} and its uncertainty using the average, minimum and maximum numbers of bands observed in a limited number of repetitions.

Assuming for the moment that we know the preferred number of bands, we can calculate the preferred distance d between the bands as:

$$d = \frac{H}{n_{bands}}, \tag{A3.20}$$

where H is the height of the domain. Assuming this distance is maintained in a spiral pattern, the angle ϑ of the spiral pattern depends on distance d and the vertical distance between spiral bands d_y:

$$\cos(\vartheta) = \frac{d}{d_y}. \tag{A3.21}$$

Vertical distance d_y is constrained by the periodicity of the spiral. The spiral covers a vertical distance D_y as it wraps around a domain of width W. This vertical distance D_y must be divisible by the vertical band-band distance d_y, such that:

$$D_y = W \tan(\vartheta) = n\, d_y \quad n \in \mathbb{N}, \tag{A3.22}$$

where $n = 1$ corresponds to a single spiral, $n = 2$ to a double spiral, etc. From equations A3.20, A3.21 and A3.22, we can calculate the admissible angles of the spiral pattern if the distance between bands is determined solely by the system dynamics and not by boundary effects:

$$\vartheta = \arcsin\left(\frac{H\, n}{W\, n_{bands}}\right). \tag{A3.23}$$

Taking into account the fact that our estimate of n_{bands} may be off by a quarter and the possibility of a suboptimal number of bands, we can determine an expected range for each admissible angle, using the minimum and maximum number of bands observed in simulations with vertical diffusion restriction:

$$\vartheta \in \left[\arcsin\left(\frac{H\, n}{W\left(n_{bands,max} + \frac{1}{4}\right)}\right), \arcsin\left(\frac{H\, n}{W\left(n_{bands,min} - \frac{1}{4}\right)}\right)\right]. \tag{A3.24}$$

3.7.6 Diffusion term decomposition

To study the influence of a pattern's geometry on the effect of vertical diffusion restriction, we decompose the diffusion term in directions z and w. For any point on the domain, direction z runs in opposite direction of the gradient of u, so that derivative $u_z = -|\nabla u|$. Direction w runs perpendicular to z, so that $u_w = 0$. To decompose the diffusion term, we ultimately need to express the second order spatial derivatives u_{xx} and u_{yy} in terms of z and w. The vectors $\vec{z}$ and $\vec{w}$ associated with these directions depend on the pattern angle ϑ, which we define as the angle between positive x-axis and the w-direction:

$$\vec{z} = \begin{bmatrix} \sin(\vartheta) \\ -\cos(\vartheta) \end{bmatrix} \quad \vec{w} = \begin{bmatrix} \cos(\vartheta) \\ \sin(\vartheta) \end{bmatrix}. \tag{A3.25}$$

Using these vectors, we can express derivatives u_z and u_w in terms of u_x and u_y:

$$\begin{aligned} u_z &= \sin(\vartheta)u_x - \cos(\vartheta)u_y \\ u_w &= \cos(\vartheta)u_x + \sin(\vartheta)u_y. \end{aligned} \tag{A3.26}$$

Solving for u_x and u_y gives:

$$\begin{aligned} u_x &= \sin(\vartheta)u_z + \cos(\vartheta)u_w \\ u_y &= -\cos(\vartheta)u_z + \sin(\vartheta)u_w. \end{aligned} \tag{A3.27}$$

Repeating this process with u_x and u_y substituted for u, gives us u_{xx} and u_{yy}:

$$\begin{aligned} u_{xx} &= \sin(\vartheta)u_{xz} + \cos(\vartheta)u_{xw} \\ u_{yy} &= -\cos(\vartheta)u_{yz} + \sin(\vartheta)u_{yw}. \end{aligned} \tag{A3.28}$$

Substituting Eq. A3.27 into Eq. A3.28 gives:

$$\begin{aligned} u_{xx} =& \sin(\vartheta)[\sin(\vartheta)u_z + \cos(\vartheta)u_w]_z \\ &+ \cos(\vartheta)[\sin(\vartheta)u_z + \cos(\vartheta)u_w]_w \\ u_{yy} =& -\cos(\vartheta)[-\cos(\vartheta)u_z + \sin(\vartheta)u_w]_z \\ &+ \sin(\vartheta)[-\cos(\vartheta)u_z + \sin(\vartheta)u_w]_w. \end{aligned} \tag{A3.29}$$

Since $u_w = 0$, we can simplify this to:

$$\begin{aligned} u_{xx} &= \sin(\vartheta)[\sin(\vartheta)u_z]_z + \cos(\vartheta)[\sin(\vartheta)u_z]_w \\ u_{yy} &= -\cos(\vartheta)[-\cos(\vartheta)u_z]_z + \sin(\vartheta)[-\cos(\vartheta)u_z]_w. \end{aligned} \tag{A3.30}$$

Applying the product and chain rules gives:

$$\begin{aligned} u_{xx} =& \sin^2(\vartheta)u_{zz} + \sin(\vartheta)\cos(\vartheta)\vartheta_z u_z \\ &+ \cos(\vartheta)\sin(\vartheta)u_{zw} + \cos^2(\vartheta)\vartheta_w u_z \\ u_{yy} =& \cos^2(\vartheta)u_{zz} - \cos(\vartheta)\sin(\vartheta)\vartheta_z u_z \\ &- \cos(\vartheta)\sin(\vartheta)u_{zw} + \sin^2(\vartheta)\vartheta_w u_z. \end{aligned} \tag{A3.31}$$

Since z is the direction of the gradient, the pattern angle does not change in this direction, so $\vartheta_z = 0$. Also, $u_{zw} = u_{wz} = [u_w]_z = 0_z = 0$. Therefore, the second and third terms of both equations vanish, leaving:

$$\begin{aligned} u_{xx} &= \sin^2(\vartheta)u_{zz} + \cos^2(\vartheta)\vartheta_w u_z \\ u_{yy} &= \cos^2(\vartheta)u_{zz} + \sin^2(\vartheta)\vartheta_w u_z. \end{aligned} \tag{A3.32}$$

Substituting these derivatives into Eq. 3.5 gives:

$$\begin{aligned} \nabla \cdot D_u \nabla u &= D_u^{zz}(\vartheta)\frac{\partial^2 u}{\partial z^2} + g(\vartheta)\frac{\partial \vartheta}{\partial w}\frac{\partial u}{\partial z} \\ D_u^{zz}(\vartheta) &= \sin^2(\vartheta) + \psi\cos^2(\vartheta) \\ g(\vartheta) &= \cos^2(\vartheta) + \psi\sin^2(\vartheta). \end{aligned} \tag{A3.33}$$

3.7.7 Parameters of models with ROP-dependent ROP diffusion

Parameters used for the functions linking ROP activity and ROP diffusion are given in Table A3.1. For the instantaneous ROP effect (Fig. 3.7B), the maximally restricted diffusion coefficient (ψ_{min}) was set to 0.25 and other parameters were chosen such that the final value of ψ would be close to its minimum for low ROP activity and close to its maximum for high ROP activity. For the simple delayed variant (Fig. 3.7C–E), the same value

of ψ_{min} was taken and the initial (homogeneous) microtubule density ρ_0 was set such that vertical ROP diffusion would start at its minimum ($\psi = \psi_{min}$). For the model with positive feedback in microtubule density (Fig. 3.8), we tuned the parameters of the density equation to get a bistability in microtuble density that could be switched at low or high ROP levels. We used the same initial microtubule density ($\rho_0 = 2$) for all simulations. To keep the starting conditions of the vertical active ROP diffusion coefficient close to that of used for the simple delay, ψ_{min} was lowered to 0.1, with $K_D = 1$. To keep vertical ROP diffusion close to its maximum at low microtubule densities, hill exponent n_D was set to 2, creating a sigmoidal curve.

Table A3.1. Parameter values used for ROP-dependent ROP diffusion. ROP can depend on the active ROP concentration either instantaneously (Instant), or with a simple delay (Delayed), or with a microtubule density relation including positive feedback (MT positive feedback). For empty fields that version of the model does not include a parameter with that name.

	ROP-dependent ROP diffusion relation		
Parameter	Instant	Delayed	MT positive feedback
ψ_{min}	0.25	0.25	0.1
n_ρ	Variable	2	1 or 2
K_ρ	Variable	0.5	
α		Variable	Variable
ρ_0		1	2
γ_ρ			20
σ_ρ			0.3
ξ_ρ			1
ζ			10
n_D			2
K_D			1
D_ρ			0.01

4

The role of nucleation complexes in cortical microtubule array homogeneity and patterning

Bas Jacobs

René Schneider

Jaap Molenaar

Laura Filion

Eva E. Deinum

Abstract

Plant cell walls are versatile materials that can adopt a wide range of mechanical properties through controlled deposition of cellulose fibrils. Wall integrity requires a sufficiently homogeneous fibril distribution to cope effectively with wall stresses. Additionally, specific conditions, such as the negative pressure in water transporting xylem vessels, may require more complex wall patterns, e.g., bands in protoxylem. The orientation and patterning of cellulose fibrils is guided by dynamic cortical microtubules. New microtubules are predominantly nucleated from parent microtubules causing positive feedback on local microtubule density with the potential to yield highly inhomogeneous patterns. Inhomogeneity indeed appears in all current cortical array simulations that include microtubule-based nucleation, suggesting that plant cells must possess an as-yet unknown balancing mechanism to prevent it. Here, in a combined simulation and experimental approach, we show that the naturally limited local recruitment of nucleation complexes to microtubules can counter the positive feedback, whereas local tubulin depletion cannot. We observe that nucleation complexes are preferentially inserted at microtubules. By incorporating our experimental findings in stochastic simulations, we find that the spatial behaviour of nucleation complexes delicately balances the positive feedback, such that differences in local microtubule dynamics – as in developing protoxylem – can quickly turn a homogeneous array into a patterned one. Our results provide insight into how the plant cytoskeleton is wired to meet diverse mechanical requirements and greatly increase the predictive power of computational cell biology studies.

4.1 Introduction

The plant cell wall is a highly versatile structure that has to adopt to diverse mechanical requirements [123, 216, 217]. Wall mechanical properties are tuned through chemical composition and, critically, through anisotropic deposition of wall material [218–220]. A key structure in this process is the cortical microtubule array, which determines where cell wall materials are inserted [117–119, 122] and guides the deposition, and hence, orientation of cellulose microfibrils, the main load-bearing component of cell walls and determinant of their anisotropic mechanical properties [115, 117, 120, 121]. The cortical array responds to various mechanical [128, 129], geometrical [124, 125, 127], developmental [31, 33, 130], and environmental [31] cues, integrating this information for future plant growth and function. This ability to respond to local wall stresses and other cues introduces a morpho-mechanical feedback loop that is considered the central ingredient of current plant growth models [131].

To make cell walls meet diverse mechanical requirements, the dynamic cortical microtubules can self-organise into various ordered structures [132], as illustrated by our focal examples: the arrays can be fully homogeneous, like the highly aligned transverse arrays of *elongating interphase cells* (Fig. 4.1A) [98], or locally patterned like the bands observed in developing *protoxylem* elements (Fig. 4.1B) [7]. Both cases require an even distribution of wall material and, therefore, of microtubules, either over the entire membrane, or among the bands. It has surfaced from multiple modelling studies [33, 135, 136, 160, 161], however, that achieving the required degree of homogeneity is far from trivial. It remains an open question how plants meet this recurring homogeneity requirement.

The cortical microtubule array is a model system for self-organisation. A rich tradition of biophysical models [103, 134–138, 160, 221] heavily founded upon quantitative experiments [104, 108–110, 222] has resulted in the current consensus model for spontaneous alignment dubbed "survival-of-the-aligned" [133]. Simulation models continue to play a crucial role in understanding array behaviour, for example in the ongoing effort of unravelling how cells weigh the various and possibly conflicting cues for array orientation [31, 42, 126, 127, 142–144].

Currently, however, there are critical limitations to the application of these models as realistic simulators of the microtubule cytoskeleton, thus hampering progress on the above and other questions. The most striking shortcoming of this model is that, whenever the important aspect of microtubule bound nucleation of new microtubules is incorporated, which is experimentally observed [109], this results in highly inhomogeneous arrays (Fig. 4.1A,B) [33, 135, 136, 160, 161]. This, what we call, *"inhomogeneity problem"* arises because microtubule-based nucleation introduces a positive feedback that amplifies fluctuations in local microtubule density.

The existence of this positive feedback is supported by multiple experimental observations: In an established array, almost all microtubules are nucleated by γ-tubulin ring complexes [105, 161]. These nucleation complexes are enriched in microtubule dense regions [108], and occur almost exclusively in the microtubule bands of developing protoxylem once these are established [33]. Microtubule bound nucleation complexes, moreover, nucleate at a higher rate than unbound complexes [108]. Therefore, some mechanism must balance this positive feedback. Two likely scenarios are: 1) a local limitation of micro-

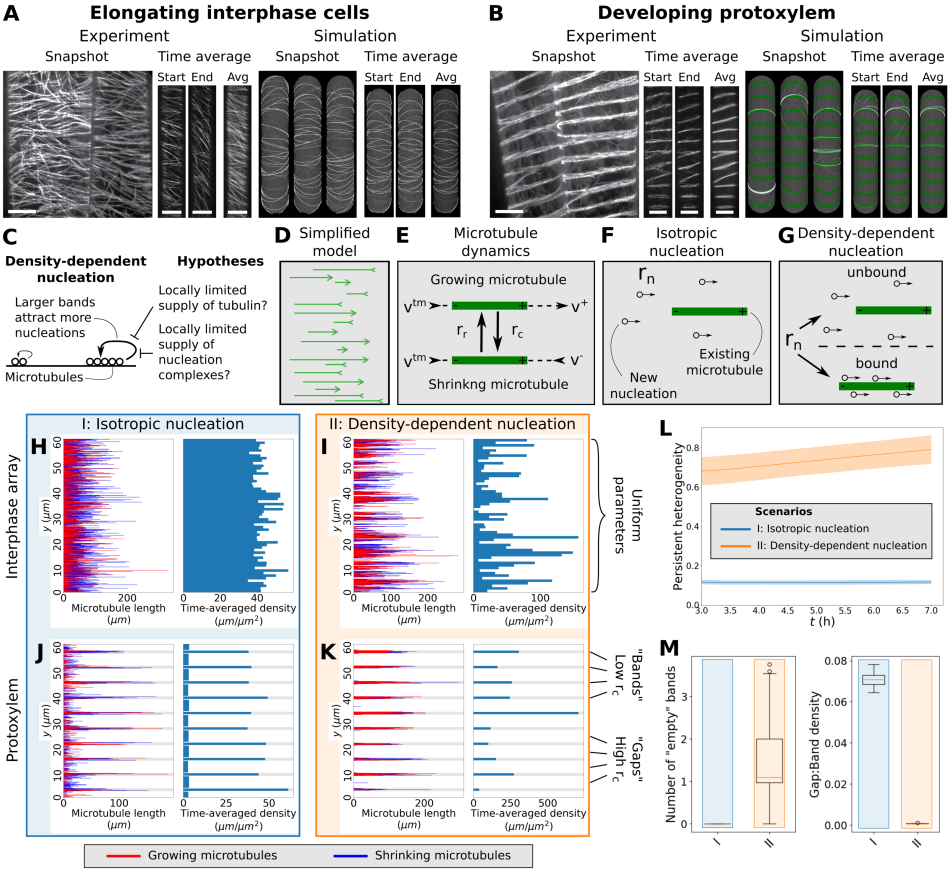

Fig. 4.1. The inhomogeneity problem is reproduced by our simplified model. (A,B) Elongating interphase cells (A, left) have homogeneous arrays of transversely oriented microtubules, while simulations with density-dependent nucleation (A, right) yield highly inhomogeneous arrays. In developing protoxylem (B), microtubules are evenly distributed over a number of bands (B, left), but in simulations with density-dependent nucleation, microtubules accumulate in a small number of bands (B, right). Scale bars are 10 μm. (C) Hypotheses for breaking the global competition caused by density-dependent nucleation. (D–G) Implementation of the simplified model with all microtubules perfectly transversely oriented (D). Under standard microtubule dynamics (E), microtubules grow or shrink at their plus ends with rates v^+ and v^- respectively, retract at their minus ends with rate v^{tm}, and undergo spontaneous catastrophes and rescues at rates r_c and r_r respectively. Under isotropic nucleation (F), microtubules nucleate at a fixed rate r_n at random (y-)positions. With density-dependent nucleation (G), nucleations still occur at a constant global rate r_n, but a portion of these nucleations is now distributed across existing microtubules proportional to their length. (H–K) Microtubule lengths and positions and time-averaged microtubule density of representative simulations using the simplified model for interphase arrays (H,I) and developing protoxylem (J,K). Protoxylem simulations were run for two hours without increased catastrophe rate in gaps followed by five hours with an increase of a factor three. Other simulations were run for seven hours. Time-averaging was done over the last 3 hours. (L) Measure of persistent heterogeneity over time for simulations of the interphase arrays of elongating cells. Lines indicate the average and shaded areas the standard deviation. (M) Number of empty bands (bands with less than 25% of average microtubule density in bands) and ratio of microtubule density between gaps and bands for the protoxylem simulations. Boxplots are based on quantities averaged over the last two hours of the simulations. Quantities in (L) and (M) were calculated from 100 independent simulations per nucleation mode.

tubule growth through the depletion of available tubulin subunits and 2) a local saturation of the amount of nucleation complexes that a microtubule-dense region can attract.

Microtubules grow through the incorporation of GTP-tubulin, mostly at their plus end. When shrinking, however, these subunits are typically released as GDP-tubulin [99, 104]. Consequently, a high local density of dynamic microtubules implies both a high consumption and release of tubulin. The two different tubulin states, however, make that tubulin is released in an inactive form, which in the very different context of small GTPase patterning provides a mechanism for the stable coexistence of multiple clusters [223]. Therefore, our first hypothesis is that local tubulin depletion could only serve as a homogenising factor when considering both tubulin states.

The second option for limiting the local increase of microtubule density may come naturally with a sufficiently detailed description of nucleation complexes, which so far have been considered only implicitly. From pioneering work [134–137] to current studies [125–127, 138], great progress has been made using *isotropic nucleation*, i.e., with uniform random location and orientation. In reality, however, most nucleations occur from nucleation complexes bound to existing microtubules, with new microtubules either parallel to their parent microtubules or branching at angles around 35° [107–109]. So far, this microtubule bound nucleation has been modelled as *density-dependent nucleation*: distributing the relevant nucleations over the existing microtubules proportional to their lengths [135, 136, 160, 161]. Density-dependent nucleation has several effects in simulations: it expands the range of biological parameters for which microtubules will spontaneously align, accelerates the alignment process in interphase arrays [160, 221], and speeds up protoxylem patterning [33]. However, this density-dependent nucleation also leads to a global competition for nucleations, in which the microtubule densest region attracts the most nucleations (Fig. 4.1C). This positive feedback loop creates the inhomogeneity problem, characterised by a strong local clustering of microtubules in simulated interphase arrays [135, 136, 160] and many missing bands in simulated protoxylem [33] (Fig. 4.1B).

The core of the inhomogeneity problem is that with density-dependent nucleation, nucleation sites are distributed as if the system is well-mixed, so doubling the local density somewhere will double the probability that it will attract a specific nucleation at the expense of the rest of the array. In reality, however, the docking of a nucleation complex is primarily a local process. Although increasing the local microtubule density may speed up this process, it will affect only nearby but not distant nucleation complexes, so the local increase of nucleation must saturate. By liberally extending the analogy with small GTPase patterning —where decreasing benefits of increased local density favour cluster coexistence (chapter 2)— we arrive at our second hypothesis that the locally saturating nucleation rates would suppress the global competition for nucleations and support array homogeneity.

Here, we explore the potential of our two hypotheses for solving the inhomogeneity problem using a simplified stochastic simulation model of transversely oriented dynamic microtubules. Because of their different homogeneity requirements, we use both the basic homogeneous interphase array and the banded transverse array from developing protoxylem as model systems. Both systems depend on the well-studied process of microtubule alignment into a transverse array, which we here take for granted. This simplification provides a computationally attractive environment for exploring two very different

mechanisms. As nucleation complex dynamics is not sufficiently studied yet to model it properly, we perform detailed observations of nucleation complex behaviour, both under normal conditions and in sparse oryzalin-treated arrays.

This way, we discover that nucleation complexes are predominantly inserted near microtubules. Although this finding, at first glance, appears to aggravate the inhomogeneity problem, it turns out that the more realistic nucleation complex dynamics allows for homogeneity, while at the same time improving the ability to form patterned arrays. Our findings pave the way for a new generation of microtubule simulation models with broad biological applications.

4.2 Results

4.2.1 A simplified model of transversely oriented microtubules reproduces the inhomogeneity problem

For solving the inhomogeneity problem, we simplified existing "full array models" (example snapshots in Fig. 4.1A,B) [103, 160] by taking alignment and orientation for granted. This means that all microtubules in our simulations are transversely oriented, i.e., they grow in the x-direction, and their positions are defined along the y-axis (Fig. 4.1D). The microtubules stochastically switch between growth and shrinkage (usually referred to as "catastrophe" and "rescue"), with parameters introduced in Fig. 4.1E and following the existing full array models. Example snapshots of the simplified arrays are shown in Fig. 4.1H–K. The *"interphase array"* has uniform parameters, whereas in *"protoxylem"*, the catastrophe rate r_c is increased in predefined gap regions after a 2-hour uniform initiation period, resulting in local destabilisation of microtubules in an existing transverse array as experimentally observed and modelled by Schneider et al. [33]. To validate our model, we use two types of microtubule nucleation from the full array models as a reference: isotropic nucleation, with uniformly distributed y-positions (Fig. 4.1F), and density-dependent nucleation, in which a density-dependent fraction of nucleation is "microtubule-bound", with positions evenly distributed over all existing microtubule lengths [160] (Fig. 4.1G). For implementation details see Methods.

With isotropic nucleation, we obtained homogeneous arrays and bands of similar density, whereas with density-dependent nucleation, arrays became inhomogeneous and band density varied substantially, often leaving bands largely empty (Figures 4.1H–M). This validates the use of our model for studying the inhomogeneity problem.

Similar to full array simulations [33], the positive feedback inherent in density-dependent nucleation greatly enhanced the clearance of the gap regions. In the process, average microtubule density in the bands increased up to 6-fold relative to isotropic nucleation, reflecting the surface covered by band regions (Fig. 4.1J,K, Fig. S4.1).

We did observe two quantitative differences with full array protoxylem simulations. First, we observed fewer empty bands with density-dependent nucleation than in the full array simulations (Fig. 4.1B,K). Second, for both nucleation modes we observed much larger differences in band vs. gap density, so that the experimentally observed $\sim$ 10-fold difference between bands and gaps [33] was easily reproduced even with isotropic nucleation, matching theoretical predictions of steady state densities for non-interacting

microtubules (see Appendix 4.7.1). Two differences from the full array simulations could underlie these quantitative effects: first, microtubules cannot leave the band or gap region they were nucleated in and second, microtubule bundles –which can live longer than individual microtubules– do not occur in the simplified model.

4.2.2 Tubulin diffusion is too fast for sufficient local variation in microtubule growth velocities

To test if local tubulin depletion could solve the inhomogeneity problem, we made the microtubule growth speed dependent on the local (GTP-)tubulin concentration. Growing microtubules consumed (GTP-)tubulin, while shrinking microtubules released (GDP-)tubulin (Fig. 4.2A, see Methods for details). GDP-tubulin was recharged into GTP-tubulin at a constant rate β.

With a realistic recharge rate of $\beta = 0.01\ s^{-1}$ [224], our simulations only produced nearly homogeneous arrays for extremely low tubulin diffusion coefficients (Fig. 4.2B,E), but not for realistic values of 1 to 10 $\mu m^2/s$ based on a measured cytoplasmic tubulin diffusion coefficient of 6 $\mu m^2/s$ [225] (Fig. 4.2C,D,F,G, Fig. S4.2).

As expected from theoretical considerations (chapter 2, [223]), arrays were more homogeneous with the distinction between GTP- and GDP-tubulin than without (Fig. S4.3). For the lowest diffusion coefficients, tubulin essentially was a local resource over the time of the simulation, and any observed array homogeneity simply reflected the homogeneous initial tubulin distribution (Fig. S4.4).

These results suggest that, although the tubulin-depletion mechanism could improve homogeneity in principle, it does not ensure homogeneity in practice.

4.2.3 Nucleation complexes are preferentially inserted at microtubules

Since we found that local tubulin depletion does not solve the inhomogeneity problem, we next focused on nucleation. Little is known, however, about the mobility of nucleation complexes in the membrane itself, because normally most complexes are bound to microtubules. We, therefore, treated cells with the microtubule-depolymerising drug oryzalin [226] to reduce the density of the cortical microtubules and observed GFP-labelled γ-tubulin complex protein (GCP)3, a component of the nucleation complex, using spinning disc confocal microscopy. We found that microtubule-bound complexes were indeed immobile, while complexes that appeared independent of microtubules in the plasma membrane showed diffusive behaviour with a diffusion coefficient of approximately 0.013 $\mu m^2/s$ (Fig. 4.3A,B). Lifetimes of bound and unbound nucleation complexes were similar to those found by others [108], validating the use of these cells.

By comparing new insertions in oryzalin-treated cells to those in mock-treated controls, we discovered that nucleation complex insertion occurred preferentially near microtubules. For the control cells, we found an average insertion rate of 0.0037 $\mu m^{-2}s^{-1}$ (Table S4.1), which is similar to the 0.0045 $\mu m^{-2}s^{-1}$ we estimated to keep the overall nucleation rate consistent with previous simulations (see Appendix 4.7.3). To maintain consistency, we used the latter number in our simulations. Even in the microtubule-sparse oryzalin-treated cells we found an overrepresentation of nucleation complexes on the few remaining microtubules. Nucleation complexes appeared at an average rate of 0.00026

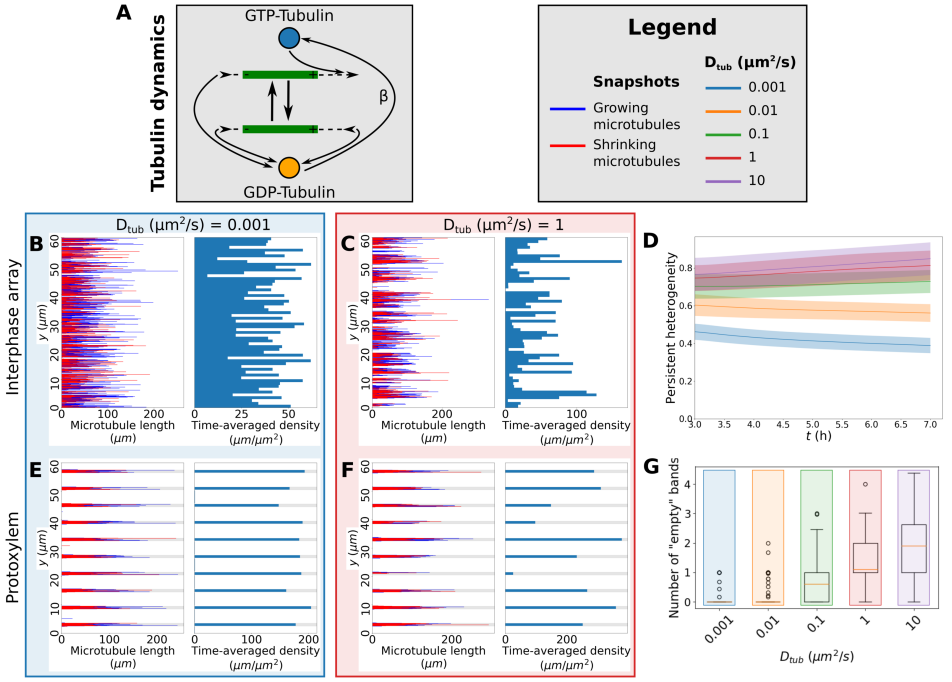

Fig. 4.2. Local tubulin limitation requires unrealistically low tubulin diffusion to enhance homogeneity. (A) In our tubulin implementation, the v^+ of the growing microtubules depends on the local GTP-tubulin pool, which is depleted as a result. Conversely, microtubule shrinkage increases the local GDP-tubulin concentration. GDP-tubulin is recharged at a constant rate β into the GTP-tubulin needed for growth. (B,C,E,F) Microtubule lengths and positions and time-averaged microtubule density of representative simulations using the simplified model with GTP- and GDP-tubulin with a tubulin recharge rate $\beta = 0.01\ s^{-1}$ and two different tubulin diffusion coefficients (D_{tub}). Protoxylem simulations were run for two hours without increased catastrophe rate in gaps followed by five hours with this increase. Other simulations were run for seven hours. Time-averaging was done over the last 3 hours. (D) Measure of persistent heterogeneity over time for simulations with five different values of D_{tub}. Lines indicate the average and shaded areas the standard deviation. (G) Number of empty bands (bands with less than 25% of average microtubule density in bands) for simulations with five different values of D_{tub}. Boxplots are based on quantities averaged over the last two hours of the simulations. Quantities in (D) and (G) were calculated from 100 independent simulations using density-dependent nucleation.

$\mu m^{-2}s^{-1}$, which could be separated in a rate of 0.013 $\mu m^{-2}s^{-1}$ for complexes appearing near/at microtubules and 0.000085 $\mu m^{-2}s^{-1}$ excluding these complexes (Table S4.1). Because nucleation complexes co-localising with microtubules may have been inserted nearby and diffused towards them between frames, the first of these three values represents an upper bound and the last a lower bound. Still, as a conservative estimate, insertion of new complexes was at least an order of magnitude smaller in absence of microtubules. Notably, the rate of 0.013 $\mu m^{-2}s^{-1}$ is only 3-3.5 times higher than in a normal density array, suggesting a strong local saturation of nucleation complex insertion.

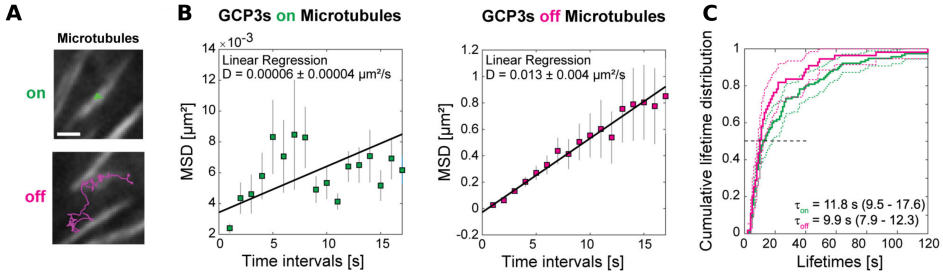

Fig. 4.3. Microtubule nucleation complexes are statically bound to microtubules and diffusively anchored to plasma membranes. (A) Example trajectories of tracked GCP3 foci located on microtubules (green, top) and off microtubules (magenta, bottom). Scale bar = 1 μm. (B) Mean-squared displacement (MSD) calculated for 115 microtubule-bound and 55 diffusing GCP3 foci. Squares and line extensions represent means ± standard deviations for the given time intervals and the solid line represents a weighted linear fit yielding the diffusion constant and fit error. The data was recorded from nine cells and five seedlings. (C) Cumulative lifetime distributions show that the median lifetime of the tracked GCP3 foci on microtubules (green) and off microtubules (magenta) are similar. Solid and dashed lines represent the empirical cumulative distribution function and the 95% lower and upper confidence bounds for the evaluated function values, respectively. The horizontal dashed line represents the median value.

4.2.4 Local limitation of nucleation complexes can solve the inhomogeneity problem

Based on these experiments, we explicitly incorporated nucleation complexes into our simulations as particles that can associate with the membrane, move around diffusively in (effectively) two dimensions, attach to a microtubule upon encounter, and eventually either disassociate or nucleate (See Fig. 4.4A and Methods for details). With this model, we investigated the impact of differential insertion rate (r_b within attraction radius R of any microtubule, $r_{b,min}$ otherwise) and differential nucleation rates for complexes on ($r_{n,bound}$) or off ($r_{n,unbound}$) microtubules [108] on array homogeneity and patterning (Fig. 4.4).

We expected that our discovery of microtubule-dependent insertion, as yet another factor that favours microtubule-dense regions, would aggravate the inhomogeneity problem. We found, however, that with a realistic attraction radius of R = 50 nm, twice the width of a microtubule, fully homogeneous arrays were formed over time (Fig. 4.4H). This was, however, a slow process, increasing the importance of a previously reported alternative source of nucleation early during *de novo* array establishment [161], here called "seeding" (Fig. 4.4G,H). By halving R, small gaps started to appear in the array, in which nucleation complex insertion was not enhanced by microtubules, lowering the total microtubule density (Fig. S4.5). The diffusion coefficient D_{NC} of unbound nucleation complexes would have had to be reduced by two orders of magnitude from our experimentally observed value to achieve a similar reduction of microtubule density. With further reductions, it would become impossible to sustain a normal density array (Fig. S4.6).

For protoxylem patterning, we found that the differential insertion rate resulted in a more effective clearing of the gap regions than the differential nucleation rate, both for data-based rate differences (Fig. 4.4B,D) as well as smaller r_b differences (Fig. S4.7A) and artificially matched differences in r_b and r_n (Fig. S4.8). Notably, the density in band regions increased only slightly during the separation process (Fig. 4.4F), in stark contrast

to the large increase under density-dependent nucleation (Fig. S4.1B,D).

Homogeneity was well maintained, as bands were never lost (Fig. 4.4B,C) except for

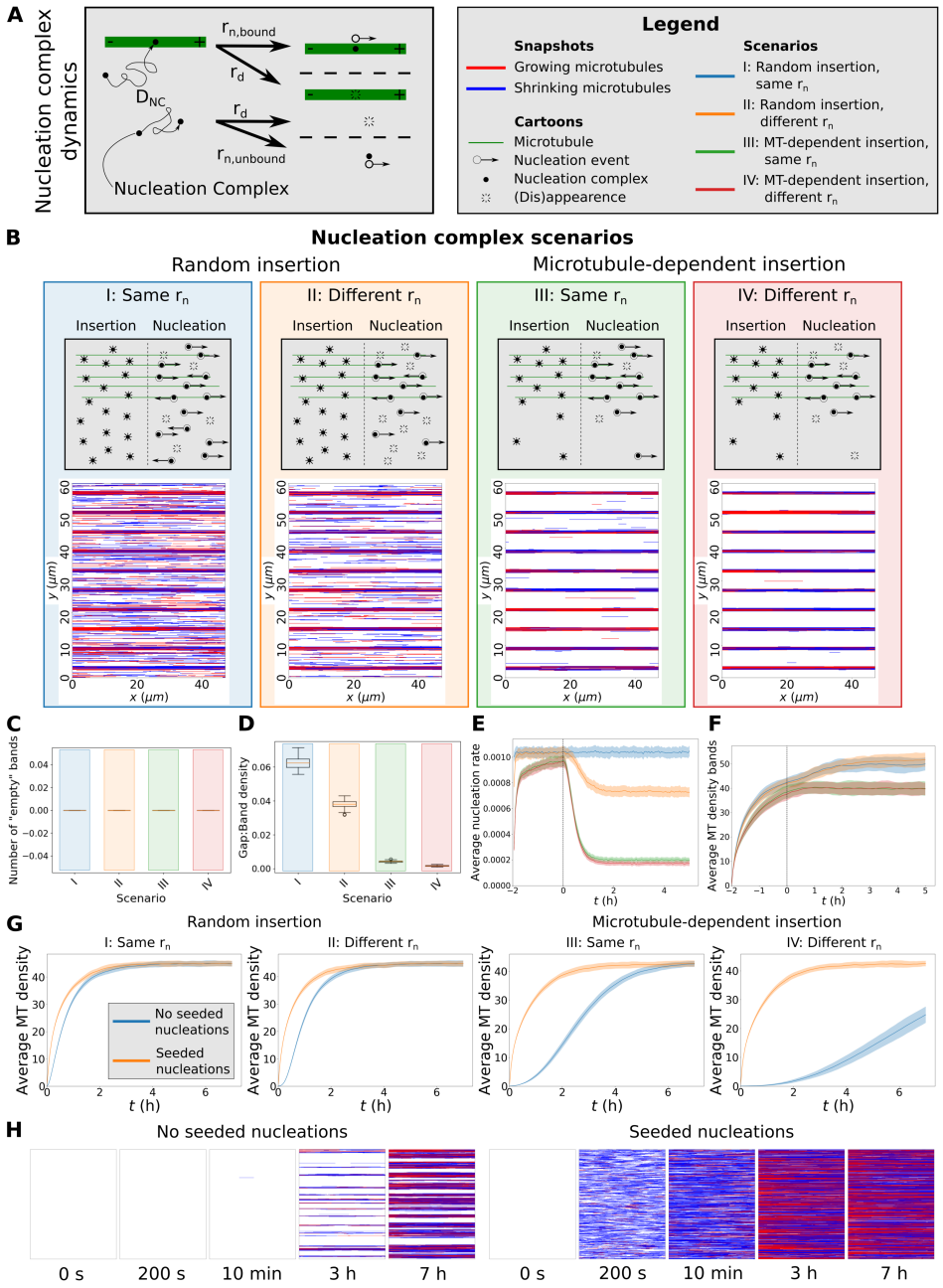

Fig. 4.4. Caption on next page.

Fig. 4.4. Local limitation of nucleation complex availability can ensure array homogeneity and enhance protoxylem band formation. (A) In our nucleation complex implementation, each complex moves within the two-dimensional plane of the membrane with diffusion coefficient D_{NC} and binds the first microtubule it encounters. A nucleation rate applies to each separate complex and, by default, this rate is higher for microtubule-bound complexes ($r_{n,bound}$) than for freely diffusing ($r_{n,unbound}$) ones. Complexes also disappear at rate r_d. Microtubule insertion into the membrane occurs at a constant rate r_b. For areas outside a distance R of a microtubule this rate is reduced to $r_{b,min}$ in case of microtubule-dependent nucleation complex insertion. (B) Final array snapshots of representative protoxylem simulations for four different nucleation complex scenarios: I,II: Random insertion. III,IV: Microtubule-dependent insertion. I,III: No difference between bound and unbound nucleation rates. II,IV: Reduced nucleation rate for unbound complexes. (C) Number of empty bands (bands with less than 25% of average microtubule density in bands) (D) Ratio of microtubule density between gaps and bands for the protoxylem simulations. (E) Average global nucleation rates. (F) Average microtubule density in band regions. (G) Average microtubule density for simulations without bands and gaps with and without seeded nucleations. (H) Snapshots at various time points of a simulated array with microtubule-dependent insertion and a reduced r_n for unbound complexes with and without seeding. All summary statistics were calculated from 100 simulations. Lines indicate the average and shaded areas the standard deviation. Boxplots are based on quantities averaged over the last two hours of the simulations. Protoxylem simulations were run for two hours without increased catastrophe rate in gaps followed by five hours with this increase. Other simulations were run for seven hours.

very low diffusion coefficients (Fig. S4.7B). Increasing D_{NC} reduced separation at most 3-fold. This observation strongly suggests that the measured value is roughly optimal for enhancing local array patterning and at the same time avoiding inhomogeneity and density loss problems (Fig. S4.7C,D). For a uniform insertion rate and reduced (but not equal) nucleation rate for unbound complexes, we also noted that there was a window of optimal D_{NC} for separation (Fig. S4.9). For decreasing D_{NC}, the enhanced separation started where the overall nucleation rate started to decrease after the initiation phase. This decrease reflects a reduction in the number of complexes encountering a microtubule, which down to $D_{NC} = 10^{-4}\mu m^2/s$ predominantly affected the gaps and enhanced the difference between bands and gaps several fold (Fig. S4.9E,F). Notably, the default D_{NC} fell within this optimal window for the default (large) difference in catastrophe rate between bands and gaps, but not for the smallest difference tested.

4.3 Discussion

We have developed a simplified model of transversely oriented microtubules and performed quantitative experimental observations of nucleation complex dynamics to investigate how plants ensure homogeneity of their cortical microtubule array and, consequently, cell wall. With our model and experiments, we identified the natural saturation of nucleation complex recruitment to microtubule dense regions as the essential realistic mechanism for countering the positive feedbacks inherent in microtubule-based nucleation that would otherwise cause severe array inhomogeneity. The key element of this mechanism is that the competition for nucleation complexes becomes local instead of global. This effect is achieved, because the local probability of attracting a specific nucleation now saturates with local microtubule density as opposed to the linear scaling under density-dependent nucleation.

Besides the two factors already known, i.e., predominant nucleation from existing microtubules [107, 109] and reduced nucleation rate for unbound complexes [108, 161], we found that the insertion of nucleation complexes in the membrane is strongly biased

towards microtubules. Together, these factors enable both completely homogeneous and complexly patterned arrays, as shown with our model systems of elongating interphase cells and developing protoxylem. Moreover, this insertion bias increases the importance of "seeding" the array with alternative ("GCP-independent") nucleations [161] to ensure its timely establishment.

Although local tubulin depletion could not ensure homogeneity, tubulin depletion can be an important factor in limiting microtubule density at the whole cell level through changes in microtubule dynamics [103, 133]. Markedly, using parameters measured in early interphase wild type cells can result in unbound microtubule growth [133, 227], whereas with all parameter sets measured in established wild type arrays, a finite steady state microtubule density exist [33, 103, 222].

Our results demonstrate the value of our simplified model as a powerful tool for solving complex problems that can be interpreted as approximately one-dimensional. The simplification of abandoning microtubule-microtubule interactions, of course, introduces some quantitative differences with the full model, which can even increase our understanding of the real system. The largest difference is that, contrary to simulations with interacting microtubules [33], we observed strong band formation with isotropic nucleation while using the same parameters for microtubule dynamics. Two factors may underlie this difference: 1) Microtubule bundling, also without microtubule-based nucleation, increases the persistence of microtubule bundles, including those in the gap regions. Indeed, in Schneider et al. [33] it is shown that microtubule turnover is an important determinant of the band/gap-separation rate. 2) The effective nucleation rate in bands is higher in the simplified model, because all nucleations inside a band give rise to microtubules that remain inside the band. In the full array model, a substantial part of these nucleations is "lost" because the microtubules quickly grow into the gap regions. Indeed, the authors also found a much stronger degree of separation with isotropic nucleation when the nucleation rate in bands was increased. Taken together, this suggests that the aspect of co-alignment between parent and new microtubule [109] plays an important role in increasing the relevant nucleation rate inside bands and, hence, band stability. Band stability could additionally be enhanced by microtubule bundling itself.

Additional speedup of the separation process occurs if the band locations match well with density fluctuations in the (initial) microtubule array [33]. This match is likely better in reality than in current models, as gap regions are defined by small GTPase patterning proteins, like Rho of plants 11 (AtROP11) in metaxylem, and their downstream effectors MIDD1 and Kinesin-13A [148, 149]. Various ROPs and the aforementioned effectors are also expressed during protoxylem formation [151, 152] and striated AtROP7 patterns are observed in protoxylem [150]. Results so far indicate that the corresponding microtubule patterns are not simply a readout of a ROP pattern, as changes in microtubule dynamics affect both the dynamics and outcome of the patterning process [33, 148, 205].

Notably, ROPs and other polarity factors are also indicated in the specification of the preprophase band [76], the single microtubule band that forms around the nucleus prior to cell division [77, 228], and altered microtubule dynamics are observed during its formation [222]. Together, these phenomena suggest that integrating ROP patterning and microtubule dynamics into a single simulation environment will provide mechanistic insight into many processes.

How could ROPs and microtubules sometimes produce a homogeneous pattern, like in

proto- and metaxylem, and sometimes a highly inhomogeneous one, like the preprophase band? Coincidentally, the literature on small GTPase patterning offers deeper insights. In the most common case, when GTPases are only interconverted between active and inactive states, the system can "phase separate" into a single cluster of active GTPases (chapter 2, [84, 173, 177]). In contrast, multiple clusters can stably coexist by (1) the addition of GTPase turnover, i.e., production and degradation (chapter 2, [158]), (2) an inactive intermediate form that cannot be reincorporated into an (active) patch immediately [223] — much like the GDP-tubulin as intermediate modelled here — or (3) an additional factor that increasingly limits the growth of active patches as they get larger, like ROP GTPase activating proteins (GAPs) that increase ROP inactivation (chapter 2). All these options have in common that the growth of larger patches is specifically limited, and a baseline supply of raw material (inactive GTPases or nucleation of new microtubules) is guaranteed for smaller patches.

This comparison immediately stresses the significance of the uniform base insertion rate of nucleation complexes into the membrane of our model as a local supply. Our experiments on oryzalin treated cells show that nucleation complexes are indeed inserted into empty regions in the plasma membrane. We expect that rapid diffusion of cytosolic nucleation complexes, likely enhanced by cytoplasmic streaming, can ensure a relatively uniform base insertion rate. Additionally, our data suggest nucleation complexes are actively released from the membrane, because despite very different insertion rates, residence times near/at and away from microtubules are very similar (Fig. 4.3C), particularly for non-nucleating complexes [108]. If, however, release were governed by thermodynamic equilibrium, complexes would have remained much longer when on microtubules. Active release would contribute to the sustenance of the cytosolic pool of nucleation complexes, and hence, the base insertion rate. As multiple nucleation complex subunits contain regulatory phosphorylation sites [229], the release could be in an inactive state, which would further support homogeneity [223]. One form of density-dependent growth limitation (the conceptual equivalent of GAP proteins in chapter 2) that is present in our model is the fact that a set of n isolated microtubules are more effective in capturing diffusing nucleation complexes from the membrane than a single bundle of n microtubules of the same length*. Additionally, a similar but potentially stronger effect would occur if bundling of microtubules leads to shielding of part of the binding sites for nucleation complexes, thereby specifically reducing the per length insertion rate of bundled microtubules.

The above mechanisms are not mutually exclusive and can enhance each other. Moreover, plant cells may operate close to the inhomogeneous regime of global competition as occurs with density-dependent nucleation, given the existence of inhomogeneous structures like the preprophase band. If cells are indeed close to this alternative regime, a substantial local increase in the factors that recruit nucleation complexes could over time trap a large fraction of these complexes to a specific region. The "group A" TPX2/TPXL proteins are ideal, though currently speculative, candidates for supporting preprophase band formation this way, as they are indicated in the recruitment of nucleation complexes

*E.g., assuming a membrane residence time of 10 s, a nucleation complex would have an average diffusion length of 361 nm. For aligned same length microtubules, this reduces to a 1D problem, with a 2*361 + 10*25 nm cross section covered by a bundle of 10 microtubules and a 10*(2*361 + 25) nm cross section for the isolated microtubules. So, as a lower bound, the bundle would be only 13% as effective in capturing free nucleation complexes.

to microtubules [230] and contain a nuclear importin domain [231], which could provide the correct perinuclear positioning of a high nucleation zone upon release. Simulations show that concentrating microtubule nucleation to the future band region can indeed reproduce a preprophase band-like structure [145].

Our novel observations of nucleation complex behaviour and the solution they provide to the inhomogeneity problem pave the way for the next generation of microtubule simulation models. Some pressing biological questions that require detailed simulations *including realistic nucleation* are: 1) How do cells integrate all the different cues affecting array orientation [31, 33, 124, 125, 127–130] and resolve conflicts between them? 2) How does the reduction of branched (and increased parallel) nucleation in the *tonneau2/fass (ton2)* mutant lead to dramatic changes in the morphology of leaf pavement cells and trichome morphology [232]? 3) How can a continuous interaction between ROPs and their downstream effectors on the one hand [148, 149] and the microtubule array on the other hand lead to various complex wall patterns like in proto- and metaxylem? In summary, our work enables various new lines of quantitative, mechanistic research that will improve our understanding of how cell wall properties are dynamically controlled.

Acknowledgements

R.S. would like to acknowledge Deutsche Forschungsgemeinschaft grant 453188536.

4.4 Methods

4.4.1 Simulation setup

Cortical microtubules exist effectively on a two-dimensional surface on the inside of the membrane. Therefore, we chose our simulation domain to represent the cortex of a cylindrical cell, with a height of 60 μm and a radius of 7.5 μm as in Schneider et al. [33]. This domain was represented by a rectangle with a horizontal periodic x-axis and a vertical y-axis representing the circumference and length of the cylinder, respectively. Except for the variant with nucleation complexes, horizontal positions were irrelevant and not tracked in the simulations.

4.4.2 Core microtubule dynamics

Microtubule growth, shrinkage, and minus end retraction (treadmilling) occur at speeds v^+, v^-, and v^{tm}, respectively, with catastrophes and rescues occurring at rates r_c and r_r, respectively (Fig. 4.1E). These are the same dynamics as described by Tindemans et al. [103] and parameters were based on [33] (see Table S4.2 for parameter values).

4.4.3 Protoxylem band and gap regions

Protoxylem simulations used ten band regions of 1 μm separated by gap regions of 5 μm (with 2.5 μm gap regions on either end of the domain). Following [33], microtubule sta-

bility was reduced in the gap regions by increasing the catastrophe rate by a factor f_{cat} (default: $f_{cat} = 3$) compared to the band regions. Before this increase in gap catastrophe rate, simulations were run for two hours with homogeneous parameters ($f_{cat} = 1$), allowing a microtubule array to form.

4.4.4 Basic nucleation modes

Isotropic nucleations were drawn at a constant global rate of $r_n \cdot A$, where r_n is the nucleation rate in $\mu m^{-2} s^{-1}$ and A is the domain area in μm^2 and given uniformly distributed y-positions (Fig. 4.1F).

Density-dependent nucleation was implemented as in Deinum et al. [160]. Nucleation events were scheduled with a total rate r_n, of which a density-dependent fraction was assigned to microtubules, resulting in a bound rate $r_{n,bound}$ following:

$$r_{n,bound} = r_n \frac{\rho}{\rho + \rho_{\frac{1}{2}}}, \tag{4.1}$$

where ρ is the global microtubule density in μm microtubule per μm^2 and $\rho_{\frac{1}{2}}$ is the microtubule density at which half of all nucleations are bound. We then assigned y-positions to the unbound nucleations, as described for isotropic nucleation. The bound nucleations were distributed randomly across the total microtubule length and then got the y-position of their parent microtubule with a small normally distributed displacement ($\sigma = 0.1 \mu m$), which was redrawn for positions falling outside the simulation domain (Fig. 4.1G).

4.4.5 Tubulin dynamics

In one dimension, tubulin dynamics for a single tubulin follows the diffusion equation:

$$\frac{\partial c_T}{\partial t} = D_{tub} \frac{\partial^2 c_T}{\partial y^2} + f(MT), \tag{4.2}$$

where c_T is the tubulin concentration, t is the time, y is the position along the longitudinal axis, D_{tub} is the tubulin diffusion coefficient, and $f(MT)$ the function of microtubule dynamics that specifies the net release of tubulin from microtubules. This last term can be calculated directly from local changes in microtubule lengths at each integration time step. Similarly, when distinguishing GTP- and GDP-tubulin, we have:

$$\begin{aligned} \frac{\partial c_{T_1}}{\partial t} &= D_{tub} \frac{\partial^2 c_{T_1}}{\partial y^2} + \beta c_{T_2} - f(MT_{Growing}) \\ \frac{\partial c_{T_2}}{\partial t} &= D_{tub} \frac{\partial^2 c_{T_2}}{\partial y^2} - \beta c_{T_2} + g(MT_{Shrinking}), \end{aligned} \tag{4.3}$$

where c_{T_1} and c_{T_2} are the concentrations of GTP- and GDP-tubulin, respectively, β is the recharge rate at which GDP-tubulin is converted back into GTP-tubulin, and $f(MT_{Growing})$ and $g(MT_{Shrinking})$ are the functions of microtubule dynamics that determine the tubulin consumption by growing microtubules and the tubulin release by shrinking microtubules,

respectively. For convenience, we express tubulin concentrations in μm of microtubule length equivalent per μm^2.

Arrays were initiated without microtubules and with a uniform (GTP-)tubulin concentration of L_{max}/A, where A is the domain area and L_{max} is the maximum total microtubule length when all tubulin is in microtubule form. Growth speed v^+ was made linearly dependent on the local (GTP-)tubulin concentration, according to:

$$v^+(y) = v_0^+ \frac{c_T(y)}{c_{T,0}} = v_0^+ \frac{A}{L_{max}} c_T(y), \tag{4.4}$$

where v_0^+ is the initial growth speed and parameter $c_{T,0}$ is the initial homogeneous (GTP-) tubulin concentration.

The diffusion equations were integrated using a Crank-Nicolson algorithm [233] with integration steps of 0.01 s in time and 0.2 μm in space. Microtubule growth speeds were adjusted to the new tubulin concentration every time step and kept constant inbetween.

4.4.6 Nucleation complexes

In our nucleation complex implementation, membrane-associated complexes diffuse with diffusion coefficient D_{NC}. If a complex runs into a microtubule, it binds the microtubule and remains stationary. Therefore, to allow complexes to pass around the ends of microtubules, the x-positions and microtubule directions are tracked for this model variant.

Nucleation complexes are inserted at a constant rate r_b, which can be reduced to $r_{b,min}$ for regions without a microtubule within a distance R in case of microtubule-dependent nucleation complex insertion.

Each individual complex can disassociate from the membrane at a rate r_d and nucleate at a rate r_n (Fig. 4.4A). Based on experimental data from Nakamura et al. [108] this nucleation rate is set a factor fifteen larger for microtubule-bound complexes than for unbound complexes (Appendix 4.7.3). Upon nucleation, the complex involved is removed from the simulation, since experimental observations indicate that complexes that nucleated hardly ever nucleate a second time before disappearing [108]. Positions of new microtubules are adopted from the parent nucleation complex, with the same small vertical displacement that is also used for density-dependent nucleation. The growing plus-end of each new microtubule is oriented either to the left or to the right with an equal probability.

Seeded nucleations are implemented by starting simulations with nucleation complexes with uniformly distributed complex-independent nucleations at a density of 1 nucleation per μm^2. This value has been chosen to be close to the steady state microtubule density.

Nucleation complex diffusion has been implemented using two-dimensional Brownian motion simulations. Complexes move independently in both horizontal and vertical directions every time step by a distance of $\sqrt{2dtD_{NC}}N(0,1)$, where dt is the time step (0.01 s in our simulations), and $N(0,1)$ is a standard normally distributed random number.

4.4.7 Model parameters

All simulation parameters are given in Table S4.2. Basic model parameters were chosen to be consistent with previous simulations of microtubule dynamics in protoxylem development [33]. In the tubulin simulations, D_{tub} and β were varied to study their effect. L_{max} and v_0^+ were tuned such that the average microtubule growth speed at steady state would be approximately equal to that used in simulations without tubulin (see Appendix 4.7.2). Parameters r_b, r_d, $r_{n,bound}$, and $r_{n,unbound}$ were estimated from data by Nakamura et al. [108] (see Appendix 4.7.3). For simulations with microtubule-dependent nucleation complex insertion, we tried several values of $r_{b,min}$ based on our experimental measurements and chose a distance R of 0.05 μm, which is about twice the width of a microtubule.

4.4.8 Measures of heterogeneity

For protoxylem simulations, we counted the number of largely empty bands, defined as bands with less than 25% of the average microtubule density in bands. The persistent heterogeneity measure for transverse interphase arrays was calculated as the standard deviation of the values from a time-averaged microtubule density histogram divided by the average density. We used a histogram bin size of 1 μm and a time average over the last three hours, with one measurement every 200 s.

4.4.9 Experimental measurements

Plant material and growth conditions

Arabidopsis (*Arabidopsis thaliana*, Columbia Col-0 ecotype) expressing the 35S promoter-driven VND7-VP16-GR (VND7) construct, the 35S promoter-driven mCHERRY-TUA5 microtubule marker as well as the GCP3-GFP microtubule nucleation marker were used [33]. Seeds were surface-sterilised and grown similar to [33]. To depolymerize MTs in epidermal cells, we applied 40μM oryzalin for 4 hours and subsequently focussed on cells that showed remaining MT polymers in their cortex.

Induction of protoxylem formation

Three-day old dark-grown seedlings were transferred to half-strength MS, 1% sucrose plates supplemented with 10μM dexamethasone (DEX). The unwrapped plates were then kept in the same phytotron for 24 hours. Subsequently, seedlings were transferred to a microscope slide for imaging.

Spinning disk microscopy

Imaging was performed similar to [33]. Briefly, we used a spinning disc microscope consisting of a CSU-X1 spinning disk head (Yokogawa), an Eclipse TI (Nikon) inverted microscope body equipped with a perfect focus system, an Evolve CCD camera (Photometrics), and a CFI Apo TIRF 100x oil-immersion objective.

Image analysis

Confocal z-stack recordings of microtubules in non-induced and VND7-induced conditions were acquired ($0.3\mu m$ z-steps, $6\mu m$ z-depth, $300ms$ integration time) and surface-projected using a custom-made Matlab code. Confocal single-plane time-lapse recordings of microtubules and GCP3 foci were acquired (1 second intervals, 2 minute duration, 300ms and 500ms integration for microtubules and GCP3, respectively) and analysed using the open-source tracking software FIESTA [234]. The in-built mean-squared displacement function was used to measure the diffusion constant of GCP3 foci. Cumulative lifetime distributions were made using the in-built Matlab function ecdf.m.

4.5 Supplementary figures

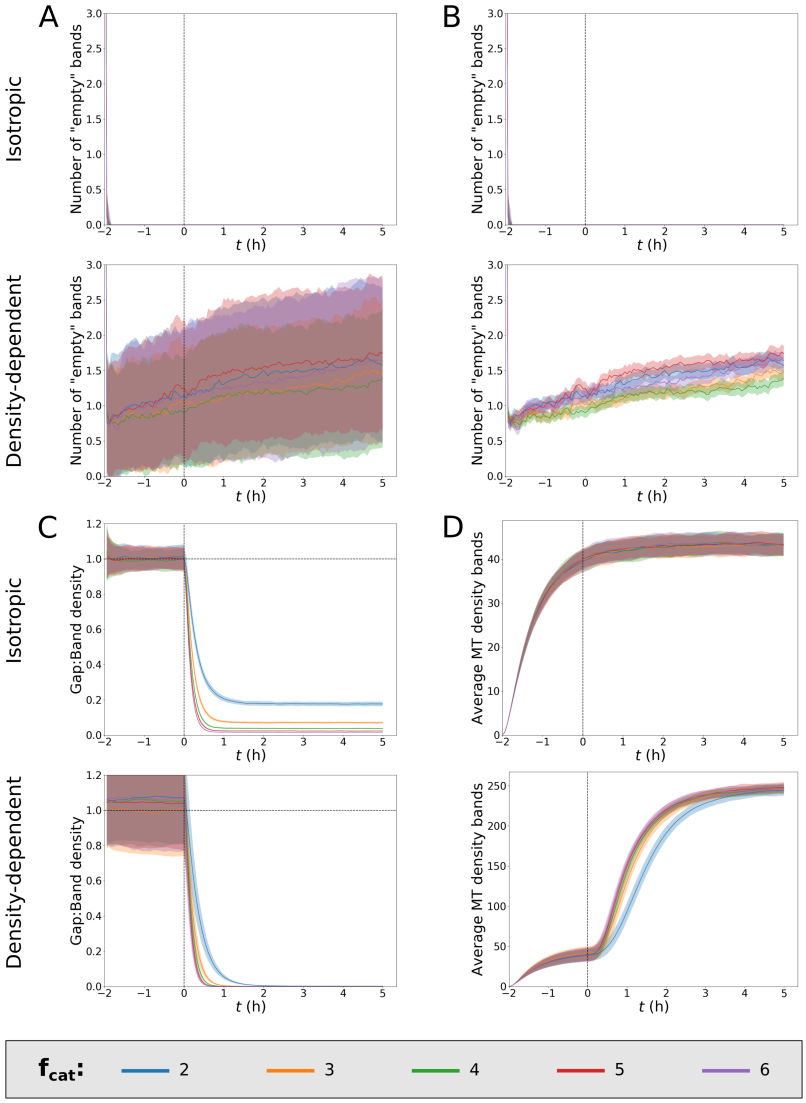

Fig. S4.1. Summary quantities for protoxylem simulations with isotropic and density-dependent nucleation for various factors of difference in the catastrophe rate between bands and gaps (f_{cat}). (A) Number of "empty" bands (defined as bands with less than 25% of average microtubule density in bands). Note that for isotropic nucleation this quantity immediately drops to zero. (B) Same as (A) but with shaded areas representing standard error instead of standard deviation to improve readability. (C) Ratio of microtubule density between gaps and bands. (D) Average microtubule density in bands. All statistics were based on 100 simulations. Lines indicate the average and shaded areas the standard deviation (A,C,D) or standard error (B). Enhanced catastrophe rates in gap regions start at $t = 0$ h for all simulations.

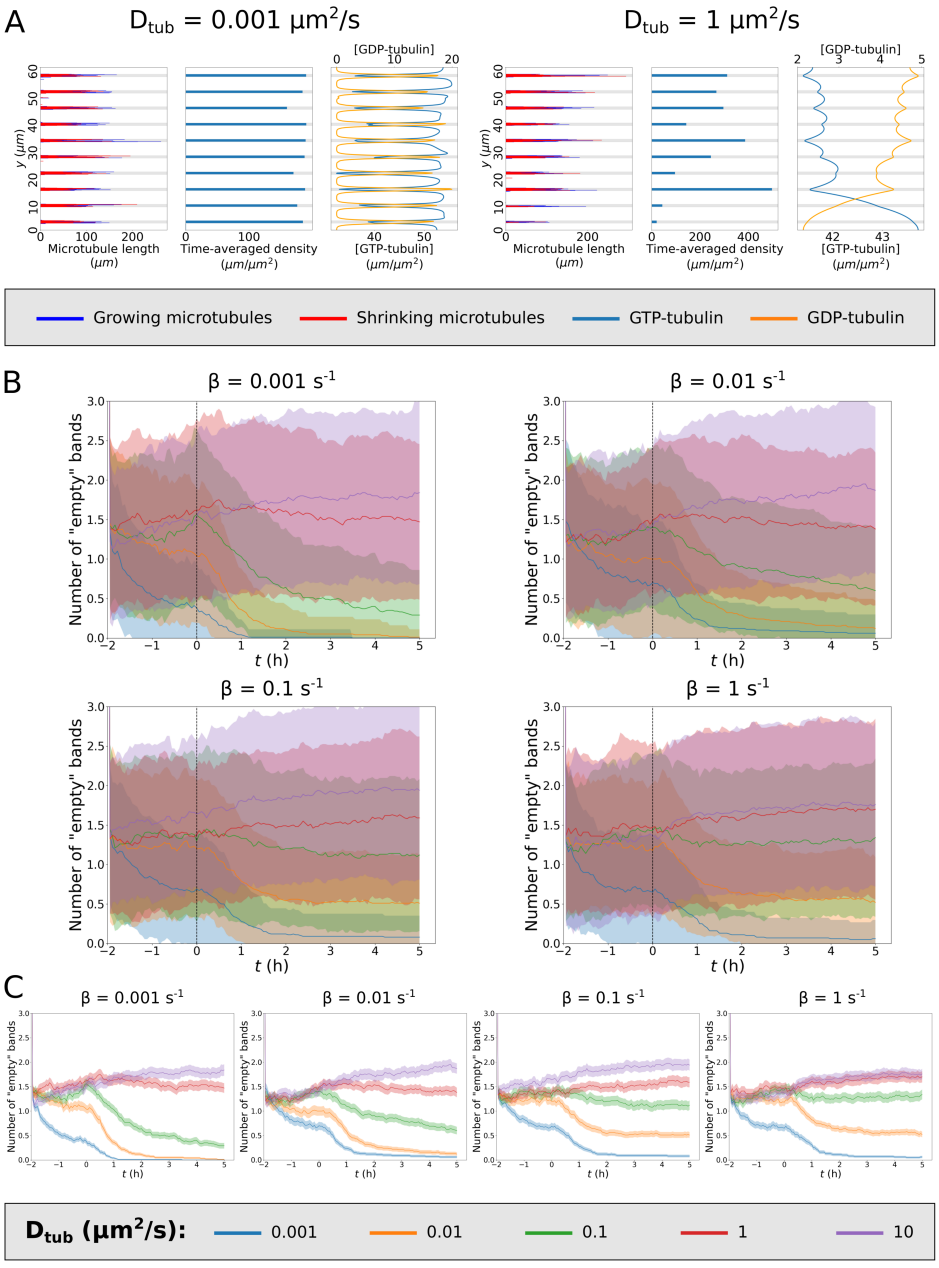

Fig. S4.2. Including the extra step of GDP-tubulin to GTP-tubulin conversion facilitates formation of homogeneously populated bands, but only for biologically unrealistic parameter values. (A) Results of representative simulations with various tubulin diffusion coefficients (D_{tub}) for tubulin recharge rate $\beta = 0.01$. (B) Numbers of empty bands for simulations with various tubulin diffusion coefficients and recharge rates. (C) Same as (B) but with shaded areas representing standard error instead of standard deviation to improve readability. All statistics were based on 100 simulations. Lines indicate the average and shaded areas the standard deviation (B) or standard error (C).

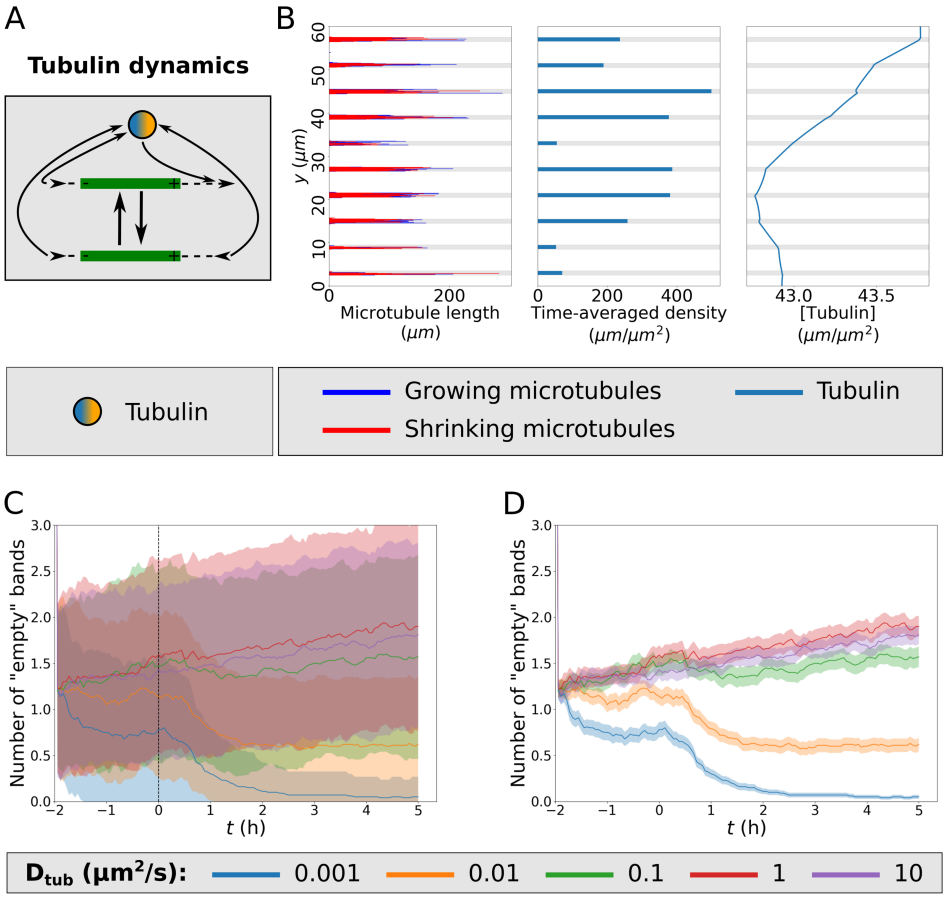

Fig. S4.3. When no distinction is made between GTP- and GDP-tubulin, homogeneously populated bands are hard to achieve. (A) In our tubulin implementation, the v^+ of the growing microtubules depends on the local tubulin concentration, which is depleted as a result. Conversely, microtubule shrinkage increases the local tubulin concentration. (B) Results of a representative simulation with a tubulin diffusion coefficient of 1 $\mu m^2/s$. (C) Number of empty bands (bands with less than 25% of average microtubule density in bands) for simulations with various tubulin diffusion coefficients. (D) Same as (C) but with shaded areas representing standard error instead of standard deviation to improve readability. All statistics were based on 100 simulations. Lines indicate the average and shaded areas the standard deviation (C) or standard error (D).

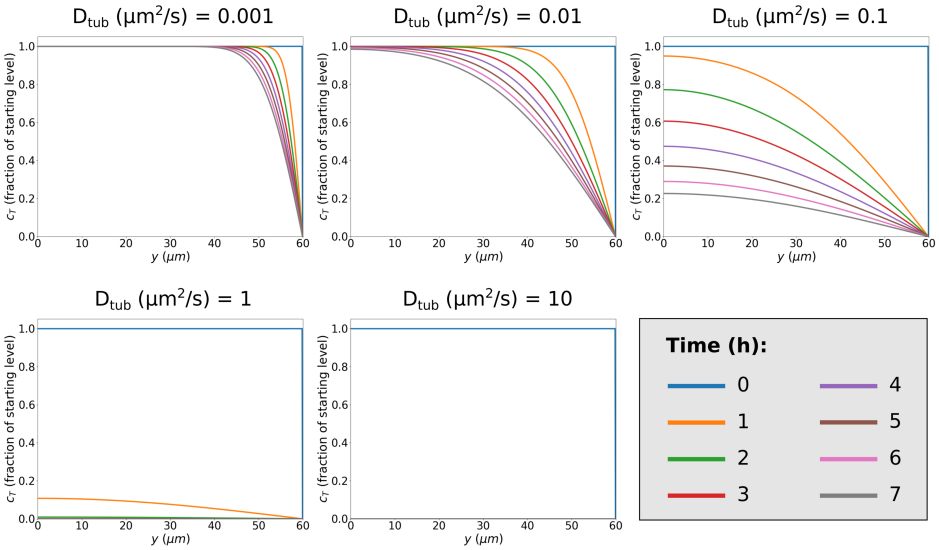

Fig. S4.4. Tubulin barely diffuses from one side of the cell to the other for the lowest diffusion coefficients used in our simulations. Analytic diffusion equation solutions show the tubulin concentration (c_T) at one hour intervals for various tubulin diffusion coefficients (D_{tub}) in absence of microtubules. The left boundary had zero flux boundary conditions and the right boundary was fixed at zero to provide a maximally effective tubulin sink.

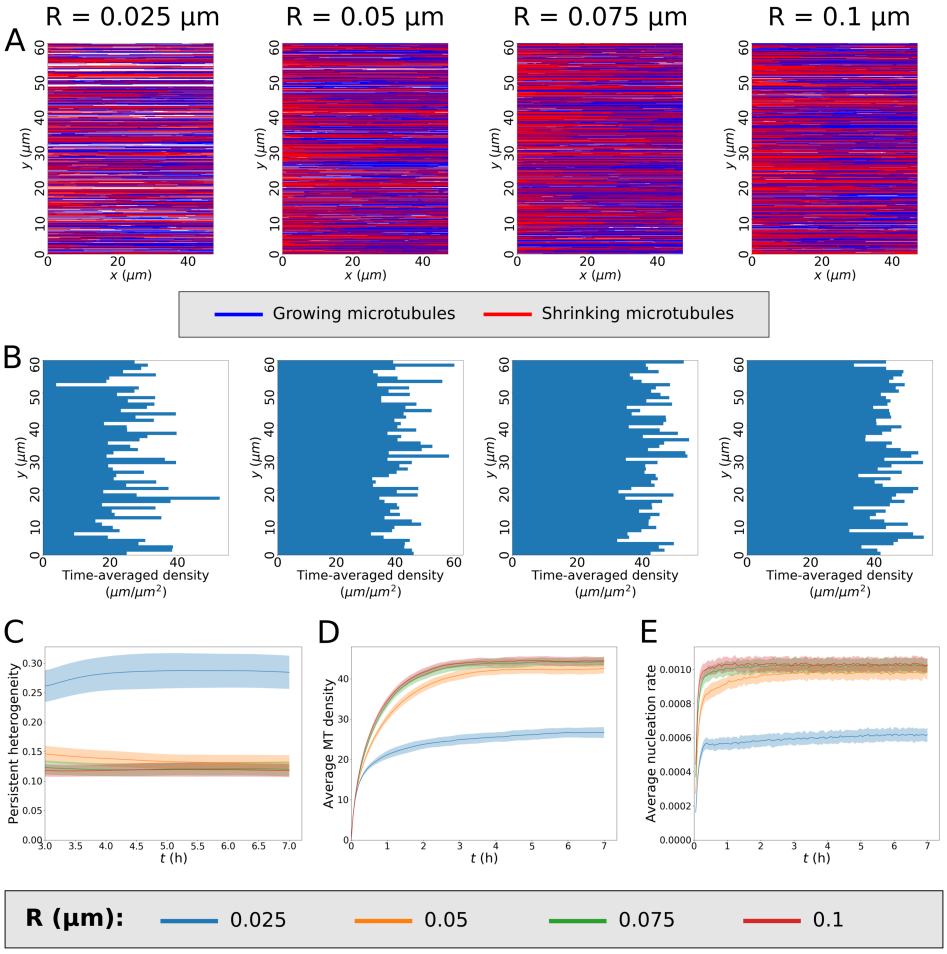

Fig. S4.5. With microtubule-dependent nucleation complex insertion, homogeneous arrays can be established as long as the radius R at which microtubules attract complexes is sufficiently large. (A) Results of representative simulations with different values of R. (B) Time-averaged microtubule densities over the last three hours of the corresponding simulations from (A). (C) Measure of persistent homogeneity. (D) Average microtubule density of the entire array over time. (E) Average global nucleation rate (nucleations/$\mu m^2/s$). All statistics were based on 100 simulations with $D_{NC} = 0.013\ \mu m^2/s$ and $r_{b,min} = r_b/40\ \mu m^{-2}s^{-1}$. Lines indicate the average and shaded areas the standard deviation.

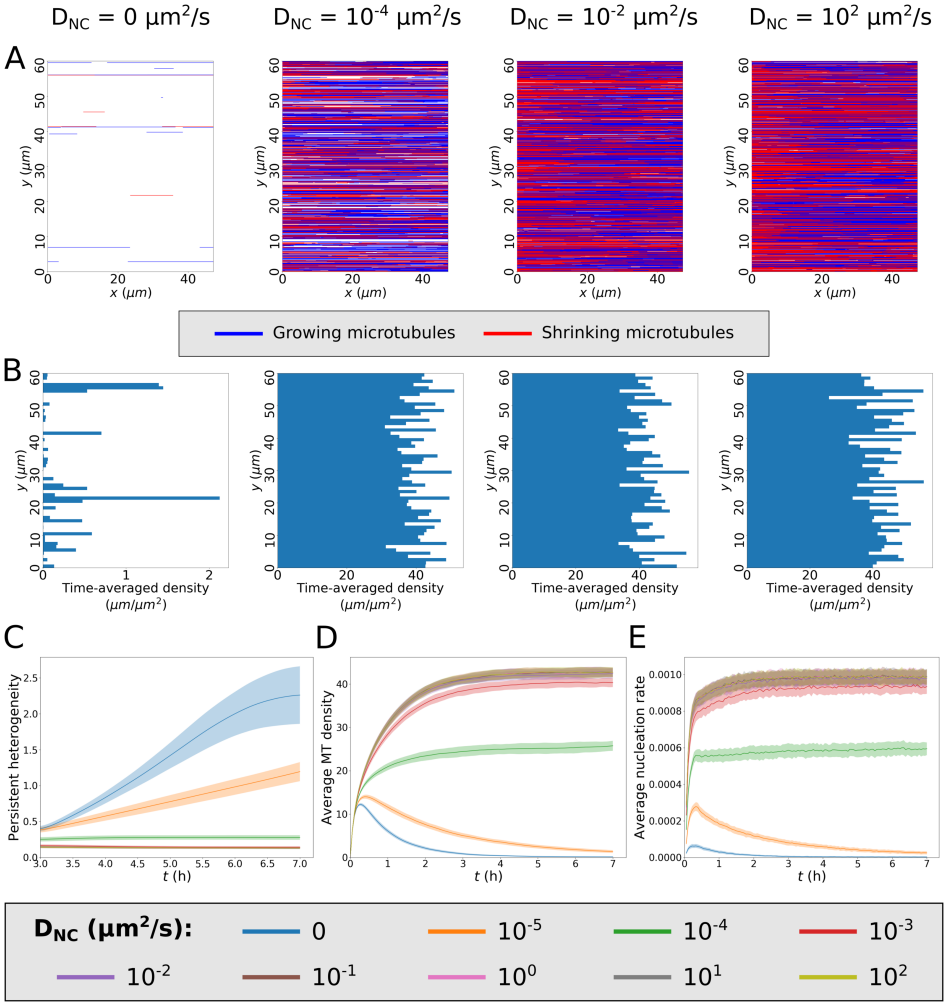

Fig. S4.6. The nucleation complex implementation with microtubule-dependent insertion and a reduced nucleation rate for unbound complex yields homogeneous arrays as long as diffusion coefficients are high enough for complexes to find and bind microtubules. (A) Results of representative simulations with different nucleation complex diffusion coefficients (D_{NC}). (B) Time-averaged microtubule densities over the last three hours of the corresponding simulations from (A). (C) Measure of persistent homogeneity. (D) Average microtubule density of the entire array over time. (E) Average global nucleation rate (nucleations/$\mu m^2/s$). All statistics were based on 100 simulations with $R = 0.05$ μm and $r_{b,min} = r_b/40$ $\mu m^{-2}s^{-1}$. Lines indicate the average and shaded areas the standard deviation.

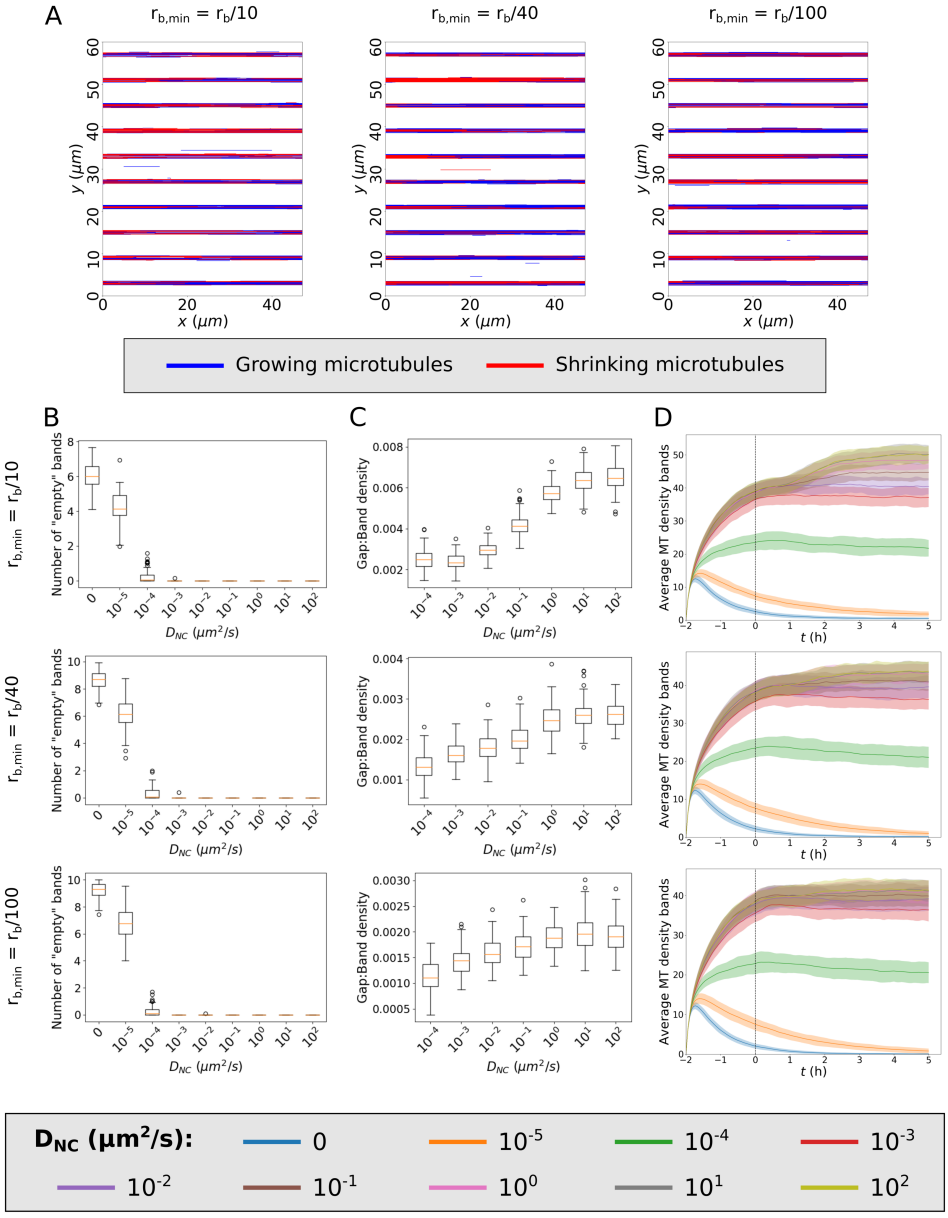

Fig. S4.7. Caption on next page.

Fig. S4.7. Microtubule-dependent nucleation complex insertions greatly improves band formation without resulting in empty bands for reasonable parameter values. (A) Overview of microtubule coverage of the cell membrane for representative simulations with a factor 3 difference in catastrophe rates between bands and gaps, using various values of $r_{b,min}$, and a D_{NC} of 0.013 $\mu m^2/s$. (B) Average numbers of empty bands (bands with less than 25% of average microtubule density in bands) during the last two hours of the simulation. (C) Average ratios between microtubule density in gaps and bands during the last two hours of the simulations. The lowest two diffusion coefficients were disregarded here, because a lack of array density resulted in zero divisions. (D) Microtubule density in bands over time. All statistics were based on 100 simulations for various values of D_{NC} and $r_{b,min}$. Lines indicate the average and shaded areas the standard deviation. Enhanced catastrophe rates in gap regions start at $t = 0$ h for all simulations.

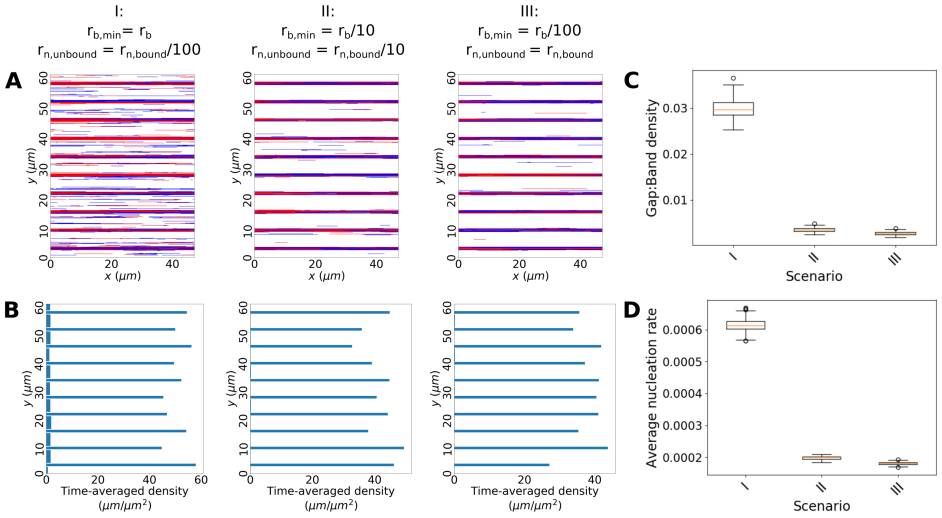

Fig. S4.8. Microtubule-dependent nucleation complex insertion is more effective at improving protoxylem band formation than increased nucleation for microtubule-bound complexes. (A) Representative simulations using a factor 3 difference in catastrophe rates between bands and gaps and $D_{NC} = 0.013 \mu m^2/s$ for various nucleation and insertion scenarios: I: No reduction in insertion rate in absence of microtubules and a hundred fold reduction in nucleation rate for unbound complexes. II: A ten fold reduction in the insertion rate without nearby microtubules and a ten fold reduction in nucleation rate for unbound complexes. III: A hundred fold reduction in the insertion rate without nearby microtubules and no difference in nucleation rate for unbound complexes. (B) Time-averaged microtubule densities over the last three hours of the corresponding simulations from (A). (C) Average ratios between microtubule density in gaps and bands during the last two hours of the simulations. (D) Average global nucleation rate during the last two hours of the simulations. All statistics were based on 100 simulations for the three scenarios described in (A). Enhanced catastrophe rates in gap regions start at $t = 0$ h after two hours without difference in catastrophe rates and end at $t = 5$ h for all simulations.

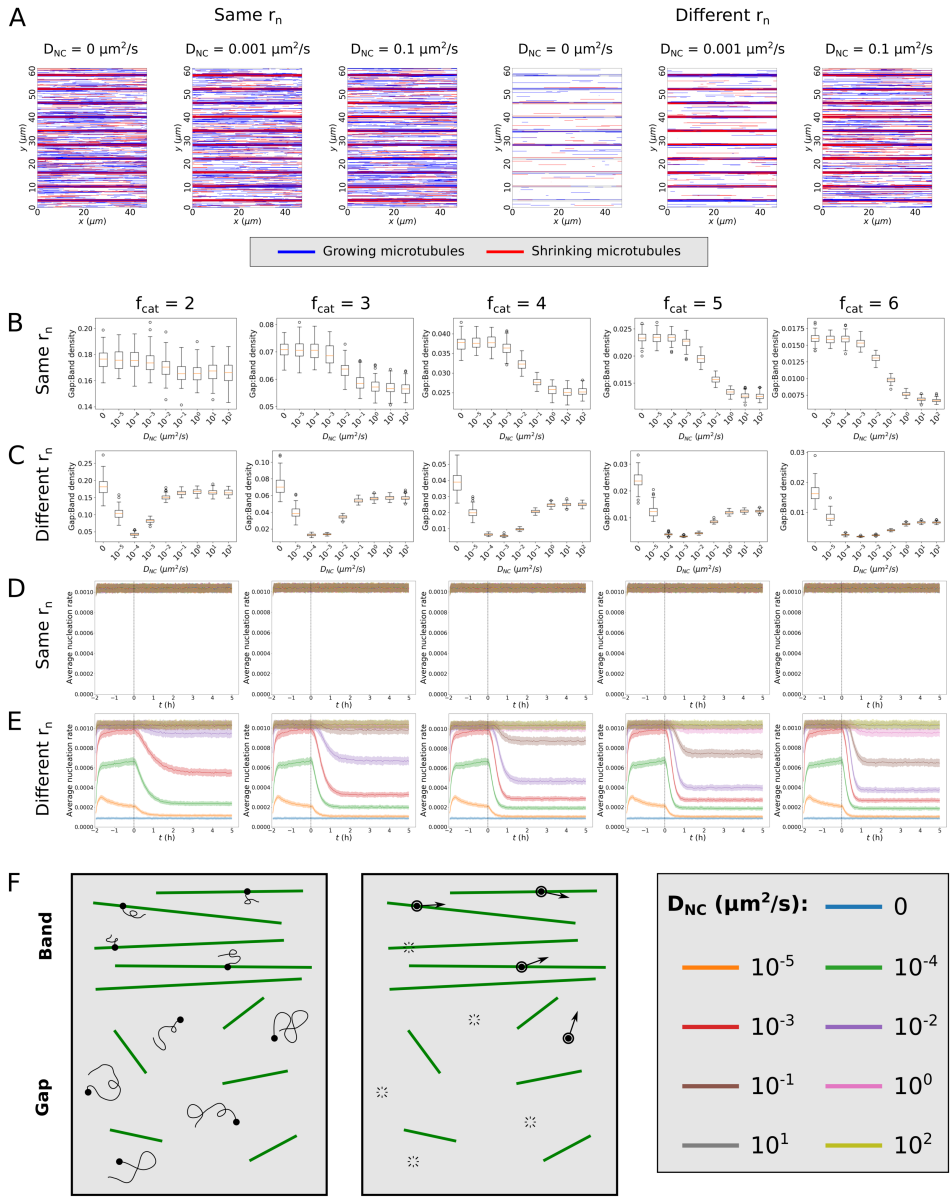

Fig. S4.9. Caption on next page.

Fig. S4.9. In absence of microtubule-dependent nucleation complex insertion, a reduced nucleation rate for unbound complexes results in an optimum in the ratio between gap and band density for intermediate values of the nucleation complex diffusion coefficient (D_{NC}). (A) Representative simulations with and without a different nucleation rate for microtubule-bound and unbound nucleation complexes using a factor 3 difference in catastrophe rates between bands and gaps and various values of D_{NC}. (B,C) Average ratios between microtubule density in gaps and bands during the last two hours of the simulations. (D,E) Average global nucleation rates over time. All statistics were based on 100 simulations with (C,E) and without (B,D) a reduced nucleation rate for unbound complexes, for various factors of difference in band and gap catastrophe rates (f_{cat}) and various nucleation complex diffusion coefficients (D_{NC}). Lines indicate the average and shaded areas the standard deviation. Enhanced catastrophe rates in gap regions start at $t = 0$ h for all simulations. (F) Proposed mechanism of separation enhancement. Nucleation complexes in the bands are likely to encounter a microtubule in their lifetime and will therefore benefit from the higher bound nucleation rate, while complexes in the gaps are more likely to disappear before they encounter a microtubule and therefore largely follow the lower unbound nucleation rate.

4.6 Supplementary tables

Table S4.1. Nucleation complexes insert more readily near existing microtubules. Comparison of nucleation complex insertions in oryzalin-treated cells and controls. The literature estimate for the insertion rate that we used in the simulations to keep the overall nucleation rate comparable was 0.0045 $\mu m^{-2}s^{-1}$.

Treatment:	Mock	Oryzalin	Oryzalin	Oryzalin	
Area:	Total	Total	Non-microtubule	Microtubule	Unit
Number of nucleation complexes inserted	338	170	55	115	-
Membrane area	873	5445	5372	73	μm^2
Measurement time	120	120	120	120	s
Estimated insertion rate	0.0037	0.00026	0.000085	0.013	$\mu m^{-2}s^{-1}$
Factor lower than literature estimate	1.4	17.3	52.7	0.35	-

Table S4.2. Default parameter values used in the simulations.

Parameter	Value	Unit	Description	Source
Simulation domain				
H	60	μm	Domain height	[33]
W	$7.5 \cdot 2\pi$	μm	Domain circumference	[33]
Standard parameters				
v^+	0.05	$\mu m/s$	Growth speed	[33]
v^-	0.08	$\mu m/s$	Shrinkage speed	[33]
v^{tm}	0.01	$\mu m/s$	Treadmilling speed	[33]
r_c	0.0016	s^{-1}	Catastrophe rate (bands)	[33]
r_r	0.001	s^{-1}	Rescue rate	[33]
r_n	0.001	$\mu m^{-2}s^{-1}$	Nucleation rate	[33]
f_{cat}	3		Factor increased catastrophe rate in gaps	
Density-dependent nucleation				
$\rho_{\frac{1}{2}}$	0.1	$\mu m/\mu m^2$	Microtubule density at which half of all nucleations are microtubule-bound	[160]
Tubulin limited growth				
D_{tub}	Variable	$\mu m^2/s$	Tubulin diffusion coefficient	
β	0.01	s^{-1}	Tubulin recharge rate	
v_0^+	0.1	$\mu m/s$	Initial growth speed	Appendix 4.7.2
L_{max}	$2.4 \cdot 10^4$	μm	Maximum total microtubule length	Appendix 4.7.2
Nucleation complexes				
r_b	0.0045	$\mu m^{-2}s^{-1}$	Insertion rate	Appendix 4.7.3
r_d	0.1	s^{-1}	Dissociation rate	Appendix 4.7.3
D_{NC}	0.013	$\mu m^2/s$	Nucleation complex diffusion coefficient	This chapter
$r_{n,bound}$	0.03	s^{-1}	Bound nucleation rate	Appendix 4.7.3
$r_{n,unbound}$	0.002	s^{-1}	Unbound nucleation rate	Appendix 4.7.3
Microtubule-dependent nucleation complex insertion				
$r_{b,min}$	$r_b/40$	$\mu m^{-2}s^{-1}$	Insertion rate in absence of microtubules	
R	0.05	μm	Radius in which nucleation complex insertion is enhanced by microtubules	

4.7 Appendices

4.7.1 Steady state densities for non-interacting microtubules

The average microtubule density at steady state $\rho^\star$ can be calculated from the theoretically derived microtubule length distribution:

$$\rho^\star = \int_{l=0}^{l=\infty} l \cdot m(l) dl \tag{A4.1}$$

where $m(l)$ is the density of microtubules with length l. Following the procedure described by Dogterom and Leibler [235] with the addition of the treadmilling speed, we obtain the following expression for the steady state length distributions for non-interacting growing and shrinking microtubules:

$$\begin{aligned} m(l) &= m^+(l) + m^-(l) = \frac{r_n}{v^+ - v^{tm}} e^{-\lambda l} + \frac{r_n}{v^- + v^{tm}} e^{-\lambda l} \\ &= r_n \frac{v^+ + v^-}{(v^+ - v^{tm})(v^- + v^{tm})} e^{-\lambda l}, \end{aligned} \tag{A4.2}$$

where r_n is the nucleation rate, v^+, v^-, and v^{tm} are the microtubule growth, shrinkage, and treadmilling speeds, respectively, and exponent λ is given by:

$$\lambda = \frac{r_c}{v^+ - v^{tm}} - \frac{r_r}{v^- + v^{tm}}, \tag{A4.3}$$

where r_c is the catastrophe rate and r_r is the rescue rate.

Using this expression for $m(l)$, Eq. A4.1 can be solved using integration by parts:

$$\begin{aligned} \rho^\star &= \int_{l=0}^{l=\infty} l \cdot r_n \frac{v^+ + v^-}{(v^+ - v^{tm})(v^- + v^{tm})} e^{-\lambda l} dl \\ &= r_n \frac{(v^+ + v^-)(v^+ - v^{tm})(v^- + v^{tm})}{(r_c(v^- + v^{tm}) - r_r(v^+ - v^{tm}))^2}. \end{aligned} \tag{A4.4}$$

Using this formula, we can now calculate the steady state ratio between microtubule densities in gap and band regions ($\rho^\star_{gaps}/\rho^\star_{bands}$) using the catastrophe rates for gap and band regions respectively and default values for the other parameters. This way, we obtain ratios of 0.18, 0.070, 0.038, 0.023, and 0.016 for a factor difference in catastrophe rates of 2, 3, 4, 5, and 6, respectively. These values are consistent with the ones found in our simulations with isotropic nucleation (Fig. S4.1C).

4.7.2 Calculating maximal total microtubule length and initial growth speed

For comparison purposes, we want to set the average effective growth speed to be comparable to that used in previous simulations by choosing appropriate values for v_0^+ and L_{max}. The average local growth speed $\bar{v^+}$ can be obtained from Eq. 4.4 in the main text as follows:

$$\bar{v^+} = v_0^+ \frac{\bar{c_T}}{L_{max}/A}, \tag{A4.5}$$

where $\bar{c_T}$ is the average (GTP-)tubulin concentration. This concentration can be calculated from the total tubulin length in microtubules L_{MT} as follows, assuming the GDP-tubulin concentration is low compared to the GTP-tubulin concentration for models with two tubulins:

$$\bar{c_T} = \frac{L_{max} - L_{MT}}{A} = \frac{L_{max} - \sum_{j=1}^{N_{MT}} l_j}{A}, \tag{A4.6}$$

where N_{MT} is the total number of microtubules and l_j is the length of the j^{th} microtubule. This means the average growth speed will be given by:

$$\bar{v^+} = v_0^+ \frac{L_{max} - L_{MT}}{L_{max}}. \tag{A4.7}$$

Therefore, the average growth speed depends on the initial growth speed and the fraction of the total amount of tubulin that is part of microtubules. Assuming that we choose an L_{max} that is larger than the required microtubule length, we can calculate a value for v_0^+ that will end up giving us the desired growth speed:

$$v_0^+ = \bar{v^+} \frac{L_{max}}{L_{max} - L_{MT}}. \tag{A4.8}$$

However, we still need an expression for L_{MT}. The total microtubule length at steady state can be calculated from the theoretically derived microtubule length distribution:

$$L_{MT} = \sum_{j=1}^{N_{MT}} l_j = \int_A \int_{l=0}^{l=\infty} l \cdot m(l) dl dA = A \int_{l=0}^{l=\infty} l \cdot m(l) dl \tag{A4.9}$$

where $m(l)$ is the density of microtubules with length l, as given by Eq. A4.2 from the previous section.

Using this expression for $m(l)$, Eq. A4.9 can be solved using integration by parts:

$$\begin{aligned} L_{MT} &= A \int_{l=0}^{l=\infty} l \cdot r_n \frac{v^+ + v^-}{(v^+ - v^{tm})(v^- + v^{tm})} e^{-\lambda l} dl \\ &= r_n A \frac{(v^+ + v^-)(v^+ - v^{tm})(v^- + v^{tm})}{(r_c(v^- + v^{tm}) - r_r(v^+ - v^{tm}))^2}. \end{aligned} \tag{A4.10}$$

With this expression we can now write down an equation for the expected growth speed at steady state (using $v^+ = \bar{v^+}$):

$$\bar{v^+} = v_0^+ \frac{L_{max} - r_n A \frac{(\bar{v^+} + v^-)(\bar{v^+} - v^{tm})(v^- + v^{tm})}{(r_c(v^- + v^{tm}) - r_r(\bar{v^+} - v^{tm}))^2}}{L_{max}}. \tag{A4.11}$$

Assuming we choose an $L_{max} > L_{MT}$, the v_0^+ we need is given by:

$$v_0^+ = \bar{v^+} \frac{L_{max}}{L_{max} - r_n A \frac{(\bar{v^+} + v^-)(\bar{v^+} - v^{tm})(v^- + v^{tm})}{(r_c(v^- + v^{tm}) - r_r(\bar{v^+} - v^{tm}))^2}}. \tag{A4.12}$$

Using averages in this way is probably not entirely accurate, because most microtubules are likely to end up in band regions where the tubulin concentration is expected to be

lower and, correspondingly, the growth speed will be below average. However, since differences in (GTP-)tubulin concentration are not expected to be very large, this estimate should result in reasonably comparable growth speeds.

The length distribution equations were derived for a homogeneous system, while our system uses bands and gaps with different catastrophe rates. However, under the density-dependent nucleation mechanism, most microtubules and nucleations end up in the band regions, making the band catastrophe rate a reasonable approximation. Also, because the density-dependent nucleation mechanism maintains the same global nucleation rate, while only changing the location of the nucleations, we can use the same value for $r_n A$, even though r_n is locally higher in microtubule dense regions and lower in regions with few microtubules.

Using our default values for the parameters we find an L_{MT} of $1.22 \cdot 10^5$ μm. The value we choose for L_{max} should be larger than this value. We set it to 240000 μm, about double the total microtubule length we expect. Using this value we can calculate that we need to set our v_0^+ to about 0.1 $\mu m/s$ to end up with more or less the same growth speed.

4.7.3 Estimation of nucleation complex parameters

There are two types of events that can occur to a nucleation complex at the membrane: dissociation and nucleation. Average times until these events occur have been measured by Nakamura et al. [108] both for complexes on microtubules and complexes not on microtubules, using labelled versions of two different nucleation complex proteins (GCP2 and GCP3). From these measurements we can make rough estimates the dissociation and nucleation rates for our simulations.

For complexes not on microtubules, the average time until an event occurs, averaged over both types of events and both GCP2 and GCP3 labels (383 observations of which 9 nucleations), is:

$$\bar{t}_{event} = 10s. \tag{A4.13}$$

The rate λ at which events occur is therefore:

$$\lambda = \frac{1}{\bar{t}_{event}} = 0.099s^{-1}. \tag{A4.14}$$

The fraction f_n of events that turn out to be nucleations is:

$$f_n = 0.023. \tag{A4.15}$$

Since this number is based on only nine observations, it is very uncertain, but it should at least give us a rough estimate of the order of magnitude. From this estimate, the individual rates for nucleation and dissociation can be calculated:

$$\begin{aligned} r_{n,unbound} &= \lambda \cdot f_n = 0.0023s^{-1} \\ r_{d,unbound} &= \lambda \cdot (1 - f_n) = 0.097s^{-1}, \end{aligned} \tag{A4.16}$$

where $r_{n,unbound}$ and $r_{d,unbound}$ are the estimated nucleation and dissociation rates for unbound complexes, respectively.

In the same way, we can calculate these parameters for microtubule-bound complexes, which have an average event time of $7.2s$ and nucleations make up a fraction of 0.24

(based on 624 nucleations out of 2555 events). These numbers yield the following values for the bound nucleation and dissociation rates:

$$\begin{aligned} r_{n,bound} &= 0.034 s^{-1} \\ r_{d,bound} &= 0.10 s^{-1}, \end{aligned} \tag{A4.17}$$

where $r_{n,bound}$ and $r_{d,bound}$ are the estimated nucleation and dissociation rates for bound complexes, respectively.

The estimated dissociation rates for bound and unbound complexes are very similar. Therefore, we used a single dissociation rate of $r_d = 0.1 s^{-1}$ for all our simulations. For the nucleation rates, however, there is approximately a factor fifteen difference between estimated rates of nucleation for bound and unbound complexes. Therefore, we used a bound nucleation rate of $r_{n,bound} = 0.03 s^{-1}$ and an unbound nucleation rate of $r_{n,unbound} = 0.002 s^{-1}$.

Finally, we estimated a membrane association rate (r_b) for nucleation complexes such that the final overall nucleation rate would be close to that of $r_n = 0.001 \mu m^{-2} s^{-1}$ used in the other simulations. To achieve this, we first need to estimate a total number of nucleation complexes. A nucleation complex density of 0.037 particles per μm^2 was reported by Nakamura et al. [108]. Using our total domain area, we find that on average the total number of particles N_{NC} on our domain should be approximately:

$$N_{NC} = 0.037 \cdot H \cdot W = 105. \tag{A4.18}$$

This is includes particles that have already had a nucleation but were not yet released. Those particles are not considered in our simulations, so this number represents an upper bound.

For a lower bound on this number, we can work backwards from the overall nucleation rate used in the previous simulations. If we turn this value into a rate per cell, we get:

$$r_{n,cell} = r_n \cdot A = 0.001 \cdot 2826 = 2.826 \text{ nucleations/cell/s}, \tag{A4.19}$$

where A is the area of the simulation domain. This number includes both nucleations of microtubule-bound complex and free complex. In our model context, $r_{n,cell}$ can be calculated from the total number of complexes available for nucleation, the fraction of complexes that is microtubule-bound (f_{bound}) and the bound and unbound nucleation rates calculated above:

$$r_{n,cell} = f_{bound} \cdot N_{NC} \cdot r_{n,bound} + (1 - f_{bound}) \cdot N_{NC} \cdot r_{n,unbound}. \tag{A4.20}$$

We can rewrite this to estimate the number of nucleation complexes for a given nucleation rate:

$$N_{NC} = \frac{r_{n,cell}}{f_{bound} \cdot r_{n,bound} + (1 - f_{bound}) \cdot r_{n,unbound}}. \tag{A4.21}$$

The fraction of bound complex can be estimated from the total number of events that were observed on microtubules (2555 for both GCP labels and event types out of 2938 total events) by Nakamura et al. [108], resulting in:

$$f_{bound} = 0.87. \tag{A4.22}$$

This is not entirely accurate since we need the bound fraction at any given time and this is the fraction of observed events where the nucleation complexes were microtubule-bound. Since bound complexes have slightly faster event rates (due to their higher chance of nucleation) there will be fewer of them in our simulations at any given time than this estimate would suggest. Because the bound nucleation rate is much higher than the unbound rate, the number of complexes estimated for a given overall nucleation rate would be an underestimate. This suggests the following lower bound on the number of nucleation complexes:

$$N_{NC} = \frac{2.826}{0.87 \cdot 0.0337 + 0.13 \cdot 0.00233} = 95.4. \tag{A4.23}$$

The number of complexes available for nucleation can be used to estimate the association rate of new nucleation complexes with the membrane. At some point the association rate must be balanced by the removal and nucleation rates to reach a steady state. Taking 100 complexes, and the overall nucleation rate from Eq. A4.19, we get:

$$\begin{aligned} r_b =& N_{NC} \cdot r_d + r_{n,cell} = 100 \cdot 0.1 + 2.826 = \\ & 12.826 \text{ associations}/s = 0.0045 \text{ associations}/\mu m^2/s. \end{aligned} \tag{A4.24}$$

Based on this estimate, we chose an association rate of 0.0045 $\mu m^{-2} s^{-1}$.

5

Protoxylem microtubule patterning requires ROP pattern co-alignment, realistic microtubule-based nucleation, and sufficient microtubule flexibility

Bas Jacobs

Laura Filion

Jaap Molenaar

Eva E. Deinum

Abstract

Water transport in plants relies on a specialised system of vessels known as the xylem. Xylem development involves the deposition of secondary cell wall reinforcements in intricate and highly functional patterns, such as the ringed or spiral patterns in early-developing protoxylem, which provide rigidity while still allowing the vessels to elongate with the surrounding tissue. The pattern of cell wall deposition follows the underlying pattern of cortical microtubules which, in turn, follows an underlying pattern of ROP proteins that determines where microtubules are destabilised. Simulation models have been crucial in understanding the self-organisation of the highly dynamic cortical microtubule array. So far, however, no one has been able to reproduce a banded pattern for realistic microtubule behaviour. Here, we extend current models with three biologically realistic aspects that improve the formation of a banded microtubule pattern: (1) co-alignment between the initial microtubule array and the underlying ROP pattern, (2) microtubule flexibility, and (3) locally saturating microtubule nucleation. We further test our simulations with measured microtubule dynamics data from individual cells. The results suggest a need for a dynamic compensation of other parameters or some alternative mechanism to improve the robustness of the patterning process. In addition, the ability of cells to start forming bands when differences in measured parameters are still too small to explain their appearance suggests the existence of additional separation factors beyond existing measurements, for which we explore several options in our simulations. Our improved simulations helped identify requirements for complex patterning in the cortical microtubule array.

5.1 Introduction

Plants, like all other forms of life, need water to grow. Even the tallest trees acquire this water through their roots and therefore need to transport this water to their leafs across sometimes more than a hundred meters. To achieve this task, vascular plants possess an extensive vascular system known as the xylem [1]. Xylem vessels develop from specialised cells which deposit thick secondary cell walls before undergoing programmed cell death, leaving a hollow tube [3]. These secondary cell wall reinforcements are required to withstand the pressures generated during water transport and can be deposited in intricate patterns. At the growing tips of roots and shoots, two types of early developing xylem ('primary xylem') can be distinguished: protoxylem and metaxylem [6]. Protoxylem matures when the surrounding tissue is still elongating, and therefore has ringed or spiral cell wall reinforcements that can be stretched themselves. Metaxylem develops later, when tissue elongation has finished, allowing for sturdier reinforcements that cannot be stretched, with regularly spaced gaps for radial transport [7–9].

The deposition of these patterned secondary cell walls follows the pattern of the cortical microtubule array, which guides both the deposition of cell wall material [119] and the orientation of the cellulose microfibrils, the main load-bearing component of the cell wall [117, 118, 120, 122]. The pattern of the microtubule array, in turn, depends on the local activity of ROP proteins that recruit microtubule-destabilising effectors [147–149]. Microtubules also feed back on the shape of the ROP pattern by anisotropically restricting active ROP diffusion [148, 154]. This diffusion restriction can flatten the ROP pattern, even change it from gaps to bands, and orient it in the direction of the microtubules (chapter 3).

Microtubules are highly dynamic tube-shaped polymers that switch between growing and shrinking states in a process called dynamic instability [99]. Since cortical microtubules are attached to the inside of the cell membrane, growing microtubules inevitably collide with other microtubules. The outcome of these collisions depends strongly on the collision angle. For collisions at small relative angles ($\lesssim 40°$), the colliding microtubule tends to bend and grow along the obstructing microtubule ('bundling'). For collisions at larger angles, the colliding microtubule either starts shrinking (a so-called 'induced catastrophe') or skips over the obstructing microtubule and continues growing (a 'crossover') [110]. Extensive modelling studies have demonstrated that these basic rules are sufficient to achieve spontaneous alignment of the microtubule array through a mechanism dubbed 'survival of the aligned' [134–137]. This alignment mechanism can be further aided by microtubule-severing protein katanin. Katanin selectively severs overlying microtubules at crossover intersections [111, 112], usually leaving the the newly formed plus end in a shrinking state, which contributes to alignment by pruning discordant microtubules [138, 140].

Protoxylem patterning starts with such an aligned array, which then progressively separates into many regularly spaced bands [122]. This microtubule band formation is caused by a difference in microtubule dynamics between future band and gap regions [33], most likely following band and gap regions specified by a ROP pattern. However, it turns out that the question how microtubules populate the bands of such a prepattern is far from trivial. A modelling study using fixed band and gap regions with different microtubule dynamics found that it was not possible to obtain a pronounced distinction in microtubule

density between band and gap regions at a realistic time scale when using isotropic nucleation of new microtubules (i.e., new microtubules are uniformly distributed with a random orientation) [33]. Adding their implementation of microtubule-based nucleation did yield a rapid differentiation of band and gap densities, but with all density in just one or two band regions, leaving the others mostly empty [33].

This accumulation of microtubules into a single band is part of a larger problem: most implementations of microtubule-based nucleation result in strongly inhomogeneous microtubule arrays [135, 136, 160, 161]. Solving this so-called inhomogeneity problem (chapter 4) is important for our understanding of plant microtubule organisation, because, in plants, the vast majority of nucleations in established arrays occur from nucleation complexes (so-called 'γ-tubulin ring complexes') bound to existing microtubules [105, 107]. The newly formed microtubule is then oriented either along the parent microtubule or 'branched' at an average angle of about 35° [109]. The cause of the inhomogeneity problem is that in the simplest implementation of microtubule-based nucleation, a globally limited amount of nucleations is distributed over all microtubules proportional to their length (density-dependent nucleation), resulting in a global competition for nucleations. We recently showed that a more detailed implementation with explicitly modelled nucleation complexes based on experimental observations, could restore homogeneity by ensuring a local limitation to the nucleation supply rather than a global one (chapter 4).

This new nucleation implementation also solved the homogeneity problem for protoxylem band formation, allowing a regular pattern of microtubule bands to form in the simplified one-dimensional microtubule model we used. However, in this simplified modelling context, regular band formation could also be achieved in a reasonable time frame with the equivalent of isotropic nucleation, i.e., uniformly distributed nucleations in the same direction (chapter 4). These results suggest that there are crucial differences with the two-dimensional context, where microtubules can cross the band-gap boundary and bundling interactions may increase the life time of local microtubule structures. Therefore, while it solves the inhomogeneity problem, the more realistic nucleation mode may not be sufficient to explain how the microtubule array can organise itself into a banded protoxylem pattern given an underlying prepattern. This raises two questions: 1) What is the impact of exact co-alignment between microtubules and ROP pattern and how well is a mismatch tolerated between ROP pattern and microtubule orientation? 2) What is the impact of biologically realistic microtubule-based nucleation on protoxylem band formation in a two-dimensional context?

Here, we explore the mechanistic requirements for microtubule band formation in developing protoxylem in a two-dimensional microtubule modelling context. We will first examine the effect of co-alignment between the initial microtubule array and the prepattern of band and gap regions. A lack of co-alignment accounts for one of the main differences between the one- and two-dimensional microtubule simulation context. However, a degree of co-alignment is biologically realistic as a result of microtubule-based ROP diffusion restriction (chapter 3), and should therefore be taken into account in two-dimensional simulations. We also investigate the potential of microtubule flexibility to compensate for small mis-alignments. Having examined the general effects of co-alignment and microtubule flexibility under isotropic nucleation, we then develop a computationally efficient nucleation mode inspired by our previous measurements and simulations of nucleation complexes (chapter 4). We use this nucleation mode to study how realistic microtubule-

based nucleations influence protoxylem patterning. Finally, we test how well our simulations perform with the microtubule-dynamics parameters obtained from experimental measurements on four different individual cells [33], which differ substantially from each other.

5.2 Results

5.2.1 Model outline

We performed simulations using an extended version of the cortical microtubule simulation software 'corticalSim', an implementation of an event-driven algorithm for simulating microtubule dynamics and interactions on a two-dimensional surface [33, 103, 134, 138, 160]. Unless stated otherwise, we used a cylindrical geometry with dimensions representative of a developing protoxylem cell. The edges of the cylinder induced catastrophes to favour a transverse array orientation [124]. Simulated microtubules showed dynamic instability by switching between growing and shrinking states (Fig. 5.1A). Microtubule collisions could result in bundling, crossovers, and induced catastrophes depending on relative collision angles (Fig. 5.1B). A constant rate of severing the overlaying microtubules at intersections represented katanin activity (Fig. 5.1C). Experimental observations of protoxylem development show that microtubule patterning starts from a well-established transversely oriented array [33, 122]. We, therefore, started our simulations with a two hour initiation phase without band-gap differences, with a biased orientation of microtubule nucleations during the first half an hour. In this biased phase, all microtubules were nucleated at a variable angle α_{init}, drawn from a normal distribution with a mean of α_{bias} and a variance of α_{noise} (Fig. 5.1D). After this first half an hour, the nucleation mode was switched to the one that would be used in the rest of the simulation. After the two hour initiation phase, we simulated protoxylem band formation by imposing predefined gap regions, where the catastrophe rate was reduced by a factor f_{cat}, and band regions where it was not (Fig. 5.1E), similar to simulations by Schneider et al. [33]. These predefined gap regions represented the local activity of proteins specifying the banded pattern, most likely ROPs and their downstream effectors [148, 150]. For further details and all parameter values see Methods.

5.2.2 Strong co-alignment of the microtubule array with a pre-existing band pattern facilitates rapid microtubule band formation

The simplest mode of nucleating new microtubules is isotropic nucleation, in which both the locations and the angles of microtubules are uniformly distributed. Previous simulation work has suggested that proper separation of the microtubule array in band and gap regions cannot be achieved with isotropic nucleation in a biologically realistic time frame of about five hours [33]. However, when we used the aforementioned initiation phase to obtain starting arrays that were sufficiently co-aligned with the predefined band regions, bands could form rapidly (Fig. 5.1F–I). Presumably, co-alignment speeds up band formation because the density already present in the band regions can be maintained. Without co-alignment, obstructing microtubules would have to be replaced by new microtubules

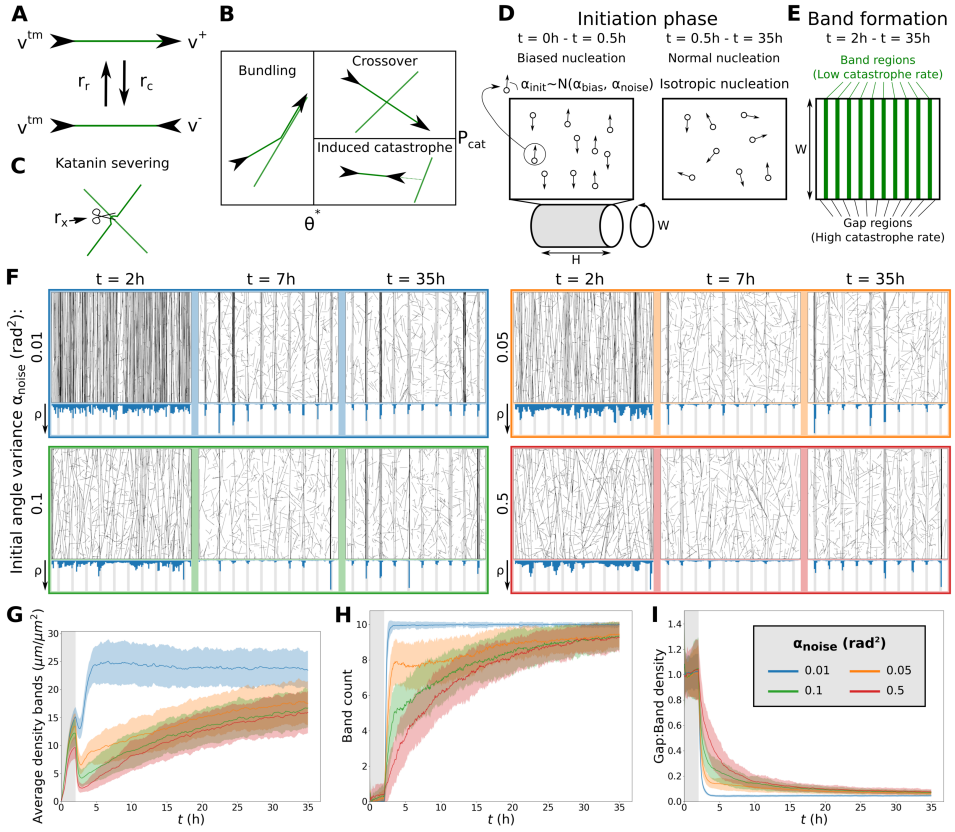

Fig. 5.1. Isotropic nucleation allows fast band formation for sufficiently co-aligned arrays. (A–E) Model outline and implementation. (A) Microtubule plus ends grow or shrink at constant rates v^+ or v^-, respectively, and minus ends retract at constant rate v^{tm}. Spontaneous catastrophes (switch from growing to shrinking) occur at a rate r_c and rescues (switch from shrinking to growing) at a rate r_r. (B) Microtubule-microtubule collision outcomes depend on the collision angle. At angles below θ^* the impinging microtubule bundles with, i.e., continues growing along, the obstructing one. At greater collision angles, the incoming microtubule undergoes an induced catastrophe with a probability P_{cat} and crosses over the other microtubule otherwise [103, 134]. (C) Katanin severs the overlying microtubule at crossovers at a constant rate r_x per crossover. (D) An initial transverse array is artificially enforced by drawing nucleation angles in the first half hour (α_{init}) from a normal distribution with an average of α_{bias} and a variance of α_{noise}. (E) Protoxylem band formation is simulated with predefined band and gap regions, where the catastrophe rate in the gap regions is increased by a factor f_{cat} after a $2h$ initiation phase, following [33], except that f_{cat} is reduced to 3. (F) Snapshots from protoxylem simulations with isotropic nucleation using starting arrays obtained with different values for α_{noise}. Histograms below snapshots showing local microtubule density ρ share the same axis within a time series, but not between time series. (G) Average microtubule density in the band regions. (H) Number of populated bands, defined as bands with a microtubule density greater than three times the average density in the gaps. (I) Ratio of density in gaps and bands. Quantities in (G–I) were calculated from 100 simulations. The band formation phase starts at the end of the grey area. Lines indicate the average and shaded areas the standard deviation.

with the correct orientation, which takes time and involves first losing most of the microtubule density that was already in the bands (Fig. 5.1G). The banded state was also the ultimately stable state that even simulations with less aligned starting arrays (high α_{noise})

ended up in after a (biologically unrealistic) 33 hours of band formation not explored previously [33]. These results suggest that timely microtubule band formation requires co-alignment between the initial microtubule array and the underlying pattern proposed to be formed by ROPs.

In the current simulations, however, the co-alignment requirement was really strict. A perfectly aligned microtubule array could not tolerate much more than a 0.01π rad (1.8°) mismatch with the band regions before bands could only form by breaking down most microtubules in the band regions and then repopulating them with properly oriented ones (Fig. 5.2A–D). Some degree of co-alignment between the initial microtubule array and this underlying ROP pattern is biologically realistic, since the orientation of the microtubule array helps shape the orientation of the ROP pattern ([148], chapter 3). However, the orientation of a ROP pattern is also influenced by geometrical constraints, as it has to form either rings or spirals that wrap around the circumference (chapter 3). This requirement on the ROP pattern creates a minimal expected mismatch with the initial array, which, unlike the ROP pattern, is not limited to a discrete set of possible orientations. From this consideration, we calculated a minimal expected mismatch that can be as high as 0.02π rad (Fig. 5.2E, see Methods for computation). Our simulations suggested that this mismatch was too large for band formation in a realistic amount of time (Fig. 5.2A–D). The point at which band formation began to suffer from the mismatch was similar to the point at which a single microtubule (bundle) could no longer stay in a band region along the entire circumference of the cell (Fig. 5.2F). For greater mismatch angles the largest length of microtubule (bundle) that could fit within a band without bending rapidly decreased (Fig. 5.2G). These effects depended on the cell circumference and band width. However, varying these geometrical parameters within a biologically relevant range did not show much potential for improving the mismatch tolerance to the levels required (Fig. 5.2F,G).

5.2.3 Microtubule flexibility can lead to density loss from bands

Thus far we have considered microtubule segments in between collision points to be perfectly straight, following most previous cortical microtubule array modelling studies [33, 134, 136, 138, 161]. In reality, however, microtubules are somewhat more flexible and often give a curved appearance in microscopic images, e.g. [33, 90, 122, 144, 162]. We hypothesised that introducing this flexibility by modelling the microtubules as (zero thickness) semiflexible rods could reduce the strictness of the co-alignment requirement by allowing microtubules at 'wrong' angles to curve back into a band or to shrink back to a point where they had a better matching orientation.

Some recent studies have modelled such semiflexible microtubules by adding microtubule subunits at small relative angles calculated to give the microtubule a predetermined persistence length [126, 127]. We extended our model with semiflexible microtubules in a similar way, but with larger intervals between deflections to keep the implementation feasible in our event-based modelling framework and correspondingly larger deflection angles per event. Deflection step sizes were drawn from an exponential distribution with mean $\bar{l}$ and deflection angles were drawn uniformly from $[-m,m]$, where m is the maximum deflection angle. Deflection angles with absolute values lower than a minimal deflection angle q were set to zero to avoid numerical problems. With these parameters we

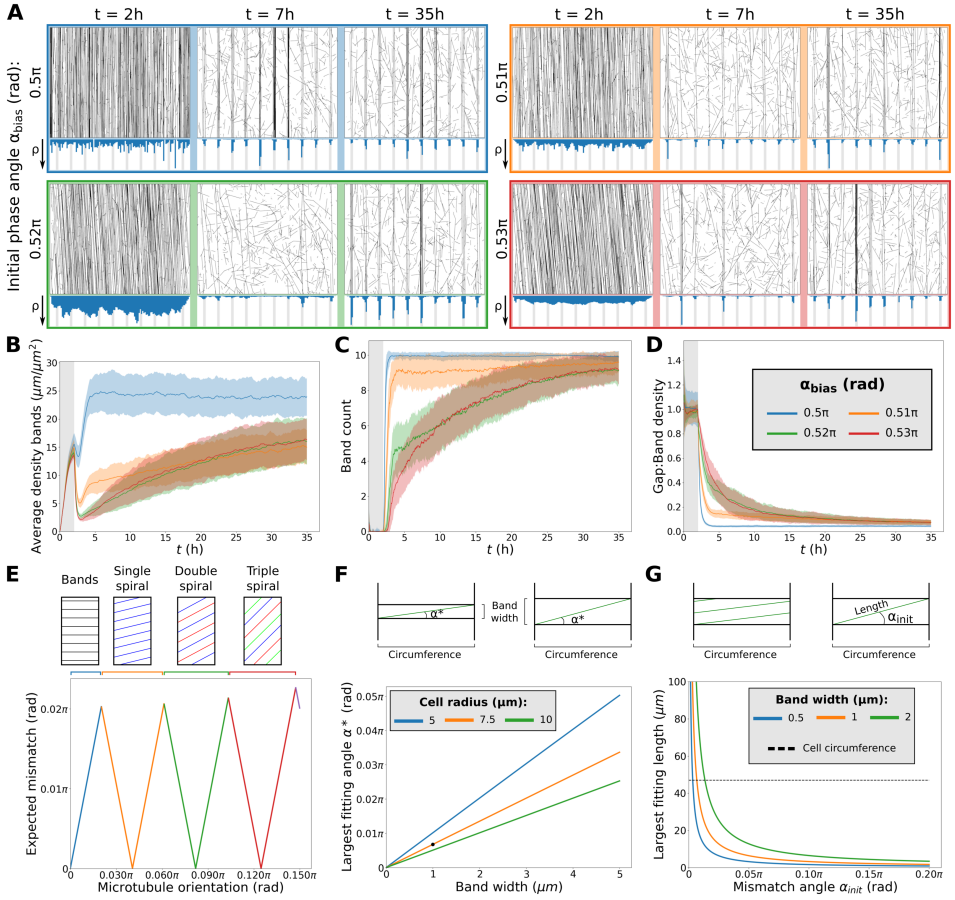

Fig. 5.2. Fast protoxylem patterning is sensitively dependent on co-alignment between microtubules and the underlying pattern. (A) Snapshots from protoxylem simulations with isotropic nucleation using starting arrays with different bias angles α_{bias} in the first half hour with only minor deviations ($\alpha_{noise} = 0.01\ rad^2$). Histograms below showing local microtubule density ρ share the same axis within a time series, but not between time series. (B) Average microtubule density in the band regions. (C) Number of populated bands, defined as bands with a microtubule density greater than three times the average density in the gaps. (D) Ratio of density in gaps and bands. Quantities in (B–D) were calculated from 100 simulations. The band formation phase starts at the end of the grey area. Lines indicate the average and shaded areas the standard deviation. (E) Minimal expected mismatch angle of a spiral (or banded) ROP pattern following a microtubule array of different orientations based on geometrical constraints for a distance of 6 μm between the centres of bands and a cylindrical domain with a radius of 7.5 μm. (F) Largest mismatch angle α^* at which a microtubule (bundle) can fit within a band along the entire circumference of the cell. Black dot indicates default simulation values. (G) Largest length that a microtubule (bundle) can have while still fitting entirely within a band region at varying mismatch angles. Band width in simulations is 1 μm (orange line). Dashed line indicates cell circumference for comparison.

could control persistence length p in a computationally tractable way within the simulation environment. To prevent microtubules from leaving bundles at every deflection point, we made microtubules follow their bundle along bends smaller than 10° (Fig. 5.3A). For

further implementation details, see Methods.

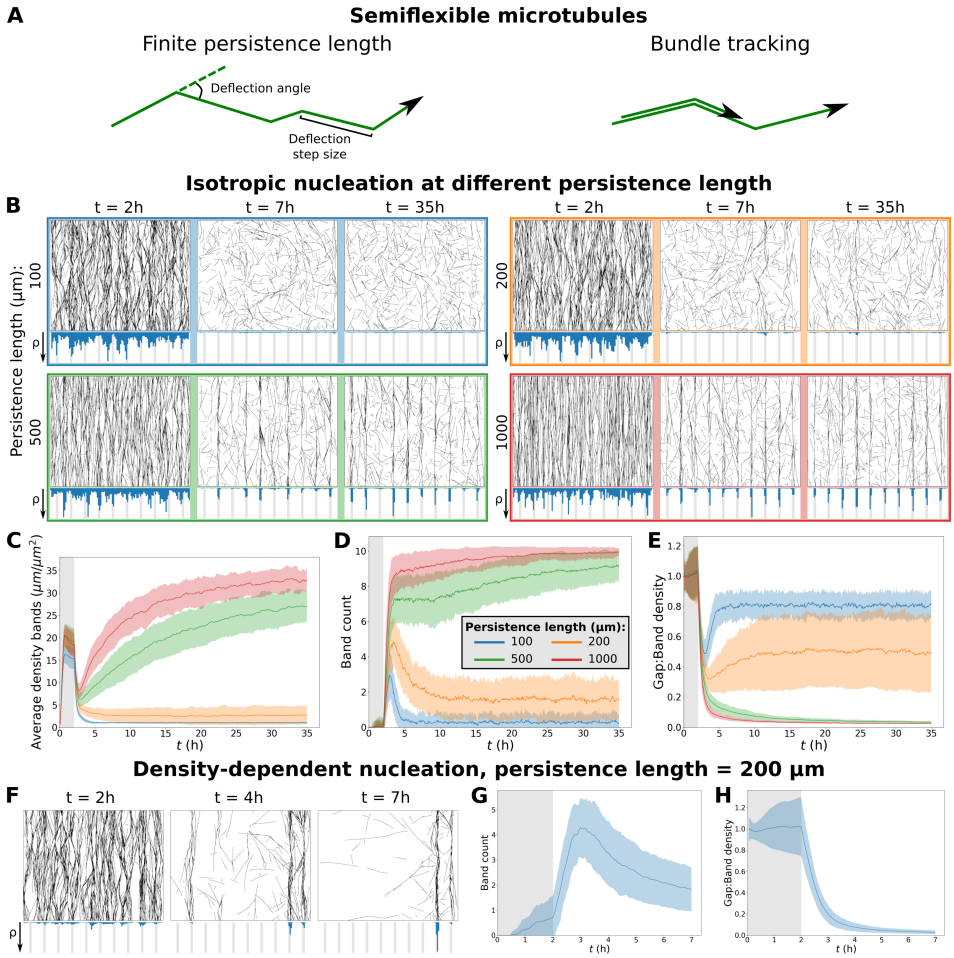

Fig. 5.3. Problems arising from semiflexible microtubules with traditional nucleation modes (A) Semiflexible microtubules of finite persistence length were simulated by performing deflections in the microtubule growth direction. In addition, microtubules in bundles follow their bundle around bends below an angle θ_b ('bundle tracking'). See Methods for details. Deflection angles in cartoons are exaggerated for visibility. (B) Snapshots from protoxylem simulations with isotropic nucleation for different microtubule persistence lengths. Histograms below showing local microtubule density ρ are plotted on the same scale within a time series, but not between time series. (F) Snapshots from protoxylem simulations with density-dependent nucleation and a persistence length of 200 μm. (B,F) Starting arrays were obtained with transverse nucleations in the first half hour ($\alpha_{bias} = 0.5\pi$, $\alpha_{noise} = 0.01$ rad^2). (C) Average microtubule density in the band regions. (D,G) Number of populated bands, defined as bands with a microtubule density greater than three times the average density in the gaps. (E,H) Ratio of density in gaps and bands. Quantities in (C–E), and (G–H) were calculated from 100 simulations. The band formation phase starts at the end of the grey area. Lines indicate the average and shaded areas the standard deviation.

Previous models with microtubule flexibility [126, 127] used persistence lengths of 20-30 μm measured *in vivo* in animal cells [236, 237]. For microtubule dynamics param-

eters based largely on measurements in developing protoxylem [33], these persistence length values caused so many extra collisions that it resulted in a loss of density and alignment even in simulations without band formation (Fig. S5.1A–C). Possibly, microtubule persistence lengths may have lower values in (often smaller) animal cells. We, therefore, investigated multiple larger persistence lengths, up to the millimetre range consistently measured in *in vitro* experiments [238]. For persistence lengths of hundreds of micrometers, aligned arrays did form (Fig. S5.1A–C). Curiously, for these intermediate persistence lengths, the edge-induced catastrophes were not always sufficient to give the array a transverse orientation (Fig. S5.1D). For our study of protoxylem band formation we therefore continued using the biased initiation phase.

With isotropic nucleation, band formation was actually hindered by semiflexible microtubules. For persistence lengths of 100 or 200 μm, stable starting arrays could be formed, but density was lost when band formation started (Fig. 5.3B–E). It would seem, therefore, that the extra flexibility, rather than helping microtubules find bands, actually makes microtubules already in bands bend out and suffer from the increased catastrophe rate in the gap regions. Proper bands only formed for more rigid microtubules with persistence lengths of 500 or 1000 μm.

The loss of density in the band regions at the lower persistence lengths could at least partially be counteracted when a significant portion of isotropic nucleations was moved to the gap regions (Fig. S5.2). Such a shift could be expected to occur dynamically in cells as gap regions start to empty, since most nucleations in plants are microtubule-bound, with a large fraction parallel to their parent microtubule [107–109]. The latter type of nucleation not only allows nucleations to shift to band regions as band formation progresses, but also increases the proportion of nucleations that follow the band direction and thus reduces microtubule loss from induced catastrophes within bands and spontaneous catastrophes on microtubules that grow out of bands.

So far, microtubule-bound nucleation has predominantly been implemented in a density-dependent way, i.e., by having the portion of microtubule-bound nucleation increase with the overall microtubule density in a saturating way and distributing all bound nucleations over the microtubules proportional to their length [160]. The positive feedback inherent in this density-dependent nucleation mode greatly enhances separation of bands and gaps [33]. In our simulations it was also able to maintain band density for a persistence length of 200 μm (Fig. 5.3F,H). However, we have previously shown that such density-dependent nucleation leads to a global competition for nucleations, eventually leaving most bands largely empty in favour of one or two large bands (chapter 4). This problem also appeared in our simulations with semiflexible microtubules (Fig. 5.3F,G). Therefore, a more realistic nucleation mode is needed.

5.2.4 Locally saturating nucleation helps to keep bands populated with semiflexible microtubules, even for misaligned starting arrays

We have previously shown that we could obtain realistic nucleation behaviour that enhances local structures without resulting in global competition by explicitly modelling nucleation complexes in a simplified microtubule context (chapter 4). The essence of this nucleation implementation was that the local nucleation rate saturates with the local

microtubule density, such that microtubule density cannot increase locally at the expense of other parts of the array. Experimental data suggests that this local saturation indeed occurs (chapter 4).

A drawback of explicitly modelling nucleation complexes is that implementing the diffusion of individual nucleation complexes is computationally expensive. Therefore, we needed to develop a more efficient algorithm while maintaining the essential behaviour. For this nucleation mode, we subdivided the domain into a number of grid cells representing local effect areas. Grid cells were kept as close to squares as the domain sizes allowed (e.g., 1 $\mu m \times 1.0026$ μm for 60 grid cells in the longitudinal direction with the default length of 60 μm and radius of 7.5 μm). Each of these grid cells had the same low rate of microtubule-independent nucleations ($r_{n,base}$), and a microtubule-based nucleation rate that saturated with the local density, such that the nucleation rate $r_{n,i}$ of grid cell i followed:

$$r_{n,i} = r_{n,base} + (r_{n,sat} - r_{n,base}) \frac{\rho_i}{\rho_i + \rho_{\frac{1}{2}}}, \tag{5.1}$$

where ρ_i is the local microtubule density of the grid cell, $\rho_{\frac{1}{2}}$ is the local density at which the microtubule-based nucleation rate is half its maximum, and $r_{n,sat}$ is the local nucleation rate at saturation (Fig. 5.4B). This equation is similar to the one used for density-dependent nucleation [160], except that ours applies to the local region rather than the entire domain and has a base nucleation rate for unbound nucleations that does not depend on microtubule density.

In chapter 4, we assumed a constant supply of nucleation complexes. In our simplified model, we relaxed that assumption by including a global availability of nucleation complexes, which influenced the rate at which microtubules could attract them. The existence of such a global limitation is supported by the experimental observation that microtubule fragments in oryzalin-treated cells attract more nucleation complexes per unit area than microtubules in populated arrays (chapter 4). It also explains why protoxylem bands attract more nucleation complexes after microtubules disappear from the gaps as observed by Schneider et al. [33]. We modelled this global limitation by making both $r_{n,base}$ and $r_{n,sat}$ proportional to the number of globally available nucleation complexes (Fig. 5.4C). Since nucleated complexes remain occupied for some time until they are released by katanin (about one minute on average [108]), we reduced the number of available nucleation complexes by one for every nucleation for a fixed amount of time $t_{occupied}$ (Fig. 5.4A). This way, microtubules in empty arrays, where most nucleation complexes are free, could attract more nucleations than microtubules in populated arrays, where a substantial fraction of nucleation complexes is occupied. For further details and parameter derivations see Methods and Appendix 5.6.1.

Microtubule-bound nucleations were distributed randomly over the total microtubule length in the relevant region, with the same relative angle distribution as in Deinum et al. [160].

We first tested our new locally saturating nucleation mode in simulations of homogeneous microtubule arrays. There, we found that more small gaps were left in the array (e.g., Fig. S5.1A,D, Fig. S5.3A) than in simulations in the simplified one-dimensional context from chapter 4, presumably due to all the branching and bundling events in the two-dimensional context. Consequently, when grid cells were small, many would not or barely contain any microtubules and so they did not contribute much to the overall nucle-

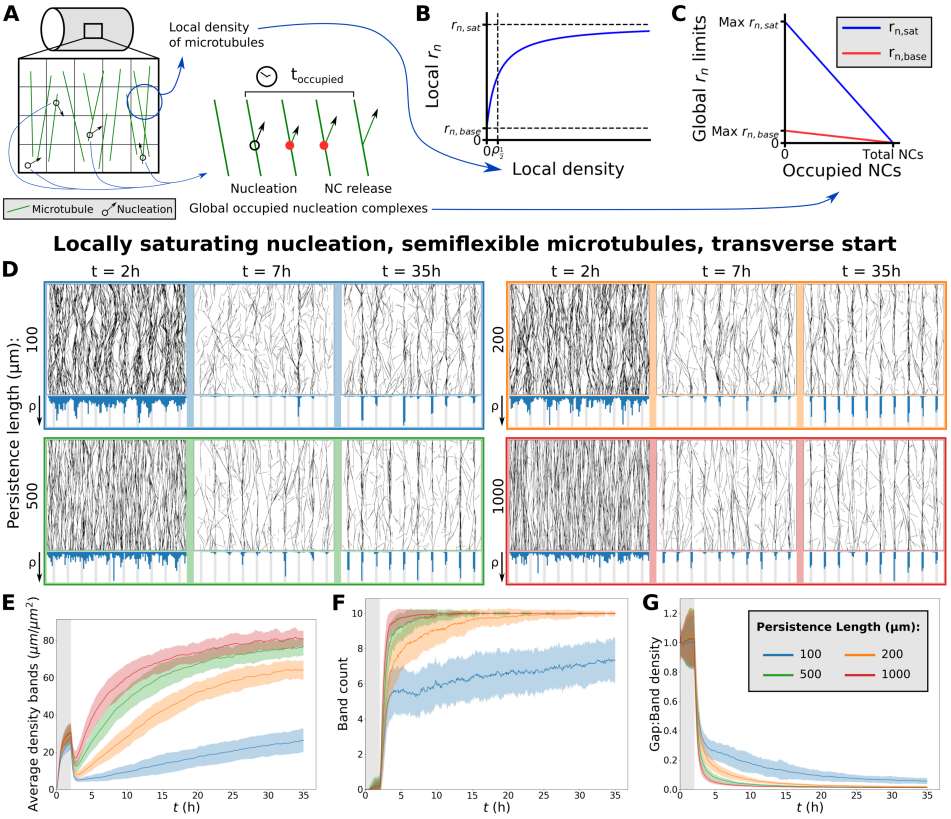

Fig. 5.4. With locally saturating nucleation, stable bands can be maintained at lower persistence lengths. (A–C) Implementation of locally saturating nucleation. (B) The nucleation rate in a local grid cell saturates with the local density in that cell. (C) The limit of $r_{n,sat}$ at full saturation and the rate of unbound nucleations linearly depend on the global availability of nucleation complexes (NCs). (A) An additional nucleation complex becomes occupied after every nucleation for a fixed duration of $t_{occupied}$, to model the time it takes for complexes to be released by katanin after nucleation. (B,C) Parameters not drawn to scale for visibility. (D) Snapshots from protoxylem simulations with locally saturating nucleation for different microtubule persistence lengths. Starting arrays were obtained with transverse nucleations in the first half hour ($\alpha_{bias} = 0.5\pi$, $\alpha_{noise} = 0.01$ rad^2). Histograms below showing local microtubule density ρ are plotted on the same scale within a time series, but not between time series. (E) Average microtubule density in the band regions. (F) Number of populated bands, defined as bands with a microtubule density greater than three times the average density in the gaps. (G) Ratio of density in gaps and bands. Quantities in (E–G) were calculated from 100 simulations. The band formation phase starts at the end of the grey area. Lines indicate the average and shaded areas the standard deviation.

ation rate. The result was a much lower nucleation rate than calculated for homogeneous microtubule arrays and, consequently, lower densities (Fig. S5.3B,C). Therefore, we here use grid cell lengths of 1 μm, which gave homogeneous arrays with effective nucleation rates close to the target value set for a fully homogeneous array (Fig. S5.3C).

The use of square grid cells in the simplification of the local saturation of the nucleation rate with microtubule density has the potential to introduce artefacts. To test for such artefacts, we ran array simulations without bands for different grid cell aspect ratios

on both the default cylindrical geometry and a periodic 80 $\mu m \times 80$ μm square grid, while keeping the surface of individual grid cells approximately constant (Fig. S5.4A,D). Since microtubules that crossed more grid cells had a larger impact on the overall nucleation rate, rectangular cells yielded a larger microtubule density when their long axis was perpendicular to the array than when it was parallel (Fig. S5.4B,E). For square grid cells, this impact was minimised, but there we can expect the diagonal direction to be more favourable, as it is a factor $\sqrt{2}$ longer than either of the sides. However, we estimated the resulting difference in density from a grid cell with an aspect ratio of $\sqrt{2}$ to be less than 10% (Fig. S5.4B). The difference in the number of grid cells covered by microtubules with different angles also had an impact on the orientation of the array. For extreme aspect ratios, the array would actually follow the direction perpendicular to the long axis of the grid cells on a periodic grid (Fig. S5.4F). This effect was much less pronounced on the cylindrical geometry with edge-induced catastrophes that favour a transverse orientation with respect to the longitudinal axis of the entire domain (Fig. S5.4C). Again, the effect was minimised for square grid cells, though some diagonal bias that was not present for isotropic nucleation, could still be found on a periodic domain (Fig. S5.4F,G). Therefore, this way of simplifying locally saturating nucleation rates is not suitable for quantitative studies of subtle effects on array orientation and density. However, for our purpose of studying protoxylem band formation, where we consider transverse arrays and bands, we expect the impact of square grid cells to be negligible. If anything, it would pose a small handicap to the formation of transversely oriented bands, making it a worst case scenario.

With rigid microtubules, protoxylem band formation with locally saturating nucleation was comparable to band formation with isotropic nucleation: As with isotropic nucleation, a banded pattern was ultimately stable, but took a long time to form, unless the mismatch between the orientation of the starting array and the predefined band regions was not much more than 0.01π rad (Fig. S5.5A–D). Therefore, the strictness of the co-alignment requirement was largely unaffected by the nucleation mode, but it may well be affected by the rigidity of the microtubules.

With semiflexible microtubules, locally saturating nucleation improved band formation for a persistence length of 100 μm, but most microtubule density was still initially lost, and took a long time to recover. However, band formation was now possible at a persistence length of 200 μm, lower than for isotropic nucleation, as nucleations were moved to the denser band regions (Fig. 5.4D–G). Furthermore, the combination of semiflexible microtubules and locally saturating nucleation also greatly improved timely band formation for a significant mismatch between the orientations of the starting array and the band pattern. A mismatch as high as 0.1π rad in the angle of the nucleations in the initiation phase still yielded a partially banded pattern after five hours of band formation (Fig. 5.5A–D). The actual mismatch of the starting array was, in practice, somewhat reduced, as we used boundary conditions promoting transversely oriented arrays. Consequently, the initial mismatch of $\alpha_{bias} = 0.1\pi$ rad in the initiation phase nucleation angle yielded a measured mismatch of about 0.06π rad in the orientation of the starting array (Fig. 5.5F), substantially more than the worst mismatches we expected theoretically (Fig. 5.2E). A reason for the increased tolerance for mismatches might be that the semiflexible microtubules inherently cover more different angles, of which a substantial portion aligns with the band regions, even though the average orientation does not (Fig. 5.5E). This gives the array more opportunities to correct its course, by microtubules bending back into the

array, or by 'wrong' orientations getting catastrophes in gap regions and rescues at a point where the orientation better matches the underlying ROP pattern.

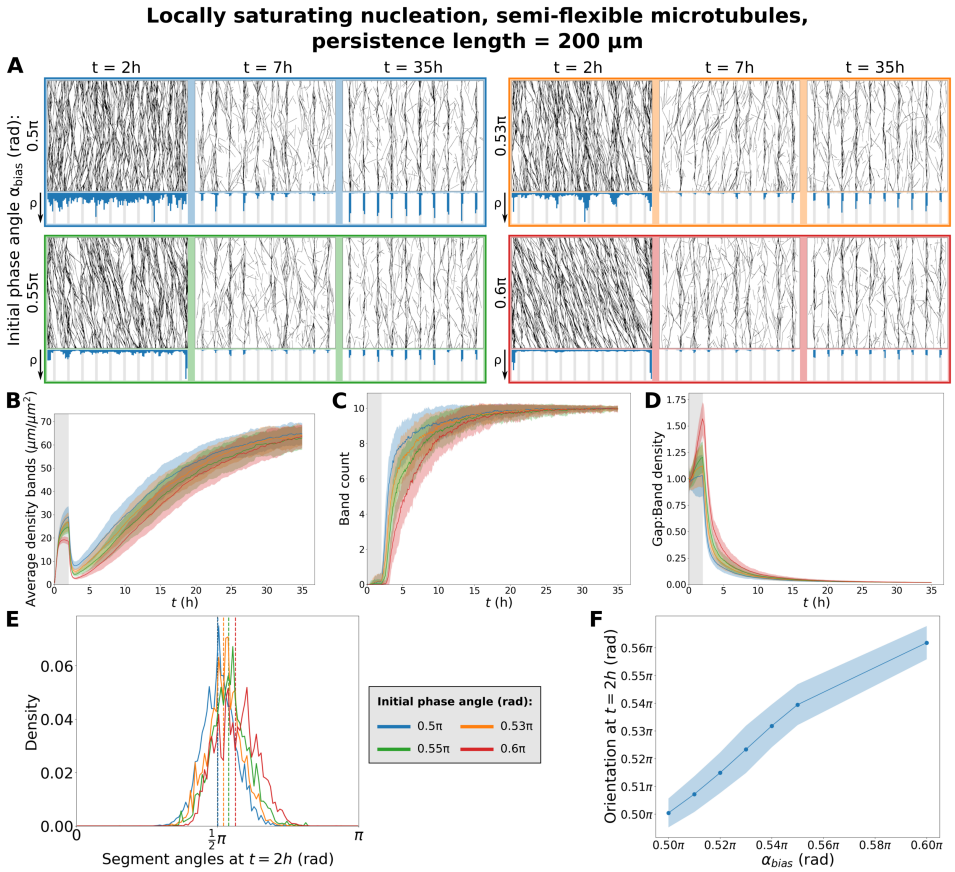

Fig. 5.5. With locally saturating nucleation (Fig. 5.4A–C), greater mismatches in the initial orientation still allow fast band formation. (A) Snapshots from protoxylem simulations with locally saturating nucleation using starting arrays with different bias angles α_{bias} in the first half hour with only minor deviations ($\alpha_{noise} = 0.01$ rad^2). The persistence length used was 200 μm. Histograms below showing local microtubule density ρ are plotted on the same scale within a time series, but not between time series. (B) Average microtubule density in the band regions. (C) Number of populated bands, defined as bands with a microtubule density greater than three times the average density in the gaps. (D) Ratio of density in gaps and bands. (E) Distribution of microtubule segment angles, weighted by segment length, at $t = 2h$ from the individual example simulations shown in (A). Dashed lines indicate the the overall array orientation. (F) Average array orientation at $t = 2h$ as a function of the bias angle in the initiation phase. Quantities in (B–D), and (J) were calculated from 100 simulations. The band formation phase starts at the end of the grey area. Lines indicate the average and shaded areas the standard deviation.

5.2.5 Array patterning must be robust against large variations in observed microtubule dynamics

Having improved our simulations and obtained a better understanding of the band formation process, we next tested our model on the original cell data, measured in four individual cells [33]. The microtubule dynamics parameters measured in these four different cells varied strongly both from cell to cell and between different time points [33]. For technical reasons, as in previous simulations [33], we calculated a difference in the spontaneous catastrophe rate between bands and gaps (f_{cat}), such that the factor difference in control parameter G (see Methods) remained the same when keeping all other parameters as in bands. This approach yielded the large variation in both the strength and duration of the differences between band and gap regions (Fig. 5.6B) also used in previous simulations [33]. Similarly, there are large differences in the calculated steady state densities that these different parameter sets would yield in absence of microtubule-microtubule interactions (Fig. S5.6).

In line with the differences between the parameter sets, the simulated arrays also behaved differently from cell to cell in our simulations with semiflexible microtubules and locally saturating nucleation (Fig. 5.6). The parameters from cells 1 and 2 produced low band densities relative to other cells, while still having a relatively strong increase in the gap region catastrophe rate towards the end of the simulations, resulting in a loss of most density, including in band regions. Cells 3 and 4, in contrast, have parameters that yielded much higher densities, leaving many microtubules in the gap regions. To some degree, these differences can be explained by differences in f_{cat}, since with idealised parameters, high values of f_{cat} resulted in density loss in bands during the first hours of band formation, while with low values of f_{cat}, more density remained in gap regions (Fig. S5.7). However, cell 3 also has a high f_{cat} during early band formation (Fig. 5.6B), but it also has parameters supporting a very high density in that phase (Fig. S5.6) to compensate the density loss in both band and gap regions.

Assuming that the differences in measured parameters are reflective of biological differences rather than technical differences (the first and last two cells were measured by different people in different labs), the banding process must be robust against the wide variety of measured parameter values. This tolerance may be achieved, for example, by tuning other parameters to compensate. An important parameter that was not measured in these cells, is the nucleation rate. For cells 1 and 2, the loss of density towards the end of the simulation could be prevented by increasing the target nucleation rate for populated arrays (Fig. 5.7). A three-fold increase yielded a strong separation in bands and gaps towards the end of the simulations, although it also gave an unrealistic increase in microtubule density in earlier stages.

Next, we considered different microtubule persistence lengths. For a higher persistence length of 1000 μm, most bands would form for all four cells, but with very unrealistic densities for cells 3 and 4 (Fig. S5.8). Placing these microtubules side to side, this would amount to two layers of microtubules. Lowering the nucleation rate could lower these densities, but reducing it to less than one layer of microtubules placed side to side interfered with the ability to form bands (Fig. S5.9). Since real cells are clearly capable of consistently forming the protoxylem microtubule pattern, our simulations are at this point not yet able to reproduce band formation in all data sets using constant values for

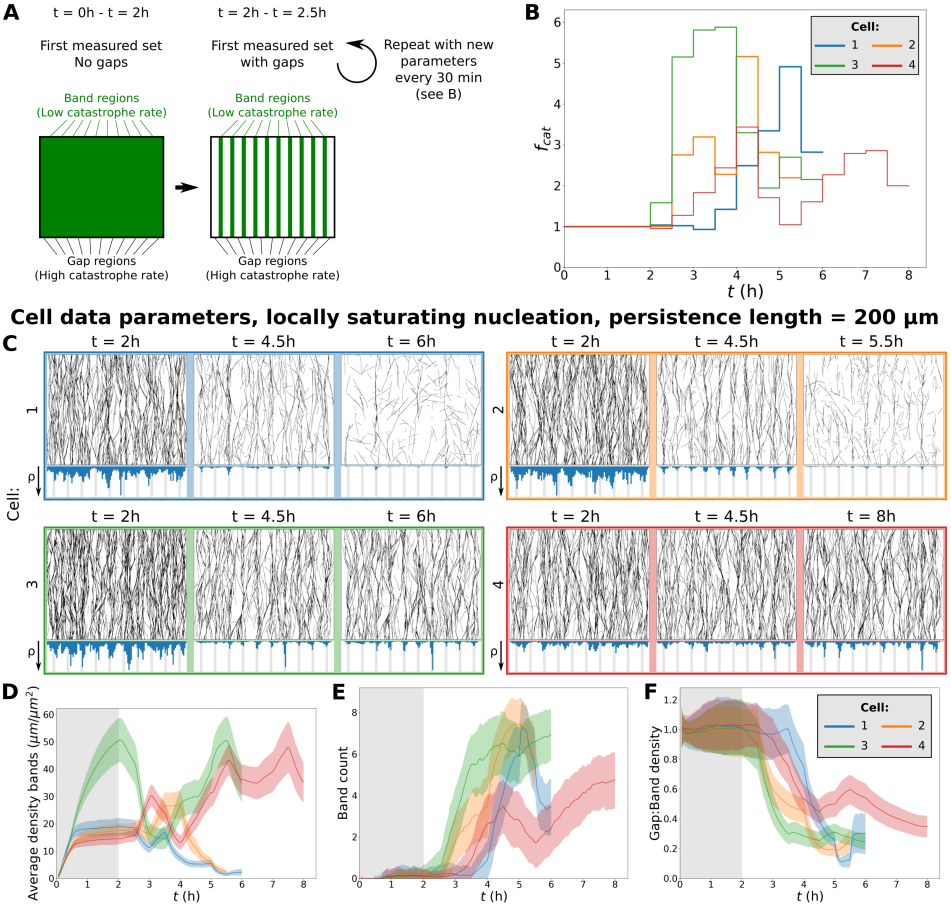

Fig. 5.6. High variation between parameter measurements in different cells complicate consistent band formation in simulations. (A) Simulation setup: Simulations based on data from individual cell measurements started with a 2h phase with the first set of band parameters applied everywhere, followed by half hour intervals with consecutive measured parameter sets from Schneider et al. [33] with the differences between band and gap regions converted to equivalent differences in catastrophe rates only. (B) Differences in catastrophe rates between bands and gaps used in simulations. Based on data from Schneider et al. [33]. For values of control parameter G and microtubule turnover rate τ in band and gap regions see Fig. S5.6. (C) Snapshots from protoxylem simulations for data from four different cells, with locally saturating nucleation, a persistence length of 200 μm, and an initiation phase with $\alpha_{bias} = 0.5\pi$ rad and $\alpha_{noise} = 0.01$ rad^2. Histograms below showing local microtubule density ρ are plotted on the same scale within a time series, but not between time series. (D) Average microtubule density in the band regions. (E) Number of populated bands, defined as bands with a microtubule density greater than three times the average density in the gaps. (F) Ratio of density in gaps and bands. Quantities in (D–F) were calculated from 100 simulations. The band formation phase starts at the end of the grey area. Lines indicate the average and shaded areas the standard deviation.

parameters that were not measured.

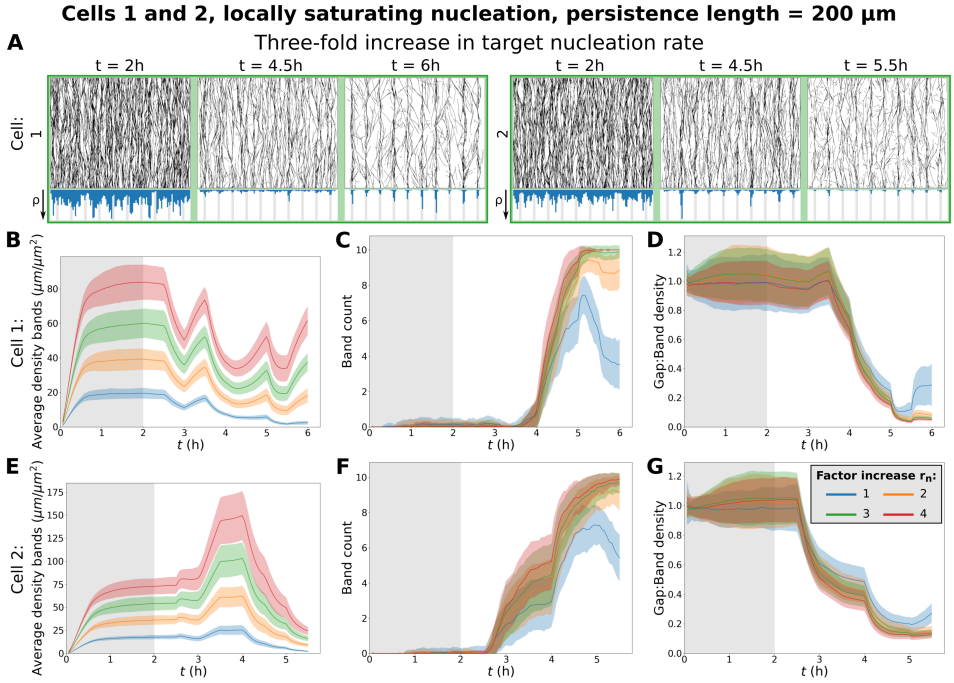

Fig. 5.7. Increased nucleation rate improved band formation with data from cells 1 and 2. (A) Snapshots from protoxylem simulations for data from cell 1 and 2, with locally saturating nucleation, a persistence length of 200 μm, and an initiation phase with $\alpha_{bias} = 0.5\pi$ rad and $\alpha_{noise} = 0.01$ rad^2. The target nucleation rate was increased from the default of 0.001 $\mu m^{-2} s^{-1}$ to 0.003 $\mu m^{-2} s^{-1}$. Histograms below showing local microtubule density ρ are plotted on the same scale within a time series, but not between time series. (B–G) Measurements from simulations of cell 1 and 2 for different target nucleation rates. (B,E) Average microtubule density in the band regions. (C,F) Number of populated bands, defined as bands with a microtubule density greater than three times the average density in the gaps. (D,G) Ratio of density in gaps and bands. Quantities in (B–G) were calculated from 100 simulations. The band formation phase starts at the end of the grey area. Lines indicate the average and shaded areas the standard deviation.

5.2.6 Band-gap separation factors outside the measured parameter differences

Perhaps the clearest example of a situation that cannot be explained in the current framework is found in the early stages of band separation from cell 1. In the microscopic pictures, a rudimentary banded pattern is already mostly formed in the first hour, only growing steadily sharper afterwards [33]. However, in this first hour, $f_{cat} \approx 1$ (Fig. 5.6B), so there is virtually no difference between band and gap regions in simulations of cell 1 (Fig. 5.6E,F). Assuming accurate parameter measurements, the separation observed in this stage may be caused by a difference in parameters that were not measured. This raises the question how large such differences would need to be to produce banding, given the measured microtubule dynamics parameters.

The two main parameters that were not measured in the four cells are the minus-end retraction speed v^{tm}, and the nucleation rate, so one of these might differ between band and gap regions to yield this early separation. We first considered a difference in v^{tm}.

However, the compensated f_{cat} only increased modestly, to about 1.5 even for a factor 4 increase of v^{tm} (Fig. S5.10A), an effect comparable to a loss of function of minus-end protection protein SPIRAL2 [144]. Changes in control parameter G were similarly modest (Fig. S5.10B). Microtubule lifetime τ was almost halved by a factor 4 increase in v^{tm} (Fig. S5.10C). Since f_{cat} did not increase further when calculated to keep τ constant (Fig. S5.10A), an increase in v^{tm} could have a larger impact when not modelled indirectly through a compensated f_{cat}. Unfortunately, the latter option is currently impossible to test using corticalSim.

Next, we investigated a possible difference in nucleation rate between band and gap regions. Mechanistically, some factor in the band region would have to increase nucleation complex recruitment independent of local microtubule density. A difference caused by microtubules in bands attracting microtubule-based nucleations is insufficient, as this can only reinforce existing bands, not initiate the formation of new ones. A factor 10 shift of the target nucleation rate from gap regions to band regions was required to achieve a band-gap separation up to a factor 2 in the early stage for a persistence length of 200 μm (Fig. 5.8). For a persistence length of 1000 μm, a similar band-gap separation could be achieved for a nucleation shift of only a factor 3 to 6 (Fig. S5.11).

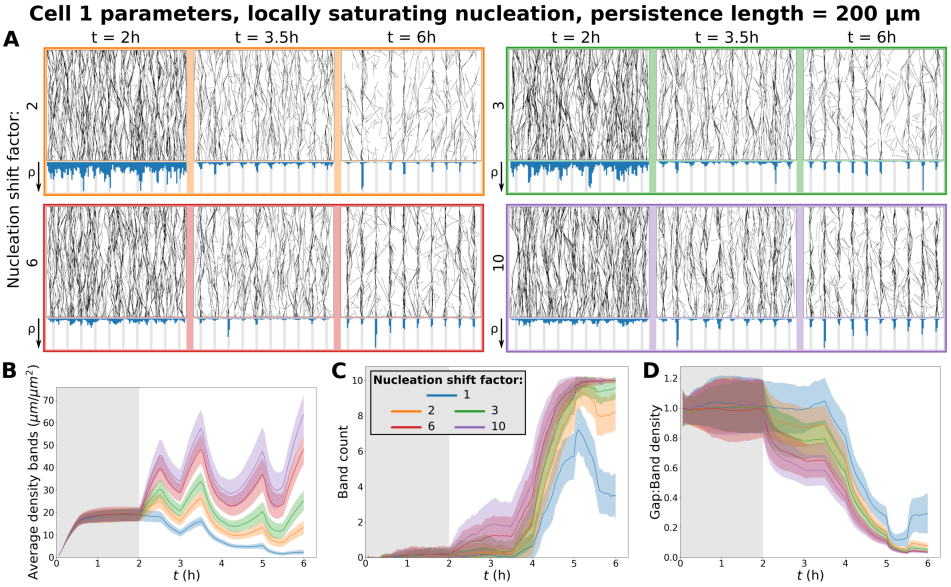

Fig. 5.8. Partially shifting the nucleation rate to the band regions minimally improved band formation in the first 1.5 hours for cell 1. (A) Snapshots from protoxylem simulations for data from cell 1, with locally saturating nucleation, a persistence length of 200 μm, and an initiation phase with $\alpha_{bias} = 0.5\pi$ rad and $\alpha_{noise} = 0.01$ rad^2. During band formation, the target nucleation rate in the band regions was increased by different factors compared to the band regions, such that the average, weighted for the difference in band and gap size, remained constant. Histograms below showing local microtubule density ρ are plotted on the same scale within a time series, but not between time series. (B) Average microtubule density in the band regions. (C) Number of populated bands, defined as bands with a microtubule density greater than three times the average density in the gaps. (D) Ratio of density in gaps and bands. Quantities in (B–D) were calculated from 100 simulations. The band formation phase starts at the end of the grey area. Lines indicate the average and shaded areas the standard deviation.

Therefore, the two main options for achieving an early difference between band and gap regions each seem to require implausibly large parameter differences. Future experiments may shed more light on these interesting early stages of band formation, focusing on possible differences between bands and gaps that have not yet been measured. Additionally, further theoretical work may focus on improving the simulation framework to allow all parameters to differ between band and gap regions directly, rather than through a compensated f_{cat}.

5.3 Discussion

We have identified three important requirements for microtubule patterning in developing protoxylem by doing detailed simulations: (1) co-alignment between the microtubule array and the underlying ROP pattern, (2) microtubule flexibility, and (3) realistic locally saturating nucleation. Together, these aspects allow microtubule bands to form on a realistic time scale in two-dimensional microtubule array simulations with idealised microtubule dynamics parameter values based on measured data [33]. We further tested our simulations on the parameter time series from individual cells measured by Schneider et al. [33]. However, given the large variation in and among these parameter sets, the simulations lacked the robustness to consistently form bands of similar, realistic densities in all cells, even when trying different (but constant) values for the parameters outside the measured set. Furthermore, one or more separating forces appear to exist beyond those currently quantified. These findings indicate that, in spite of the progress made here, further key aspects of protoxylem microtubule patterning remain to be discovered.

One important aspect that we did not model explicitly is the interplay between microtubule patterning and ROP patterning. Here, we modelled the ROP pattern as a static, regularly banded prepattern, whereas in reality, it is most likely shaped by a reaction diffusion process similar to that in metaxylem [32], with microtubules acting as ROP diffusion barriers that orient the pattern (chapter 3). Here, we partly modelled this orienting effect by generating starting arrays with various degrees of co-alignment. However, while real microtubule arrays generally align in a transverse orientation before the start of protoxylem patterning, they rarely have exactly the same orientation along the entire length [33, 122]. The resulting bands also tend to have a variation in their orientation and they are not all perfectly straight or equally spaced in ways that reflect initial densities and orientations in the starting arrays [33, 122]. These observations suggest that the underlying ROP pattern also provides co-alignment at a local level, which may help microtubule band formation. At the same time, the possibility of curved bands provides more options for straight-growing microtubules to leave band regions, which we found could be detrimental to band formation. To help growing microtubules follow these curved bands, microtubule associated proteins (MAPs) involved in microtubule bundling may be important, e.g., MAP65-8, which is expressed in developing xylem [239]. In addition, microtubules must be sufficiently flexible to follow these curves.

In our simulations, we showed the importance of microtubule flexibility even when assuming straight band and gap regions. Flexibility improved the ability of microtubules to follow predefined band regions in spite of small mismatches in the orientation of the microtubules and the band regions. However, our simulations also pointed at a trade-off,

where increased flexibility means more microtubules curve into gap regions where they are more likely to suffer catastrophes. Here too, microtubule bundling proteins may be important to help prevent this problem.

The need for microtubule flexibility becomes even more obvious when we consider metaxylem patterning, where arrays need to form roughly circular gaps. In microscopic pictures, microtubules appear to curve around these gaps [155]. The gapped structure also means that microtubule patterning cannot rely on co-alignment with the ROP pattern as in protoxylem patterning. Therefore, metaxylem patterning may require additional proteins to help the microtubules form this structure that are absent or less important in protoxylem patterning. These may include CORD proteins, which disorder microtubules by partially detaching them from the membrane [155], possibly facilitating corrections in the microtubule orientation. In addition, CORD proteins help enlarge the gap regions by reducing the ability of microtubules to act as ROP diffusion barriers [155]. Another protein that may help metaxylem patterning is the ROP effector BDR1, which may recruit Wallin, a protein that promotes actin assembly, to the borders of the gap regions, a process that may help shape the borders of bordered pits [240]. In addition, actin networks can provide physical barriers to microtubules or cross-link with microtubules to redirect them [241, 242], suggesting that the actin recruitment in metaxylem may also help create microtubule gaps.

In addition to the importance of microtubule flexibility, our simulations also showed the importance of realistic nucleation. We have already shown the importance of locally saturating microtubule-based nucleation for array homogeneity in chapter 4. There, we assumed a constant, uniform supply of nucleation complexes as an important source of local saturation. Here, we relaxed this assumption by allowing microtubules to draw from a global pool of nucleation complexes, while maintaining the saturation of the nucleation rate with the local density. Consequently, the reduction of microtubule density in the gap regions would free up nucleation complexes that could then be used to boost the nucleation rate in the bands. This effect helped compensate for microtubule loss from catastrophes suffered by microtubules leaving the band region. This partial shift in the location of nucleation complexes is in line with microscopic observations of nucleation complexes during protoxylem development [33] and upon oryzalin treatment (chapter 4).

Now that the nucleation supply is no longer constant, however, each local region is no longer guaranteed to have exclusive access to its own source of nucleations. If not for the assumption of local saturation, a global competition for nucleation complexes would be the result, just like for density-dependent nucleation. This local saturation may still result from a locally limited availability of nucleation complexes, assuming cytosolic diffusion is sufficiently limited to prevent rapid mixing. In that case, a redistribution of cytosolic complex through turnover or an inactive intermediate is required to counteract a diffusive flux towards dense areas (chapter 4). Therefore, if the local saturation of the nucleation rate with microtubule density that we assumed Alternatively, there may be a local saturation of the number of available binding places on microtubules from which a nucleation complex could form a new microtubule. In denser patches, nearby microtubules might shield such binding places, or at least make it more difficult for a new microtubule to be inserted where there is no space for it. Electron microscopy studies suggest that microtubules can, at least locally, create a very crowded membrane [243–245], suggesting that such a shielding effect may be substantial. Testing this hypothesis

would require a model that includes microtubule width, so that steric hindrance would limit microtubule density. An interesting option would be to implement basic density-dependent nucleation in a model that already meets this criterion, such as the one by Mirabet et al. [126].

While the extensions we made to the simulations improved their ability to generate a banded microtubule pattern, they still lacked robustness when tested with the large variety of microtubule dynamics parameters that have been measured in living cells [33]. Part of the reason for this variation may be that microtubule dynamics are difficult to measure, especially in dense regions like the bands, where individual microtubules may not be resolved by light microscopy. Also, for the gap regions, there are strong differences between the first two cells and the last two cells (e.g., Fig. S5.6), which have been measured in different places by different people, so the measured differences may have resulted from subtle differences in the approach or experimental conditions.

However, some degree of biological variability can be expected and the system should be robust enough to form bands across the full range of biologically plausible parameters. Such robustness might be achieved by further factors that stabilise bands, such as the activity of microtubule associated proteins (MAPs) not included in our model. Proteins from the MAP65 family, of which MAP65-8 is preferentially expressed during xylem development [239], promote microtubule bundling [246–248]. MAP65-1 has also been reported to increase rescues of bundled microtubules [249], though others found no difference in the dynamics of bundled microtubules *in vivo* [250]. In addition, MAP70-5 is suggested localise to the edges of microtubule bands, increasing their stability [153, 251]. Another possibility may be that cells compensate for parameter variations through some of the parameters that have not been measured, most notably the nucleation rate. Here, we only tested different nucleation rates that remained constant throughout the simulation. However, it is possible that the nucleation rate varies in time, like the other parameters. In particular, the nucleation rate depends on the amount of free tubulin [252, 253], as tubulin is required for both elongation and nucleation of microtubules. Therefore, the nucleation rate may start high, to build a dense array as a starting point for band formation, and subsequently decline as the available tubulin is depleted.

The lack of such a tubulin-dependent nucleation rate in our model may also be the reason for the large variation in microtubule densities we obtained, often far exceeding reasonable values to the point where there would be more microtubules than could fit on the membrane side to side. Tubulin depletion provides a natural limitation to the microtubule density. Tubulin depletion also limits the microtubule growth speed [252, 253], a limitation that has been implemented in past models [103] (chapter 4). However, the growth speed was one of the measured parameters and so a tubulin-limited growth speed is clearly insufficient to prevent unrealistic densities on its own. For dense arrays, microtubule density may be further limited by an increase in physical microtubule-microtubule interactions in the crowded environment. However, for sparse arrays, where microtubule density is much lower than 40 $\mu m/\mu m^2$ (100% microtubule coverage for a width of 25 nm), this effect is likely to be limited.

In addition to the large variation between measured cells, one of the four measured cells already had clearly formed bands before any differences in measured parameters appeared [33]. Therefore, there are likely other factors that contribute to band formation. We showed that a band-gap difference between the two most important unmeasured pa-

rameters, the nucleation rate and the treadmilling speed, only had limited potential for facilitating early band formation. Possibly, other factors, such as the aforementioned MAPs, may also show differential activity in band and gap regions to help facilitate band formation. This would require that MAPs end up in band regions not just because they bind microtubules, as they would need to move there before microtubule bands have started to form. These MAPs would also need to act on something other than the measured parameters, for example, by locally binding together microtubules in a bundle to keep them from leaving the bands. Alternatively, the lack of early separation in simulations may be an inadvertent consequence of trying to map all differences between parameters to a difference in catastrophe rates. This option seems less likely, as microtubule turnover rate τ has similar values for measured and simulation parameters in gaps (Fig. S5.6F). However, a possible difference in treadmilling speed between bands and gaps may have more effect when modelled directly, as the reduction in τ in the gaps with increased gap treadmilling is more pronounced than the increase in compensated f_{cat} (Fig. S5.10). In that case, obtaining realistic simulations of protoxylem band formation would require adapting the computational framework to allow differences in microtubule growth and shrink speeds between band and gap regions.

Another interesting finding was that the introduction of a finite persistence length made it harder to obtain global alignment from edge-induced catastrophes alone. Since alignment was not the focus of this chapter, we did not investigate this issue further and used pre-aligned starting arrays instead. With rigid microtubules, edge-induced catastrophes can ensure a global transverse orientation for cell sizes and other parameters as realistic for relatively small plant cells [124, 254]. However, for larger domain sizes or rescaled parameters, multiple separate patches of locally aligned microtubules may occur even with rigid microtubules [254]. Reducing the persistence length with the introduction of semiflexible microtubules reduced the domain size at which this patch formation occured. These observations suggest that an additional global alignment factor is required to obtain globally aligned arrays *de novo*. A good candidate is the tendency of microtubules to align themselves in the direction of maximal tensile stress [128, 255, 256]. While the precise way in which this type of alignment occurs remains poorly understood, there are some indications that the microtubules themselves may act as stress sensors directly [257]. If all individual microtubules then perceive a similar tensile stress, as seems likely on a simple cylindrical domain, a tendency to align in the direction of maximum stress will promote global alignment. Indeed, a bias in the orientation of each additional tubulin subunit can improve alignment and alter the orientation of the array in simulations with microtubule flexibility [126].

There is a large gap between the microtubule persistence lengths of 20-30 μm measured in animal cells [236, 237] and those in the millimetre range measured *in vitro* [238]. This difference suggests a large uncertainty in the value of the microtubule persistence length in plant cells, as well as a possibility for cells to modulate it. In absence of sufficient membrane attachment, strong microtubule bending can be induced by forces generated by active cellulose synthase complexes [258] and cytoplasmic streaming [104, 259]. Therefore, good candidates for persistence length modulation are proteins involved in microtubule-membrane linkage, such as CMU (cellulose-microtubule uncoupling) proteins [258], and certain IQD proteins [260], of which IQD13 functions in metaxylem development [154]. IQD proteins can also be regulated dynamically, in particular through

calcium signalling, as they have calmodulin-binding domains [261, 262]. This kind of regulation may dynamically influence microtubule persistence length. Therefore, persistence lengths measured in one situation may not necessarily apply to the next, making it necessary to obtain *in vivo* persistence length measurements for plant cells of different types.

In conclusion, we have shown that co-alignment, microtubule flexibility, and realistic nucleation are important aspects of protoxylem patterning. We have also shown that additional differences between band and gap regions are required for band formation given the measured microtubule dynamics parameters in band and gap regions. Our findings lay the groundwork for future studies on patterns generated by microtubule-ROP interactions. These studies may include simulations of other systems, such as metaxylem, as well as simulations that combine existing ROP models (e.g., chapter 3) with microtubule simulations.

5.4 Methods

5.4.1 Simulation setup

Simulations were performed with an extended version of 'corticalSim', a well established and fast two-dimensional microtubule simulation platform [33, 103, 134, 138, 160]. To account for the katanin severings at crossover intersections that may have been interpreted as induced catastrophes [138] in the original experiments by Dixit and Cyr [110], the probability P_{cat} that collisions at large angles result in catastrophes was lowered compared to previous studies [134, 160]. Contrary to those studies, we included katanin severing by default, with a rate of 0.023 s^{-1} per crossover, similar to values found in experiments [112, 113, 144].

Protoxylem simulations were performed with 1 μm wide band regions separated by 5 μm wide gap regions as in Schneider et al. [33]. Simulations started with a $2h$ initiation phase without bands followed by a $5h$ or $33h$ band formation phase in which the catastrophe rate in the gap regions was increased by a factor $f_{cat} = 3$, which in experimental observations tends to be achieved or exceeded during a substantial part of the patterning process [33]. In the first $0.5h$ of the initiation phase, nucleations were distributed uniformly and given an angle α_{bias}, with a small amount of normally distributed noise. For simulations with rigid microtubules, this biased phase has almost no collisions that could lead to induced catastrophes or crossovers. To compensate the nucleation rate for this phase was reduced by a factor 4 for simulations with rigid microtubules. The remainder of the initiation phase used the same nucleation mode as the band formation phase. Simulations without bands were run for $7h$ starting from an empty array with additional isotropic nucleations added at the beginning speed up the population of the array. These 'seeded' nucleations were added at a density of 0.1 $\mu m^{-2} s^{-1}$ and a rate of 0.003 s^{-1} as in Lindeboom et al. [161]. See Table 5.1 for default parameter values.

Table 5.1. Default parameter values used in the simulations.

Parameter	Value	Unit	Description	Source
Simulation domain				
H	60	μm	Domain length	[33]
W	$7.5 \cdot 2\pi$	μm	Domain circumference	[33]
Dynamic instability				
v^+	0.05	$\mu m/s$	Growth speed	[33]
v^-	0.08	$\mu m/s$	Shrinkage speed	[33]
v^{tm}	0.01	$\mu m/s$	Treadmilling speed	[33]
r_c	0.0016	s^{-1}	Catastrophe rate (bands)	[33]
r_r	0.001	s^{-1}	Rescue rate	[33]
Microtubule interaction				
θ_c	40°		Collision angle where outcome switches from bundling to crossover or induced catastrophe	[110]
P_{cat}	0.09		Fraction of induced catastrophes	[138]
r_x	0.023	s^{-1}	Crossover severing rate	
Nucleation				
r_n	0.001	$\mu m^{-2}s^{-1}$	Nucleation rate for isotropic and density-dependent nucleation	[33]
$r_{n,target}$	0.001	$\mu m^{-2}s^{-1}$	Nucleation rate for a populated homogeneous array with locally saturating nucleation	[33]
$\rho_{\frac{1}{2}}$	0.1	$\mu m/\mu m^2$	Microtubule density at which the (local) bound nucleation rate is half its maximum	[160]
h_{region}	1	μm	Region size	
$r_{n,sat,max}$	0.0035	$\mu m^{-2}s^{-1}$	Theoretical maximum nucleation rate when all nucleation complexes are free.	
$f_{unbound}$	0.0005		Fraction of the nucleation rate reserved for unbound nucleations	
$t_{occupied}$	60	s	Time a nucleation complex stays occupied after a nucleation	[108]
Band formation				
f_{cat}	3		Factor increased catastrophe rate in gaps	
Band width	1	μm	Width of band regions	[33]
Gap width	5	μm	Width of gap regions	[33]
Semiflexible microtubules				
p	200	μm	Persistence length	
$\bar{l}$	$0.01p$	μm	Average deflection step size	
q	0.1°		Minimum deflection angle	
θ_b	10°		Maximum bundle tracking angle	

5.4.2 Nucleation modes

Isotropic and density-dependent nucleation

Isotropic nucleations were implemented as in Tindemans et al. [103]. They were drawn at a constant global nucleation rate r_n, with uniformly distributed position and orientation.

Density-dependent nucleation follows [160]. Nucleations were again drawn at a total

rate r_n. This rate was divided into an isotropic rate and a microtubule-bound rate $r_{n,bound}$, with the latter following:

$$r_{n,bound} = r_n \frac{\rho}{\rho + \rho_{\frac{1}{2}}}, \tag{5.2}$$

with ρ being the global microtubule density, and $\rho_{\frac{1}{2}}$ the microtubule density at which half of all nucleations are microtubule-bound. Bound nucleations were distributed uniformly over the total length of all microtubules. Of all bound nucleations, 31% was oriented parallel to the parent microtubule, 7% anti-parallel, and the remainder branching left or right at 31% each. Branched nucleations were given an average angle relative to the parent microtubule of 35°, drawn from the elliptic distribution described in Deinum et al. [160] with $\varepsilon = 0.89$.

Locally saturating nucleation

With locally saturating nucleation, the nucleation rate in each local grid cell follows Eq. 5.1. The effect of a global limitation of nucleation complexes was modelled through a linear reduction in the saturated nucleation rate $r_{n,sat}$ with the number of occupied nucleation complexes N_{occ}:

$$r_{n,sat} = r_{n,sat,max} \frac{N_{tot} - N_{occ}}{N_{tot}}, \tag{5.3}$$

where N_{tot} is the total number of nucleation complexes and $r_{n,sat,max}$ is the theoretical maximum nucleation rate when all complexes are free and the local microtubule density is saturated.

The base nucleation rate $r_{n,base}$, which corresponds to the nucleations that occur independently of microtubules, depends on the number of occupied nucleation complexes in the same way, and thus is always a fraction $f_{unbound}$ of the saturated rate:

$$r_{n,base} = f_{unbound} \cdot r_{n,sat}, \tag{5.4}$$

where $r_{n,base,max}$ is the microtubule-independent nucleation rate when all nucleation complexes are free.

Microtubule-bound nucleations were executed as for density-dependent nucleations, only with the nucleations distributed uniformly over the length of the microtubules within each grid cell, rather than globally. Unbound nucleations were executed as for isotropic nucleation.

For estimation of parameter values, see Appendix 5.6.1.

5.4.3 Expected mismatch angles

Although a ROP pattern is expected to follow the general orientation of the initial microtubule array, this match may not be exact, as the ROP pattern needs to wrap smoothly around the geometry, while maintaining an intrinsic band spacing (chapter 3). We have previously shown (chapter 3) that the orientation of a spiral ROP pattern that that allows the distance between bands to be maintained follows:

$$\vartheta = \arcsin\left(\frac{H \cdot n}{W \cdot n_{bands}}\right), \tag{5.5}$$

where H is the domain length, W the domain circumference, n the spiral number (1 for a single spiral, 2 for a double spiral, etc.), and n_{bands} is the number of bands in a banded array. For our 10 bands, this equation gives a set of discreet angles that a ROP pattern is likely to follow. Assuming that the ROP pattern will always adopt the orientation closest to that of the microtubule array (reasonable at least for low spiral numbers; see chapter 3), microtubule arrays with orientations in between these discreet spiral angles will have the mismatch shown in Fig. 5.2E.

5.4.4 Semiflexible microtubules

To implement semiflexible microtubules, we adapted an approach from Mirabet et al. [126]. We gave microtubules deflections in their growth direction every step of variable size l that they grow, with l drawn from an exponential distribution with mean $\bar{l}$. Deflection angles were drawn from a uniform interval $[-m,m]$. Angles of which the absolute value was smaller than the minimum deflection angle $q = 0.1^\circ$ were set to zero to avoid numerical problems. For $\bar{l}$ we chose a value of 1% of the desired persistence length by default. This value prevents large numbers of very small deflections from resulting in many very similar trajectories that give technical difficulties with the simulation software, while still keeping the step size small relative to the persistence length. For details on how the maximum deflection angle m was chosen to give microtubules a given persistence length p, see Appendix 5.6.2.

In our current simulations, microtubule bundles consist of multiple microtubules on the same trajectory, without any space in between. Therefore, there is no distinction between microtubules on the sides, which could still deflect outwards, and microtubules on the inside, that don't have any room to deflect at all. To partially compensate for the lack of deflection restriction of microtubules in bundles, we rejected a portion of deflections in bundles, keeping only $1/(n+1)$ deflections, where n is the number of other microtubules in the bundle at the point of the deflection.

Another bundling-related issue is that microtubules in bundles now regularly encounter bend points (deflection points or bundling points) from the microtubules to which they are bundled. Without any adjustment, bundles would regularly separate at these points. Therefore, we made microtubules track their bundles along bend points. Since bundling events also create bend points and these may have considerably larger angles (up to 40°), we implemented a maximum bundle tracking angle of $\theta_b = 10^\circ$. If a bundle splits with an angle below this value, an incoming microtubule randomly follows one of the bundles, proportional to their occupancy.

For individual microtubules averaged over sufficient length, the length of the average deflection step size $\bar{l}$ does not matter for the persistence length of the total microtubule as long as the appropriate deflection angle is used. However, microtubules in a populated array interact with each other, and so there may well be a difference between many small deflections and fewer larger deflections. Therefore, we tested the effect of different step sizes for the same persistence length, in the range of step sizes feasible in the current simulation setup (Fig. S5.12). For the same persistence length, the deflection step size seemed to have little effect on the alignment and orientation of arrays without bands (Fig. S5.12D,E). For lower persistence lengths in particular, there seems to be a small effect on the overall density, likely resulting from differences in the rates of encounters that

could lead to crossover-severing [138] or induced catastrophes (Fig. S5.12A–C). Therefore, the precise way in which microtubules are flexible, may also have some impact on the array as a whole, but the magnitude of this impact on array alignment, orientation, and density is limited.

5.4.5 Cell data simulations

Simulations based on measured parameters from individual cells were performed similar to the study in which they were measured [33]. We used a similar two hour initiation phase as in our other simulations, but with the measured band parameters from the first measured time point of each cell. Measured parameters were: r_c, r_r, v^+, and v^-. Other parameters were kept at their default values. During the band formation phase, parameters were switched every half hour to the next measured set, for the duration of the measurements (not the same for each cell). Band parameters were set to the values measured, while gap parameters were set equal to the band values except for r_c, which was adjusted to accommodate band-gap differences in all parameters while maintaining the same value of control parameter G in the gap regions as in the measured set. Control parameter G is a quantity that derived from theoretical studies on microtubule alignment that combines the microtubule dynamic parameters into a single determinant of microtubule alignment [137, 160]:

$$G = \left(\frac{2(v^+ - v^{tm})^2 \cdot (v^- + v^{tm})}{r_n v^+ (v^+ + v^-)} \right)^{\frac{1}{3}} \cdot \left(\frac{r_r}{v^- + v^{tm}} - \frac{r_c}{v^+ - v^{tm}} \right). \tag{5.6}$$

It can be interpreted as a ratio between the average microtubule length in absence of microtubule interactions and the average length between microtubule interactions. As an alternative strategy, we also calculated gap catastrophe rates by keeping the ratio of average microtubule lifetime τ in bands and gaps constant:

$$\tau = \frac{v^+ + v^-}{r_c(v^- + v^{tm}) - r_r(v^+ - v^{tm})} \tag{5.7}$$

This approach gave very similar values for the factor difference in r_c between band and gap regions (f_{cat}), though, so for all simulations we only used the values based on parameter G.

For calculating steady state densities ρ^* in absence of microtubule-microtubule interactions, we followed the procedure from Dogterom and Leibler [235], as described in chapter 4:

$$\rho^\star = r_n \frac{(v^+ + v^-)(v^+ - v^{tm})(v^- + v^{tm})}{(r_c(v^- + v^{tm}) - r_r(v^+ - v^{tm}))^2}. \tag{5.8}$$

5.4.6 Summary statistics

Array alignment was quantified using the two-dimensional nematic order parameter S_2 as commonly used in polymer physics and often used for quantifying cortical microtubule alignment [103, 134, 160]:

$$S_2 = \sqrt{\langle\langle \cos(2\theta) \rangle\rangle^2 + \langle\langle \sin(2\theta) \rangle\rangle^2}, \tag{5.9}$$

where θ is the angle of individual microtubule segments with the x-axis of the simulation domain, and double angular brackets indicate a length-weighted average over all microtubule segments. Alignment parameter S_2 is zero for a completely isotropic array and one for a perfectly aligned array (ignoring microtubule polarity).

Overall array orientation Θ was also computed as commonly used in simulation studies [103, 160]:

$$\Theta = \arctan\left(\frac{\langle\langle\sin(2\theta)\rangle\rangle}{\langle\langle\cos(2\theta)\rangle\rangle + S_2}\right). \tag{5.10}$$

Band counts were calculated as the number of bands with a microtubule density at least three times higher than the average density in the gaps. This measure was selected after testing multiple options for best representing visual inspections of array snapshots and histograms.

Averages and standard deviations of orientations from multiple simulation runs were calculated using the average and standard deviation for angular quantities. The average orientation $\bar{\phi}$ over N simulations is:

$$\bar{\phi} = \frac{1}{2}\arg\left(\frac{1}{N}\sum_{n=1}^{N} e^{i2\phi_n}\right) \tag{5.11}$$

where arg is the argument of a complex number, and ϕ_n is the orientation of the n^{th} simulation. The factor 2 in the exponent and factor 1/2 before the argument correct the fact that we consider orientations without direction (so in $[0,\pi)$ rather than $[0,2\pi)$). The circular standard deviation sd_ϕ is:

$$sd_\phi = -2\ln\left(\left|\frac{1}{N}\sum_{n=1}^{N} e^{i2\phi_n}\right|\right), \tag{5.12}$$

where ln is the natural logarithm and the vertical bars indicate the absolute value of a complex number.

5.5 Supplementary figures

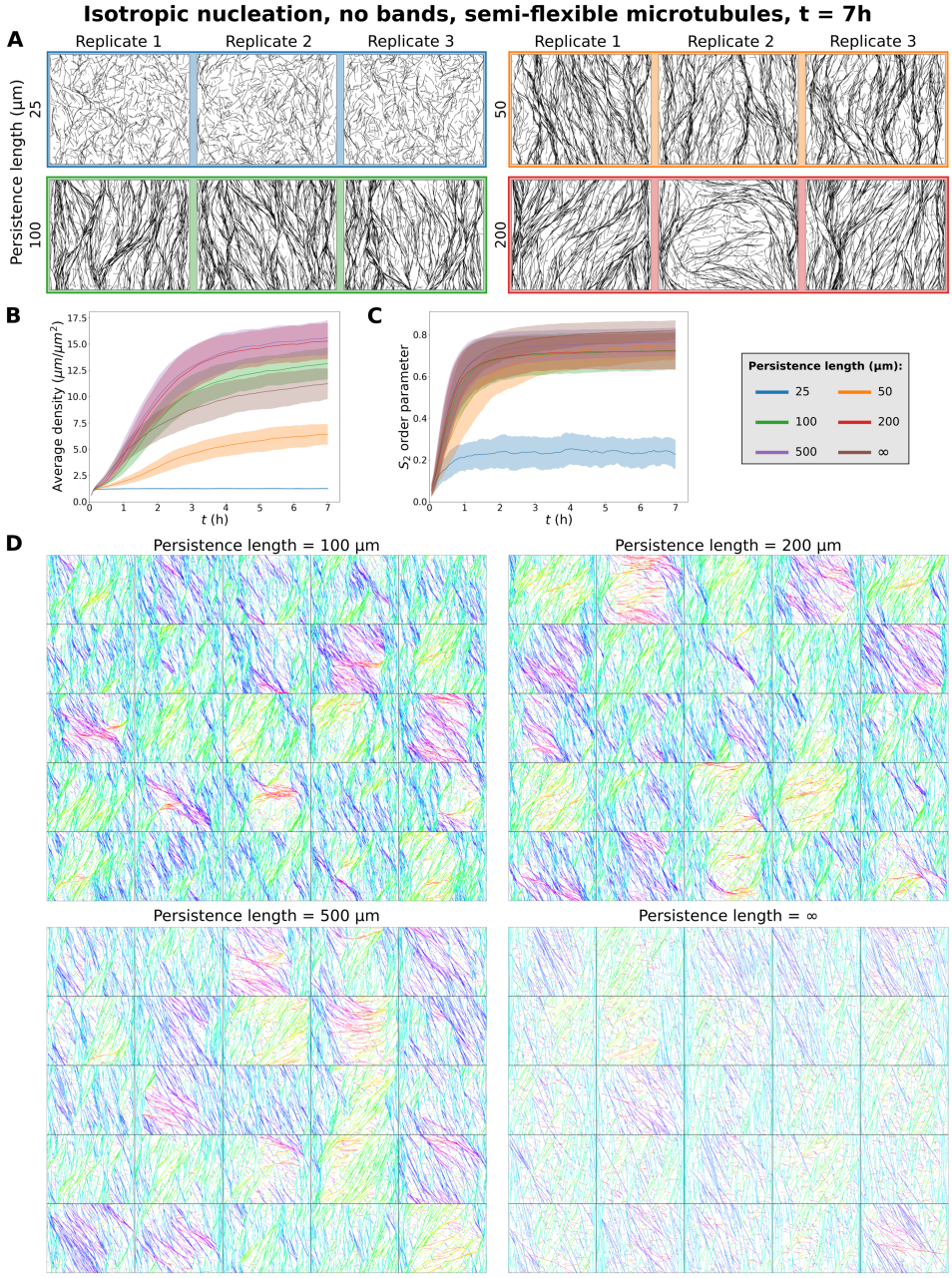

Fig. S5.1. Caption on next page.

Fig. S5.1. Semiflexible microtubules result in low densities and failure to align at low persistence lengths and global alignment difficulties at intermediate persistence length. (A) Snapshots at $t = 7h$ from array simulations without bands with isotropic nucleation for different microtubule persistence lengths. (B) Average microtubule density. (C) S_2 order parameter, showing degree of alignment. Quantities in (B–C) were calculated from 100 simulations. Lines indicate the average and shaded areas the standard deviation. (D) Snapshots at $t = 7h$ from 25 independent array simulations with isotropic nucleation without bands for different persistence lengths, and rigid microtubules (infinite persistence length). Microtubule segments are coloured by their orientation.

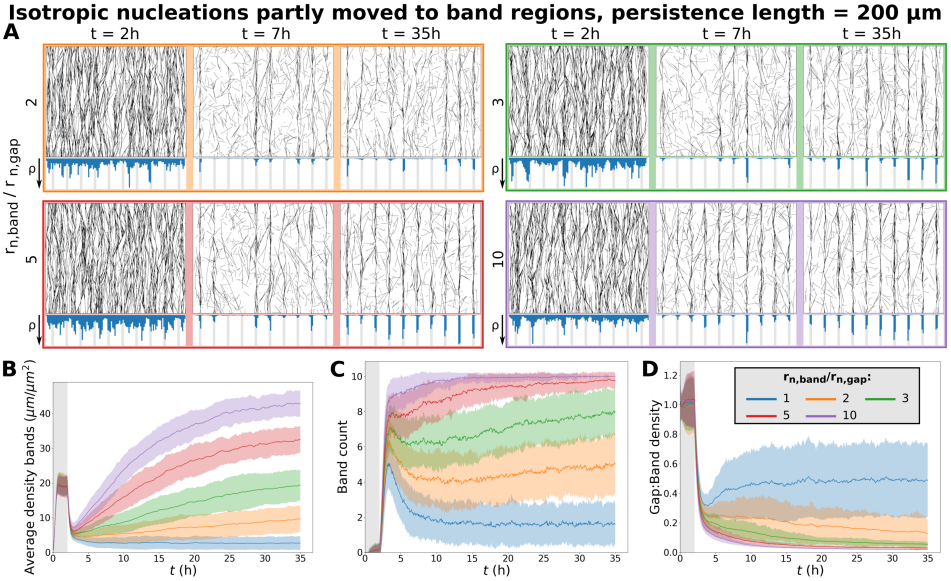

Fig. S5.2. With isotropic nucleation, maintenance of microtubule density in bands at a persistence length of 200 μm **is improved by shifting nucleations to bands.** (A) Snapshots from protoxylem simulations with a fraction of isotropic nucleations moved from gaps to bands, keeping the overall nucleation rate the same. The persistence length used was 200 μm. Starting arrays were obtained with transverse nucleations in the first half hour ($\alpha_{bias} = 0.5\pi$, $\alpha_{noise} = 0.01\ rad^2$). Histograms below showing local microtubule density ρ are plotted on the same scale within a time series, but not between time series. (B) Average microtubule density in the band regions. (C) Number of populated bands, defined as bands with a microtubule density greater than three times the average density in the gaps. (D) Ratio of density in gaps and bands. Quantities in (B–D) were calculated from 100 simulations. The band formation phase starts at the end of the grey area. Lines indicate the average and shaded areas the standard deviation.

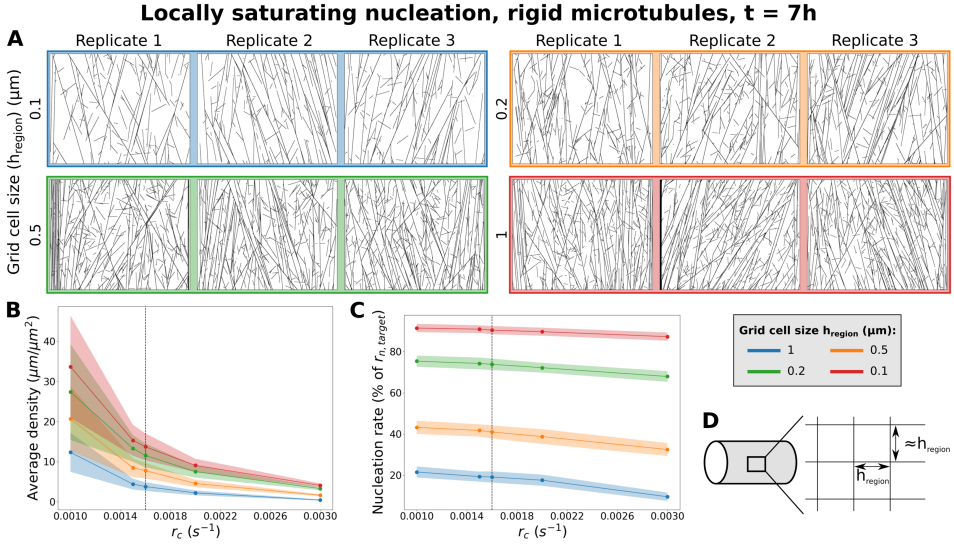

Fig. S5.3. With locally saturating nucleation, obtaining a dense array and achieving the maximal nucleation rate requires relatively large grid cells. (A) Snapshots at $t = 7h$ from array simulations without bands with locally saturating nucleation for different grid cell sizes. (B) Average microtubule density for different grid cell sizes and spontaneous catastrophe rates. (C) Realised nucleation rate, calculated over a 200 s measurement interval, as a percentage of the expected rate for a dense array with homogeneous microtubule coverage ($r_{n,target}$). Quantities in (B–C) were calculated from 100 simulations. Lines indicate the average and shaded areas the standard deviation. (D) Grid cells were as close to squares as possible for a given longitudinal size h_{region}.

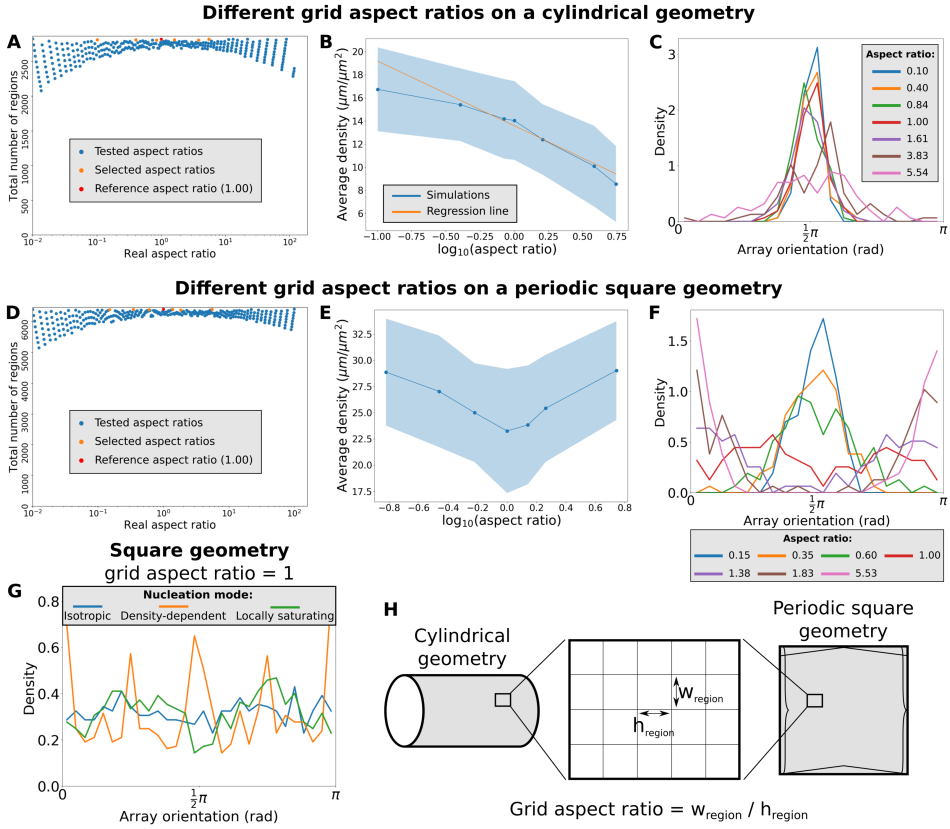

Fig. S5.4. The use of discreet grid cells with locally saturating nucleation results in a minor orienting bias for square grid cells. (A–C) Different grid cell aspect ratios on a cylindrical geometry with a length of 60 μm and a radius of 7.5 μm. (D–F) Different grid cell aspect ratios on an 80x80 μm periodic square geometry. (A,D) Grid cell aspect ratios and total number of grid cells that fit on the geometry. Selected aspect ratios (orange) were chosen to keep the total number of grid cells as similar as possible. (B,E) Average density at $t = 7h$ for simulations with locally saturating nucleation, different grid cell aspect ratios, no bands, and rigid microtubules. Blue lines indicate the average, and the shaded areas the standard deviation. The orange line in (B) is a linear regression fit through the centre five log-transformed aspect ratios, with equation: Average density $= 13.59 - 5.6\log_{10}(\text{aspect ratio})$. From this regression line we estimate a density difference of 6.2% for an aspect ratio of $\sqrt{2}$ (the ratio between the length of the side and the diagonal of a square grid cell). (C,F) Histograms of average array orientations at $t = 7h$ for different grid cell aspect ratios. Quantities in (B,C,E,F) were calculated over 100 simulations for each aspect ratio. (G) Histograms for average array orientations at $t = 7h$ for different nucleation modes on an 80x80 μm square grid geometry. Histograms were computed using 1000 simulations for each nucleation mode. (H) Cylindrical grid versus periodic square grid. Grid cell aspect ratios were calculated as the ratio of w_{region} and h_{region}.

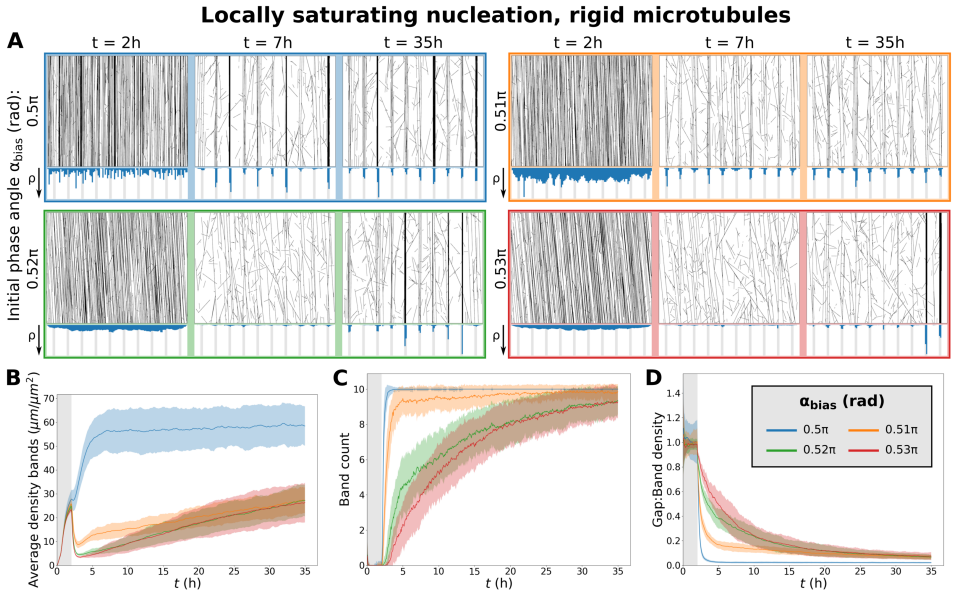

Fig. S5.5. With locally saturating nucleation, fast band formation still requires strong co-alignment for rigid microtubules. (A) Snapshots from protoxylem simulations with locally saturating nucleation using starting arrays with different bias angles α_{bias} in the first half hour with only minor deviations ($\alpha_{noise} = 0.01\ rad^2$). Histograms below showing local microtubule density ρ are plotted on the same scale within a time series, but not between time series. (B) Average microtubule density in the band regions. (C) Number of populated bands, defined as bands with a microtubule density greater than three times the average density in the gaps. (D) Ratio of density in gaps and bands. Quantities in (B–D) were calculated from 100 simulations. The band formation phase starts at the end of the grey area. Lines indicate the average and shaded areas the standard deviation.

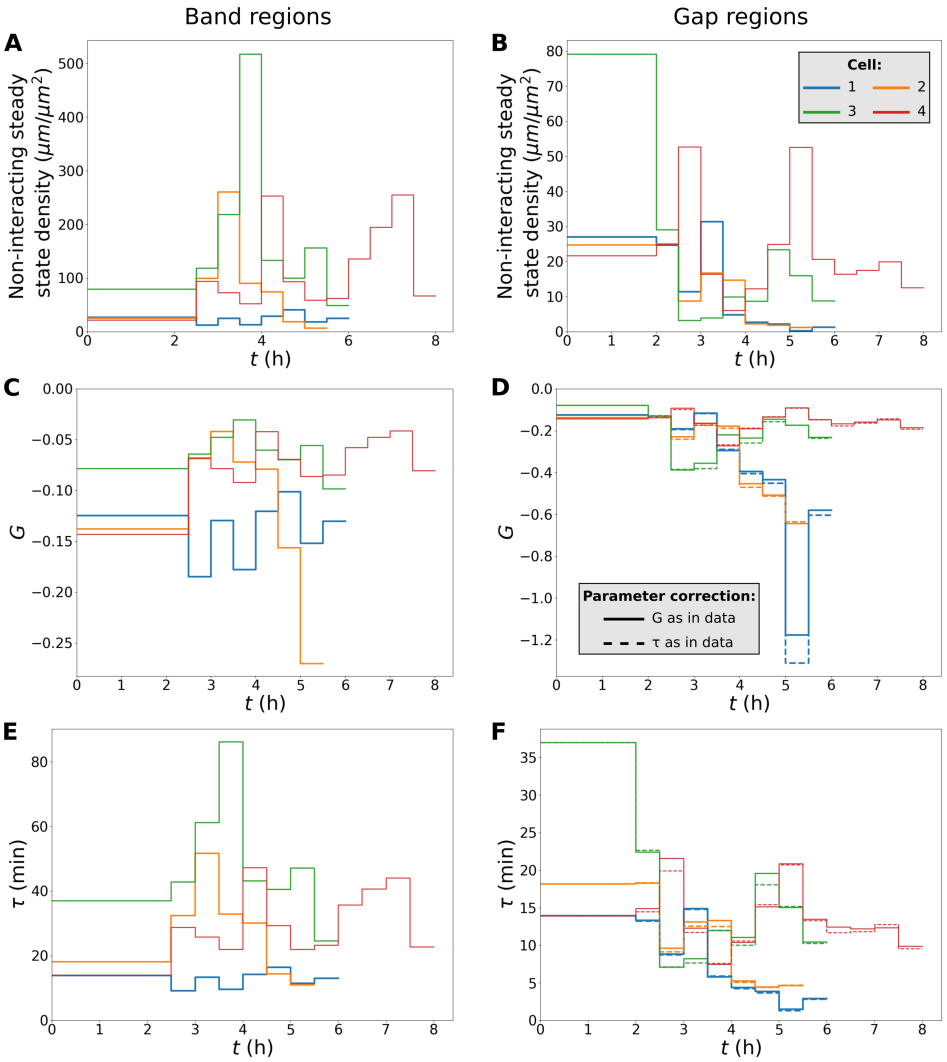

Fig. S5.6. Large differences between different cells in theoretical quantities relevant for array behaviour computed from experimentally measured microtubule dynamics parameters. (A,B) Steady state microtubule density in bands (A) and gaps (B) for simulation parameters from different cells assuming no microtubule-microtubule interactions and constant nucleation rate. (C,D) Control parameter G in bands (C) and gaps (D). For gaps, G is shown both as used in simulations (same as in data, solid line) and what it would be if $r_{c,gap}$ had been calculated to keep the value of τ in the bands the same as in the data (dashed lines). (E,F) Microtubule lifetime τ in bands (E) and gaps (F). For gaps τ is shown both as in simulations (solid line) and as in data (dashed line). Note that the y-axes of left and right panels differ. In the first two hours, all parameters are are the same for bands and gaps. Measured time series start after the first two hours. Graphs of G and τ quantities from data also appear in Schneider et al. [33].

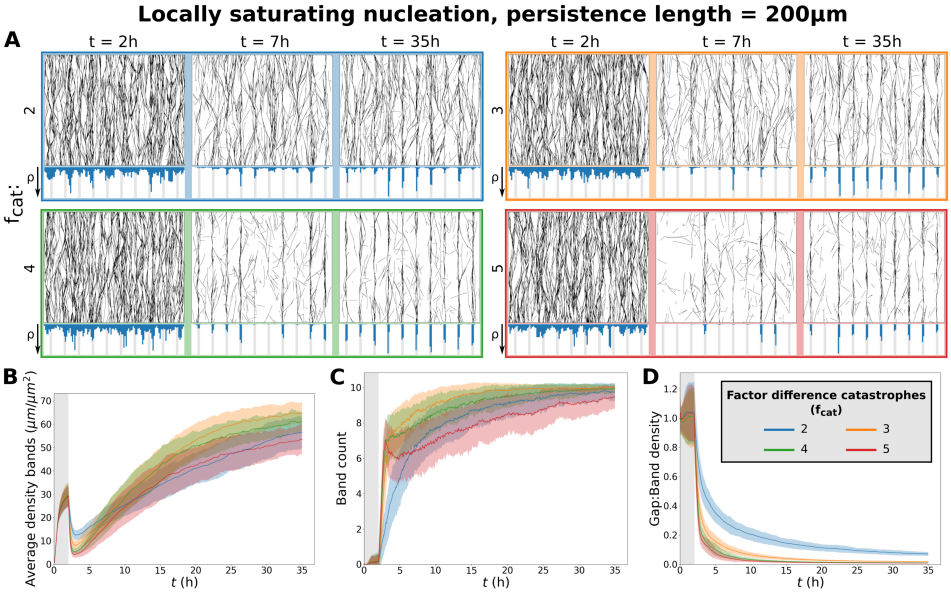

Fig. S5.7. With default parameters, f_{cat} has a strong influence on band formation and maintenance of microtubule density in bands. (A) Snapshots from protoxylem simulations for different values of f_{cat} using locally saturating nucleation. The persistence length used was 200 μm. Starting arrays were obtained with transverse nucleations in the first half hour ($\alpha_{bias} = 0.5\pi$, $\alpha_{noise} = 0.01\ rad^2$). Histograms below showing local microtubule density ρ are plotted on the same scale within a time series, but not between time series. (B) Average microtubule density in the band regions. (C) Number of populated bands, defined as bands with a microtubule density greater than three times the average density in the gaps. (D) Ratio of density in gaps and bands. Quantities in (B–D) were calculated from 100 simulations. The band formation phase starts at the end of the grey area. Lines indicate the average and shaded areas the standard deviation. The default value of f_{cat} is 3.

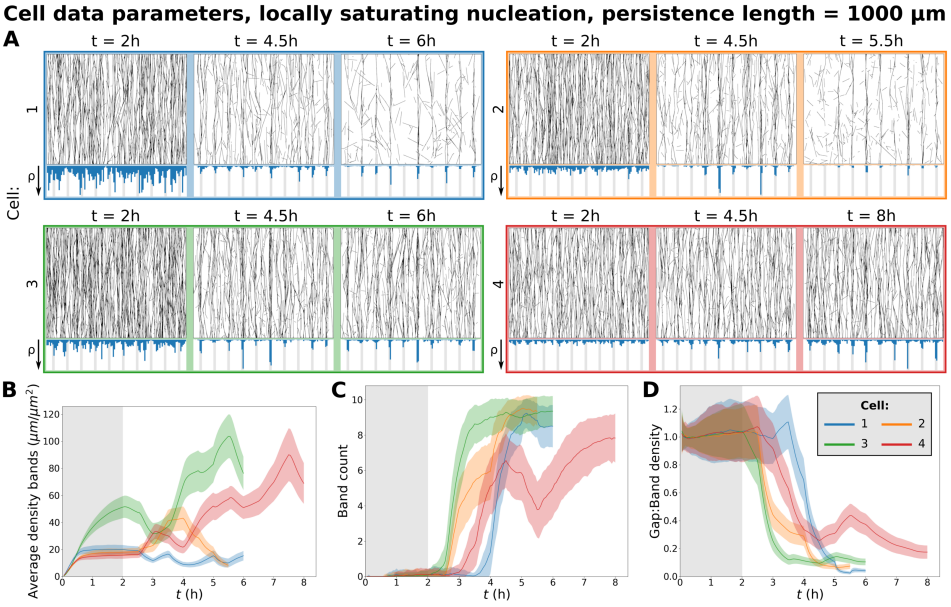

Fig. S5.8. At a higher persistence length, band formation with measured parameters improves, but with unrealistic densities for some cells. (A) Snapshots from protoxylem simulations for data from the four different measured cells, with locally saturating nucleation, a persistence length of 1000 μm, and an initiation phase with $\alpha_{bias} = 0.5\pi$ rad and $\alpha_{noise} = 0.01$ rad^2. Histograms below showing local microtubule density ρ are plotted on the same scale within a time series, but not between time series. (B) Average microtubule density in the band regions. (C) Number of populated bands, defined as bands with a microtubule density greater than three times the average density in the gaps. (D) Ratio of density in gaps and bands. Quantities in (B–D) were calculated from 100 simulations. The band formation phase starts at the end of the grey area. Lines indicate the average and shaded areas the standard deviation.

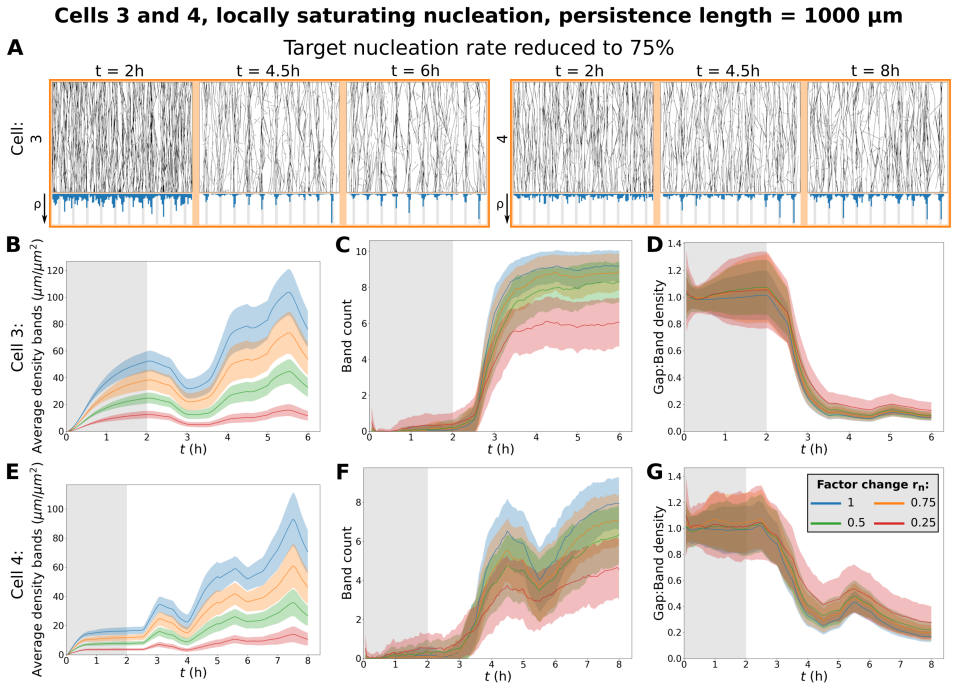

Fig. S5.9. Band formation with data from cell 3 and 4 tolerates a reduction in the nucleation rate, but not large enough to obtain reasonable densities. (A) Snapshots from protoxylem simulations for data from cell 3 and 4, with locally saturating nucleation, a persistence length of 1000 μm, and an initiation phase with $\alpha_{bias} = 0.5\pi$ rad and $\alpha_{noise} = 0.01$ rad^2). The nucleation rate was 75% of the default value. Histograms below showing local microtubule density ρ are plotted on the same scale within a time series, but not between time series. (B–G) Measurements from simulations of cell 3 and 4 for different target nucleation rates. (B,E) Average microtubule density in the band regions. (C,F) Number of populated bands, defined as bands with a microtubule density greater than three times the average density in the gaps. (D,G) Ratio of density in gaps and bands. Quantities in (B–G) were calculated from 100 simulations. The band formation phase starts at the end of the grey area. Lines indicate the average and shaded areas the standard deviation. The default value of r_n is 0.001 $\mu m^{-2}s^{-1}$.

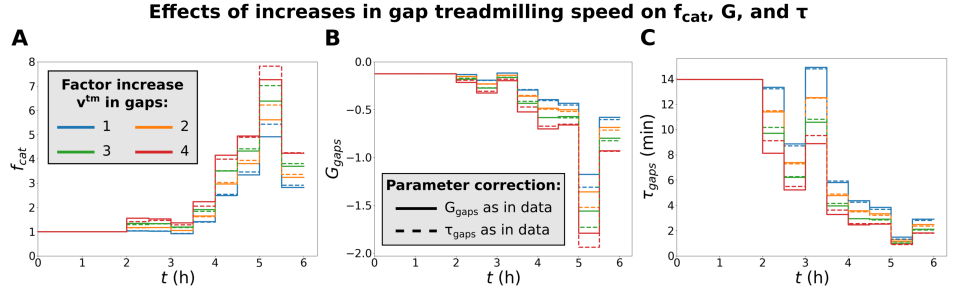

Fig. S5.10. A difference in treadmilling speeds between band and gap regions has little potential for improving initial band formation in cell 1. Difference in catastrophe rates between band and gap regions f_{cat} (A), control parameter G (B), and microtubule lifetime τ (C), calculated to conserve G (solid lines) or τ (dashed lines) in gaps, for different treadmilling speeds (v^{tm}) in gaps. In bands, v^{tm} was kept at its default value of 0.01 $\mu m/s$.

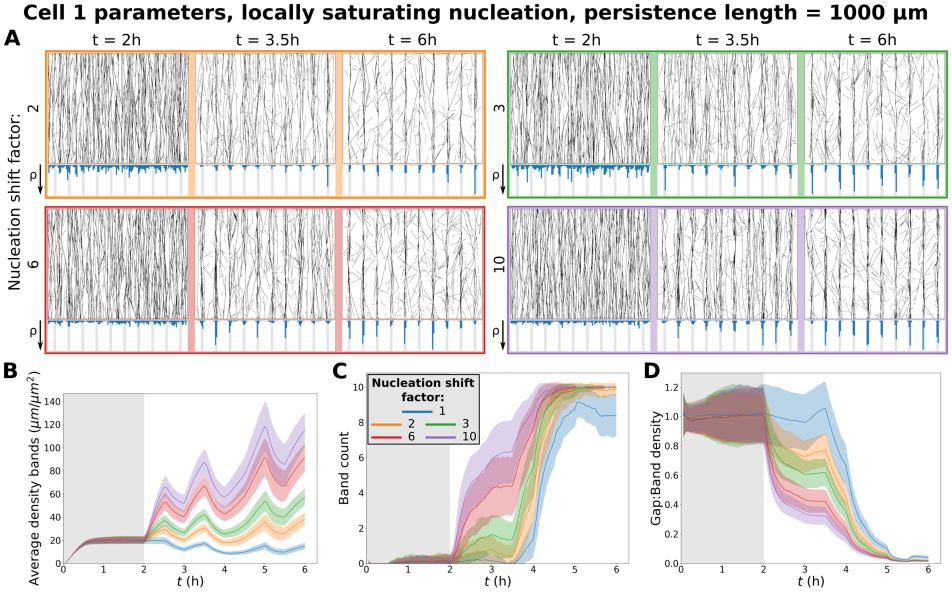

Fig. S5.11. With a persistence length of 1000 μm, a large nucleation rate shift to the band regions would allow band formation in the first 1.5 hours for cell 1. (A) Snapshots from protoxylem simulations for data from cell 1, with locally saturating nucleation, a persistence length of 1000 μm, and an initiation phase with $\alpha_{bias} = 0.5\pi$ rad and $\alpha_{noise} = 0.01$ rad^2. During band formation, the target nucleation rate in the band regions was increased by different factors compared to the band regions, keeping the weighted average constant. Histograms below showing local microtubule density ρ are plotted on the same scale within a time series, but not between time series. (B) Average microtubule density in the band regions. (C) Number of populated bands, defined as bands with a microtubule density greater than three times the average density in the gaps. (D) Ratio of density in gaps and bands. Differences are more substantial than for a persistence length of 200 μm (Fig. 5.8). Quantities in (B–D) were calculated from 100 simulations. The band formation phase starts at the end of the grey area. Lines indicate the average and shaded areas the standard deviation. Values of $r_{n,sat,max}$ in bands and gaps respectively were (in $\mu m^{-2} s^{-1}$): 0.0035 and 0.0035 for shift factor 1, 0.006 and 0.003 for shift factor 2, 0.0079 and 0.0026 for shift factor 3, 0.011 and 0.0019 for shift factor 6, and 0.014 and 0.0014 for shift factor 10.

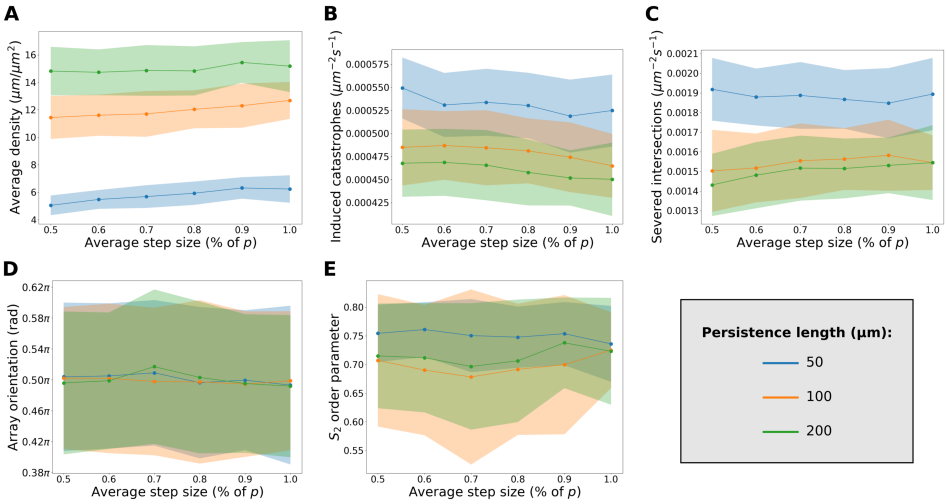

Fig. S5.12. Influence on array behaviour of different step sizes for the same persistence length. (A–E) Quantification of array state and simulation processes at $t = 7h$ from simulations without bands using isotropic nucleation for various difference persistence lengths and deflection step sizes. Simulations used the default cylindrical geometry and were initiated with seeded nucleations as described in Methods. (A) Average microtubule density. (B) Overall number of induced catastrophes per area per second. (C) Overall number of intersection severing events per area per second. (D) Average array orientation. (E) S_2 order parameter, showing degree of alignment. (A,D,E) Quantities measured at $t = 7h$ intervals. (B,C) Quantities averaged over the last 200 s measurement interval. Quantities in (A–E) were calculated from 100 simulations. Lines indicate the average and shaded areas the standard deviation. Step sizes are expressed as a percentage of the persistence length p.

5.6 Appendices

5.6.1 Parameters for locally saturating nucleation

For calculating parameter values associated with the locally saturating nucleation mode, we aimed at an overall target nucleation rate $r_{n,target}$ for homogeneous arrays of 0.001 nucleations per μm^2 per s, consistent with previous work [33, 160] (Chapter 4). For the fairly low value of $\rho_{\frac{1}{2}} = 0.1\mu m/\mu m^2$ (as in Deinum et al. [160]), this means a homogeneous array will achieve a nucleation rate close to the saturated value of $r_{n,sat}$. We will therefore set the target value of $r_{n,sat}$ to $r_{n,target} = 0.001\mu m^{-2}s^{-1}$.

To calculate $r_{n,sat,max}$ (the value of $r_{n,sat}$ when all nucleation complexes are free), we use the factor difference f_{rn} between the nucleation rate when all complexes are available and the target nucleation rate. We estimate this rate from the ratio between microtubule-associated insertions in nearly empty oryzalin-treated arrays (0.013 insertions per μm^2 per s) and total, mostly microtubule-associated, insertions in established arrays (0.0037 insertions per μm^2 per s) that we measured in Chapter 4. This approach gives us the following value for $r_{n,sat,max}$:

$$r_{n,sat,max} = f_{rn} \cdot r_{n,target} = \frac{0.013}{0.0037} \cdot 0.001 = 0.0035\mu m^{-2}s^{-1}. \tag{A5.1}$$

The unbound nucleation rate $r_{n,base}$ is always a fixed factor $f_{unbound}$ below $r_{n,sat}$. In absence of microtubules, the nucleation complex insertion rate is about a factor 40 lower than in a populated array (Chapter 4) and the rate at which complexes nucleate is about a factor 15 lower [108], making the total nucleation rate in absence of microtubules $r_{n,base,max}$ about a factor 600 less than $r_{n,target}$. Therefore, our estimate for $f_{unbound}$ becomes:

$$f_{unbound} = \frac{r_{n,base,max}}{r_{n,sat,max}} = \frac{0.001/600}{0.0035} = 0.0005. \tag{A5.2}$$

We further use a fixed duration $t_{occupied}$ of 60s during which a nucleation complex remains occupied upon nucleation, based on an average of 58.9s observed in experimental work [108].

Using our estimates for parameters $r_{n,target}$, $r_{n,sat,max}$, $f_{unbound}$, and $t_{occupied}$, we can now calculate the remaining parameter N_{tot}. At nucleation rate $r_{n,target}$, a number of $N_{occ,target}$ nucleation complexes are expected to be occupied, following:

$$r_{n,target} = r_{n,sat,max}\frac{N_{tot} - N_{occ,target}}{N_{tot}}, \tag{A5.3}$$

where N_{tot} is the total number of nucleation complexes. Using this expression and the fact that the number of occupied complexes depends on the duration of occupancy $t_{occupied}$ and the rate at which they become occupied (i.e., the global nucleation rate), we find the following expression for N_{tot}:

$$N_{tot} = \frac{r_{n,sat,max} \cdot N_{occ,target}}{r_{n,sat,max} - r_{n,target}} = \frac{r_{n,sat,max} \cdot r_{n,target} \cdot t_{occupied} \cdot A}{r_{n,sat,max} - r_{n,target}}, \tag{A5.4}$$

where A is the total domain area.

5.6.2 Persistence length calculations

Persistence length p measures how fast the correlation between the orientation of two different points on a microtubule decays with the microtubule length between these points. We use the following definition of persistence length p:

$$\langle r_n \cdot r_{n+k} \rangle = e^{-\frac{L}{2p}}, \tag{A5.5}$$

where $\langle r_n \cdot r_{n+k} \rangle$ is the average inner product of unit vectors r_i in the direction of the microtubule at points n and $n+k$ and L is the length along the microtubule between these two points.

Since Eq. A5.5 holds for any two points n and $n+k$, and we are using independent deflections, it is sufficient to look at a single deflection after length l between points n and $n+1$:

$$\langle r_n \cdot r_{n+1} \rangle = e^{-\frac{l}{2p}}. \tag{A5.6}$$

For a given deflection angle ϑ (Fig. A5.1A), setting the arbitrary initial angle to 0, r_{n+1} is given by:

$$r_{n+1} = \begin{bmatrix} \cos(\vartheta) \\ \sin(\vartheta) \end{bmatrix}. \tag{A5.7}$$

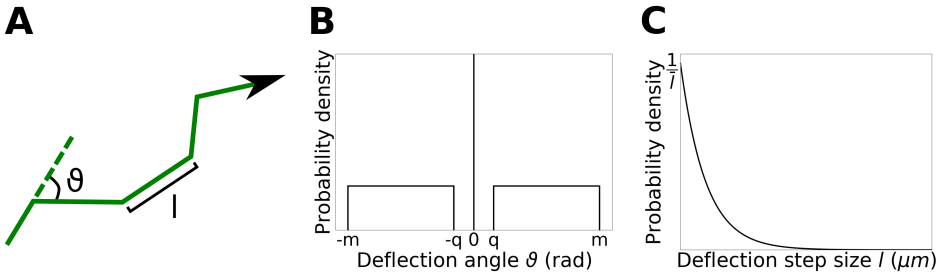

Fig. A5.1. Semiflexible microtubule implementation details. (A) Simulated microtubules get deflections of angle ϑ every deflection step size l. Angles in cartoon have been exaggerated for visibility. (B) Deflection angles are drawn from a uniform interval $[-m,m]$, with all angles in $[-q,q]$ set to zero. Value of q in graph is exaggerated for visibility. (C) Deflection step sizes are drawn from an exponential distribution with average $\bar{l}$.

For the inner product in Eq. A5.6, we then get:

$$\langle r_n \cdot r_{n+1} \rangle = \left\langle \begin{bmatrix} 1 \\ 0 \end{bmatrix} \cdot \begin{bmatrix} \cos(\vartheta) \\ \sin(\vartheta) \end{bmatrix} \right\rangle = \langle \cos(\vartheta) \rangle. \tag{A5.8}$$

We take deflection angles ϑ, drawn from a uniform interval $[-m,m]$, with the smallest angles ($|\vartheta| < q$) set to zero for numerical reasons (Fig. A5.1B). In that case, we get:

$$\langle \cos(\vartheta) \rangle = \frac{q}{m}\cos(0) + \frac{m-q}{m}\frac{1}{m-q}\int_q^m \cos(\vartheta)\,d\vartheta = \frac{\sin(m)-\sin(q)+q}{m}. \tag{A5.9}$$

Taking deflection step lengths l drawn from an exponential distribution with mean $\bar{l}$ (Fig. A5.1C), we can now determine the persistence length p for a given value of m:

$$p = \langle p \rangle = \left\langle -\frac{l}{2\ln(\langle r_n \cdot r_{n+1} \rangle)} \right\rangle = \left\langle -\frac{l}{2\ln\left(\frac{\sin(m)-\sin(q)+q}{m}\right)} \right\rangle = -\frac{\bar{l}}{2\ln\left(\frac{\sin(m)-\sin(q)+q}{m}\right)}. \tag{A5.10}$$

Therefore, if we draw our deflection step sizes from a distribution with average $\bar{l}$, we can solve the boundary value m of the interval from which we draw the deflection angles from the above equation for the desired persistence length p. This means that we can control the microtubule persistence length in our simulations using $\bar{l}$, m, and q as input parameters, with one of m and $\bar{l}$ calculated to obtain the desired p.

6

General discussion

6.1 Insights into mechanisms of xylem patterning

In this thesis, we aimed to gain insights into the mechanisms underlying xylem patterning by ROPs and microtubules, using dynamic models. We first focused on patterning of ROPs, starting from generic small GTPase models, using partial differential equation models to describe the behaviour of the proteins involved. Starting from existing GTPase models, which exclusively produce a single stable cluster of active GTPase [84, 168], we showed that addition of turnover or negative feedback to these models allows patterns of coexisting clusters to form (**chapter 2**). This way, we could generate a spotted metaxylem ROP pattern, as well as patterns of gaps and curved stripes. We next showed that these patterns could be flattened longitudinally and oriented transversely by a longitudinal ROP diffusion restriction, to obtain a banded protoxylem pattern (**chapter 3**). Then, we switched to the patterning of the microtubule array, using stochastic simulation models to describe microtubule dynamics and interactions. Xylem patterns require an even distribution of microtubules along the non-gap regions, as do many other cortical array structures. In **chapter 4**, we used a simplified one-dimensional microtubule model to show that an even distribution of microtubules could be achieved with a realistic implementation of microtubule-bound nucleations. The critical ingredient of this implementation was a local saturation of the nucleation rate with the microtubule density. In **chapter 5**, we investigated the requirements for microtubules to follow a predefined banded protoxylem pattern in a two-dimensional context. We identified crucial roles for co-alignment of the initial microtubule array with the underlying ROP pattern, microtubule flexibility, and realistic nucleation. Here, I will first discuss the insights we obtained into the mechanisms of xylem patterning by ROPs and microtubules, followed by insights into other patterning processes and the strategies we used to obtain these mechanistic insights.

6.1.1 A ROP-based Turing pattern as the basis of xylem patterning

For metaxylem, there is strong evidence that local ROP activity is at the basis of secondary cell wall patterning. ROP11 accumulates at future gap sites and recruits effector proteins like MIDD1 and Kinesin13A to these sites, which destabilise microtubules [147–149]. In addition, ROPGEF4 and ROPGAP3 also accumulate at these sites, providing a potential for positive and negative feedback [148]. Under the right conditions, ROPs and other small GTPases can spontaneously form patterns through a Turing-style reaction diffusion mechanism [44, 45] and positive feedback activation is an essential ingredient of such a mechanism [46, 47]. A potential mechanism for this positive feedback may be a dimerisation of GEF4, allowing recruitment of new ROP proteins [32]. Such GEF-effector coupling is common in many small GTPase systems [68] and has been shown to be sufficient for spontaneous patterning *in vitro* [69]. Assuming the presence of a positive feedback, we could obtain metaxylem-like spotted patterns with a simple reaction-diffusion model (chapter 2). Others have obtained similar results with a more elaborate model [32]. All these lines of evidence strongly point to a Turing-style reaction diffusion system as the basis of the spotted metaxylem pattern.

For protoxylem patterning, however, it is less well-established whether and how ROPs are involved. One paper did report accumulation of ROP7 in a banded pattern in developing protoxylem [150], but no further experimental verification of this observation has ap-

peared since. However, various ROPs, as well as ROP effectors MIDD1 and Kinesin13A are expressed in developing protoxylem [151, 152]. In addition, the areas where the gaps fall in the cortical array have different microtubule dynamics parameters [33], suggesting local activity of microtubule-modulating proteins, which could be controlled by ROPs and their downstream effectors. Furthermore, the metaxylem gaps can be stretched into spiral or net-like patterns resembling protoxylem by treatment with the microtubule-stabilising drug taxol [148, 263], as well as by overexpression of microtubule-associated proteins MAP70-5 and MAP70-1 [153], indicated to stabilise microtubules [251]. A similar effect can be achieved by overexpressing IQD13, which is involved in microtubule-membrane linkage [154], or knocking out CORD proteins, which partially detach microtubules from the membrane [155]. For these reasons, it seems likely that the closely related proto- and metaxylem employ similar patterning mechanisms.

6.1.2 Protoxylem ROP pattern orientation

Assuming ROP involvement in protoxylem is similar to that in metaxylem, we further investigated how a protoxylem ROP pattern could be formed and oriented in chapter 3. One way in which a Turing pattern might be oriented is through anisotropic diffusion [209], which has been used to model oriented stripe formation in fish skin [208]. In protoxylem, anisotropic ROP diffusion may occur since microtubules can act as ROP diffusion barriers [148], a property that depends on IQD13 [154] and is diminished by microtubule-detaching CORD proteins [155]. In addition, protoxylem patterning starts with the microtubule array adopting a transverse orientation [33, 122]. We therefore explored the effect of a longitudinal diffusion restriction of active ROPs on each of the classical reaction-diffusion patterns of spots, curved stripes, and gaps [49, 50]. We found that diffusion restriction could impose a transverse orientation on a striped pattern and flatten spots and gaps (chapter 3). A sufficiently strong diffusion restriction could even flatten spots and gaps into a transverse banded pattern. By using oblique starting arrays, we could also obtain spiral ROP patterns that would correspond to the spiral cell wall reinforcements that are also commonly observed in protoxylem [7].

We also looked into the mechanism behind the orientation process and found that diffusion restriction allows patterns with curved features to expand predominantly in the unrestricted direction. Straight patterns, however, are not affected by this mechanism and required a significant spatial perturbation to make reorientation possible. This observation further emphasises the importance of a well-aligned and properly oriented starting array.

6.1.3 Coexistence in ROP and microtubule patterns

While classical reaction-diffusion systems are well-known for their ability to generate regular patterns of spots and stripes [49, 50] as required in xylem patterning, most models for small GTPase patterning generate competing clusters that ultimately yield a single surviving cluster [40, 83–86]. Similarly, most implementations of microtubule-dependent microtubule nucleation result in competition for nucleations. In protoxylem simulations, competition between microtubule bands leaves most bands largely empty [33], while in classical array simulations, competition between local microtubule clusters yields highly inhomogeneous arrays [135, 136, 160, 161]. These two major hurdles to modelling xylem

patterning both arise from an unrestricted global competition for a limited resource, in which larger clusters attract a larger share of that resource and therefore grow even larger. Indeed, such global competition for the GTPase Cdc42 and its GEF Cdc24 has been proposed to drive the consistent formation of a single yeast bud [40, 264]. We explored ways to obtain coexisting ROP clusters in chapter 2 and coexisting protoxylem bands in chapter 4.

In chapter 2, we showed two types of modifications to classical GTPase models that would allow for coexisting clusters: adding turnover, and adding negative feedback. Classical GTPase models for polarisation commonly assume mass conservation, i.e., a conservation of the total amount of GTPase. These mass-conserved reaction-diffusion models generate a number of clusters that compete with each other until only one survives in a process similar to surface-tension-driven coarsening [87]. Adding GTPase turnover breaks mass conservation and allows smaller clusters access to a constant supply of GTPase, independent of their size, stabilising cluster coexistence (chapter 2). Mathematically, this stabilisation can be described as an interrupted coarsening process [265]. Alternatively, in the mass conserved model, the active GTPase may activate GAPs. This way, clusters with more GTPase will activate more GAPs and therefore hinder their own growth, allowing smaller clusters to compete (chapter 2). Some variant of this mechanism is plausible for xylem patterning, since ROPGAP3 has been observed to accumulate around ROP clusters [148].

A different modelling study later added a third mechanism, in which the inactive form requires an additional conversion step before it can be activated again [223]. In this indirect substrate mechanism, the inactivated form that appears from inactivation at large clusters has some time to diffuse away from the cluster before it can be activated again, allowing for GTPase redistribution. While there are no obvious indications that this last mechanism would apply to ROP patterning in xylem development, it does, in theory, have potential for stabilising coexisting microtubule bands, through tubulin redistribution. In chapter 4, we examined the possibility that a local tubulin limitation might counteract the competition for nucleations. Such a tubulin limitation would be a natural implementation of the indirect substrate coexistence mechanism, since growing microtubules consume GTP-tubulin, while shrinking microtubules release GDP-tubulin, which cannot be incorporated again until it has been converted back into GTP-tubulin. However, while this could work in principle, we found that in practice this mechanism would require an unrealistically low tubulin diffusion coefficient.

Instead, we found that a locally limited supply of nucleation complexes was sufficient to prevent global competition and congruent with experimental data. With a constant, homogeneous supply of nucleation complexes, the nucleation rate saturates locally with microtubule density. Therefore, dense local regions cannot take complexes from less dense regions, just like adding turnover to a GTPase model prevents large clusters from using the inactive GTPase supply from smaller clusters. With this local saturation, microtubule-dependent nucleation could enhance formation of local structures like protoxylem bands, without the majority of the bands losing their microtubules to a global competition. This conclusion applied both to detailed nucleation complex simulations in a simplified microtubule model (chapter 4), and to a simplified nucleation complex representation in a detailed microtubule model (chapter 5).

6.1.4 ROP-microtubule interplay

One of the reasons that developing xylem is such an interesting model system for pattern formation at the cell membrane is that it relies on mutual interactions between ROPs and microtubules. ROP activity destabilises microtubules in gap regions, shaping the microtubule pattern [33, 148, 149], while microtubules restrict ROP diffusion [148, 154, 155], orienting the ROP pattern (chapter 3). We have learned much about xylem patterning by studying the behaviour of ROPs and microtubules separately. Some aspects, however, can only be understood by looking at the behaviour of ROPs and microtubules together. We have studied two of these aspects: the effect of the microtubule diffusion barrier disappearing in response to ROP activity on ROP patterning (chapter 3) and the effect of co-alignment of the ROP pattern with the microtubule array on microtubule patterning (chapter 5).

During protoxylem ROP patterning, the microtubule diffusion barriers that orient the ROP pattern are themselves broken down at places where active ROP accumulates. In chapter 3, we showed that the orienting mechanism breaks down if this response is instantaneous. With a delayed response, the orienting effect of the diffusion restriction could linger long enough to create a banded protoxylem pattern. However, this variant made the bands move like travelling waves, with microtubule density getting broken down on one side of a ROP band and created on the other. These waves resulted from the delayed negative feedback of this model variant, which, in general, is known to give rise to oscillations and travelling waves [191, 266]. We could obtain a static banded pattern, however, by assuming a positive feedback that maintains local microtubule density. A good biological candidate for this positive feedback is the microtubule-dependent microtubule nucleation that we examined in chapters 4 and 5. Alternatively, waves may be prevented by other aspects of microtubule behaviour not included in the differential equation description used in chapter 3. For example, microtubules are long polymers and most of their dynamics occur at their tips [99]. Testing this hypothesis would require combining the ROP model with a more realistic microtubule model, like the one from chapter 5.

The interplay between ROPs and microtubules does not just create additional hurdles to overcome. In chapter 5, we showed that protoxylem microtubule band formation strongly depends on a co-alignment with the underlying ROP pattern. A ROP pattern that closely follows the initial orientation of the microtubule array as we propose in chapter 3 is, therefore, very helpful to subsequent microtubule patterning. This shows that the ROP-microtubule interplay provides some tolerance to local and global differences in the initial array orientation. However, proper alignment of the microtubule array is still required, both to orient the ROP pattern consistently and to end up with microtubules that largely follow the pattern set by ROP activity. Indeed, poor alignment of the starting array as observed in the *katanin* mutant correlates with aberrant protoxylem patterns in experiments, with poor separation of microtubule bands [33]. Furthermore, the degree of co-alignment that can reasonably be expected based on our simulations in chapter 3 is not sufficient by itself. Some degree of microtubule flexibility, beyond the ability to from bundles upon collision, is also required to reduce the detrimental effect of small mismatches (chapter 5).

6.2 Insights into non-xylem membrane patterning

Small GTPases and microtubules are involved in many different patterning processes even in plants alone [92, 267]. Therefore, many of the insights from previous chapters can be generalised to other membrane patterning processes.

6.2.1 Coexistence in non-xylem small GTPase patterns

Patterns of coexisting GTPase clusters do not only occur in xylem patterning. Another interesting example is found in leaf epidermal cells (pavement cells). In isotropically growing leaf epidermis, species with larger cells form pavement cells with a puzzle piece shape, proposed to limit mechanical stress in the tissue [217]. Three ROPs are involved in producing this morphology of regular lobes and indents: ROP2 and ROP4, which act redundantly to specify the lobes, and ROP6, which specifies the indents [89–91]. Therefore, complementary regular patterns of coexisting ROP clusters have to form. The ROPs in the lobes and the indents act antagonistically, providing a double negative feedback loop [78], which behaves as net positive feedback in a reaction diffusion mechanism [168]. However, a minimal model with mutual inhibition of two GTPases still yields competing clusters with, ultimately, one remaining (chapter 2). A more elaborate model developed specifically for the ROPs in pavement cells suffers from the same problem [30, 268, 269]. As for models with direct positive feedback, stable coexistence can be obtained in mutual inhibition models by including ROP turnover or adding a kind of negative feedback to ROP activity (chapter 2).

Mechanisms supporting stable coexistence also allow for the appearance of additional clusters in an existing pattern (chapter 2). In xylem development, this feature is not necessary, as the pattern is only required to exist more or less statically for several hours while the secondary cell wall is formed [122]. Pavement cells, however, maintain their interdigitated structure for their lifetime, with additional lobes and indents appearing as they grow [176], requiring an increase in the number of ROP clusters. Branching tip growing systems also require an increase in the number of GTPase clusters specifying the growing tips. Fungal hyphae, for example, may branch either apically (i.e., by tip splitting) or laterally [88]. In chapter 2, we showed that the negative feedback coexistence mechanism could give a cell control over the splitting of a GTPase cluster by adjusting the amount of available GTPase and GAP. This ability to dynamically control the number of clusters makes the negative feedback mechanism particularly suitable for branching tip growing systems. In pavement cells, on the other hand, ROP turnover might be sufficient, since the domain will be able to accommodate more stable clusters as it grows larger, although involvement of negative feedback cannot be ruled out.

6.2.2 Patterns of a single GTPase cluster

The efforts to find possibilities of coexistence in small GTPase models, both by us (chapter 2) and others [177, 223], might suggest that it is trivial to obtain patterns of a single GTPase cluster, as required in many biological systems. One could argue that the coarsening behaviour that generates a single cluster is the default state, since a two-variable mass-conserved model with positive feedback activation is a minimal model that allows

spontaneous patterning [168]. However, it turns out that this coarsening behaviour is easily perturbed by including additional structural elements in the model, including turnover, negative feedback (chapter 2), and a temporarily unusable inactive form [223]. These elements are common in biological systems and there may be many other kinds of interactions that allow for coexistence in reaction-diffusion systems. This raises the question if biological systems that require one cluster really use a coarsening mechanism to generate such a single cluster under all circumstances. In models that allow coexistence, the number of clusters on a given domain could be reduced by reducing the production and degradation rates in models with turnover and reducing the amount of GTPase and GAP in models with negative feedback (chapter 2). This way, cells can control the number of clusters formed and even produce just a single cluster when required. Therefore, many biological systems that form a single GTPase cluster may just be special cases of systems that form coexisting clusters.

An example can be found in the case of root hair initiation, which requires formation of a single cluster of ROP2 at the basal end of the cell [193]. This process has been modelled with a reaction-diffusion model with ROP turnover, with an auxin-dependent self-activation term that ties ROP patterning to the auxin gradient and ensures that the ROP cluster forms at the basal side of the cell [35]. Simulations of various auxin mutants resulted in formation of a second ROP cluster, in line with experimental observations of the formation of a second root hair [35]. In addition, growing root hairs do not normally branch but strong branching can be observed in root hairs overexpressing ROP2 [193]. Furthermore, in yeast budding, competition for the relevant GTPase (Cdc42) and its GEF (Cdc24) has been proposed as an explanation for the consistent formation of a single bud [40, 264]. However, this process also contains a negative feedback loop, which accelerates the polarisation process and makes it less sensitive to the GTPase concentration, but also makes coexistence possible, allowing formation of multiple buds in certain mutants [157]. These examples illustrate how mass-conserved reaction-diffusion models may not provide a correct understanding of how single GTPase clusters form in biological reality.

6.2.3 Cortical array homogeneity and nucleation

Realistic microtubule nucleation is not just important for coexistence of protoxylem bands, but also for microtubule array homogeneity in general. Elongating interphase cells for example, have more or less homogeneous microtubule arrays with a transverse orientation [98]. This ensures a similar pattern of cellulose fibrils in the cell wall, which is required to make the cell expand only in the longitudinal direction [123]. In chapter 4, we showed that homogeneous microtubule arrays could be formed with the same locally limited supply of nucleation complexes that allows for coexisting protoxylem bands.

However, with a microtubule-dependent insertion of nucleation complexes in the membrane, it takes a long time to populate a new array from scratch. This problem could be solved by assuming that an additional source of nucleations independent of the standard nucleation complexes helps to get array formation started (chapter 4). These additional nucleations are in line with experimental work, which has shown that formation of a new array after cytokinesis or oryzalin treatment involves a large number of nucleations not associated with γ-tubulin ring complexes containing GCP2 (γ-tubulin complex protein 2) [161]. Combined with these extra nucleations, the more realistic nucleation mechanism

solves the inhomogeneity problem that has been plaguing all previous simulations that have tried to incorporate microtubule-based nucleation thus far [135, 136, 160, 161]. This solution applies not only to fully homogeneous arrays and coexisting protoxylem bands, but to any array structure that requires an even distribution of microtubules rather than a single large band, including developing metaxylem [155], and growing pavement cells [90].

There is, however, at least one situation where a single band of microtubules is required: the formation of the preprophase band. This single microtubule band forms around the nucleus before cell division [77]. This specific localisation suggests involvement of factors from the nucleus in the positioning of the preprophase band. In simulations, a single microtubule band in the right location could be formed by increasing the local nucleation rate at the future band site [145]. Such an increase could be achieved, for example, by a sudden release of nucleation factors from the nucleus. TPX2/TPXL proteins of 'group A' are good candidates, because they recruit nucleation complexes to microtubules via augmin complexes [230] and contain a nuclear importin domain [231]. Therefore, a possibility is that these proteins are first sequestered in the nucleus and then suddenly released, temporarily creating a band around the nucleus in which microtubules are more effective at recruiting nucleation complexes. If this effect is sufficiently strong, the microtubules in this band may end up winning a global competition for nucleation complexes with the rest of the array, resulting in the formation of a single local band at the correct position. This way, cells may tune the microtubule array to produce both homogeneous and highly inhomogeneous structures. However, many other factors are involved in determining the location of the preprophase band as well. These include various polarity factors, such as ROPs, which accumulate in the membrane on opposing sides of the cell, with the preprophase band in between [76]. These factors might, therefore, also help a single microtubule band to form, for example by creating unfavourable microtubule dynamics in their respective halves of the cell.

6.2.4 Microtubule flexibility and alignment

In chapter 5, we introduced microtubule flexibility to mitigate the effect of small misalignments of the microtubule array with the ROP pattern. As a side effect, we observed that microtubule flexibility in simulations reduced the ability of the array to align consistently in a transverse orientation along the entire length of the cell (chapter 5). Consequently, semiflexible microtubules were more likely to produce arrays with swirls or longitudinal stretches. Since the mechanism of 'survival of the aligned' only promotes local alignment [134, 137], this outcome may be obtained even with rigid microtubules on sufficiently large domains [254]. Similar results have been reported at a tissue level for cells influencing the polarity of their neighbours, which could only achieve global alignment with polarity organising cells on either end of the domain [270]. The edge-induced catastrophes we used in chapter 5 could probably be considered as a kind of polarity organisers for making a transverse microtubule array [124]. However, their effect does not appear to carry all the way through to the centre of the array very well, especially for microtubules of finite persistence length (chapter 5). This observation suggests that a globally active orientating force is required. In many cases, a good candidate for this force may be the tendency of microtubules to align with the direction of maximal tensile

stress through some as yet unknown mechanism [128, 255, 256, 271]. However, this candidate may be less suitable when the array suddenly changes its orientation in response to a non-mechanical cue, such as the sudden reorientation of the array in hypocotyl cells exposed to blue light [31, 113, 143].

6.3 Modelling choices

Modelling involves making many choices, including the aim of the model, which biological elements will be included, and how the model will be analysed. Throughout this thesis, the aim has been to develop a mechanistic understanding of the processes involved in xylem patterning, i.e., to understand not just which interactions yield the right patterns, but also how. Here, I will discuss some of the choices we made in our modelling approach to try to achieve this goal, and why we made them.

6.3.1 Model comparisons

We have generally built our models incrementally. In the process, we encountered multiple examples where models that did not reproduce the desired behaviour were more helpful to our understanding than models that did. Our approach allowed us to compare models that failed to produce the right pattern with models that performed better to help us understand what makes certain models work, while others do not. For example, our understanding of cluster coexistence in small GTPase models was informed in part by comparisons with models that failed to generate coexisting clusters (chapter 2). Similarly, in chapters 3 and 5, we added additional biological elements one at a time, to study the effect of each element separately. Such incremental model building, while not necessarily giving the desired outcome immediately, has provided more mechanistic understanding than we could have obtained by combining all potentially relevant biological interactions at the same time, which would also have been unlikely to succeed on the first attempt. For example, patterns of coexisting spots have been found in a highly detailed model for ROP patterning in metaxylem, in which ROPs cycled through six different states, with several different feedback loops [32]. Due to its complexity, it would have been hard to discover coexistence mechanisms taking this model as a starting point. The total amount of ROPs, GEFs, and GAPs in that model are conserved, but coexistence could be obtained through negative feedback, redistribution of some intermediate, a completely new mechanism, or any combination thereof.

Where our models were yet to complex to understand the mechanism at work, we examined simplified abstract versions that retain essential characteristics. In chapter 2, we derived an abstract model for the GTPase content of a fixed number of interacting clusters under different conditions. This approach allowed us to compare the effects of mass conservation, turnover, and negative feedback in an ordinary differential equation framework, which is easier to study than the full spatial model. In chapter 3, some simplifying assumptions about how ROP clusters deform allowed us to compare the orienting power of diffusion restriction on differently shaped ROP patterns by decomposing the diffusion term. This way, we found that diffusion restriction could only reorient patterns with curved features. We then confirmed this mechanistic insight with simulations we

would probably not have considered without this theoretical analysis.

6.3.2 Parameters

Biological systems often contain many complex interactions that translate into large models with many parameters. It is often challenging, if at all possible, to determine these parameters experimentally. Consequently, we only had measured values for some of the parameters in our models (mostly for the microtubule models) and the ones we did have were often uncertain or highly variable. Dimensional analysis helped reduce the number of parameters in our small GTPase models, but still left many unknowns. For the remaining parameters, we could only explore their influence on model behaviour by trying different values. Since our large spatial models were slow to simulate and the output was hard to capture in a single number, full scale global sensitivity analysis was not feasible, so we mostly varied parameter values one at a time, much like in a one-factor-at-a-time sensitivity analysis [272]. Even though this approach ignores potential interaction effects between parameters, it still proved useful in improving our understanding of the mechanisms at play throughout this thesis. It revealed, for example, that increasing the total amount of GTPase or its production rate could change a pattern from spots to stripes to gaps (chapter 2), that increasing the diffusion restriction in one direction would progressively flatten the pattern in the other direction (chapter 3), that unrealistically low diffusion rates were required for a tubulin limitation to keep the microtubule array homogeneous (chapter 4), and that a strong co-alignment of the microtubule array with predefined band regions can help microtubule band formation (chapter 5).

Another reason for exploring a range of parameter values was to test for model robustness, i.e., the ability of the model to yield the desired behaviour over a large range of parameter values. However, it was often difficult to determine what this range of parameter values should be. Furthermore, it was often not just the parameter values that were uncertain. In many cases, there were large uncertainties in the structure of the model as well. For this reason, we used multiple different reaction-diffusion model formulations to test the effects of diffusion restriction (chapter 3) and the different coexistence mechanisms (chapter 2). This way, we could show that the effects of the orientation and coexistence mechanisms do not specifically depend on a single type of model formulation.

6.4 Future directions

6.4.1 Active ROP immobilisation by GDI cycling

A sufficiently large difference in diffusion coefficients between active and inactive forms is a general requirement of Turing patterning [46, 47, 49]. In our models for GTPase patterning (chapters 2 and 3), we assumed that this difference was provided by GDIs that selectively remove the inactive form from the membrane allowing for faster diffusion in the cytosol, as is common among GTPase models [44, 45]. This GDI cycling is required for patterning in many systems including yeast budding [273] and animal cell wound healing [274]. In plants, GDI cycling appears to be important in root hair initiation [275] and pollen tube tip growth [276] as well. However, there may be a difference in active ROP immobilisation between type-II ROPs (ROP9, ROP10, and ROP11 in *Arabidopsis*)

and type-I ROPs (the others) [277, 278], as these rely on different types of lipid modifications for membrane targeting [279, 280]. A recent study found that type-II ROPs do not undergo GDI cycling and that GDI cycling is not required for pattern formation with any ROP, at least when ROPGAP1 and ROPGEF3 are used [281].

Given the GDI-dependency of type-I ROP patterning in root hairs and pollen tubes [275, 276], GDI-cycling may contribute to achieving a difference in type-I ROP mobility for patterning with their native GAPs and GEFs. Metaxylem patterning, however, cannot rely on GDI-cycling, as it uses a type-II ROP (ROP11). Still, models used here (chapters 2 and 3) and elsewhere [32] all depend on a difference in diffusion rate between active and inactive forms. Furthermore, experiments have shown the existence of an immobile subpopulation of ROP11 [281] and a reduced diffusion of one of the activated ROP11 stages [32]. Therefore, a different way of obtaining a faster diffusion of the inactive form than the active form must exist for type-II ROP patterning.

6.4.2 Nanodomain formation

An alternative to GDI membrane cycling to create a difference in active and inactive ROP diffusion may relate to the formation of ROP nanodomains. Nanodomains are nanometer-sized clusters that together can constitute the micrometer-sized clusters (sometimes called microdomains) that have been the focus of chapters 2 and 3. They are emerging as a recurring feature in GTPase patterning, as GTPase nanodomains appear not only in pollen tube tip growth [282], root hair initiation [283], and a variety of other type-I and type-II ROP patterns [281] in plants, but also in mammalian cell motility [284] and yeast budding [285]. At least for ROP6, a combination of lipid modifications and interactions between a polybasic region of amino acids and anionic phospholipids is required for the formation of ROP nanodomains [286–288]. The type-II ROP11 also interacts with anionic lipids through its polybasic region and this interaction is required for ROP11 patterning [281].

While more research is needed to determine the purpose of these nanodomains, many potential functions have been suggested [278]. One possibility is that they help restrict diffusion of the (active) GTPases involved, either through their interactions with anionic lipids, or the confinement to local compartments through liquid-liquid phase separation [289]. In that case, nanodomains may contribute to the immobilisation of active GTPase and provide an alternative to GDI-cycling for creating a difference in diffusion between active and inactive forms.

6.4.3 Selectivity of microtubule-based diffusion barriers

A form of active ROP immobilisation without membrane cycling may, however, undermine the orientation mechanism for protoxylem ROP patterning that we proposed in chapter 3. This mechanism relies on an inactive form that is less affected by microtubule-based diffusion restriction than the active form, and GDI-based membrane cycling provides a natural way to achieve this distinction. Since we do not actually know which ROP is involved in protoxylem patterning, one possibility is that protoxylem patterning uses a type-I ROP that does rely on GDI-cycling. ROP7, a type-I ROP, has been observed microscopically in developing protoxylem [150], but more research is needed to determine its precise role in the process. However, the ROP11-based metaxylem pattern is also af-

fected by the presence of proposed microtubule-membrane linker IQD13 [154] as well as the microtubule-stabilising drug taxol [148]. To explain these effects on the metaxylem ROP pattern, a microtubule diffusion barrier function specific to active ROP is also required for ROP11. To test for such a difference in diffusion restriction between active and inactive ROP11, a way to distinguish between active and inactive ROP is required. Active GTPase sensors have been developed for other GTPases [290–292], and a similar design may be employed to measure ROP activity in metaxylem.

If there is a difference in microtubule-based diffusion restriction between active and inactive ROP11, it must have some other cause than GDI cycling. An alternative may be that microtubules with IQD13 membrane linkers do not restrict diffusion of all membrane-bound proteins equally. Possibly, bulky ROP-effector complexes in active ROP nanodomains are not just less mobile, but also more easily obstructed by obstacles. Alternatively, rather than physically blocking all membrane-bound proteins, IQD13 might influence the ROP pattern by selectively interacting with active ROP or associated proteins or lipids in ROP nanodomains. IQD13 is part of a large family of IQD proteins, which are emerging as important players in microtubule organisation with an ability to respond to calcium signalling through a calmodulin-binding domain [261, 262, 293, 294]. These ongoing efforts to characterise the functions of IQDs are likely to yield new insights into their regulation and interactions with active and inactive ROPs.

6.4.4 Microtubule density

Models of the plant cortical microtubule array have thus far focused on a variety of properties, including alignment [134–138, 160], orientation [42, 124, 126, 127], re-orientation [142, 143], homogeneity (chapter 4), and the formation of specific structures like the patterned protoxylem array ([33] and chapters 4 and 5), and the preprophase band [145]. The microtubule densities that are achieved in the process, however, are often disregarded and not explicitly reported. In the simulations from chapter 4, density values regularly exceeded a value of 40 μm microtubule per μm^2, which would imply more microtubules that could fit side-to-side in a single layer. As these simulations did not include microtubule-microtubule interactions, this high density was mostly due to a lack of induced catastrophes and crossover severing, which even with largely parallel microtubule-dependent nucleations strongly impact array density (chapter 5). However, in chapter 5 we saw that densities produced in a more realistic model simulations can vary wildly and may still exceed realistic values, even when using measured values for most microtubule dynamics parameters (though not the nucleation rate). Early simulation studies by Allard et al. [135] and Eren et al. [136] even used sets of parameters, measured early in array development, that would allow unlimited density increase if they were maintained indefinitely.

In reality, microtubule density must stop increasing at some point, as the cell contains a finite amount of tubulin. As such, the tubulin concentration affects the microtubule growth speed, the nucleation rate [252, 253], and the spontaneous catastrophe rate [295]. There are two ways in which this effect may be included: explicitly modelling tubulin limitation (e.g., [103] and chapter 4 for growth speed), or using microtubule dynamics parameters measured at regular time intervals. While we used measured parameter time series in chapter 5, these did not include the nucleation rate, which may explain the high densities in those simulations. Alternatively, at densities where microtubules occupy a

substantial part of the membrane, microtubule density may also be limited by steric hindrance and it becomes important to include a finite microtubule width in the model, as some studies have done [126, 127, 135].

Having reliable estimates of the microtubule density for the system under study can help validate microtubule simulation models. While resolution limits may make bundled microtubules difficult to count directly in living cells [245], densities can be estimated from fluorescent intensities [296]. Novel microscopy and image processing techniques may contribute to obtaining accurate local microtubule densities in this way [297, 298]. Alternatively, polymeric and monomeric tubulin fractions may be isolated [299, 300], though this method is destructive and therefore not suitable for measuring dynamic changes in a single cell.

6.4.5 Microtubule persistence length

Another aspect that has not yet received much attention in cortical array models is microtubule flexibility. Recent modelling efforts tried to incorporate the effect of such flexibility by adding random fluctuations to the microtubule growth direction, using microtubule persistence length values measured *in vivo* in animal cells [126, 127]. These persistence lengths of about 20-30 μm [236, 237] are much smaller than the values in the millimetre range that have been measured *in vitro* [238]. However, in our simulations with realistic microtubule dynamics parameters for developing protoxylem, 25 μm persistence lengths lead to so many extra collisions that not enough density could be maintained to form aligned arrays (chapter 5). Due to the large difference between *in vitro* measurements and measurements from animal cells, there is a large uncertainty on what would be realistic values for plant cells as well as a large scope for potential tuning of the persistence length to different values in different situations. *In vivo* persistence length measurements in plant cells, using the same methods as for animal cells [236, 237], may help narrow down the potential range of realistic values. In addition, *in vivo* persistence length measurements will include the results of microtubule bundling events, which in the simulations occur on top of the random fluctuations in growth direction. Therefore, the persistence length values used to inform these fluctuations may be too low.

Good candidates for proteins that may be involved in tuning the persistence length would be microtubule-membrane linkers, like IQD13 in metaxylem [154], and CMU (cellulose-microtubule uncoupling) proteins [258], which also interact with members of the IQD family [301]. Microtubules that are detached from the membrane show strong bending, both as a result of cytoplasmic streaming [104, 259] and pushing and pulling forces from cellulose synthase complexes [258], suggesting that the presence of microtubule-membrane linkers greatly increases the *in vivo* microtubule persistence length. Similarly, proteins like CORDs that detach microtubules from the membrane [155], may decrease the persistence length. Cells may tune the microtubule persistence length both by controlling the relative number of these proteins, and by regulating their affinities. IQD proteins have calmodulin-binding domains and can therefore be regulated by calcium signalling [261, 262], which is in turn influenced by auxin signalling [302]. As there are many IQDs with the ability to bind microtubules and the membrane [260], it is possible that more of them function in a similar way in other cell types. The ongoing efforts to unravel the functions of IQD proteins [294, 303], may well yield further insights into their effect on

microtubule flexibility and regulation by calcium and other factors in the future.

6.4.6 The effect of mechanical stress on microtubule orienation

A final important but poorly understood microtubule-related aspect is their ability to orient themselves in the direction of maximal tensile stress [128, 255, 256]. As mentioned before, this might provide the orienting force that microtubules with a finite persistence length seem to require in order to align globally. There are indications that individual microtubules may be able to act as tensile sensors directly, by being more stable under tension, though the precise mechanism remains unclear [257]. Alternatively, microtubule stress sensing may involve stress-induced damage to the microtubule lattice [304], possibly involving katanin [305] or microtubule motors [306], followed by repair with GTP-tubulin [307]. The resulting GTP-tubulin islands can then function as starting points for rescues when the microtubule depolymerises [308, 309]. The potency of this mechanism in explaining the microtubule stress response may be explored using microtubule simulations with an orientation-dependent rescue rate, coupled with measurements of the rescue rate for different microtubule orientations.

6.4.7 Microtubule nucleation

The nucleation mechanism that we modelled in chapter 4 relies on a constant, uniform supply of nucleation complexes to achieve a local saturation of the nucleation rate with microtubule density. The simplified mechanism we used in chapter 5 relaxes this assumption by allowing local microtubule patches to draw from a global pool of nucleation complexes that become temporarily occupied upon nucleation. However, we still assumed a local saturation of the nucleation rate with microtubule density. This local saturation might be achieved at the microtubule level, if, for example, the binding sites for nucleation complexes on the microtubule get shielded in microtubule bundles. An interesting way to test this option would be to study the effect of the globally saturating density-dependent nucleation mode in a model where microtubules have finite widths (e.g., [126, 127]). This way, microtubules in bundles can be subdivided into receptive microtubules along the edges of the bundle and shielded microtubule on the inside. If this shielding effect can sufficiently ensure local saturation of the nucleation rate with microtubule density, it should allow homogeneous arrays to form even with otherwise density-dependent nucleation. Super resolution microscopy techniques have been used to resolve individual microtubules in bundles [310, 311] and could, therefore, be used to determine precisely where nucleations occur in bundles.

Alternatively, local saturation may result from a locally limited influx of cytosolic nucleation complexes. This kind of limitation requires that a local patch of microtubules that attracts many nucleation complexes cannot drain the global cytosolic supply, as this would introduce global competition. As mentioned in the context of GTPase coexistence, this problem may be circumvented by introducing a turnover (chapter 2) or releasing used nucleation complexes in an inactive form, allowing redistribution before reactivation [223]. Since nucleation complex subunits can be regulated by phosphorylation [229], their release in an altered inactive state is at least plausible. Since coexistence mechanisms can also produce a single cluster given the right parameter values (chapter 2), this

mechanism has potential to explain formation of homogeneous arrays and coexisting protoxylem bands as well as a single preprophase band. The ability of such a mechanism to ensure array homogeneity for biologically realistic parameter values may be tested by modelling cytosolic nucleation complexes explicitly. This approach would, however, require quantitative knowledge of the availability of cytosolic complexes and their dynamics, which may be hard to measure experimentally, to make a conclusive judgement. In chapter 5 we estimated the total nucleation complex availability from data on nucleation complex insertions in oryzalin treated cells and controls from chapter 4, which may serve as a starting point.

6.4.8 Metaxylem patterning

Our microtubule models in chapter 5 have focused on protoxylem rather than metaxylem patterning, as we had quantitative information on microtubule dynamics for this system [33]. It would, however, be interesting to see how well the current microtubule model performs in forming arrays with round gaps, since such a pattern cannot simply rely on microtubules that all have the same orientation. Presumably, microtubule flexibility would therefore be even more important in metaxylem patterning. This flexibility may be enhanced by the activity of CORD proteins, which disorganise microtubules by partially detaching them from the plasma membrane [155]. These CORD proteins also reduce the microtubule barrier activity on active ROP domains, thereby preventing a strong flattening of the spotted pattern [155], which can result from a strong directional diffusion restriction (chapter 3). An interesting aspect of metaxylem pits is that they form distinct borders, in a process that involves the actin cytoskeleton and border-marking ROP effector BDR1 [240]. Possibly, the resulting recruitment of filamentous actin to the pit borders may also help to keep microtubules out of the gap regions. Studying protoxylem and metaxylem patterning in parallel could help us understand how cells can use these different components to control the shape of the xylem pattern. Moreover, modelling the additional interactions that may be required for metaxylem microtubule patterning may well prove to be an interesting challenge in its own right.

6.4.9 Challenges in designing an integrated microtubule-ROP model

The aforementioned examples also highlight the importance of ROP-microtubule interplay in metaxylem patterning. In chapters 3 and 5, we already saw some ways in which this interplay mattered in protoxylem patterning. Exploring this interplay fully requires an integrated model that combines the reaction-diffusion model for ROP patterning with the stochastic microtubule simulation model. The insights developed throughout this work should provide a good starting point for the construction of such a model.

When planning such an integrated microtubule-ROP model for xylem patterning, several aspects must be considered. Firstly, a nucleation mechanism must be chosen that is both sufficiently accurate and reasonably efficient. The mechanism from chapter 5 will provide a good starting point. However, if the model is to be used in cases where its orientation bias is a larger problem than for transverse arrays and bands, the mechanism may need to be adapted with a better way to determine local density than with a regular square grid. One option would be to consider the local density within a circle at a ran-

domly chosen location for each nucleation. This way, the local saturation effect could be maintained, without any orientation bias, though it would be computationally expensive. Alternatively, simulations could use global density-dependent nucleation with the aforementioned shielding of nucleation sites on microtubules inside bundles. This option, if sufficient to ensure homogeneity, may be both more biologically realistic and computationally efficient, making it a good candidate to investigate first.

Another consideration is whether the model also has to be applied to systems with a more complicated geometry than developing xylem. A ROP-microtubule interplay is also prominent, for example, in pavement cells [89–91]. A microtubule simulation framework that allows for arbitrary cell geometries, including puzzle-shaped pavement cells, exists [125] and could be extended with ROPs and a realistic nucleation mode. The use of these more complicated geometries would also provide a technical challenge for the implementation of ROP simulations, for which finite volume or element methods that can deal with arbitrary domain shapes would be required (e.g., [312–314]). A successful integration of ROP simulations into this more advanced framework would provide great versatility for studying many different systems with ROP-microtubule interplay.

Finally, the microtubule implementation may have to be reconsidered. As mentioned before, it might be important to model microtubules with a finite width to allow for bundles where microtubules can be either along the edges or on the inside. Also, the current simulation implementation struggles with flexible microtubules, as with every deflection, a new microtubule trajectory is created to determine possible intersections. This leads to a much larger density of trajectories than in the original case, many of which, moreover, contain large sections that will never be occupied. Therefore, it may pay to revise this approach to make it more efficient. One alternative may be to use stepwise additions to microtubule length, as is done by some other labs [126, 127, 135, 136], though this approach still requires a way to test for collisions, which may also be slow. This type of simulation has its own computational drawbacks, though. Discreet changes mean that conflicting events may occur in the same time step (e.g., a collision with a shrinking microtubule end that just disappeared) and, consequently, small time steps may be required to keep the simulations realistic [315]. However, if the aim is a combined ROP-microtubule model, these small time steps may be less problematic, as the ROP simulations may well be the computational bottleneck.

6.4.10 Priorities in microtubule modelling

Combining all these suggestions into a single model is a very large step. However, it may be broken down in smaller steps that each have the potential to reveal interesting insights into microtubule patterning. A good starting point may be to test if the shielding of nucleation sites in microtubule bundles is sufficient to ensure array homogeneity, as this would both provide interesting insights into microtubule array formation and add a new nucleation mode that may also improve computational efficiency. A good next step would be to look into microtubule density control and flexibility, as these affect all microtubule systems. This may also be a good stage for a comprehensive comparison of different hypotheses on the way microtubules respond to mechanical stress, which is a big question in its own right [131, 257]. The next big step is then to choose an appropriate modelling framework and use it to implement a combined ROP-microtubule model. The information

from the previous steps and the steps already taken in this thesis may help in setting up and studying this model in a meaningful way, thus providing a better understanding of the interplay between ROPs and microtubules in developing xylem and potentially other systems as well.

References

[1] H. R. Brown, *The theory of the rise of sap in trees: Some historical and conceptual remarks*, Physics in Perspective **15**, 320 (2013).

[2] M. D. Venturas, J. S. Sperry, and U. G. Hacke, *Plant xylem hydraulics: What we understand, current research, and future challenges*, Journal of Integrative Plant Biology **59**, 356 (2017).

[3] S. Turner, P. Gallois, and D. Brown, *Tracheary element differentiation*, Annual Review of Plant Biology **58**, 407 (2007).

[4] E. Kamon and M. Ohtani, *Xylem vessel cell differentiation: A best model for new integrative cell biology?*, Current Opinion in Plant Biology **64**, 102135 (2021).

[5] E. Roumeli, L. Ginsberg, R. McDonald, G. Spigolon, R. Hendrickx, M. Ohtani, T. Demura, G. Ravichandran, and C. Daraio, *Structure and biomechanics during xylem vessel transdifferentiation in Arabidopsis thaliana*, Plants **9**, (2020).

[6] K. Růžička, R. Ursache, J. Hejátko, and Y. Helariutta, *Xylem development – from the cradle to the grave*, New Phytologist **207**, 519 (2015).

[7] Y. Oda and H. Fukuda, *Secondary cell wall patterning during xylem differentiation*, Current Opinion in Plant Biology **15**, 38 (2012).

[8] J. Sperry, *Evolution of water transport and xylem structure*, International Journal of Plant Sciences **164**, S115 (2003).

[9] B. Choat, A. R. Cobb, and S. Jansen, *Structure and function of bordered pits: new discoveries and impacts on whole-plant hydraulic function*, New Phytologist **177**, 608 (2008).

[10] J. B. Bard, *A model for generating aspects of zebra and other mammalian coat patterns*, Journal of Theoretical Biology **93**, 363 (1981).

[11] D. Jeong, Y. Li, Y. Choi, M. Yoo, D. Kang, J. Park, J. Choi, and J. Kim, *Numerical simulation of the zebra pattern formation on a three-dimensional model*, Phys. A. **475**, 106 (2017).

[12] S. Kondo and R. Asai, *A reaction-diffusion wave on the skin of the marine angelfish Pomacanthus*, Nature **376**, 765 (1995).

[13] A. Nakamasu, G. Takahashi, A. Kanbe, and S. Kondo, *Interactions between zebrafish pigment cells responsible for the generation of Turing patterns*, Proc. Natl. Acad. Sci. **106**, 8429 (2009).

[14] M. Inaba, H. Yamanaka, and S. Kondo, *Pigment pattern formation by contact-dependent depolarization*, Science **335**, 677 (2012).

[15] H. Meinhardt, *The algorithmic beauty of sea shells* (Springer Science & Business Media, 2009).

[16] H. Meinhardt and M. Klingler, *A model for pattern formation on the shells of molluscs*, Journal of Theoretical Biology **126**, 63 (1987).

[17] C. A. Klausmeier, *Regular and irregular patterns in semiarid vegetation*, Science **284**, 1826 (1999).

[18] S. Kéfi, M. B. Eppinga, P. C. de Ruiter, and M. Rietkerk, *Bistability and regular spatial patterns in arid ecosystems*, Theoretical Ecology **3**, 257 (2010).

[19] L. Mander, S. C. Dekker, M. Li, W. Mio, S. W. Punyasena, and T. M. Lenton, *A morphometric analysis of vegetation patterns in dryland ecosystems*, Royal Society Open Science **4**, 160443 (2017).

[20] E. Siero, *Resolving soil and surface water flux as drivers of pattern formation in Turing models of dryland vegetation: A unified approach*, Physica D **414**, 132695 (2020).

[21] K. Satō and Y. Iwasa, *Modeling of wave regeneration in subalpine abies forests: Population dynamics with spatial structure*, Ecology **74**, 1538 (1993).

[22] V. Klika, R. E. Baker, D. Headon, and E. A. Gaffney, *The influence of receptor-mediated interactions on reaction-diffusion mechanisms of cellular self-organisation*, Bulletin of mathematical biology **74**, 935 (2012).

[23] C. Mou, F. Pitel, D. Gourichon, F. Vignoles, A. Tzika, P. Tato, L. Yu, D. W. Burt, B. Bed'hom, M. Tixier-Boichard, K. J. Painter, and D. J. Headon, *Cryptic patterning of avian skin confers a developmental facility for loss of neck feathering*, PLOS Biology **9**, 1 (2011).

[24] R. Balkunde, A. Deneer, H. Bechtel, B. Zhang, S. Herberth, M. Pesch, B. Jaegle, C. Fleck, and M. Hülskamp, *Identification of the trichome patterning core network using data from weak ttg1 alleles to constrain the model space*, Cell Reports **33**, 108497 (2020).

[25] R. Sheth, L. Marcon, M. F. Bastida, M. Junco, L. Quintana, R. Dahn, M. Kmita, J. Sharpe, and M. A. Ros, *Hox genes regulate digit patterning by controlling the wavelength of a Turing-type mechanism*, Science **338**, 1476 (2012).

[26] D. J. Hearn, *Turing-like mechanism in a stochastic reaction-diffusion model recreates three dimensional vascular patterning of plant stems*, PLOS ONE **14**, 1 (2019).

[27] M. Laskowski, V. A. Grieneisen, H. Hofhuis, C. A. t. Hove, P. Hogeweg, A. F. M. Marée, and B. Scheres, *Root system architecture from coupling cell shape to auxin transport*, PLOS Biology **6**, 1 (2008).

[28] M. Laskowski and K. H. ten Tusscher, *Periodic lateral root priming: What makes it tick?*, Plant Cell **29**, 432 (2017).

[29] E. E. Deinum, W. Kohlen, and R. Geurts, *Quantitative modelling of legume root nodule primordium induction by a diffusive signal of epidermal origin that inhibits auxin efflux*, BMC Plant Biology **16**, 254 (2016).

[30] V. Grieneisen, *Dynamics of auxin patterning in plant morphogenesis - A multilevel model study*, Ph.D. thesis, Utrecht University, 2009.

[31] J. J. Lindeboom, M. Nakamura, A. Hibbel, K. Shundyak, R. Gutierrez, T. Ketelaar, A. M. C. Emons, B. M. Mulder, V. Kirik, and D. W. Ehrhardt, *A mechanism for reorientation of cortical microtubule arrays driven by microtubule severing*, Science **342**, 1245533 (2013).

[32] Y. Nagashima, S. Tsugawa, A. Mochizuki, T. Sasaki, H. Fukuda, and Y. Oda, *A Rho-based reaction-diffusion system governs cell wall patterning in metaxylem vessels*, Scientific Reports **8**, 11542 (2018).

[33] R. Schneider, K. v. Klooster, K. L. Picard, J. van der Gucht, T. Demura, M. Janson, A. Sampathkumar, E. E. Deinum, T. Ketelaar, and S. Persson, *Long-term single-cell imaging and simulations of microtubules reveal principles behind wall patterning during proto-xylem development*, Nature Communications **12**, 669 (2021).

[34] A. F. M. Marée, V. A. Grieneisen, and L. Edelstein-Keshet, *How cells integrate complex stimuli: The effect of feedback from phosphoinositides and cell shape on cell polarization and motility*, PLoS Computational Biology **8**, e1002402 (2012).

[35] R. J. H. Payne and C. S. Grierson, *A theoretical model for ROP localisation by auxin in arabidopsis root hair cells*, PLoS One **4**, 1 (2009).

[36] A. Yan, G. Xu, and Z.-B. Yang, *Calcium participates in feedback regulation of the oscillating ROP1 Rho GTPase in pollen tubes*, Proc. Natl. Acad. Sci. **106**, 22002 (2009).

[37] N. Luo, A. Yan, G. Liu, J. Guo, D. Rong, M. M. Kanaoka, Z. Xiao, G. Xu, T. Higashiyama, X. Cui, and Z. Yang, *Exocytosis-coordinated mechanisms for tip growth underlie pollen tube growth guidance*, Nature Communications **8**, 1687 (2017).

[38] K.-T. Park, M. T. Villar, A. Artigues, and J. Lutkenhaus, *MinE conformational dynamics regulate membrane binding, MinD interaction, and Min oscillation*, Proc. Natl. Acad. Sci. **114**, 7497 (2017).

[39] J.-g. Chiou, M. K. Balasubramanian, and D. J. Lew, *Cell polarity in yeast*, Annual Review of Cell and Developmental Biology **33**, 77 (2017).

[40] A. B. Goryachev and A. V. Pokhilko, *Dynamics of Cdc42 network embodies a Turing-type mechanism of yeast cell polarity*, FEBS Letters **582**, 1437 (2008).

[41] S. Müller, *Plant cell division — defining and finding the sweet spot for cell plate insertion*, Current Opinion in Cell Biology **60**, 9 (2019).

[42] B. Chakrabortty, V. Willemsen, T. de Zeeuw, C.-Y. Liao, D. Weijers, B. Mulder, and B. Scheres, *A plausible microtubule-based mechanism for cell division orientation in plant embryogenesis*, Current Biology **28**, 3031 (2018).

[43] Y. Oda and H. Fukuda, *The dynamic interplay of plasma membrane domains and cortical microtubules in secondary cell wall patterning*, Frontiers in Plant Science **4**, 511 (2013).

[44] A. Jilkine and L. Edelstein-Keshet, *A comparison of mathematical models for polarization of single eukaryotic cells in response to guided cues*, PLoS Computational Biology **7**, 1 (2011).

[45] S. Khatibi, K. I. Rios, and L. K. Nguyen, *Computational modeling of the dynamics of spatiotemporal Rho GTPase signaling: A systematic review*, in *Rho GTPases: Methods and Protocols*, edited by F. Rivero (Springer New York, New York, NY, 2018).

[46] A. M. Turing, *The chemical basis of morphogenesis*, Philosophical Transactions of the Royal Society of London. Series B, Biological Sciences **237**, 37 (1952).

[47] A. Gierer and H. Meinhardt, *A theory of biological pattern formation*, Kybernetik **12**, 30 (1972).

[48] H. Meinhardt and A. Gierer, *Pattern formation by local self-activation and lateral inhibition*, Bioessays **22**, 753 (2000).

[49] H. Meinhardt, *Turing's theory of morphogenesis of 1952 and the subsequent discovery of the crucial role of local self-enhancement and long-range inhibition.*, Interface Focus **2**, 407 (2012).

[50] A. J. Koch and H. Meinhardt, *Biological pattern formation: from basic mechanisms to complex structures*, Rev. Mod. Phys. **66**, 1481 (1994).

[51] N. Tuncer, A. Madzvamuse, and A. Meir, *Projected finite elements for reaction–diffusion systems on stationary closed surfaces*, Applied Numerical Mathematics **96**, 45 (2015).

[52] K. Eroumé, A. Vasilevich, S. Vermeulen, J. de Boer, and A. Carlier, *On the influence of cell shape on dynamic reaction-diffusion polarization patterns*, PLOS ONE **16**, 1 (2021).

[53] L. Wolpert, *Positional information and the spatial pattern of cellular differentiation*, Journal of Theoretical Biology **25**, 1 (1969).

[54] S. Kondo and T. Miura, *Reaction-diffusion model as a framework for understanding biological pattern formation*, Science **329**, 1616 (2010).

[55] M. Akam, *Making stripes inelegantly*, Nature **341**, 282 (1989).

[56] M. J. Pankratz and H. Jäckle, *Making stripes in the Drosophila embryo*, Trends in Genetics **6**, 287 (1990).

[57] E. Clark, A. D. Peel, and M. Akam, *Arthropod segmentation*, Development **146**, (2019).

[58] R. Baker, S. Schnell, and P. Maini, *A clock and wavefront mechanism for somite formation*, Developmental Biology **293**, 116 (2006).

[59] Headon, D. J. and Painter, K. J., *Stippling the skin: Generation of anatomical periodicity by reaction-diffusion mechanisms*, Math. Model. Nat. Phenom. **4**, 83 (2009).

[60] J. B. Green and J. Sharpe, *Positional information and reaction-diffusion: two big ideas in developmental biology combine*, Development **142**, 1203 (2015).

[61] E. Nielsen, *The small GTPase superfamily in plants: A conserved regulatory module with novel functions*, Annual Review of Plant Biology **71**, 247 (2020).

[62] A. K. Mishra and D. G. Lambright, *Invited review: Small GTPases and their GAPs*, Biopolymers **105**, 431 (2016).

[63] J. Cherfils and M. Zeghouf, *Regulation of small GTPases by GEFs, GAPs, and GDIs*, Physiological Reviews **93**, 269 (2013).

[64] S. Y. Moon and Y. Zheng, *Rho GTPase-activating proteins in cell regulation*, Trends in Cell Biology **13**, 13 (2003).

[65] B. Olofsson, *Rho guanine dissociation inhibitors: Pivotal molecules in cellular signalling*, Cellular Signalling **11**, 545 (1999).

[66] M. Postma, L. Bosgraaf, H. M. Loovers, and P. J. M. Van Haastert, *Chemotaxis: signalling modules join hands at front and tail*, EMBO reports **5**, 35 (2004).

[67] R. Fritz and O. Pertz, *The dynamics of spatio-temporal Rho GTPase signaling: formation of signaling patterns [version 1; referees: 2 approved]*, F1000Research **5**, 749 (2016).

[68] A. Goryachev and M. Leda, *Autoactivation of small GTPases by the GEF-effector positive feedback modules [version 1; peer review: 2 approved]*, F1000Research **8**, 1676 (2019).

[69] A. Cezanne, J. Lauer, A. Solomatina, I. F. Sbalzarini, and M. Zerial, *A non-linear system patterns Rab5 GTPase on the membrane*, eLife **9**, e54434 (2020).

[70] A. Mendrinna and S. Persson, *Root hair growth: it's a one way street*, F1000prime reports **7**, 23 (2015).

[71] Y. Fu, *The cytoskeleton in the pollen tube*, Current Opinion in Plant Biology **28**, 111 (2015).

[72] X. Cheng, B. W. Mwaura, S. R. Chang Stauffer, and M. Bezanilla, *A fully functional ROP fluorescent fusion protein reveals roles for this GTPase in subcellular and tissue-level patterning*, Plant Cell **32**, 3436 (2020).

[73] S. D. Harris, *Cdc42/Rho GTPases in fungi: variations on a common theme*, Molecular microbiology **79**, 1123 (2011).

[74] M. Raftopoulou and A. Hall, *Cell migration: Rho GTPases lead the way*, Developmental Biology **265**, 23 (2004).

[75] S. Seiler and D. Justa-Schuch, *Conserved components, but distinct mechanisms for the placement and assembly of the cell division machinery in unicellular and filamentous ascomycetes*, Molecular Microbiology **78**, 1058 (2010).

[76] Y. Zhang and J. Dong, *Cell polarity: compassing cell division and differentiation in plants*, Current Opinion in Plant Biology **45**, 127 (2018).

[77] P. Livanos and S. Müller, *Division plane establishment and cytokinesis*, Annual Review of Plant Biology **70**, 239 (2019).

[78] W. Lin and Z. Yang, *Unlocking the mechanisms behind the formation of interlocking pavement cells*, Current Opinion in Plant Biology **57**, 142 (2020).

[79] Y. Oda and H. Fukuda, *Spatial organization of xylem cell walls by rop gtpases and microtubule-associated proteins*, Current Opinion in Plant Biology **16**, 743 (2013).

[80] D. Ghose, T. Elston, and D. Lew, *Orientation of cell polarity by chemical gradients*, Annual Review of Biophysics **51**, 431 (2022).

[81] B. Woods and D. J. Lew, *Polarity establishment by Cdc42: Key roles for positive feedback and differential mobility*, Small GTPases **10**, 130 (2019).

[82] W.-J. Rappel and L. Edelstein-Keshet, *Mechanisms of cell polarization*, Current Opinion in Systems Biology **3**, 43 (2017).

[83] M. Otsuji, S. Ishihara, C. Co, K. Kaibuchi, A. Mochizuki, and S. Kuroda, *A mass conserved reaction–diffusion system captures properties of cell polarity*, PLoS Computational Biology **3**, 1 (2007).

[84] Y. Mori, A. Jilkine, and L. Edelstein-Keshet, *Wave-pinning and cell polarity from a bistable reaction-diffusion system*, Biophysical Journal **94**, 3684 (2008).

[85] A. S. Howell, N. S. Savage, S. A. Johnson, I. Bose, A. W. Wagner, T. R. Zyla, H. F. Nijhout, M. C. Reed, A. B. Goryachev, and D. J. Lew, *Singularity in polarization: Rewiring yeast cells to make two buds*, Cell **139**, 731 (2009).

[86] C.-F. Wu and D. J. Lew, *Beyond symmetry-breaking: competition and negative feedback in GTPase regulation*, Trends in Cell Biology **23**, 476 (2013).

[87] M. Tateno and S. Ishihara, *Interfacial-curvature-driven coarsening in mass-conserved reaction-diffusion systems*, Phys. Rev. Research **3**, 023198 (2021).

[88] P. Knechtle, F. Dietrich, and P. Philippsen, *Maximal polar growth potential depends on the polarisome component AgSpa2 in the filamentous fungus Ashbya gossypii*, Molecular Biology of the Cell **14**, 4140 (2003).

[89] Y. Fu, H. Li, and Z. Yang, *The ROP2 GTPase controls the formation of cortical fine F-actin and the early phase of directional cell expansion during Arabidopsis organogenesis*, Plant Cell Online **14**, 777 (2002).

[90] Y. Fu, Y. Gu, Z. Zheng, G. Wasteneys, and Z. Yang, *Arabidopsis interdigitating cell growth requires two antagonistic pathways with opposing action on cell morphogenesis*, Cell **120**, 687 (2005).

[91] Y. Fu, T. Xu, L. Zhu, M. Wen, and Z. Yang, *A ROP GTPase signaling pathway controls cortical microtubule ordering and cell expansion in Arabidopsis*, Current Biology **19**, 1827 (2009).

[92] Y. Oda, *Cortical microtubule rearrangements and cell wall patterning*, Frontiers in Plant Science **6**, 236 (2015).

[93] G. O. Wasteneys and M. E. Galway, *Remodeling the cytoskeleton for growth and form: An overview with some new views*, Annual Review of Plant Biology **54**, 691 (2003).

[94] P. Gross, K. V. Kumar, and S. W. Grill, *How active mechanics and regulatory biochemistry combine to form patterns in development*, Annual Review of Biophysics **46**, 337 (2017).

[95] T. Hohmann and F. Dehghani, *The cytoskeleton—a complex interacting meshwork*, Cells **8**, (2019).

[96] W. R. Holmes and L. Edelstein-Keshet, *A comparison of computational models for eukaryotic cell shape and motility*, PLOS Computational Biology **8**, 1 (2012).

[97] P. J. Hussey, T. Ketelaar, and M. J. Deeks, *Control of the actin cytoskeleton in plant cell growth*, Annual Review of Plant Biology **57**, 109 (2006).

[98] D. W. Ehrhardt and S. L. Shaw, *Microtubule dynamics and organization in the plant cortical array*, Annual Review of Plant Biology **57**, 859 (2006).

[99] A. Desai and T. J. Mitchison, *Microtubule polymerization dynamics*, Annual Review of Cell and Developmental Biology **13**, 83 (1997).

[100] N. B. Gudimchuk and J. R. McIntosh, *Regulation of microtubule dynamics, mechanics and function through the growing tip*, Nature Reviews Molecular Cell Biology **22**, 777 (2021).

[101] B. J. LaFrance, J. Roostalu, G. Henkin, B. J. Greber, R. Zhang, D. Normanno, C. O. McCollum, T. Surrey, and E. Nogales, *Structural transitions in the GTP cap visualized by cryo-electron microscopy of catalytically inactive microtubules*, Proc. Natl. Acad. Sci. **119**, (2022).

[102] A. Aher and A. Akhmanova, *Tipping microtubule dynamics, one protofilament at a time*, Current Opinion in Cell Biology **50**, 86 (2018).

[103] S. Tindemans, E. Deinum, J. Lindeboom, and B. Mulder, *Efficient event-driven simulations shed new light on microtubule organization in the plant cortical array*, Frontiers in Physics **2**, 19 (2014).

[104] S. L. Shaw, R. Kamyar, and D. W. Ehrhardt, *Sustained microtubule treadmilling in Arabidopsis cortical arrays*, Science **300**, 1715 (2003).

[105] T. Hashimoto, *A ring for all: γ-tubulin-containing nucleation complexes in acentrosomal plant microtubule arrays*, Current Opinion in Plant Biology **16**, 698 (2013).

[106] P. Liu, M. Würtz, E. Zupa, S. Pfeffer, and E. Schiebel, *Microtubule nucleation: The waltz between γ-tubulin ring complex and associated proteins*, Current Opinion in Cell Biology **68**, 124 (2021).

[107] T. Murata, S. Sonobe, T. I. Baskin, S. Hyodo, S. Hasezawa, T. Nagata, T. Horio, and M. Hasebe, *Microtubule-dependent microtubule nucleation based on recruitment of γ-tubulin in higher plants*, Nature Cell Biology **7**, 961 (2005).

[108] M. Nakamura, D. W. Ehrhardt, and T. Hashimoto, *Microtubule and katanin-dependent dynamics of microtubule nucleation complexes in the acentrosomal Arabidopsis cortical array*, Nature Cell Biology **12**, 1064 (2010).

[109] J. Chan, A. Sambade, G. Calder, and C. Lloyd, *Arabidopsis cortical microtubules are initiated along, as well as branching from, existing microtubules*, Plant Cell Online **21**, 2298 (2009).

[110] R. Dixit and R. Cyr, *Encounters between dynamic cortical microtubules promote ordering of the cortical array through angle-dependent modifications of microtubule behavior*, Plant Cell Online **16**, 3274 (2004).

[111] V. Stoppin-Mellet, J. Gaillard, and M. Vantard, *Functional evidence for in vitro microtubule severing by the plant katanin homologue*, Biochemical Journal **365**, 337 (2002).

[112] Q. Zhang, E. Fishel, T. Bertroche, and R. Dixit, *Microtubule severing at crossover sites by katanin generates ordered cortical microtubule arrays in Arabidopsis*, Current Biology **23**, 2191 (2013).

[113] J. J. Lindeboom, M. Nakamura, M. Saltini, A. Hibbel, A. Walia, T. Ketelaar, A. M. C. Emons, J. C. Sedbrook, V. Kirik, B. M. Mulder, and D. W. Ehrhardt, *CLASP stabilization of plus ends created by severing promotes microtubule creation and reorientation*, Journal of Cell Biology **218**, 190 (2018).

[114] J. Lindeboom, B. Mulder, J. W. Vos, T. Ketelaar, and A. M. C. Emons, *Cellulose microfibril deposition: coordinated activity at the plant plasma membrane*, Journal of Microscopy **231**, 192 (2008).

[115] R. Schneider, T. Hanak, S. Persson, and C. A. Voigt, *Cellulose and callose synthesis and organization in focus, what's new?*, Current Opinion in Plant Biology **34**, 9 (2016).

[116] Y. Gu and C. G. Rasmussen, *Cell biology of primary cell wall synthesis in plants*, Plant Cell **34**, 103 (2021).

[117] R. Gutierrez, J. J. Lindeboom, A. R. Paredez, A. M. C. Emons, and D. W. Ehrhardt, *Arabidopsis cortical microtubules position cellulose synthase delivery to the plasma membrane and interact with cellulose synthase trafficking compartments*, Nature Cell Biology **11**, 797 (2009).

[118] Y. Watanabe, M. J. Meents, L. M. McDonnell, S. Barkwill, A. Sampathkumar, H. N. Cartwright, T. Demura, D. W. Ehrhardt, A. Samuels, and S. D. Mansfield, *Visualization of cellulose synthases in Arabidopsis secondary cell walls*, Science **350**, 198 (2015).

[119] N. Vukašinović, Y. Oda, P. Pejchar, L. Synek, T. Pečenková, A. Rawat, J. Sekereš, M. Potocký, and V. Žárský, *Microtubule-dependent targeting of the exocyst complex is necessary for xylem development in Arabidopsis*, New Phytologist **213**, 1052 (2017).

[120] A. R. Paredez, C. R. Somerville, and D. W. Ehrhardt, *Visualization of cellulose synthase demonstrates functional association with microtubules*, Science **312**, 1491 (2006).

[121] J. Chan and E. Coen, *Interaction between autonomous and microtubule guidance systems controls cellulose synthase trajectories*, Current Biology **30**, 941 (2020).

[122] R. Schneider, L. Tang, E. R. Lampugnani, S. Barkwill, R. Lathe, Y. Zhang, H. E. McFarlane, E. Pesquet, T. Niittyla, S. D. Mansfield, Y. Zhou, and S. Persson, *Two complementary mechanisms underpin cell wall patterning during xylem vessel development*, Plant Cell **29**, 2433 (2017).

[123] T. I. Baskin, *Anisotropic expansion of the plant cell wall*, Annual Review of Cell and Developmental Biology **21**, 203 (2005).

[124] C. Ambrose, J. F. Allard, E. N. Cytrynbaum, and G. O. Wasteneys, *A CLASP-modulated cell edge barrier mechanism drives cell-wide cortical microtubule organization in Arabidopsis*, Nature Communications **2**, 430 (2011).

[125] B. Chakrabortty, I. Blilou, B. Scheres, and B. M. Mulder, *A computational framework for cortical microtubule dynamics in realistically shaped plant cells*, PLOS Computational Biology **14**, 1 (2018).

[126] V. Mirabet, P. Krupinski, O. Hamant, E. M. Meyerowitz, H. Jönsson, and A. Boudaoud, *The self-organization of plant microtubules inside the cell volume yields their cortical localization, stable alignment, and sensitivity to external cues*, PLOS Computational Biology **14**, 1 (2018).

[127] P. Durand-Smet, T. A. Spelman, E. M. Meyerowitz, and H. Jönsson, *Cytoskeletal organization in isolated plant cells under geometry control*, Proc. Natl. Acad. Sci. **117**, 17399 (2020).

[128] O. Hamant, M. G. Heisler, H. Jönsson, P. Krupinski, M. Uyttewaal, P. Bokov, F. Corson, P. Sahlin, A. Boudaoud, E. M. Meyerowitz, Y. Couder, and J. Traas, *Developmental patterning by mechanical signals in arabidopsis*, Science **322**, 1650 (2008).

[129] L. Colin, A. Chevallier, S. Tsugawa, F. Gacon, C. Godin, V. Viasnoff, T. E. Saunders, and O. Hamant, *Cortical tension overrides geometrical cues to orient microtubules in confined protoplasts*, Proc. Natl. Acad. Sci. **117**, 32731 (2020).

[130] L. Vineyard, A. Elliott, S. Dhingra, J. R. Lucas, and S. L. Shaw, *Progressive transverse microtubule array organization in hormone-induced arabidopsis hypocotyl cells.*, Plant Cell **25**, 662 (2013).

[131] D.-C. Trinh, J. Alonso-Serra, M. Asaoka, L. Colin, M. Cortes, A. Malivert, S. Takatani, F. Zhao, J. Traas, C. Trehin, et al., *How mechanical forces shape plant organs*, Current Biology **31**, R143 (2021).

[132] P. Nick, *Plant microtubules: development and flexibility* (Springer Science & Business Media, 2008).

[133] E. E. Deinum and B. M. Mulder, *Modelling the role of microtubules in plant cell morphology*, Current Opinion in Plant Biology **16**, 688 (2013).

[134] S. H. Tindemans, R. J. Hawkins, and B. M. Mulder, *Survival of the aligned: Ordering of the plant cortical microtubule array*, Phys. Rev. Lett. **104**, 058103 (2010).

[135] J. F. Allard, G. O. Wasteneys, and E. N. Cytrynbaum, *Mechanisms of self-organization of cortical microtubules in plants revealed by computational simulations*, Molecular Biology of the Cell **21**, 278 (2010).

[136] E. C. Eren, R. Dixit, and N. Gautam, *A three-dimensional computer simulation model reveals the mechanisms for self-organization of plant cortical microtubules into oblique arrays*, Molecular Biology of the Cell **21**, 2674 (2010).

[137] R. J. Hawkins, S. H. Tindemans, and B. M. Mulder, *Model for the orientational ordering of the plant microtubule cortical array*, Phys. Rev. E **82**, 011911 (2010).

[138] E. E. Deinum, S. H. Tindemans, J. J. Lindeboom, and B. M. Mulder, *How selective severing by katanin promotes order in the plant cortical microtubule array*, Proc. Natl. Acad. Sci. **114**, 6942 (2017).

[139] R. Wightman and S. R. Turner, *Severing at sites of microtubule crossover contributes to microtubule alignment in cortical arrays*, Plant Journal **52**, 742 (2007).

[140] Y.-W. Kuo and J. Howard, *Cutting, amplifying, and aligning microtubules with severing enzymes*, Trends in Cell Biology **31**, 50 (2021).

[141] M. Nakamura, *Microtubule nucleating and severing enzymes for modifying microtubule array organization and cell morphogenesis in response to environmental cues*, New Phytologist **205**, 1022 (2015).

[142] M. Saltini and B. M. Mulder, *Critical threshold for microtubule amplification through templated severing*, Phys. Rev. E **101**, 052405 (2020).

[143] M. Saltini and B. M. Mulder, *A plausible mechanism for longitudinal lock-in of the plant cortical microtubule array after light-induced reorientation*, Quantitative Plant Biology **2**, e9 (2021).

[144] M. Nakamura, J. J. Lindeboom, M. Saltini, B. M. Mulder, and D. W. Ehrhardt, *Spr2 protects minus ends to promote severing and reorientation of plant cortical microtubule arrays*, J Cell Biol **217**, 915 (2018).

[145] B. Chakrabortty, *Plant cortical microtubule dynamics and cell division plane orientation*, Ph.D. thesis, Wageningen University, 2017.

[146] D. Lin, H. Ren, and Y. Fu, *ROP GTPase-mediated auxin signaling regulates pavement cell interdigitation in Arabidopsis thaliana*, Journal of Integrative Plant Biology **57**, 31 (2015).

[147] Y. Oda, Y. Iida, Y. Kondo, and H. Fukuda, *Wood cell-wall structure requires local 2D-microtubule disassembly by a novel plasma membrane-anchored protein*, Current Biology **20**, 1197 (2010).

[148] Y. Oda and H. Fukuda, *Initiation of cell wall pattern by a rho- and microtubule-driven symmetry breaking*, Science **337**, 1333 (2012).

[149] Y. Oda and H. Fukuda, *Rho of plant GTPase signaling regulates the behavior of Arabidopsis kinesin-13A to establish secondary cell wall patterns*, Plant Cell Online **25**, 4439 (2013).

[150] T. Brembu, P. Winge, and A. M. Bones, *The small GTPase AtRAC2/ROP7 is specifically expressed during late stages of xylem differentiation in Arabidopsis*, Journal of Experimental Botany **56**, 2465 (2005).

[151] M. Yamaguchi, N. Mitsuda, M. Ohtani, M. Ohme-Takagi, K. Kato, and T. Demura, *VASCULAR-RELATED NAC-DOMAIN 7 directly regulates the expression of a broad range of genes for xylem vessel formation*, Plant Journal **66**, 579 (2011).

[152] S. M. Brady, D. A. Orlando, J.-Y. Lee, J. Y. Wang, J. Koch, J. R. Dinneny, D. Mace, U. Ohler, and P. N. Benfey, *A high-resolution root spatiotemporal map reveals dominant expression patterns*, Science **318**, 801 (2007).

[153] E. Pesquet, A. V. Korolev, G. Calder, and C. W. Lloyd, *The microtubule-associated protein AtMAP70-5 regulates secondary wall patterning in arabidopsis wood cells*, Current Biology **20**, 744 (2010).

[154] Y. Sugiyama, M. Wakazaki, K. Toyooka, H. Fukuda, and Y. Oda, *A novel plasma membrane-anchored protein regulates xylem cell-wall deposition through microtubule-dependent lateral inhibition of rho GTPase domains*, Current Biology **27**, 2522 (2017).

[155] T. Sasaki, H. Fukuda, and Y. Oda, *CORTICAL MICROTUBULE DISORDERING1 is required for secondary cell wall patterning in xylem vessels*, Plant Cell , (2017).

[156] Y. Oda, *Emerging roles of cortical microtubule-membrane interactions*, Journal of Plant Research **131**, 5 (2018).

[157] A. Howell, M. Jin, C.-F. Wu, T. Zyla, T. Elston, and D. Lew, *Negative feedback enhances robustness in the yeast polarity establishment circuit*, Cell **149**, 322 (2012).

[158] N. Verschueren and A. Champneys, *A model for cell polarization without mass conservation*, SIAM Journal on Applied Dynamical Systems **16**, 1797 (2017).

[159] K. van 't Klooster, *Patterning of plant cell wall deposition by cortical microtubules*, Ph.D. thesis, Wageningen University, 2017.

[160] E. E. Deinum, S. H. Tindemans, and B. M. Mulder, *Taking directions: the role of microtubule-bound nucleation in the self-organization of the plant cortical array*, Physical Biology **8**, 056002 (2011).

[161] J. J. Lindeboom, A. Lioutas, E. E. Deinum, S. H. Tindemans, D. W. Ehrhardt, A. M. C. Emons, J. W. Vos, and B. M. Mulder, *Cortical microtubule arrays are initiated from a non-random prepattern driven by atypical microtubule initiation*, Plant Physiology **161**, 1189 (2013).

[162] G. Chomicki, R. Wightman, and S. R. Turner, *A specific class of short treadmilling microtubules enhances cortical microtubule alignment*, Molecular Plant **9**, 1214 (2016).

[163] B. Jacobs, J. Molenaar, and E. E. Deinum, *Small GTPase patterning: How to stabilise cluster coexistence*, PLOS ONE **14**, 1 (2019).

[164] H.-O. Park and E. Bi, *Central roles of small GTPases in the development of cell polarity in yeast and beyond*, Microbiology and Molecular Biology Reviews **71**, 48 (2007).

[165] Z. Yang and I. Lavagi, *Spatial control of plasma membrane domains: ROP GTPase-based symmetry breaking*, Current Opinion in Plant Biology **15**, 601 (2012).

[166] S. Etienne-Manneville and A. Hall, *Rho GTPases in cell biology*, Nature **420**, 629 (2002).

[167] C. A. Lancaster, P. M. Taylor-Harris, A. J. Self, S. Brill, H. E. van Erp, and A. Hall, *Characterization of rhoGAP. A GTPase-activating protein for rho-related small GTPases.*, Journal of Biological Chemistry **269**, 1137 (1994).

[168] W. R. Holmes and L. Edelstein-Keshet, *Analysis of a minimal Rho-GTPase circuit regulating cell shape*, Physical Biology **13**, 046001 (2016).

[169] A. Jilkine, A. F. M. Marée, and L. Edelstein-Keshet, *Mathematical model for spatial segregation of the Rho-family GTPases based on inhibitory crosstalk*, Bulletin of Mathematical Biology **69**, 1943 (2007).

[170] R. A. Arkowitz and M. Bassilana, *Regulation of hyphal morphogenesis by Ras and Rho small GTPases*, Fungal Biology Reviews **29**, 7 (2015).

[171] J.-U. Hwang, G. Wu, A. Yan, Y.-J. Lee, C. S. Grierson, and Z. Yang, *Pollen-tube tip growth requires a balance of lateral propagation and global inhibition of Rho-family GTPase activity*, Journal of Cell Science **123**, 340 (2010).

[172] Y. Bauer, P. Knechtle, J. Wendland, H. Helfer, and P. Philippsen, *A Ras-like GTPase is involved in hyphal growth guidance in the filamentous fungus Ashbya gossypii*, Molecular Biology of the Cell **15**, 4622 (2004).

[173] Y. Mori, A. Jilkine, and L. Edelstein-Keshet, *Asymptotic and bifurcation analysis of wave-pinning in a reaction-diffusion model for cell polarization*, SIAM Journal on Applied Mathematics **71**, 1401 (2011).

[174] S. Ishihara, M. Otsuji, and A. Mochizuki, *Transient and steady state of mass-conserved reaction-diffusion systems*, Phys. Rev. E **75**, 015203 (2007).

[175] J. Rubinstein and P. Sternberg, *Nonlocal reaction—diffusion equations and nucleation*, IMA Journal of Applied Mathematics **48**, 249 (1992).

[176] W. J. Armour, D. A. Barton, A. M. Law, and R. L. Overall, *Differential growth in periclinal and anticlinal walls during lobe formation in Arabidopsis cotyledon pavement cells*, Plant Cell Online **27**, 2484 (2015).

[177] J.-G. Chiou, S. A. Ramirez, T. C. Elston, T. P. Witelski, D. G. Schaeffer, and D. J. Lew, *Principles that govern competition or co-existence in Rho-GTPase driven polarization*, PLoS Computational Biology **14**, e1006095 (2018).

[178] W. Giese, M. Eigel, S. Westerheide, C. Engwer, and E. Klipp, *Influence of cell shape, inhomogeneities and diffusion barriers in cell polarization models*, Physical Biology **12**, 066014 (2015).

[179] P. W. Voorhees, *Ostwald ripening of two-phase mixtures*, Annual Review of Materials Science **22**, 197 (1992).

[180] T. M. Rogers, K. R. Elder, and R. C. Desai, *Numerical study of the late stages of spinodal decomposition*, Phys. Rev. B **37**, 9638 (1988).

[181] J. Halatek, F. Brauns, and E. Frey, *Self-organization principles of intracellular pattern formation*, Philosophical Transactions of the Royal Society of London B **373**, (2018).

[182] Y. J. Lee, A. Szumlanski, E. Nielsen, and Z. Yang, *Rho-GTPase–dependent filamentous actin dynamics coordinate vesicle targeting and exocytosis during tip growth*, Journal of Cell Biology **181**, 1155 (2008).

[183] H. Meinhardt, *Orientation of chemotactic cells and growth cones: models and mechanisms*, Journal of Cell Science **112**, 2867 (1999).

[184] C. P. Semighini and S. D. Harris, *Regulation of apical dominance in Aspergillus nidulans hyphae by reactive oxygen species*, Genetics **179**, 1919 (2008).

[185] S. D. Harris, *Branching of fungal hyphae: regulation, mechanisms and comparison with other branching systems*, Mycologia **100**, 823 (2008).

[186] P. S. Backlund, *Post-translational processing of RhoA: Carboxyl methylation of the carboxyl-terminal prenylcysteine increases the half-life of RhoA*, Journal of Biological Chemistry **272**, 33175 (1997).

[187] M. O. Bergo, B. J. Gavino, C. Hong, A. P. Beigneux, M. McMahon, P. J. Casey, and S. G. Young, *Inactivation of Icmt inhibits transformation by oncogenic K-Ras and B-Raf*, Journal of Clinical Investigation **113**, 539 (2004).

[188] R. L. Friede, *The relationship of body size, nerve cell size, axon length, and glial density in the cerebellum*, Proc. Natl. Acad. Sci. **49**, 187 (1963).

[189] S. A. Rincón, M. Estravís, and P. Pérez, *Cdc42 regulates polarized growth and cell integrity in fission yeast*, Biochemical Society Transactions **42**, 201 (2014).

[190] M. Das, T. Drake, D. J. Wiley, P. Buchwald, D. Vavylonis, and F. Verde, *Oscillatory dynamics of cdc42 GTPase in the control of polarized growth*, Science **337**, 239 (2012).

[191] B. Novák and J. J. Tyson, *Design principles of biochemical oscillators*, Nature Reviews Molecular Cell Biology **9**, 981 (2008).

[192] J.-U. Hwang, V. Vernoud, A. Szumlanski, E. Nielsen, and Z. Yang, *A tip-localized RhoGAP controls cell polarity by globally inhibiting Rho GTPase at the cell apex*, Current Biology **18**, 1907 (2008).

[193] M. A. Jones, J.-J. Shen, Y. Fu, H. Li, Z. Yang, and C. S. Grierson, *The Arabidopsis Rop2 GTPase is a positive regulator of both root hair initiation and tip growth*, Plant Cell **14**, 763 (2002).

[194] A. Makhzoum, M. Yousefzadi, S. Malik, P. Gantet, and J. Tremouillaux-Guiller, *Strigolactone biology: genes, functional genomics, epigenetics and applications*, Critical Reviews in Biotechnology **37**, 151 (2017).

[195] K. J. Burns, G. M. Vasil, J. S. Oishi, D. Lecoanet, and B. Brown. *Dedalus: Flexible framework for spectrally solving differential equations*. Astrophysics Source Code Library, (2016).

[196] E. Cleary, *The Scientific Way to Simulate Pattern Formation in Reaction-Diffusion Equations*, Ph.D. thesis, University of Guelph, 2013.

[197] S. Smith and N. Dalchau, *Model reduction enables Turing instability analysis of large reaction-diffusion models*, Journal of The Royal Society Interface **15**, 20170805 (2018).

[198] P. K. Trong, E. M. Nicola, N. W. Goehring, K. V. Kumar, and S. W. Grill, *Parameter-space topology of models for cell polarity*, New Journal of Physics **16**, 065009 (2014).

[199] J. D. Murray, *Mathematical Biology II: Spatial Models and Biomedical Applications* (Springer-Verlag New York Incorporated, 2001).

[200] W. R. Holmes, *An efficient, nonlinear stability analysis for detecting pattern formation in reaction diffusion systems*, Bulletin of Mathematical Biology **76**, 157 (2014).

[201] W. Holmes, M. Mata, and L. Edelstein-Keshet, *Local perturbation analysis: A computational tool for biophysical reaction-diffusion models*, Biophysical Journal **108**, 230 (2015).

[202] A. Dhooge, W. Govaerts, and Y. A. Kuznetsov, *Matcont: a matlab package for numerical bifurcation analysis of odes*, ACM Transactions on Mathematical Software **29**, 141 (2003).

[203] T. Miura and P. K. Maini, *Speed of pattern appearance in reaction-diffusion models: Implications in the pattern formation of limb bud mesenchyme cells*, Bulletin of Mathematical Biology **66**, 627 (2004).

[204] L. Edelstein-Keshet, W. R. Holmes, M. Zajac, and M. Dutot, *From simple to detailed models for cell polarization*, Philosophical Transactions of the Royal Society of London B **368**, (2013).

[205] B. Jacobs, J. Molenaar, and E. E. Deinum, *Robust banded protoxylem pattern formation through microtubule-based directional ROP diffusion restriction*, Journal of Theoretical Biology **502**, 110351 (2020).

[206] F. Mertens and R. Imbihl, *Square chemical waves in the catalytic reaction NO + H_2 on a rhodium(110) surface*, Nature **370**, 124 (1994).

[207] A. R. Sanderson, R. M. Kirby, C. R. Johnson, and L. Yang, *Advanced reaction-diffusion models for texture synthesis*, Journal of Graphics Tools **11**, 47 (2006).

[208] H. Shoji, Y. Iwasa, A. Mochizuki, and S. Kondo, *Directionality of stripes formed by anisotropic reaction–diffusion models*, Journal of Theoretical Biology **214**, 549 (2002).

[209] T. Hiscock and S. Megason, *Orientation of Turing-like patterns by morphogen gradients and tissue anisotropies*, Cell Systems **1**, 408 (2015).

[210] D. W. Peaceman and H. H. Rachford, Jr, *The numerical solution of parabolic and elliptic differential equations*, Journal of the Society for industrial and Applied Mathematics **3**, 28 (1955).

[211] R. Schneider, K. van 't Klooster, K. Picard, J. van der Gucht, T. Demura, M. Janson, A. Sampathkumar, E. E. Deinum, T. Ketelaar, and S. Persson, *Long-term single-cell imaging and simulations of microtubules reveal driving forces for wall pattering during proto-xylem development*, bioRxiv , (2020).

[212] E. M. Ozbudak, A. Becskei, and A. van Oudenaarden, *A system of counteracting feedback loops regulates Cdc42p activity during spontaneous cell polarization*, Developmental Cell **9**, 565 (2005).

[213] Y. Sako, K. Hibino, T. Miyauchi, Y. Miyamoto, M. Ueda, and T. Yanagida, *Single-molecule imaging of signaling molecules in living cells*, Single Molecules **1**, 159 (2000).

[214] B. Zhang and Y. Zheng, *Regulation of RhoA GTP hydrolysis by the GTPase-activating proteins p190, p50RhoGAP, Bcr, and 3BP-1*, Biochemistry **37**, 5249 (1998).

[215] M. Laubscher, K. Brown, L. B. Tonfack, A. A. Myburg, E. Mizrachi, and S. G. Hussey, *Temporal analysis of Arabidopsis genes activated by Eucalyptus grandis NAC transcription factors associated with xylem fibre and vessel development*, Scientific Reports **8**, 10983 (2018).

[216] A. Boudaoud, *An introduction to the mechanics of morphogenesis for plant biologists*, Trends in plant science **15**, 353 (2010).

[217] A. Sapala, A. Runions, A.-L. Routier-Kierzkowska, M. Das Gupta, L. Hong, H. Hofhuis, S. Verger, G. Mosca, C.-B. Li, A. Hay, O. Hamant, A. H. Roeder, M. Tsiantis, P. Prusinkiewicz, and R. S. Smith, *Why plants make puzzle cells, and how their shape emerges*, eLife **7**, e32794 (2018).

[218] S. A. Braybrook and H. Jönsson, *Shifting foundations: the mechanical cell wall and development*, Current opinion in plant biology **29**, 115 (2016).

[219] G. Levesque-Tremblay, J. Pelloux, S. A. Braybrook, and K. Müller, *Tuning of pectin methylesterification: consequences for cell wall biomechanics and development*, Planta **242**, 791 (2015).

[220] M. Ogden, R. Hoefgen, U. Roessner, S. Persson, and G. A. Khan, *Feeding the walls: how does nutrient availability regulate cell wall composition?*, International journal of molecular sciences **19**, 2691 (2018).

[221] P. Foteinopoulos and B. M. Mulder, *The effect of anisotropic microtubule-bound nucleations on ordering in the plant cortical array*, Bulletin of mathematical biology **76**, 2907 (2014).

[222] J. W. Vos, M. Dogterom, and A. M. C. Emons, *Microtubules become more dynamic but not shorter during preprophase band formation: A possible "search-and-capture" mechanism for microtubule translocation*, Cell Motility and the Cytoskeleton **57**, 246 (2004).

[223] J.-g. Chiou, K. D. Moran, and D. J. Lew, *How cells determine the number of polarity sites*, eLife **10**, e58768 (2021).

[224] B. J. Terry and D. L. Purich, *Nucleotide release from tubulin and nucleoside-5'-diphosphate kinase action in microtubule assembly.*, Journal of Biological Chemistry **254**, 9469 (1979).

[225] E. D. Salmon, W. M. Saxton, R. J. Leslie, M. L. Karow, and J. R. McIntosh, *Diffusion coefficient of fluorescein-labeled tubulin in the cytoplasm of embryonic cells of a sea urchin: video image analysis of fluorescence redistribution after photobleaching.*, Journal of Cell Biology **99**, 2157 (1984).

[226] L. Morejohn, T. Bureau, J. Mole-Bajer, A. Bajer, and D. Fosket, *Oryzalin, a dinitroaniline herbicide, binds to plant tubulin and inhibits microtubule polymerization in vitro*, Planta **172**, 252 (1987).

[227] E. Kawamura and G. O. Wasteneys, *Mor1, the arabidopsis thaliana homologue of xenopus map215, promotes rapid growth and shrinkage, and suppresses the pausing of microtubules in vivo*, Journal of cell science **121**, 4114 (2008).

[228] Y. Mineyuki, *The preprophase band of microtubules: Its function as a cytokinetic apparatus in higher plants*, in *International Review of Cytology (Volume 187)*, edited by K. W. Jeon (Academic Press, 1999).

[229] C. A. Tovey and P. T. Conduit, *Microtubule nucleation by γ-tubulin complexes and beyond*, Essays in Biochemistry **62**, 765 (2018).

[230] A. Thawani, H. A. Stone, J. W. Shaevitz, and S. Petry, *Spatiotemporal organization of branched microtubule networks*, eLife **8**, e43890 (2019).

[231] E. Dvořák Tomaštíková, T. Rutten, P. Dvořák, A. Tugai, K. Ptošková, B. Petrovská, D. Van Damme, A. Houben, J. Doležel, and D. Demidov, *Functional divergence of microtubule-associated TPX2 family members in Arabidopsis thaliana*, International journal of molecular sciences **21**, 2183 (2020).

[232] A. Kirik, D. W. Ehrhardt, and V. Kirik, *TONNEAU2/FASS regulates the geometry of microtubule nucleation and cortical array organization in interphase Arabidopsis cells*, Plant Cell Online **24**, 1158 (2012).

[233] J. Crank and P. Nicolson, *A practical method for numerical evaluation of solutions of partial differential equations of the heat-conduction type*, Mathematical Proceedings of the Cambridge Philosophical Society **43**, 50 (1947).

[234] F. Ruhnow, D. Zwicker, and S. Diez, *Tracking single particles and elongated filaments with nanometer precision*, Biophysical Journal **100**, 2820 (2011).

[235] M. Dogterom and S. Leibler, *Physical aspects of the growth and regulation of microtubule structures*, Phys. Rev. Lett. **70**, 1347 (1993).

[236] C. P. Brangwynne, F. C. MacKintosh, and D. A. Weitz, *Force fluctuations and polymerization dynamics of intracellular microtubules*, Proc. Natl. Acad. Sci. **104**, 16128 (2007).

[237] C. Pallavicini, V. Levi, D. Wetzler, J. Angiolini, L. Benseñor, M. Despósito, and L. Bruno, *Lateral motion and bending of microtubules studied with a new single-filament tracking routine in living cells*, Biophysical Journal **106**, 2625 (2014).

[238] T. Hawkins, M. Mirigian, M. Selcuk Yasar, and J. L. Ross, *Mechanics of microtubules*, Journal of Biomechanics **43**, 23 (2010).

[239] M. Kubo, M. Udagawa, N. Nishikubo, G. Horiguchi, M. Yamaguchi, J. Ito, T. Mimura, H. Fukuda, and T. Demura, *Transcription switches for protoxylem and metaxylem vessel formation*, Genes & Development **19**, 1855 (2005).

[240] Y. Sugiyama, Y. Nagashima, M. Wakazaki, M. Sato, K. Toyooka, H. Fukuda, and Y. Oda, *A Rho-actin signaling pathway shapes cell wall boundaries in Arabidopsis xylem vessels*, Nature Communications **10**, 468 (2019).

[241] M. Dogterom and G. H. Koenderink, *Actin-microtubule crosstalk in cell biology*, Nature Reviews Molecular Cell Biology **20**, 38 (2019).

[242] J. Petrášek and K. Schwarzerová, *Actin and microtubule cytoskeleton interactions*, Current Opinion in Plant Biology **12**, 728 (2009).

[243] P. A. Vesk, D. G. Rayns, and M. Vesk, *Imaging of plant microtubules with high resolution scanning electron microscopy*, Protoplasma **182**, 71 (1994).

[244] P. A. Vesk, M. Vesk, and B. E. S. Gunning, *Field emission scanning electron microscopy of microtubule arrays in higher plant cells*, Protoplasma **195**, 168 (1996).

[245] D. Barton, J. Gardiner, and R. Overall, *Towards correlative imaging of plant cortical microtubule arrays: combining ultrastructure with real-time microtubule dynamics*, Journal of Microscopy **235**, 241 (2009).

[246] V. Fache, J. Gaillard, D. Van Damme, D. Geelen, E. Neumann, V. Stoppin-Mellet, and M. Vantard, *Arabidopsis kinetochore fiber-associated MAP65-4 cross-links microtubules and promotes microtubule bundle elongation*, Plant Cell Online **22**, 3804 (2010).

[247] J. Gaillard, E. Neumann, D. Van Damme, V. Stoppin-Mellet, C. Ebel, E. Barbier, D. Geelen, and M. Vantard, *Two microtubule-associated proteins of Arabidopsis MAP65s promote antiparallel microtubule bundling*, Molecular Biology of the Cell **19**, 4534 (2008).

[248] A. Tulin, S. McClerklin, Y. Huang, and R. Dixit, *Single-molecule analysis of the microtubule cross-linking protein MAP65-1 reveals a molecular mechanism for contact-angle-dependent microtubule bundling*, Biophysical Journal **102**, 802 (2012).

[249] V. Stoppin-Mellet, V. Fache, D. Portran, J.-L. Martiel, and M. Vantard, *MAP65 coordinate microtubule growth during bundle formation*, PLoS One **8**, 1 (2013).

[250] S. L. Shaw and J. Lucas, *Intrabundle microtubule dynamics in the Arabidopsis cortical array*, Cytoskeleton **68**, 56 (2011).

[251] A. V. Korolev, H. Buschmann, J. H. Doonan, and C. W. Lloyd, *AtMAP70-5, a divergent member of the MAP70 family of microtubule-associated proteins, is required for anisotropic cell growth in arabidopsis*, Journal of Cell Science **120**, 2241 (2007).

[252] M. Wieczorek, S. Bechstedt, S. Chaaban, and G. J. Brouhard, *Microtubule-associated proteins control the kinetics of microtubule nucleation*, Nature Cell Biology **17**, 907 (2015).

[253] A. Thawani, M. J. Rale, N. Coudray, G. Bhabha, H. A. Stone, J. W. Shaevitz, and S. Petry, *The transition state and regulation of γ-TuRC-mediated microtubule nucleation revealed by single molecule microscopy*, eLife **9**, e54253 (2020).

[254] E. E. Deinum, *Simple models for complex questions on plant development*, Ph.D. thesis, Wageningen University, 2013.

[255] S. Verger, Y. Long, A. Boudaoud, and O. Hamant, *A tension-adhesion feedback loop in plant epidermis*, eLife **7**, e34460 (2018).

[256] S. Takatani, S. Verger, T. Okamoto, T. Takahashi, O. Hamant, and H. Motose, *Microtubule response to tensile stress is curbed by NEK6 to buffer growth variation in the arabidopsis hypocotyl*, Current Biology **30**, 1491 (2020).

[257] O. Hamant, D. Inoue, D. Bouchez, J. Dumais, and E. Mjolsness, *Are microtubules tension sensors?*, Nature Communications **10**, 2360 (2019).

[258] Z. Liu, R. Schneider, C. Kesten, Y. Zhang, M. Somssich, Y. Zhang, A. R. Fernie, and S. Persson, *Cellulose-microtubule uncoupling proteins prevent lateral displacement of microtubules during cellulose synthesis in Arabidopsis*, Developmental Cell **38**, 305 (2016).

[259] F. Sainsbury, D. A. Collings, K. Mackun, J. Gardiner, J. D. Harper, and J. Marc, *Developmental reorientation of transverse cortical microtubules to longitudinal directions: a role for actomyosin-based streaming and partial microtubule-membrane detachment*, Plant Journal **56**, 116 (2008).

[260] K. Bürstenbinder, B. Möller, R. Plötner, G. Stamm, G. Hause, D. Mitra, and S. Abel, *The IQD family of calmodulin-binding proteins links calcium signaling to microtubules, membrane subdomains, and the nucleus*, Plant Physiology **173**, 1692 (2017).

[261] K. Bürstenbinder, D. Mitra, and J. Quegwer, *Functions of IQD proteins as hubs in cellular calcium and auxin signaling: A toolbox for shape formation and tissue-specification in plants?*, Plant Signaling & Behavior **12**, e1331198 (2017).

[262] M. Kölling, P. Kumari, and K. Bürstenbinder, *Calcium- and calmodulin-regulated microtubule-associated proteins as signal-integration hubs at the plasma membrane–cytoskeleton nexus*, Journal of Experimental Botany **70**, 387 (2018).

[263] Y. Oda, T. Mimura, and S. Hasezawa, *Regulation of secondary cell wall development by cortical microtubules during tracheary element differentiation in arabidopsis cell suspensions*, Plant Physiology **137**, 1027 (2005).

[264] A. B. Goryachev and M. Leda, *Compete or coexist? why the same mechanisms of symmetry breaking can yield distinct outcomes*, Cells **9**, (2020).

[265] F. Brauns, H. Weyer, J. Halatek, J. Yoon, and E. Frey, *Wavelength selection by interrupted coarsening in reaction-diffusion systems*, Phys. Rev. Lett. **126**, 104101 (2021).

[266] O. Brandman and T. Meyer, *Feedback loops shape cellular signals in space and time*, Science **322**, 390 (2008).

[267] G. Feiguelman, Y. Fu, and S. Yalovsky, *ROP GTPases structure-function and signaling pathways*, Plant Physiology **176**, 57 (2017).

[268] V. A. Grieneisen, A. F. Marée, and L. Østergaard, *Juicy stories on female reproductive tissue development: Coordinating the hormone flows*, Journal of Integrative Plant Biology **55**, 847 (2013).

[269] A. R. Champneys, F. Al Saadi, V. F. Breña-Medina, V. A. Grieneisen, A. F. Marée, N. Verschueren, and B. Wuyts, *Bistability, wave pinning and localisation in natural reaction-diffusion systems*, Physica D **416**, 132735 (2021).

[270] K. Abley, P. B. De Reuille, D. Strutt, A. Bangham, P. Prusinkiewicz, A. F. M. Marée, V. A. Grieneisen, and E. Coen, *An intracellular partitioning-based framework for tissue cell polarity in plants and animals*, Development **140**, 2061 (2013).

[271] A. Sampathkumar, P. Krupinski, R. Wightman, P. Milani, A. Berquand, A. Boudaoud, O. Hamant, H. Jönsson, and E. M. Meyerowitz, *Subcellular and supracellular mechanical stress prescribes cytoskeleton behavior in Arabidopsis cotyledon pavement cells*, eLife **3**, e01967 (2014).

[272] G. ten Broeke, G. van Voorn, and A. Ligtenberg, *Which sensitivity analysis method should I use for my agent-based model?*, Journal of Artificial Societies and Social Simulation **19**, 5 (2016).

[273] J. M. Johnson, M. Jin, and D. J. Lew, *Symmetry breaking and the establishment of cell polarity in budding yeast*, Current Opinion in Genetics & Development **21**, 740 (2011).

[274] A. E. Golding, I. Visco, P. Bieling, and W. M. Bement, *Extraction of active RhoGTPases by RhoGDI regulates spatiotemporal patterning of RhoGTPases*, eLife **8**, e50471 (2019).

[275] R. J. Carol, S. Takeda, P. Linstead, M. C. Durrant, H. Kakesova, P. Derbyshire, S. Drea, V. Zarsky, and L. Dolan, *A RhoGDP dissociation inhibitor spatially regulates growth in root hair cells*, Nature **438**, 1013 (2005).

[276] J. Sun, D. M. Eklund, A. Montes-Rodriguez, and B. Kost, *In vivo Rac/Rop localization as well as interaction with RhoGAP and RhoGDI in tobacco pollen tubes: analysis by low-level expression of fluorescent fusion proteins and bimolecular fluorescence complementation*, Plant Journal **84**, 83 (2015).

[277] P. Winge, T. Brembu, R. Kristensen, and A. M. Bones, *Genetic structure and evolution of RAC-GTPases in Arabidopsis thaliana*, Genetics **156**, 1959 (2000).

[278] M. Smokvarska, Y. Jaillais, and A. Martinière, *Function of membrane domains in rho-of-plant signaling*, Plant Physiology **185**, 663 (2021).

[279] M. Lavy and S. Yalovsky, *Association of Arabidopsis type-II ROPs with the plasma membrane requires a conserved C-terminal sequence motif and a proximal polybasic domain*, Plant Journal **46**, 934 (2006).

[280] N. Sorek, L. Poraty, H. Sternberg, E. Buriakovsky, E. Bar, E. Lewinsohn, and S. Yalovsky, *Corrected and republished from: Activation status-coupled transient S-acylation determines membrane partitioning of a plant Rho-related GTPase*, Molecular and Cellular Biology **37**, e00333 (2017).

[281] H. Sternberg, E. Buriakovsky, D. Bloch, O. Gutman, Y. I. Henis, and S. Yalovsky, *Formation of self-organizing functionally distinct Rho of plants domains involves a reduced mobile population*, Plant Physiology **187**, 2485 (2021).

[282] M. Fratini, P. Krishnamoorthy, I. Stenzel, M. Riechmann, M. Matzner, K. Bacia, M. Heilmann, and I. Heilmann, *Plasma membrane nano-organization specifies phosphoinositide effects on Rho-GTPases and actin dynamics in tobacco pollen tubes*, Plant Cell **33**, 642 (2020).

[283] V. A. F. Fuchs, P. Denninger, M. Župunski, Y. Jaillais, U. Engel, and G. Grossmann, *Nanodomain-mediated lateral sorting drives polarization of the small GTPase ROP2 in the plasma membrane of root hair cells*, bioRxiv , (2021).

[284] A. Remorino, S. De Beco, F. Cayrac, F. Di Federico, G. Cornilleau, A. Gautreau, M. C. Parrini, J.-B. Masson, M. Dahan, and M. Coppey, *Gradients of Rac1 nanoclusters support spatial patterns of Rac1 signaling*, Cell Reports **21**, 1922 (2017).

[285] J. Meca, A. Massoni-Laporte, D. Martinez, E. Sartorel, A. Loquet, B. Habenstein, and D. McCusker, *Avidity-driven polarity establishment via multivalent lipid–GTPase module interactions*, EMBO Journal **38**, e99652 (2019).

[286] M. P. Platre, V. Bayle, L. Armengot, J. Bareille, M. del Mar Marquès-Bueno, A. Creff, L. Maneta-Peyret, J.-B. Fiche, M. Nollmann, C. Miège, P. Moreau, A. Martinière, and Y. Jaillais, *Developmental control of plant Rho GTPase nano-organization by the lipid phosphatidylserine*, Science **364**, 57 (2019).

[287] X. Pan, L. Fang, J. Liu, B. Senay-Aras, W. Lin, S. Zheng, T. Zhang, J. Guo, U. Manor, J. Van Norman, W. Chen, and Z. Yang, *Auxin-induced signaling protein nanoclustering contributes to cell polarity formation*, Nature Communications **11**, 3914 (2020).

[288] M. Smokvarska, C. Francis, M. P. Platre, J.-B. Fiche, C. Alcon, X. Dumont, P. Nacry, V. Bayle, M. Nollmann, C. Maurel, Y. Jaillais, and A. Martiniere, *A plasma membrane nanodomain ensures signal specificity during osmotic signaling in plants*, Current Biology **30**, 4654 (2020).

[289] Y. Jaillais and T. Ott, *The nanoscale organization of the plasma membrane and its importance in signaling: A proteolipid perspective*, Plant Physiology **182**, 1682 (2019).

[290] A. Seth, T. Otomo, H. L. Yin, and M. K. Rosen, *Rational design of genetically encoded fluorescence resonance energy transfer-based sensors of cellular Cdc42 signaling*, Biochemistry **42**, 3997 (2003).

[291] B. N. Goguen, G. S. Loving, and B. Imperiali, *Development of a fluorogenic sensor for activated Cdc42*, Bioorganic & Medicinal Chemistry Letters **21**, 5058 (2011).

[292] B. T. Bajar, X. Guan, A. Lam, M. Z. Lin, R. Yasuda, T. Laviv, and J. Chu, *FRET imaging of Rho GTPase activity with red fluorescent protein-based FRET pairs*, in *Cell Polarity Signaling: Methods and Protocols*, edited by C. Chang and J. Wang (Springer US, New York, NY, 2022).

[293] S. Abel, K. Bürstenbinder, and J. Müller, *The emerging function of IQD proteins as scaffolds in cellular signaling and trafficking*, Plant Signaling & Behavior **8**, e24369 (2013).

[294] Z. Bao, Z. Xu, J. Zang, K. Bürstenbinder, and P. Wang, *The morphological diversity of plant organs: Manipulating the organization of microtubules may do the trick*, Frontiers in Cell and Developmental Biology **9**, (2021).

[295] V. Farmer, G. Arpağ, S. L. Hall, and M. Zanic, *XMAP215 promotes microtubule catastrophe by disrupting the growing microtubule end*, Journal of Cell Biology **220**, e202012144 (2021).

[296] I. Loiodice, M. E. Janson, P. Tavormina, S. Schaub, D. Bhatt, R. Cochran, J. Czupryna, C. Fu, and P. T. Tran, *Quantifying tubulin concentration and microtubule number throughout the fission yeast cell cycle*, Biomolecules **9**, (2019).

[297] L. Jin, X. Zhou, P. Xiu, W. Luo, Y. Huang, F. Yu, C. Kuang, Y. Sun, X. Liu, and Y. Xu, *Imaging and reconstruction of cell cortex structures near the cell surface*, Optics Communications **402**, 699 (2017).

[298] L. Colin, R. Martin-Arevalillo, S. Bovio, A. Bauer, T. Vernoux, M.-C. Caillaud, B. Landrein, and Y. Jaillais, *Imaging the living plant cell: from probes to quantification*, Plant Cell , (2021).

[299] G. G. Gundersen, S. Khawaja, and J. C. Bulinski, *Postpolymerization detyrosination of alpha-tubulin: a mechanism for subcellular differentiation of microtubules.*, Journal of Cell Biology **105**, 251 (1987).

[300] D. L. Gard and M. W. Kirschner, *Microtubule assembly in cytoplasmic extracts of Xenopus oocytes and eggs.*, Journal of Cell Biology **105**, 2191 (1987).

[301] K. Bürstenbinder, T. Savchenko, J. Müller, A. W. Adamson, G. Stamm, R. Kwong, B. J. Zipp, D. C. Dinesh, and S. Abel, *Arabidopsis calmodulin-binding protein IQ67-domain 1 localizes to microtubules and interacts with kinesin light chain-related protein-1*, Journal of Biological Chemistry **288**, 1871 (2013).

[302] S. Vanneste and J. Friml, *Calcium: The missing link in auxin action*, Plants **2**, 650 (2013).

[303] C. Guo, J. Zhou, and D. Li, *New insights into functions of IQ67-domain proteins*, Frontiers in Plant Science **11**, (2021).

[304] M. Théry and L. Blanchoin, *Microtubule self-repair*, Current Opinion in Cell Biology **68**, 144 (2021).

[305] A. Vemu, E. Szczesna, E. A. Zehr, J. O. Spector, N. Grigorieff, A. M. Deaconescu, and A. Roll-Mecak, *Severing enzymes amplify microtubule arrays through lattice GTP-tubulin incorporation*, Science **361**, eaau1504 (2018).

[306] S. Triclin, D. Inoue, J. Gaillard, Z. M. Htet, M. E. DeSantis, D. Portran, E. Derivery, C. Aumeier, L. Schaedel, K. John, C. Leterrier, S. L. Reck-Peterson, L. Blanchoin, and M. Théry, *Self-repair protects microtubules from destruction by molecular motors*, Nature Materials **20**, 883 (2021).

[307] L. Schaedel, K. John, J. Gaillard, M. V. Nachury, L. Blanchoin, and M. Théry, *Microtubules self-repair in response to mechanical stress*, Nature Materials **14**, 1156 (2015).

[308] C. Aumeier, L. Schaedel, J. Gaillard, K. John, L. Blanchoin, and M. Théry, *Self-repair promotes microtubule rescue*, Nature Cell Biology **18**, 1054 (2016).

[309] H. de Forges, A. Pilon, I. Cantaloube, A. Pallandre, A.-M. Haghiri-Gosnet, F. Perez, and C. Poüs, *Localized mechanical stress promotes microtubule rescue*, Current Biology **26**, 3399 (2016).

[310] M. Mikhaylova, B. M. C. Cloin, K. Finan, R. van den Berg, J. Teeuw, M. M. Kijanka, M. Sokolowski, E. A. Katrukha, M. Maidorn, F. Opazo, S. Moutel, M. Vantard, F. Perez, P. M. P. van Bergen en Henegouwen, C. C. Hoogenraad, H. Ewers, and L. C. Kapitein, *Resolving bundled microtubules using anti-tubulin nanobodies*, Nature Communications **6**, 7933 (2015).

[311] S. G. Duncombe, S. G. Chethan, and C. T. Anderson, *Super-resolution imaging illuminates new dynamic behaviors of cellulose synthase*, Plant Cell **34**, 273 (2021).

[312] A. Rätz, *Turing-type instabilities in bulk–surface reaction–diffusion systems*, Journal of Computational and Applied Mathematics **289**, 142 (2015).

[313] I. L. Novak, F. Gao, Y.-S. Choi, D. Resasco, J. C. Schaff, and B. M. Slepchenko, *Diffusion on a curved surface coupled to diffusion in the volume: Application to cell biology*, Journal of Computational Physics **226**, 1271 (2007).

[314] C. M. Elliott and T. Ranner, *Finite element analysis for a coupled bulk–surface partial differential equation*, IMA Journal of Numerical Analysis **33**, 377 (2012).

[315] E. E. Deinum and B. M. Mulder, *Modelling the plant microtubule cytoskeleton*, in *Mathematical Modelling in Plant Biology*, edited by R. J. Morris (Springer International Publishing, Cham, 2018).

Summary

Vascular plants employ an extensive vascular system, known as the xylem, to transport water from their roots to their leaves. Xylem vessels possess thick secondary cell walls that help them withstand the pressures generated during water transport. The cell wall reinforcements are deposited in a variety of intricate patterns, depending on the type of xylem. There are two types of primary xylem, the xylem that develops first in growing roots and shoots: protoxylem and metaxylem. Each type has a characteristic kind of wall pattern. Protoxylem has a ringed or spiral pattern, to allow further elongation, together with the surrounding tissue. Metaxylem has a pattern of regularly spaced gaps for radial transport. This pattern appears after the elongation phase and is more rigid than the protoxylem pattern. The xylem cell wall patterns are determined by underlying patterns of cortical microtubules, which guide the deposition of cell wall material. Establishing the microtubule pattern, in turn, requires localised activity so-called Rho of Plant (ROP) proteins. ROPs are a type of small GTPase, molecular switches with an active and an inactive form. Microtubules and small GTPases often act together in pattern formation at the cell membrane. Examples include tip growth of root hairs and pollen tubes, and development of the complex puzzle-pieced shape of the pavement cells in the leaf epidermis. In view of its fixed cylindrical cell shape, developing xylem is a good model system for understanding this type of process. In this thesis, I aim to improve our understanding of the way in which ROPs and microtubules generate the xylem patterns using dynamic models. Chapters 2 and 3 focus on ROP patterning, while chapters 4 and 5 deal with microtubule dynamics.

Xylem patterning requires the formation of spotted (metaxylem) or banded (protoxylem) ROP patterns. The molecular properties of ROPs and other small GTPases make them particularly suited to spontaneously form patterns through so-called reaction-diffusion mechanisms. Many models for this process exist, but most of them only yield a pattern with just one single stable cluster. Initially, these models may give rise to multiple clusters, but in the long run these clusters compete with each other until only one remains. This process resembles surface-tension-driven coarsening. Beyond the standard reaction-diffusion ingredients of self-activation and an inactive form that diffuses faster than the active form, these polarisation models have one more ingredient in common: conservation of the total amount of GTPase. In **chapter 2**, we show that a pattern of stable, coexisting clusters can be obtained when this so-called mass conservation is broken by adding GTPase turnover. We also show that adding negative feedback through GAPs (GTPase activating proteins) — proteins which inactivate GTPases by activating their GTP hydrolysis activity — allows for coexistence, even in mass conserved models. To study the mechanism driving coexistence, we construct an ordinary differential equation model, as a simplified version of the full partial differential equation model. With this simplified model, we show that turnover stabilises coexistence by providing a constant local source of GTPase to smaller clusters, effectively providing a GTPase redistribution, while GAP feedback makes larger clusters lose relatively more GTPase. These findings are relevant not only to xylem patterning, but to any GTPase-based patterning process

that requires multiple coexisting GTPase clusters. In particular, we show that models that allow coexistence also allow cluster splitting, which is vital for branching in tip growing fungal hyphae, where the tip is determined by a GTPase cluster.

While reaction-diffusion systems that allow coexistence reproduce the spotted metaxylem pattern well, they do not reproduce ringed or spiral protoxylem patterns, since they miss an intrinsic orienting force. In **chapter 3**, we investigate the possibility that this orienting force might be provided by a microtubule-based diffusion restriction of active ROP. Experimental studies have found that in metaxylem microtubules form a diffusion barrier to ROP proteins. It has also been observed that enhancing this barrier effect transforms the circular metaxylem gaps into more elongated stripes. Since protoxylem patterning starts with a transversely oriented microtubule array, we model the barrier effect as a longitudinal ROP diffusion restriction. That way, we show that this diffusion restriction is able to orient the ROP pattern into protoxylem-like bands, as long as inactive ROPs can bypass the barriers more easily than active ROP. Similarly, spiral ROP patterns can be obtained by making the direction of the diffusion restriction oblique. Furthermore, by analysing the diffusion term, we show that the orienting mechanism only affects patterns with curved features. This implies that existing banded or spiral patterns cannot be reoriented by a change in the direction of diffusion restriction. Finally, we study the effect of a ROP-driven reduction of microtubule density and, consequently, ROP diffusion restriction. We show that an instantaneous reduction of diffusion restriction with ROP activity is detrimental to the pattern orientation, while a delayed reduction allows formation of oriented bands. In its simplest form, this delay results in travelling waves of the ROP and microtubule densities. However, occurrence of these waves can be prevented by adding a positive feedback loop acting on the microtubule density. This demonstrates that the details of the microtubule implementation matter for the formation of the ROP pattern in protoxylem.

With these new insights into ROP patterning, we change our focus to questions related to microtubule patterning. Many structures formed by the plant cortical microtubule array require a uniform distribution of microtubules. The homogeneous, transversely oriented arrays of elongating interphase cells form a clear example of this requirement. However, the patterned arrays of developing xylem vessels also require a uniform distribution of microtubules over the regions where future cell wall formation will take place. This homogeneity requirement appears to be at odds with the experimental finding that most microtubules nucleate from existing microtubules, which introduces a positive feedback loop on local microtubule density: more nucleations are expected in denser microtubule patches, which may then grow even denser at the expense of the rest of the array. Indeed, modelling efforts that have tried to include these microtubule-based nucleations have generated highly inhomogeneous arrays, with, in the case of protoxylem patterning, all microtubules ending up in one or two bands. This process is strongly related to the competition between GTPase clusters from chapter 2. In **chapter 4**, we use a combination of experiments and a simplified one-dimensional microtubule model to study how this inhomogeneity problem could be avoided. To that end, we investigate two hypotheses: (1) a local limitation of the amount of tubulin available for microtubule growth, and (2) a locally limited availability of nucleation complexes for making new microtubules. Our simulations reveal that the first option requires an unrealistically low tubulin diffusion coefficient. For testing the second option, we experimentally determine the diffusion

coefficient of nucleation complexes at the membrane and characterise the rates at which nucleation complexes are inserted at the membrane, both in presence and in absence of microtubules. This way, we find that nucleation complexes are preferentially inserted near microtubules, and that these insertions appear to saturate locally with microtubule density. Using detailed simulations of nucleation complex behaviour at the cell membrane we show that the local saturation of nucleation complex insertion with microtubule density allows for the formation of homogeneous arrays as well as structured protoxylem arrays.

In the protoxylem simulations with the simplified one-dimensional model, all microtubules are perfectly aligned with the predefined band regions that we use to represent the underlying ROP pattern. In a two-dimensional context, microtubule orientations can be more variable, potentially complicating microtubule band formation. In **chapter 5**, we therefore use two-dimensional microtubule simulations to study protoxylem band formation. With these simulations, we show that protoxylem band formation in a biologically realistic time frame requires three important ingredients: (1) sufficient co-alignment of the initial microtubule array with the underlying ROP pattern, (2) sufficiently flexible microtubules with random fluctuations in their growth direction, and (3) a sufficiently realistic nucleation implementation in line with our findings from chapter 4. The first requirement may be biologically satisfied by the orienting effect of the microtubule array on the ROP pattern (as discussed in chapter 3). However, the co-alignment that could reasonably be expected from this orienting effect is only sufficient in our simulations if both microtubule flexibility and realistic nucleation are taken into account. Microtubule flexibility allows small mismatches in the initial co-alignment. However, the flexible microtubules can also bend in the direction of the microtubule destabilising gap regions, which is detrimental to maintaining microtubule density in the bands. A simplified version of the nucleation mechanics presented in chapter 4, moves some of the nucleations from the gaps to the bands, compensating for the negative effect of flexibility. Our improved simulations explain band formation with microtubule dynamics parameters measured in real cells undergoing the protoxylem differentiation program better than previous efforts. The discrepancies that remain, reveal the involvement of additional band formation forces in protoxylem patterning that are not captured by the currently measured parameters.

In conclusion, our efforts to study ROP and microtubule patterning separately not only improve our understanding of their individual contributions to xylem patterning, but also reveal the points where their interplay is vital. Our findings pave the way for future research integrating ROP and microtubule models to better study the interplay between the two, both in xylem patterning and in other cases of patterning involving ROPs and microtubules.

Samenvatting

Om water van wortels naar bladeren te transporteren hebben vaatplanten een uitgebreid stelsel van zogeheten houtvaten: het xyleem. Deze houtvaten hebben een stevige secundaire celwand, die nodig is om bestand te zijn tegen drukverschillen die ontstaan tijdens het watertransport. De eerste houtvaten die in groeiende wortels en scheuten gevormd worden behoren tot het zogeheten primaire xyleem, waarvan er twee soorten bestaan: protoxyleem en metaxyleem. De celwandverdikkingen van protoxyleem worden in ringen of spiralen aangelegd, zodat dit type houtvaten nog mee kan rekken met het omringende weefsel. Metaxyleem ontstaat pas als dit strekken gestopt is en krijgt daarom stevigere celwandverdikkingen, met gaten voor radiaal transport op regelmatige afstanden. Deze celwandpatronen worden bepaald door een onderliggend patroon van corticale microtubuli aan de binnenkant van het celmembraan. Deze microtubuli bepalen waar en in welke richting de celwand wordt verstevigd. Het patroon van microtubuli vereist op zijn beurt weer een lokale activiteit van zogeheten ROP (Rho of Plant) eiwitten op de plekken waar de gaten in het celwandpatroon moeten vallen. ROP eiwitten zijn kleine GTPases, moleculaire schakelaars met een actieve en een inactieve vorm. Patroonvorming aan het celmembraan vereist vaker samenwerking van microtubuli en kleine GTPases, bijvoorbeeld bij het vaststellen van de groeiende punt in wortelharen en pollenbuizen, en bij het ontstaan van de puzzelstukjes-vorm van de epidermiscellen in bladeren. De ontwikkeling van xyleempatronen vormt een goed modelsysteem om dit proces te leren begrijpen, vanwege de constante, cilindrische vorm van de cellen. Mijn doel in dit proefschrift is daarom om ons inzicht in de vorming van deze patronen door ROPs en microtubuli te vergroten met behulp van dynamische modellen. Daarbij ligt de focus in hoofdstuk 2 en 3 op patroonvorming door ROPs, en in hoofdstuk 4 en 5 op patroonvorming door microtubuli.

Voor het vormen van de verschillende xyleempatronen moeten ROPs zowel een regelmatig patroon van stippen (metaxyleem) als van bandjes (protoxyleem) kunnen vormen. ROPs en andere kleine GTPases zijn door hun moleculaire eigenschappen zeer geschikt voor het vormen van dit soort regelmatige patronen via zogeheten reactie-diffusie-mechanismes. Er zijn veel modellen gemaakt om patroonvorming door GTPases via dit type mechanisme te beschrijven. De meeste daarvan kunnen echter alleen de vorming van één enkel stabiel GTPase-cluster reproduceren. In die modellen verschijnen er in eerste instantie weliswaar meerdere clusters, maar die concurreren vervolgens met elkaar tot er maar één overblijft. De modellen die dit gedrag vertonen, hebben, naast de standaard elementen van reactie-diffusie-modellen, ook met elkaar gemeen dat de totale hoeveelheid GTPase constant is. In **hoofdstuk 2** laten we zien dat het toevoegen van productie en afbraak van GTPase aan deze modellen voldoende is om een patroon van meerdere stabiele GTPase-clusters te krijgen. Daarnaast tonen we aan dat het toevoegen van negatieve feedback via GAPs (GTPase activating proteins) aan de modellen met massabehoud ook tot meerdere stabiele clusters leidt. Verder bestuderen we het co-existentie-mechanisme met een versimpeld model gebaseerd op gewone differentiaalvergelijkingen in plaats van partiële. Zo ontdekken we dat het verbreken van massabehoud kleinere clusters voorziet van een constante lokale bron van nieuw GTPase, terwijl negatieve feedback grotere

clusters zwaarder treft dan kleinere. Deze conclusies zijn relevant voor alle patronen waarin meerdere GTPase-clusters naast elkaar moeten bestaan en niet alleen voor protoen metaxyleem. Dit geldt ook voor systemen waarin clusters moeten kunnen splitsen, zoals cellen van schimmelhyfen die aan de punt groeien en vertakken door splitsing van deze groeiende punt.

Hoewel reactie-diffusie-mechanismes het stippenpatroon van metaxyleem goed kunnen reproduceren, hebben ze geen inherente voorkeur voor een bepaalde oriëntatie. Hierdoor kunnen ze niet zomaar een protoxyleempatroon van ringen of spiralen vormen. In **hoofdstuk 3** onderzoeken we of de oriëntatie van het ROP-patroon in protoxyleem opgelegd kan worden door microtubuli die een diffusie-barrière vormen voor actieve ROP-eiwitten. Experimentele studies gericht op metaxyleem hebben aangetoond dat microtubuli de diffusie van ROPs kunnen beperken en dat verhoogde diffusie-restrictie leidt tot een sterk afgeplat stippenpatroon dat meer op het protoxyleempatroon gaat lijken. We modelleren dit barrière-effect van microtubuli met een verlaagde diffusie van actieve ROP in de lengterichting, aangezien protoxyleemvorming begint met overdwars opgelijnde corticale microtubuli. In onze simulaties geeft deze diffusie-restrictie het ROP patroon de juiste oriëntatie, waardoor een bandenpatroon vergelijkbaar met dat in protoxyleem kan ontstaan. Dit effect werkt alleen zolang inactieve ROPs minder diffusie-restrictie ondervinden dan actieve ROPs. Op een vergelijkbare manier kunnen spiraalvormige patronen gevormd worden met een schuine diffusie-restrictie. Een analyse van de diffusieterm laat zien dat dit oriëntatie-mechanisme alleen werkt op patronen waar nog kromme lijnen in zitten. Eenmaal gevormd kunnen patronen van bandjes of spiralen dus geen andere oriëntatie meer krijgen via dit mechanisme. Tot slot bootsen we het effect van ROPs op de dichtheid van microtubuli na, door de diffusie-restrictie te verlagen bij hogere ROPconcentraties. Als dit effect direct ingaat, dan werkt het oriëntatie-mechanisme niet meer, maar als er een vertraging op zit, dan kunnen bandjes met de juiste oriëntatie wel vormen. De meest eenvoudige implementatie van deze vertraging veroorzaakt golven in de dichtheid van ROPs en microtubuli. Deze golven verdwijnen echter onder de aanname van een positieve feedback op de dichtheid van de microtubuli. De precieze implementatie van de microtubuli maakt dus sterk uit voor het ROP patroon dat gevormd wordt en een realistischer implementatie lijkt beter te werken voor het vormen van een protoxyleempatroon.

Na het bestuderen van de ROP-patronen richten we onze aandacht op de organisatie van de corticale microtubuli. Veel structuren die door microtubuli gevormd worden, vereisen een evenwichtige verdeling van de microtubuli. Een goed voorbeeld hiervan is te vinden in strekkende interfase-cellen, die een homogene verdeling van microtubuli hebben met een oriëntatie dwars op de lengterichting van de cel. De complexere patronen die zich vormen in ontwikkelende houtvaten vereisen echter ook een gelijkmatige verdeling van microtubuli over de plekken waar de celwand verstevigd moet worden. Veel microtubuli-modellen genereren echter sterk inhomogene structuren als ze nucleatie van nieuwe microtubuli laten plaatsvinden zoals dit in plantencellen voornamelijk gebeurt, namelijk vanaf bestaande microtubuli. Dit type nucleatie leidt al snel tot een positieve feedback waarbij meer nucleatie van nieuwe microtubuli plaatsvindt op plekken waar de dichtheid van microtubuli groter is, zodat de lokale dichtheid alleen maar verder toeneemt ten koste van plekken met een lagere dichtheid. Dit proces is sterk gerelateerd aan de concurrentie tussen GTPase-clusters uit hoofdstuk 2. In simulaties van protoxyleem

eindigen vrijwel alle microtubuli hierdoor in slechts één of twee bandjes. In **hoofdstuk 4** zoeken we oplossing voor dit inhomogeniteitsprobleem met een combinatie van experimenten en een vereenvoudigd eendimensionaal microtubuli-model. We bekijken twee verschillende hypotheses: (1) een lokale beperking in the hoeveelheid beschikbare tubuline voor de groei van microtubuli en (2) een lokaal beperkte beschikbaarheid van de nucleatiecomplexen die nodig zijn voor het maken van nieuwe microtubuli. In onze simulaties vereist de eerste hypothese een onrealistisch lage diffusiecoëfficiënt voor tubuline. Voor het testen van de tweede hypothese bepalen we experimenteel de diffusiecoëfficiënt van membraangebonden nucleatiecomplexen en de snelheid waarmee deze complexen in het membraan geplaatst worden in aan- en afwezigheid van microtubuli. Zo komen we erachter dat nucleatiecomplexen overwegend in het membraan verschijnen in de buurt van microtubuli en dat de snelheid waarmee dit gebeurt lijkt te verzadigen met de lokale dichtheid van de microtubuli. Aan de hand van deze bevindingen breiden we onze simulaties uit met een gedetailleerde implementatie van nucleatiecomplexen. Deze simulaties laten zien dat corticale microtubuli zowel homogene structuren als regelmatige patronen kunnen vormen wanneer de associatie van nieuwe complexen met het membraan lokaal verzadigt met de dichtheid van de microtubuli.

In de protoxyleemsimulaties met het eendimensionale model hebben alle microtubuli precies dezelfde oriëntatie als de vooraf opgelegde bandregio's die het onderliggende ROP-patroon vertegenwoordigen. Corticale microtubuli bevinden zich echter in een effectief tweedimensionale ruimte, waarin ze ook andere oriëntaties aan kunnen nemen. In **hoofdstuk 5** gebruiken we daarom tweedimensionale simulaties om bandvorming in protoxyleem te bestuderen. Deze simulaties laten zien dat voor bandvorming op een biologisch realistische tijdschaal drie dingen nodig zijn: (1) de initiële corticale microtubuli moeten grotendeels dezelfde oriëntatie hebben als het onderliggende ROP patroon, (2) de microtubuli moeten voldoende flexibiliteit hebben, in de vorm van willekeurige fluctuaties in hun groeirichting, en (3) de implementatie van de nucleaties moet voldoende realistisch zijn, in lijn met de resultaten van hoofdstuk 4. De eerste eis zou biologisch vervuld kunnen worden door doordat microtubuli de oriëntatie van het ROP-patroon kunnen bepalen, zoals we zagen in hoofdstuk 3. Dit mechanisme kan echter niet precies genoeg dezelfde oriëntatie garanderen als nodig is voor bandvorming door microtubuli in simulaties, tenzij er ook aan de laatste twee eisen wordt voldaan. De flexibele microtubuli zijn nodig om kleine discrepanties in de oriëntatie op te vangen. De flexibiliteit betekent echter ook dat microtubuli in de bandjes naar buiten kunnen buigen en in de gaten terecht kunnen komen, waar ze minder stabiel zijn. De realistische nucleatie is vervolgens nodig om hiervoor te compenseren en de dichtheid in de bandjes te behouden door nucleaties van de gaten naar de bandjes te verplaatsen. Met onze vernieuwde simulaties kunnen we bandvorming met parameters gemeten in echte cellen die differentiatie naar protoxyleem ondergaan beter verklaren dan eerdere simulatiestudies. Wel zijn er nog verschillen met de experimentele observaties. Deze verschillen duiden op vooralsnog onbekende bijdragen aan bandvorming die buiten de al gemeten parameters vallen.

In conclusie dragen de bevindingen die we hebben verkregen door ROPs en microtubuli apart te bestuderen niet alleen bij aan ons begrip van hun losse contributies, maar laten ze ook zien waar hun samenspel essentieel is. Hiermee leggen we de basis voor onderzoek waarin de modellen van ROPs en microtubuli samengevoegd worden, om zo dit samenspel beter te kunnen bestuderen, zowel bij de vorming van houtvaten als bij andere

patroonvormingsprocessen.

Acknowledgements

Although I am hardly the kind of person who went running around conferences networking with everyone, there are still many people who helped me in various ways over the past few years. I realise that saying "thanks" over and over for several pages is hardly the most imaginative way of expressing gratitude, but that does not make it any less sincere.

First of all, Eva, if you hadn't encouraged me, I probably wouldn't even have applied for the position. Thank you for being my supervisor and always trying to get the best out of me, both as a master student and during my PhD. The endless, sometimes illegible, handwritten red scribbles may have been demotivating at times, but they ultimately helped me improve my writing skills. Best of luck with your future research projects.

Jaap, thank you for being my promotor and always believing in me with you seemingly inexhaustible and sometimes slightly infuriating optimism. Also thank you for suggesting my current postdoc. I'm glad I don't have to say goodbye to Biometris just yet. Enjoy your retirement!

Tijs, thank you for being my external supervisor and for welcoming me to the cell biology group meetings. Your biological insights have been invaluable. Laura, thank you for letting me stay at the soft matter group in Utrecht and temporarily taking over from Eva as supervisor during her maternity leave. Your help on the technical simulation details has been most welcome. René, thanks for your efforts in obtaining the experimental data as well as all discussions and explanations relating to the cell biology and experimental methods.

Lia, thank you for all your advice, asked and unasked, and for always speaking your mind the way only you can do. Onno, thank you for the painstaking clarity of your education organisation. Thanks to you, I always knew exactly where to be and what to do. Enjoy your well-deserved retirement. Geerten, thanks for welcoming me into a cool new project. Hopefully it will be just as interesting as the last. Peter, in spite of all the pandemic restrictions at the start, you have made a great "new Jaap", with a nearly equally inexhaustible optimism. Gerard, thanks for all your philosophical conversations and for sparring with me about my propositions. Maikel, thanks for all computer-related assistance and figuring out all the linux-related issues.

Dinie, thank you for always knowing everything about anything non-scientific. You are the best secretary any group could wish for. I remember one day there was a minor fire in my apartment complex and the very next day you asked me about it, having somehow both learned about this obscure incident and remembered that I lived there.

Many thanks as well to all the other Biometris people who came and went over the years and made me feel part of the group, including Guus, Hilde, Dominique, Sylvana, Bart-Jan, Marco, Stephan, George, Patrick, Nadia, Vincent, Emilie, Henry, Kevin, Anna, Emma, Caspar, Casper, Milan, Christian, Laura, Hans, George, Evert-Jan, René, and many others that I am undoubtedly forgetting right now.

Thankfully, there was also room for non-work activities during my PhD, which are also an important part of life, as I sometimes tend to forget. Therefore, a big thanks to all friends, family, and others who made life enjoyable.

In particular, many thanks to my two paranymphs. Sylvana, thanks for dragging me off to climbing halls and larps in spite of always being so incredibly busy. Best of luck finishing your own PhD and don't work too hard. Bart-Jan, thanks for all the great Biometris board game evenings. May this tradition always continue.

Speaking of game evenings, Dorus, Jelle, Alma, Anouk, Liset, Merlijn, Joëlle, Ilse, Jeroen, Lonneke, and others, thank you for all the wonderful game evenings, movie nights, diners, and other activities, including online game nights during the pandemic.

Thanks as well to everyone I worked with on designing questions for the Dutch Biology Olympiad, as well as all the other wonderful Rubisco people. I've learned a lot from you all and it's great to be a part of such a fine group of bio-nerds. Hopefully there can be another KOEN again this year.

Also, a big thanks to all "Schermutselaers", for over a decade of fencing, and many associated social activities.

Pien, thanks for all the wonderful conversations about books and movies and more books. It's great to have someone to talk about super geeky stuff with. Rosalie, thanks for all our discussions and for starting up corridor activities. Thanks to your efforts, I've actually known my neighbours for a change.

I would also like to thank Bouwe, Marinke, Jeanine, Romano, Eline, Norbert, and everyone else at Jados. Your help has been invaluable, from my bachelor to my PhD.

Last but not least, I would like to thank my family, in particular my parents, brother and sister. Rik, I don't know how you manage to work as hard as you do and yet still do tons of social stuff as well. Just save some time for a game with your brother every now and then. Lynn, if we could just swap some of my carefulness with some of your boldness, we would both be unstoppable. Enjoy your time in Spain, but do come home eventually. Mom and dad, thank you for always supporting me, even when things are not going so well. There is no way I would have made it this far without you to fall back on.

List of publications

- Bas Jacobs, Jaap Molenaar, and Eva E. Deinum, *Small GTPase patterning: How to stabilise cluster coexistence*, PLOS ONE 14(3): e0213188 (2019)
- Bas Jacobs, Jaap Molenaar, and Eva E. Deinum, *Robust banded protoxylem pattern formation through microtubule-based directional ROP diffusion restriction*, Journal of Theoretical Biology 502: 110351 (2020)
- Bas Jacobs, René Schneider, Jaap Molenaar, Laura Filion, Eva E. Deinum, *Nucleation complex behaviour is critical for cortical microtubule array homogeneity and patterning* (submitted)

Education Statement of the Graduate School
Experimental Plant Sciences

Issued to: Bas Jacobs
Date: 01 July 2022
Group: Biometris
University: Wageningen University & Research

1) Start-Up Phase	date	cp
► **First presentation of your project**		
Polarisation and coexistence in small GTPase-based membrane patterning	June 1, 2018	1,5
► **Writing or rewriting a project proposal**		
Modelling of cellular patterning during plant growth	1-dec-17	6,0
► **Writing a review or book chapter**		
► **MSc courses**		
Multivariate Mathematics Applied (MAT-23306)	2017	6,0
Subtotal Start-Up Phase		13,5

2) Scientific Exposure	date	cp
► **EPS PhD student days**		
EPS PhD student days 'Get2Gether' 2018, Soest (NL)	Feb 15-16, 2018	0,6
EPS PhD student days 'Get2Gether' 2019, Soest (NL)	Feb 11-12, 2019	0,6
Biometris PhD day 2018, Wageningen (NL)	Aug 31, 2018	0,3
► **EPS theme symposia**		
EPS theme 1 'Developmental Biology of Plants', Wageningen (NL)	Jan 30, 2018	0,3
EPS theme 1 'Developmental Biology of Plants', Wageningen (NL)	Feb 5, 2020	0,3
EPS theme 1 'Developmental Biology of Plants', online	Jan 28, 2021	0,1
► **Lunteren Days and other national platforms**		
Annual Meeting Experimental Plant Sciences (EPS), Lunteren (NL)	Apr 9-10, 2018	0,6
Annual Meeting Experimental Plant Sciences (EPS), Lunteren (NL)	Apr 8-9, 2019	0,6
Annual Meeting Dutch Society for Theoretical Biology (NVTB), Schoorl (NL)	May 23-24, 2019	0,6
Annual Bioinformatics & Systems Biology Conference (BioSB), Lunteren (NL)	May 15-16, 2018	0,6
Dutch Biophysics meeting, Veldhoven (NL)	Oct 1-2, 2018	0,6
Dutch Biophysics meeting, online	Oct 5-6, 2020	0,6
► **Seminars (series), workshops and symposia**		
Seminar Lisanne Rens: Hybrid cellular Potts model including focal adhesions as catch bond clusters explains cell response to substrate stiffness	Sep 22, 2017	0,1
Seminar Jean-Francois Arrighi: Evolution of Nod factor-independent rhizobium symbiosis	Oct 18, 2017	0,1
Seminar Giles Oldroyd: Recognition of symbiotic microorganisms by plants	Oct 19, 2017	0,1
Seminar Thomas Surrey: Mechanistic insight from reverse engineering the microtubule cytoskeleton	Nov 17, 2017	0,1
Seminar David Bouchez: Division site selection in plant cells	Nov 17, 2017	0,1
Seminar Jörg Blasius: Assessing the quality of survey data	Mar 9, 2018	0,1
Seminar Yin Shenglai: Habitat loss facilitates infection outbreak and pathogen dispersal: An agent-based model of infected migratory waterfowl	May 4, 2018	0,1
Seminar Frank van Langevelde: Social resilience in honeybee colonies	May 18, 2018	0,1
Seminar Yvon Jaillais: A tunable lipid rheostat steers Rho-mediated auxin signalling	Sep 7, 2018	0,1
Seminar Alexis Maizel: Lateral root morphogenesis in Arabidopsis: from cytoskeleton to metabolism	Dec 17, 2018	0,1
Seminar Romain Frelat: Complexity in fish diversity: a multi-scale, multi-dimensional and multidisciplinary approach	Apr 26, 2019	0,1
Seminar Massimiliano Chiappini: Biaxial, twist-bend, and splay-bend nematic phases of bananashaped particles revealed by lifting the "Smectic Blanket"	Jan 15, 2020	0,1
Seminar Ingrid Graz: Bio-inspired soft electronics and robotics	Feb 7, 2020	0,1
Seminar Els Weinans: A potential feedback loop underlying glacial-interglacial cycles	Jun 19, 2020	0,1
Seminar Hilje Doekes: Modelling the evolution of microbes at multiple scales	Jan 29, 2021	0,1
Seminar Marco Saltini: Adaptive diversification and ontogenetic niche shifts: potential for evolutionary branching in stage-structured populations	Sep 10, 2021	0,1
Symposium: Mathematical biology in the Netherlands, Utrecht (NL)	Aug 29, 2018	0,3
Mini-symposium: Cell biology of biotic interactions, Wageningen (NL)	Oct 17, 2019	0,2
► **Seminar plus**		
► **International symposia and congresses**		
Symposium Plant Developmental Systems Biology, Wageningen (NL)	Oct 4, 2017	0,3
European Plant Science Retreat (EPSR) 2018, Utrecht (NL)	Jul 3-6, 2018	1,0
EMBO | EMBL Symposium: Microtubules: From Atoms to Complex Systems, online	Jun 3-6, 2020	1,2
EMBO | EMBL Symposium: Life at the Periphery: Mechanobiology of the Cell Surface, online	Mar 2-3, 2021	0,6
Annual Conference Society for Mathematical Biology (SMB) 2021, online	Jun 14-17, 2021	1,2
► **Presentations**		
Poster: Modelling pattern formation in proto- and metaxylem by ROP signalling (EPS meeting 2018)	Apr 9, 2018	1,0
Poster: Polarisation vs multiple peaks in GTPase-based membrane patterning (BioSB meeting 2018)	May 15, 2018	1,0
Poster: From spots to stripes: Models for ROP-based xylem patterning (EPSR 2018)	Jul 5, 2018	1,0
Poster: Small GTPases: Similar systems, different membrane patterns (Dutch Biophysics 2018)	Oct 1, 2018	1,0
Digital poster: Mechanisms for band formation in the plant cortical microtubule array (EMBO | EMBL Symposium: Microtubules: From Atoms to Complex Systems 2020)	Jun 3-6, 2020	1,0
Talk: Models reveal possible mechanisms for stable coexistence of ROP clusters (EPS meeting 2019)	Apr 9, 2019	1,0
Talk: Small GTPase patterning: How to stabilise cluster coexistence (NVTB meeting 2019)	May 24, 2019	1,0
Talk: Microtubule barriers shape ROP patterning in protoxylem (Dutch Biophysics 2020)	Oct 6, 2020	1,0
Talk: How nucleation complexes ensure homogeneity in the plant cortical microtubule array (EPS theme 1 symposium 2021)	Jan 28, 2021	1,0
Talk: Nucleation complex dynamics supports both homogeneous and intricately structured plant cortical microtubule arrays (EMBO | EMBL Symposium: Life at the Periphery: Mechanobiology of the Cell Surface 2021)	Mar 2, 2021	1,0
► **IAB interview**		
► **Excursions**		
Subtotal Scientific Exposure		22,2

3) In-Depth Studies	date	cp
► **Advanced scientific courses & workshops**		
BioSB course: Quantitative and predictive modelling, Wageningen (NL)	Jun 26-30, 2017	3,0
High Performance Computing Cluster (HPC) basic course (FB-IT), Wageningen (NL)	May 17, 2018	0,2
High Performance Computing Cluster (HPC) GPU basic course (FB-IT and Dell EMC), Wageningen (NL)	Jun 21, 2019	0,3
PH125.8x Data Science: Machine Learning (edX), online	May 2020	0,9
► **Journal club**		
► **Individual research training**		
Lab visit and computational physics training with Laura Filion at the soft condensed matter group of Utrecht University	Dec 2019 - Mar 2020	3,0
Subtotal In-Depth Studies		7,4

CONTINUED ON NEXT PAGE

4) Personal Development		date	cp
►	**General skill training courses**		
	PhD Competence Assessment, Wageningen (NL)	Nov 14, 2017	0,3
	EPS PhD Introduction Course, Wageningen (NL)	Mar 27, 2018	0,3
	Course: The Essentials of Scientific Writing and Presenting, Wageningen (NL)	Oct 5-15, 2018	1,2
	Course: Career Orientation, Wageningen (NL)	Oct 8-29, 2019	1,5
►	**Organisation of meetings, PhD courses or outreach activities**		
	Organisation Biometris PhD day 2018	Aug 31, 2018	1,5
	Question design for the general theoretical test of the Dutch national biology olympiad	2017-2022	1,5
►	**Membership of EPS PhD Council**		
	Subtotal Personal Development		6,3

TOTAL NUMBER OF CREDIT POINTS*	**49,4**

Herewith the Graduate School declares that the PhD candidate has complied with the educational requirements set by the Educational Committee of EPS with a minimum total of 30 ECTS credits.

** A credit represents a normative study load of 28 hours of study.*

The research described in this thesis was carried out at Biometris, chair group of Mathematical and Statistical Methods, Wageningen University, the Netherlands. The work in chapter 4 was initiated at Utrecht University during a three month research internship in the soft condensed matter group.

Financial support from Wageningen University for printing this thesis is gratefully acknowledged.

Cover design by Bas Jacobs

Printed by Proefschriftmaken || DigiForce